# IOWA STATE UNIVERSITY
**Digital Repository**

2012

# Numerical and experimental investigations on unsteady aerodynamics of flapping wings

Meilin Yu

*Iowa State University*

### Recommended Citation

**Numerical and experimental investigations on unsteady aerodynamics of flapping wings**


by


**Meilin Yu**



A dissertation submitted to the graduate faculty

In partial fulfillment of the requirements for the degree of

DOCTOR OF PHILOSOPHY



Major:  Aerospace Engineering


Program of Study Committee:
Hui Hu, Co-major Professor
Z. J. Wang, Co-major Professor
Paul Durbin
Alric Rothmayer
Xinwei Wang
Jue Yan



Iowa State University

Ames, Iowa

2012

# TABLE OF CONTENTS

# LIST OF FIGURES

# LIST OF TABLES

# Abstract

The development of a dynamic unstructured grid high-order accurate spectral difference (SD) method for the three dimensional compressible Navier-Stokes (N-S) equations and its applications in flapping-wing aerodynamics are carried out in this work. Grid deformation is achieved via an algebraic blending strategy to save computational cost. The Geometric Conservation Law (GCL) is imposed to ensure that grid deformation will not contaminate the flow physics. A low Mach number preconditioning procedure is conducted in the developed solver to handle the bio-inspired flow. The capability of the low Mach number preconditioned SD solver is demonstrated by a series of two dimensional (2D) and three dimensional (3D) simulations of the unsteady vortex dominated flow.

Several topics in the flapping wing aerodynamics are numerically and experimentally investigated in this work. These topics cover some of the cutting-edge issues in flapping wing aerodynamics, including the wake structure analysis, airfoil thickness and kinematics effects on the aerodynamic performances, vortex structure analysis around 3D flapping wings and the kinematics optimization. Wake structures behind a sinusoidally pitching NACA0012 airfoil are studied with both experimental and numerical approaches. The experiments are carried out with Particle Image Velocimetry (PIV) and two types of wake transition processes, namely the transition from a drag-indicative wake to a thrust-indicative wake and that from the symmetric wake to the asymmetric wake are distinguished. The numerical results from the developed SD solver agree well with the experimental results. It is numerically found that the deflective direction of the asymmetric wake is determined by the initial conditions, e.g. initial phase angle.

As most insects use thin wings (i. e., wing thickness is only a few percent of the chord length) in flapping flight, the effects of airfoil thickness on thrust generation are numerically investigated by simulating the flow fields around a series of plunging NACA symmetric airfoils with thickness ratio ranging from 4.0% to 20.0% of the airfoil chord length. The contribution of viscous force to flapping propulsion is accessed and it is found that viscous force becomes thrust producing, instead of drag producing, and plays a non-negligible role in thrust generation for thin airfoils. This is closely related to the variations of the dynamics of the unsteady vortex structures around the plunging airfoils.

As nature flyers use complex wing kinematics in flapping flight, kinematics effects on the aerodynamic performance with different airfoil thicknesses are numerically studied by using a series of NACA symmetric airfoils. It is found that the combined plunging and pitching motion can outperform the pure plunging or pitching motion by sophisticatedly adjusting the airfoil gestures during the oscillation stroke. The thin airfoil better manipulates leading edge vortices (LEVs) than the thick airfoil (NACA0030) does in studied cases, and there exists an optimal thickness for large thrust generation with reasonable propulsive efficiency. With the present kinematics and dynamic parameters, relatively low reduced frequency is conducive for thrust production and propulsive efficiency for all tested airfoil thicknesses. In order to obtain the optimal kinematics parameters of flapping flight, a kinematics optimization is then performed. A gradient-based optimization algorithm is coupled with a second-order SD Navier-Stokes solver to search for the optimal kinematics of a certain airfoil undergoing a combined plunging and pitching motion. Then a high-order SD scheme is used to verify the optimization results and reveal the detailed vortex structures associated with the optimal kinematics of the flapping flight. It is found that for the case with maximum propulsive efficiency, there exists no leading edge separation during most of the oscillation cycle.

In order to provide constructive suggestions to the design of micro-air-vehicles (MAVs), 3D simulations of the flapping wings are carried out in this work. Both the rectangular and bio-inspired wings with different kinematics are investigated. The formation process of two-jet-like wake patterns behind the finite-span flapping wing is found to be closely related to the interaction between trailing edge vortices and tip vortices. Then the effects of the wing planforms on the aerodynamics performance of the finite-span flapping wings are elucidated in terms of the evolution and dynamic interaction of unsteady vortex structures.

# General Introduction

## Introduction

Unstructured grid based high-order (order of accuracy ≥3) methods have received ever increasing research interest in the Computational Fluid Dynamics (CFD) community due to their potential of delivering higher accuracy with less computational cost than the low order methods for problems involving complex physics and geometry, such as aero-acoustic flow and vortex dominated flow. Several reviews on the high-order methods for the Navier-Stokes equations can be found in [1, 2]. Despite the many attractive properties of high-order methods, in order to gain further popularity in even larger engineering context, which is currently dominated by their low-order counterparts, robust, easy-to-use and efficient high-order schemes are greatly desired.

The spectral difference (SD) method [3] is an unstructured grid based high-order method for solving hyperbolic conservation laws. Its precursor is the conservative staggered-grid Chebyshev multi-domain method [4]. The general formulation of the SD method was first described in [3] for the simplex element. It is then extended to two dimensional (2D) Euler [5] and N-S equations [6, 7]. After that, the SD method was implemented for three dimensional (3D) N-S equations on unstructured hexahedral grids [8]. Later, a weak instability in the original SD method was found independently by Van den Adeele et al. [9] and Huynh [10]. Huynh [10] further found that the use of Legendre-Gauss quadrature points as flux points resulted in a stable SD method. This was later proved by Jameson [11] for the one dimensional linear advection equation under an energy stable framework. In Ref. [12], the SD method was extended to handle the deformable dynamic grid and its ability to cope with complex vortex dominated bio-inspired flow was demonstrated as well. A parallel development of the dynamic unstructured grid based SD method was reported in [13].

Unsteady flapping-wing aerodynamics has witnessed great prosperity in the last three decades. This prosperity is not only attributed to the human being's continuous curiosity on the effective propulsion exhibited by fascinating nature flyers, but also is due to the increasing interest in the design of Micro Air Vehicles (MAVs), which have been considered to have the potential to open up new opportunities for surveillance-like missions and to

revolutionize the sensing and information gathering technologies in the near future. A large amount of experimental and computational research has been conducted on flapping-wing related topics and many comprehensive reviews and book chapters [14, 15, 16, 17, 18, 19, 20, 21] have systematically summarized these works from different aspects. These topics include kinematics of flapping flight, wing/foil geometry and aero-elasticity, multiple wing/foil configuration, unsteady flow structure analyses, especially on the wake structures, leading edge vortices (LEVs) dynamics and vortex interactions, and aerodynamic forces and propulsion efficiency analyses, etc. Great progress has been made on the unsteady flapping-wing aerodynamics due to the appearance of advanced flow diagnostic technologies and the development of high-fidelity computational fluid dynamics (CFD). Before moving forward, previous studies on some of the aforementioned topics, which will be further investigated in the present thesis, are briefly reviewed as follows.

It is well known that flapping motions can effectively generate thrust at low Reynolds and Mach numbers. The explanation for the thrust generation with oscillating airfoils was given by Knoller [22] and Betz [23] independently based on the inviscid assumption and the effective angle of attack (AOA) concept. This was experimentally confirmed by Katzmayr [24] through mounting a stationary wing in an oscillating flow. After that, von Karman and Burgers [25] showed a thought-provoking way to explain the thrust or drag production by checking momentum surfeit or deficit in the wake based on the wake vortices orientation and location. This has gradually become a qualitative principle to judge whether an oscillating mechanism generate thrust or drag. The aforementioned wake structure analyses originate from this work and have attracted intensive research attentions.

In this branch, some interesting wake vortices phenomena have been discovered and their impact on the aerodynamic performance of the oscillating foils/wings has been discussed. Freymuth [26] experimentally documented the vortex street of the thrust-indicative type for pure plunging or pitching motion of NACA0015 airfoil. Koochesfahani [27] found that the wake pattern after a pitching airfoil can be controlled by adjusting the pitching frequency, amplitude and the shape of the oscillation wave. After that, Triantafyllou et al. [28] found that the optimal thrust development in oscillating foils can occur at Strouhal number ranging from 0.25 to 0.35 by performing stability analyses of measured average velocity profiles.

Jones et al. [29] used the water-tunnel experiments and inviscid flow simulations to study the evolution of wake structures behind a plunging airfoil. A comprehensive classification of wake types was summarized in their results. Lai and Platzer [30] further studied the jet characteristics behind a plunging NACA0012 airfoil with the dye flow visualization and laser Doppler velocimetry (LDV) measurements. Wang [31] confirmed that the optimal flapping was closely related to the interaction between leading edge vortices (LEVs) and trailing edge vortices (TEVs) for the pure plunging motion. Lewin and Haj-Hariri [32] numerically classified the wake patterns behind a plunging airfoil and discussed the LEVs' effects on the wake pattern and propulsive efficiency. Young and Lai [33] studied different types of wake structures behind a plunging airfoil and the associated aerodynamic forces. They found that the aerodynamic forces relied more on the dynamic behaviors of LEVs while the wake structures were mainly controlled by the TEVs. Recently, Schnipper et al. [34] performed a systematic study on the wake patterns behind a pitching foil in the vicinity of the drag-thrust transition region in order to reveal the connection between wake structures and aerodynamic force generation.  As a continuation of previous work, Bohl and Koochesfahani [35] studied the wake structures behind a sinusoidally pitching NACA0020 airfoil of various reduced frequencies using molecular tagging velocimetry (MTV).

All the aforementioned studies on wake structures are tied to simple airfoil kinematics, namely pure plunging or pitching motions. As reported by many researchers, a combined plunging and pitching motion is a more elaborate modeling of the flapping wing kinematics. This forms another branch of the flapping-wing aerodynamics studies. Jones and Platzer [36] argued that the combined plunging and pitching motion could adjust the effective angle of attack (AOA) of the airfoil, enhancing the thrust generation or power extraction performance. Anderson et al. [37] experimentally examined the propulsive performance of a NACA0012 airfoil with a combined plunging and pitching motion, and showed the parameters for optimal thrust production. Isogai et al. [38] concluded from their results of a NACA0012 airfoil undergoing combined pitching and plunging motion that a high propulsive efficiency could be obtained when pitching lead plunging by 90 degrees and no apparent leading edge separation appears. Similarly, Tuncer and Platzer [39] found that high propulsive efficiency came with an attached flow over the full period of the oscillatory cycle for a NACA0012

airfoil. Note that in both cases the free stream Mach number was 0.3, which may be a bit large for the flapping wing simulations. Ramamurti and Sandberg [40] used a finite element incompressible flow solver to study an oscillating NACA0012 airfoil and investigated the effect of the phase difference between pitching and plunging motions on the thrust generation and propulsive efficiency. Kang et al. [41] used a Reynolds-Averaged Navier-Stokes (RANS) approach to study the flow over an oscillating SD7003 airfoil, and discussed the effects of turbulence model on the prediction of flow features.

Also, there has been long-standing research interest in optimizing the kinematics of a flapping wing to achieve optimal aerodynamic performance in different scenarios. Jones [42] calculated the optimum load distribution along the wing for a given wing-root bending momentum during the pure flapping motion, and found that the optimum loading was able to generate thrust more efficiently compared with an elliptic loading, which was suggested to be optimal for steady flight. Hall and Hall [43] computed the optimal circulation distribution along the span of flapping wings in fast forward flight using a 1D integral solution for small-amplitude motions and vortex-lattice techniques for large-amplitude motions. Ito [44] utilized vortex lattice method in conjunction with a hybrid optimization algorithm combining genetic algorithm and sequential quadratic programming to optimize the flapping wing motion. Vortex lattice model was also adopted by other research groups [45, 46] as a suitable compromise between computational cost and accuracy, but it might fail to provide appropriate level of complexity of the motion when viscous effects became non-negligible [45]. In addition, Hamdaoui et al. [47] optimized the efficient flapping kinematics using a multi-objective evolutionary algorithm coupled with flapping flight physics models. Tuncer and Kaya [48] optimized the weighted sum consisted of thrust and propulsive efficiency of an flapping airfoil in combined plunging and pitching motion by coupling gradient-based optimization method with 2D Navier-Stokes solver supporting moving overset grid. Willis et al. [49] exploited a collection of computation tools with multiple fidelity level in the design of effective flapping wing vehicles. In 2009, Pesavento and Wang [50] further confirmed that 2D flapping flight can be aerodynamically more efficient than the optimal steady motion. Recently, Culbreth et al. [51] presented several optimization results for flapping airfoils and wings obtained from an optimization framework constructed by a gradient-based

optimization algorithm and a low-dissipation kinetic energy preserving (KEP) finite volume Navier-Stokes solver. They found that the maximum propulsive efficiency appeared to occur right before the incipience of leading edge separation.

There is a growing awareness in the community that the wing/foil geometry can affect thrust generation and propulsive efficiency in cruise flight. Some research on the airfoil thickness effects on the aerodynamic performances is briefly reviewed as follows. Lentink and Gerritsma [52] compared the performances of several plunging airfoils with different thickness at Reynolds number 150, and concluded that airfoils with larger thickness could generate greater thrust than the airfoils with small thickness. An et al. [53] found that thickness ratio was a crucial parameter for thrust production and their results indicated that there existed an optimal thickness ratio for the thrust generation at Reynolds number 185. Ashraf et al. [54] systematically studied the thickness effects on the propulsive performances of flapping airfoils at different Reynolds numbers ranging from 200 to $2 \times 10^6$. They found that for low Reynolds numbers, thin airfoils outperformed thick airfoils, while for high Reynolds numbers there existed an optimal thickness for the thrust production and propulsive efficiency. These results were different from Cebeci et al.'s [55] conclusion based on an unsteady panel code simulation that thickness had a negligible effect on the propulsive efficiency. This might be due to the fact that the inviscid analysis could not handle the dynamic behaviors of LEVs, which play a vital role in the aerodynamic performance evaluation.

Another vigorous and important branch of the flapping-wing aerodynamic studies is the investigation of the flow structures around 3D finite-span wings with or without wing-body interactions. According to the study in Ref. [19], wings with low aspect ratios (ARs), which are adopted by most insects [56], are beneficial for the agile locomotion. Therefore, many studies [17, 18, 19, 57, 58, 59, 60, 61] have been concentrated on the aerodynamic performances of low AR wings. Ellington et al. [59] first discovered that the intense leading edge vortex (LEV) created by dynamic stall is the reason for the high-lift forces generation during the hovering flight of the hawkmoth. They also pointed out that the spanwise flow is essential for the stability of such leading edge vortex. However, Birch and Dickinson [57] found that even there does not exist the spanwise flow, the LEV can still be stabilized for the

flapping wings of the fruit fly. They confirmed that the downwash effect of the wing tip vortex can explain the stability of the LEV. In fact, according to Ref. [61], under the regime of high Reynolds numbers, the spanwise flow can enhance the stability of the LEV, while for lower Reynolds numbers, wing tip vortex and wake vorticity play a vital role on prolonging the attachment of the LEV. Recently, Shyy et al. [61] further confirmed that the wing kinematics can greatly affect the wing tip effects on the aerodynamic performance of a low AR wing. Von Ellenrieder et al. [62] and Parker et al. [63] have studied the 3D vortex structures after a finite-span flapping wing with two free ends. Their research was restricted to the effects of aerodynamic parameters and the wing motion kinemics on the wake structures. Blondeaux et al. [64] numerically investigated the wake structures produced by a flapping foil and found that there existed strong interaction among the adjacent rings shed in one oscillating cycle when the Strouhal number was large. Buckholtz and Smits [65] used the dye visualization to interrogate the wake structure behind a low-aspect-ratio pitching panel. It was observed that a 3D von Karman vortex street was formed behind the panel and the vortex skeleton model was proposed based on the visualization. Dong et al. [58] found that the flow fields behind a low-aspect-ratio flapping foil with two free ends are characterized by two oblique jets and such wake topology is dominated by two sets of interconnected vortex loops. Similar phenomena were reported by Hu et al. [60] experimentally and Yu et al. [66] numerically for a fixed-root flapping wing and Dewey et al. [67] experimentally for a batoid-inspired flexible fin. Dewey et al. [67] also built up the connection between the propulsive efficiency and the wake structures. In Spentzos et al.'s [68] work, the wing tip effects on the dynamic stall are studied. They confirmed that different wing planforms could have similar flow topology.

As aforementioned, the high-order CFD method can be more accurate and efficient for the vortex-dominated flow simulations than the traditional second order method, which can be too dissipative to resolve the elaborate vortex structures. Therefore there is a trend in the CFD community to develop high-order viscous flow solvers to resolve the vortex dominated bio-inspired flow recently. Visbal et al. [69] have successfully utilized a high-order compact method to simulate the flow field around a SD7003 airfoil. Persson et al. [70] have developed a dynamic unstructured grid based discontinuous Galerkin (DG) method for a finite-span

wing simulation and compared the results with other numerical methods. Liang et al. [13] have successfully used a 2D SD method for a plunging NACA0012 airfoil simulation. Several applications for 2D and 3D SD method in the bio-inspired flow have been reported by Yu et al. [12, 66]. Their results demonstrated the effectiveness of the dynamic unstructured grid based SD method for some challenging bio-inspired flow simulations. Ou et al. [71] recently developed a 3D SD solver for the finite-span flapping wing simulations. Results from the paper confirmed the potential of using high order methods as an efficient tool for the full scale flapping wing aerodynamics studies.

In the present study, the development of the dynamic unstructured grid based SD method is presented at first. The geometric conservation law [72] during the time-dependent coordinate transformation is discussed in detail and the grid deformation strategy is well specified. Then high-fidelity numerical simulations of the flapping-wing aerodynamics are carried out by using the developed solver. The 2D topics covered in the numerical simulations include the wake structure analyses of oscillating airfoils, the airfoil thickness and kinematics effects on the aerodynamic performances, and the optimization of the airfoil kinematics for maximum propulsive efficiency. The effects of wing planforms and kinematics on the aerodynamic performance of 3D thin finite-span flapping wings are also investigated using numerical simulations. A particle image velocimetry (PIV) based experimental study is carried out to visualize the wake structures behind a sinusoidally pitching NACA0012 airfoil. Two types of wake transition processes, namely the transition from a drag-indicative wake to a thrust-indicative wake and that from the symmetric wake to the asymmetric wake are thoroughly investigated.

## Dissertation Organization

The rest of this dissertation is organized as follows.

Chapter 2, "A High-Order Spectral Difference Method for Unstructured Dynamic Grids" is a paper published in *Computers & Fluids*. I am the primary author of the paper, responsible for most of the work and writing.

Chapter 3, "Experimental and Numerical Investigations on the Asymmetric Wake Vortex Structures around an Oscillating Airfoil" is a paper published in the 50th AIAA ASM

conference proceedings. I am the primary author of the paper, responsible for most of the work and writing.

Chapter 4, "Airfoil Thickness Effects on the Thrust Generation of Plunging Airfoils" is a paper published in *Journal of Aircraft*. I am the primary author of the paper, responsible for most of the work and writing.

Chapter 5, "A High-Fidelity Numerical Study of Kinematics and Airfoil Thickness Effects on the Thrust Generation of Oscillating Airfoils" is a paper published in the 42$^{nd}$ AIAA Fluid Dynamics Conference and Exhibit. I am the primary author of the paper, responsible for most of the work and writing.

Chapter 6, "High-Fidelity Optimization of Flapping Airfoils for Maximum Propulsive Efficiency" introduces the framework of the optimization of the flapping wing kinematics and discusses the optimization results.

Chapter 7, "The Effects of Wing Planforms on the Aerodynamic Performance of Thin Finite-Span Flapping Wings" is a paper published in the 50$^{th}$ AIAA ASM conference proceedings. I am the primary author of the paper, responsible for most of the work and writing.

Chapter 8 is devoted to general conclusions.

## Reference

[1]   J. A. Ekaterinaris, "High-order accurate, low numerical diffusion methods for aerodynamics," *Prog. Aerosp. Sci.,* vol. 41, pp. 192-300, 2005.

[2]   Z. J. Wang, "High-order methods for the Euler and Navier–Stokes equations on unstructured grids," *J. Prog. Aerosp. Sci.,* vol. 43, pp. 1-47, 2007.

[3]   Y. Liu, M. Vinokur and Z. J. Wang, "Discontinuous spectral difference method for conservation laws on unstructured grids," *J. Comput. Phys.,* vol. 216, pp. 780-801, 2006.

[4]   D. A. Kopriva and J. H. Kolias, "A conservative staggered-grid Chebyshev multi-domain method for compressible flows," *J.Comput.Phys.,* vol. 125, no. 1, pp. 244-261, 1996.

[5]   Z. J. Wang, Y. Liu, G. May and A. Jameson, "Spectral difference method for unstructured grids II: extension to the Euler equations," *J. Sci. Comput.,* vol. 32, pp. 45-71, 2007.

[6]   G. May and A. Jameson, "A spectral difference method for the Euler and Navier–Stokes equations," in *AIAA Paper 2006-304*, 2006.

[7]   Z. J. Wang, Y. Sun, C. Liang and Y. Liu, "Extension of the SD method to viscous flow on unstructured grids," in *the 4th international conference on computational fluid dynamics*, Ghent, Belgium, 2006.

[8] Y. Z. Sun, Z. J. Wang and Y. Liu, "High-order multidomain spectral difference method for the Navier-Stokes equations on unstructured hexahedral grids," *Commun. Comput. Phys.,* vol. 2, pp. 310-333, 2006.

[9] K. V. d. Abeele, C. Lacor and Z. J. Wang, "On the stability and accuracy of the spectral difference method," *J.Sci.Comput.,* vol. 37, no. 2, pp. 162-188, 2008.

[10] H. T. Huynh, "A flux reconstruction approach to high-order schemes including discontinuous Galerkin methods," in *AIAA Paper 2007-4079*, 2007.

[11] A. Jameson, "A proof of the stability of the spectral difference method for all orders of accuracy," *J. Sci. Comput.,* vol. 45, pp. 348-358, 2010.

[12] M. L. Yu, Z. J. Wang and H. Hu, "A high-order spectral difference method for unstructured dynamic grids," *Computer & Fluids,* vol. 48, pp. 84-97, 2011.

[13] C. L. Liang, K. Ou, S. Premasuthan, A. Jameson and Z. J. Wang, "High-order accurate simulations of unsteady flow past plunging and pitching airfoils," *Computer & Fluids,* vol. 40, pp. 236-248, 2010.

[14] S. Ho, H. Nassef, N. Pornsinsirirak, Y. C. Tai and C. M. Ho, "Unsteady aerodynamics and flow control for flapping wing flyers," *Progress in Aerospace Sciences,* vol. 39, no. 8, pp. 635-681, 2003.

[15] M. F. Platzer, K. D. Jones, J. Young and J. C. S. Lai, "Flapping-wing aerodynamics: progress and challenges," *AIAA J.,* vol. 46, no. 9, pp. 2136-2149, 2008.

[16] K. V. Rozhdestvensky and V. A. Ryzhov, "Aerohydrodynamics of flapping-wing propulsors," *Progress in Aerospace Sciences,* vol. 39, no. 8, pp. 585-633, 2003.

[17] W. Shyy, H. Aono, S. Chimakurthi, P. Trizila, C. Kang, C. Cesnik and H. Liu, "Recent progress in flapping wing aerodynamics and aeroelasticity," *Progress in Aerospace Sciences,* vol. 48, no. 7, pp. 284-327, 2010.

[18] W. Shyy, M. Berg and D. Ljungqvist, "Flapping and flexible wings for biological and micro air vehicles," *Progress in Aerospace Sciences,* vol. 35, no. 5, pp. 455-505, 1999.

[19] W. Shyy, Y. Lian, J. Tang, D. Viieru and H. Liu, Aerodynamics of low Reynolds number flyers, New York: Cambridge Univ. Press, 2008.

[20] M. S. Triantaflyllou, A. H. Techet and F. S. Hover, "Review of experimental work in biomimetic foils," *IEEE Journal of Oceanic Engineering,* vol. 29, no. 3, pp. 585-594, 2004.

[21] Z. J. Wang, "Dissecting insect flight," *Annu. Rev. Fluid Mech.,* vol. 37, no. 1, pp. 183-210, 2005.

[22] R. Knoller, "Die Gesetze des Luftwiderstandes," *Flug- und Motortechnik (Wien),* vol. 3, no. 21, pp. 1-7, 1909.

[23] A. Betz, "Ein Beitrag zur Erklaerung des Segelfluges," *Zeitschrift fur Flugtechnik und Motorluftschiffahrt,* vol. 3, pp. 269-272, 1912.

[24] R. Katzmayr, "Effect of periodic changes of angle of attack on behavior of airfoils," *National Advisory Committee for Aeronautics,* 1922.

[25] T. Von Karman and J. M. Burgers, *Aerodynamic Theory: A General Review of Progress,* vol. 2, 1935.

[26] P. Freymuth, "Propulsive vortical signature of plunging and pitching airfoils," *AIAA J.,* vol. 26, pp. 881-883, 1988.

[27] M. M. Koochesfahani, "Vortical patterns in the wake of an oscillating airfoil," *AIAA J.,* vol. 27, pp. 1200-1205, 1989.

[28] G. S. Triantaflyllou, M. S. Triantaflyllou and M. A. Grosenbaugh, "Optimal thrust development in oscillating foils with application to fish propulsion," *Journal of Fluids and Structures,* vol. 7, pp. 205-224, 1993.

[29] K. D. Jones, C. M. Dohring and M. F. Platzer, "Experimental and computational investigation of the Knoller–Betz effect," *AIAA J.,* vol. 36, pp. 1240-1246, 1998.

[30] J. C. S. Lai and M. F. Platzer, "Jet characteristics of a plunging airfoil," *AIAA J.,* vol. 37, pp. 1529-1537, 1999.

[31] Z. J. Wang, "Vortex shedding and frequency selection in flapping flight," *J. Fluid Mech.,* vol. 410, pp. 323-341, 2000.

[32] G. C. Lewin and H. Haj-Hariri, "Modeling thrust generation of a two-dimensional heaving airfoil in a viscous flow," *J. Fluid Mech.,* vol. 492, pp. 339-362, 2003.

[33] J. Young and J. C. S. Lai, "Oscillation frequency and amplitude effects on the wake of a plunging airfoil," *AIAA J.,* vol. 42, pp. 2042-2052, 2004.

[34] T. Schnipper, A. Andersen and T. Bohr, "Vortex wakes of a flapping foil," *J. Fluid Mech.,* vol. 633, pp. 411-423, 2009.

[35] D. G. Bohl and M. M. Koochesfahani, "MTV measurements of the vertical field in the wake of an airfoil oscillating at high reduced frequency," *J. Fluid Mech.,* vol. 620, pp. 63-88, 2009.

[36] K. D. Jones and M. F. Platzer, "Numerical computation of flapping-wing propulsion and power extraction," in *AIAA Paper 97-0826*, 1997.

[37] J. M. Anderson, K. Streitlien, D. S. Barrett and M. S. Triantafyllou, "Oscillating foils of high propulsive efficiency," *J. Fluid Mech.,* vol. 360, pp. 41-72, 1998.

[38] K. Isogai, Y. Shinmoto and Y. Watanabe, "Effects of dynamic stall on propulsive efficiency and thrust of flapping airfoil," *AIAA J.,* vol. 37, pp. 1145-1151, 1999.

[39] I. H. Tuncer and M. F. Platzer, "Computational study of flapping airfoil aerodynamics," *Journal of Aircraft,* vol. 37, pp. 514-520, 2000.

[40] R. Ramamurti and W. Sandberg, "Simulation of flow about flapping airfoils using finite element incompressible flow solver," *AIAA J.,* vol. 39, pp. 253-260, 2001.

[41] C. K. Kang, H. Aono, P. Trizila, Y. Baik, J. M. Rausch, L. Bernal, M. V. Ol and W. Shyy, "Modeling of pitching and plunging airfoils at Reynolds number between $1\times10^4$ and $6\times10^4$," in *AIAA Paper 2009-4100*, 2009.

[42] R. T. Jones, "Wing Flapping with Minimum Energy," NASA Technical Memorandum 81174 , 1980.

[43] K. C. Hall and S. R. Hall, "Minimum induced power requirements for flapping flight," *Journal of Fluid Mechanics,* vol. 323, pp. 285-315, 1996.

[44] K. Ito, "Optimization of Flapping Wing Motion," in *ICAS 2002 CONGRESS*, 2002.

[45] B. K. Stanford and P. S. Beran, "Analytical Sensitivity Analysis of an Unsteady Vortex-Lattice Method for Flapping-Wing Optimization," *Journal of Aircraft,* vol. 47, no. 2, pp. 647-662, 2010.

[46] M. Ghommem, M. R. Hajj, L. T. Watson, D. T. Mook, R. D. Snyder and P. S. Beran, "Deterministic Global Optimization of Flapping Wing Motion for Micro Air Vehicles," in *2010 AIAA ATIO/ISSMO Conference*, 2010.

[47] M. Hamdaoui, J.-B. Mouret, S. Doncieux and P. Sagaut, "Optimization of Kinematics for Birds and UAVs using Evolutionary Algorithms," *World Academy of Science, Engineering and Technology,* vol. 47, pp. 181-192, 2008.

[48] I. H. Tuncer and M. Kaya, "Optimization of Flapping Airfoils for Maximum Thrust and Propulsive Efficiency," *AIAA Journal,* vol. 43, no. 11, pp. 2329-2336, 2005.

[49] D. J. Willis, P.-O. Persson, E. R. Israeli, J. Peraire, S. M. Swartz and K. S. Breuer, "Multifidelity

Approaches for the Computational Analysis and Design of Effective Flapping Wing Vehicles," in *AIAA 2008-518*, Reno, Nevada, 2008.

[50] U. Pesavento and Z. J. Wang, "FlappingWing Flight Can Save Aerodynamic Power Compared to Steady Flight," *Physical Review Letters,* vol. 103, pp. 118102-4, 2009.

[51] M. Culbreth, Y. Allaneau and A. Jameson, "High-Fidelity Optimization of Flapping Airfoils and Wings," in *AIAA 2011-3521*, Honolulu, Hawaii, 2011.

[52] D. Lentink and M. Gerritsma, "Influence of airfoil shape on performance in insect flight," in *AIAA Paper 2003-3447*, 2003.

[53] S. An, J. Maeng and C. Han, "Thickness effect on the thrust generation of heaving airfoils," *Journal of Aircraft,* vol. 46, pp. 216-222, 2009.

[54] M. A. Ashraf, J. Young and J. C. S. Lai, "Reynolds number, thickness and camber effects on flapping airfoil propulsion," *Journal of Fluids and Structures,* vol. 27, pp. 145-160, 2011.

[55] T. Cebeci, M. Platzer, H. Chen, K. C. Chang and J. P. Shao, Analysis of low-speed unsteady airfoil flows, Horizons Publishing Inc., 2004.

[56] M. J. Ringuette, M. Milano and M. Gharib, "Role of the tip vortex in the force generation of low-aspect-ratio normal flat plates," *J. Fluid Mech.,* vol. 581, pp. 453-468, 2007.

[57] J. M. Birch and M. H. Dickinson, "Spanwise flow and the attachment of the leading-edge vortex on insect wings," *Nature (London),* vol. 412, pp. 729-733, 2001.

[58] H. Dong, R. Mittal and F. M. Najjar, "Wake topology and hydrodynamic performance of low-aspect-ratio flapping foils," *J. Fluid Mech.,* vol. 566, pp. 309-343, 2006.

[59] C. P. Ellington, C. v. d. Berg, A. P. Willmott and A. L. R. Thomas, "Leading-edge vortices in insect flight," *Nature (London),* vol. 384, pp. 626-630, 1996.

[60] H. Hu, L. Clemons and H. Igarashi, "An experimental study of the unsteady vortex structures in the wake of a root-fixed flapping wing," *Exp. Fluids,* vol. 51, no. 2, pp. 347-359, 2011.

[61] W. Shyy, P. Trizila, C. Kang and H. Aono, "Can tip vortices enhance lift of a flapping wing?," *AIAA J.,* vol. 47, pp. 289-293, 2009.

[62] K. D. v. Ellenrieder, K. Parker and J. Soria, "Flow structure behind a heaving and pitching finite-span wing," *J. Fluid Mech.,* vol. 490, pp. 129-138, 2003.

[63] K. Parker, K. D. v. Ellenrieder and J. Soria, "Using stereo multigrid DPIV (SMDPIV) measurements to investigate the vortical skeleton behind a finite-span flapping wing," *Exp. Fluids,* vol. 39, no. 2, pp. 281-298, 2005.

[64] P. Blondeaux, F. Fornarelli, L. Guglielmini, M. S. Triantafyllou and R. Verzicco, "Numerical experiments on flapping foils mimicking fish-like locomotion," *Phys. Fluids,* vol. 17, pp. 113601-12, 2005.

[65] J. H. J. Buckholtz and A. J. Smits, "On the evolution of the wake structure produced by a low-aspect-ratio pitching panel," *J. Fluid Mech.,* vol. 546, pp. 433-443, 2006.

[66] M. L. Yu, Z. J. Wang and H. Hu, "The effects of wing planforms on the aerodynamic performance of thin finite-span flapping wings," in *AIAA Paper 2012-0757*, 2012.

[67] P. A. Dewey, A. Carriou and A. J. Smits, "On the relationship between efficiency and wake structure of a batoid-inspired oscillating fin," *J. Fluid Mech.,* vol. 691, pp. 245-266, 2012.

[68] A. Spentzos, G. N. Barakos, K. J. Badcock, B. E. Richards, F. N. Coton, R. A. McD., G. E. Berton and D. Favier, "Computational fluid dynamics study of three dimensional dynamic stall of various planform shapes," *Journal of Aircraft,* vol. 44, no. 4, pp. 1118-1128, 2007.

[69] M. R. Visbal, "High-fidelity simulation of transitional flows past a plunging airfoil," in *AIAA Paper 2009-391*, 2009.

[70] P. O. Persson, D. J. Willis and J. Peraire, "The numerical simulation of flapping wings at low Reynolds numbers," in *AIAA Paper 2010-72*, 2010.

[71] K. Ou, P. Castonguay and A. Jameson, "3D flapping wing simulation with high order spectral difference method on deformable mesh," in *AIAA Paper 2011-1316*, 2011.

[72] P. D. Thomas and C. K. Lombard, "Geometric conservation law and its application to flow computations on moving grids," *AIAA J.,* vol. 17, pp. 1030-1037, 1979.

# CHAPTER 2. A High-Order Spectral Difference Method for Unstructured Dynamic Grids

A paper published in Computers & Fluids

Meilin Yu, Z. J. Wang and Hui Hu

## Abstract

A high-order spectral difference (SD) method has been further extended to solve the three dimensional compressible Navier-Stokes (N-S) equations on deformable dynamic meshes. In the SD method, the solution is approximated with piece-wise continuous polynomials. The elements are coupled with common Riemann fluxes at element interfaces. The extension to deformable elements necessitates a time-dependent geometric transformation. The Geometric Conservation Law (GCL), which is introduced in the time-dependent transformation from the physical domain to the computational domain, has been discussed and implemented for both explicit and implicit time marching methods. Accuracy studies are performed with a vortex propagation problem, demonstrating that the spectral difference method can preserve high-order accuracy on deformable meshes. Further applications of the method to several moving boundary problems including bio-inspired flow problems are shown in the paper to demonstrate the capability of the developed method.

## Keywords

High order; Unstructured dynamic grids; Spectral difference; Navier-Stokes; Bio-inspired flow.

## 1. Introduction

Computational fluid dynamics (CFD) has attracted a surge of research activities during the last three decades, and it has become a routine tool in the aerodynamic design of aircraft, wind turbines, and centrifugal pumps, etc. For general engineering applications, nearly all production flow solvers are based on at most second-order numerical methods. Although they proved very useful, the second-order methods may not be accurate enough for problems

requiring high accuracy, such as vortex dominated flows, and acoustic noise predictions. Therefore, there has been a growing interest in the development of high-order methods for unstructured grids in recent years. The reasons for this are obvious. High-order methods enjoy remarkably high accuracy with low numerical dissipations, and unstructured grids can provide flexibility in handling complex geometries. A review of the high-order methods for the Euler and Navier-Stokes equations can be found in [31].

The spectral difference (SD) method [12] is a recently developed high-order method to solve compressible flow problems on simplex meshes. Its precursor is the conservative staggered-grid Chebyshev multi-domain method [11]. The general formulation of the SD method was first described in [12] and applied for computational electromagnetic problems. It is then extended to 2D Euler [33] and Navier-Stokes equations [14,34]. After that, Sun et al. [22,23] implemented the SD method for 3D N-S equations on unstructured hexahedral meshes. Later, a weak instability in the original SD method was found independently by Van den Adeele, et al. [26] and Huynh [8]. Huynh [8] further found that the use of Legendre-Gauss quadrature points as flux points results in a stable SD method. This was later proved by Jameson [9] for the one dimensional linear advection equation. The present study is based on Sun et al. [22,23] and further extends the method to 3D deformable meshes. The basic idea to achieve high-order accuracy in the SD method is to use a high degree polynomial to approximate the exact solution in a standard element (a local cell). However, unlike the discontinuous Galerkin (DG) [3] method and spectral volume (SV) method [32], the SD method is in the differential form, which is efficient and simple to implement. As all the computations are performed on the fixed standard element in the computational domain, it is reasonable to expect that the SD method can preserve high-order features for moving boundary problems in the physical domain.

Since a time-dependent curvilinear transformation from the physical domain to the standard element is needed in the SD method, the Geometric Conservation Law (GCL), first discussed in [25], should be strictly enforced in order to eliminate the grid motion induced errors. For high-order methods, an approach to guarantee GCL for the finite difference method has been proposed in [27]. It is straightforward to extend this approach to the present SD method. In addition, a GCL compliant high-order time integration method is developed

for the implicit scheme with a similar method used in [13]. Note that there is an alternative way to deal with moving boundary problems, which is called the arbitrary Lagrangian-Eulerian (ALE) method [4]. In that approach, a mapping from a fixed reference configuration to the physical domain is needed. In the mapping, a time dependent GCL is introduced for the reference domain [17-19]. It is quite similar to the coordinate transformation approach aforementioned in the SD or the finite difference methods in [24,27]. It can be shown that the final form of the time dependent GCL is exactly the same for both approaches.

The remainder of the paper is organized as follows. In Section 2, the SD method is briefly reviewed including both the space discretization procedure and time integration approach. The GCL of the transformation from the physical domain to the computational one is then discussed in detail. After that, the implementation of GCL into the numerical schemes is described for different time marching methods. An algebraic grid deformation method together with the corresponding blending strategy is given in Section 2 as well. Then several numerical test cases are presented in Section 3. For a single flapping airfoil, the numerical results are obtained with both a rigid moving grid and a deformable grid. The comparisons of these results with experimental data are also presented. Moreover, some superior features of high-order methods over the lower ones are also illustrated in Section 3. Section 4 briefly concludes the paper.

## 2. Numerical Method

### 2.1 Governing Equations

We consider the unsteady compressible Navier-Stokes (N-S) equations in conservation form in the physical domain $(t, x, y, z)$

$$\frac{\partial Q}{\partial t} + \frac{\partial F}{\partial x} + \frac{\partial G}{\partial y} + \frac{\partial H}{\partial z} = 0 , \tag{2.1}$$

where $Q$ is the vector of conservative variables, and $F, G, H$ are the total fluxes including both the inviscid and viscous flux vectors.

After introducing a time-dependent coordinate transformation (Fig. 1(a)) from the physical domain $(t, x, y, z)$ to the computational domain $(\tau, \xi, \eta, \zeta)$, Eq. (2.1) can be rewritten as

$$\frac{\partial \widetilde{Q}}{\partial \tau} + \frac{\partial \widetilde{F}}{\partial \xi} + \frac{\partial \widetilde{G}}{\partial \eta} + \frac{\partial \widetilde{H}}{\partial \zeta} = 0, \tag{2.2}$$

where

$$\begin{cases} \widetilde{Q} = |J|Q \\ \widetilde{F} = |J|(Q\xi_t + F\xi_x + G\xi_y + H\xi_z) \\ \widetilde{G} = |J|(Q\eta_t + F\eta_x + G\eta_y + H\eta_z) \\ \widetilde{H} = |J|(Q\zeta_t + F\zeta_x + G\zeta_y + H\zeta_z) \end{cases}. \tag{2.3}$$

Herein, $\tau = t$, and $(\xi, \eta, \zeta) \in [-1,1]^3$, are the local coordinates in the computational domain. In the transformation shown above, the Jacobian matrix $J$ takes the following form

$$J = \frac{\partial(x,y,z,t)}{\partial(\xi,\eta,\zeta,\tau)} = \begin{bmatrix} x_\xi & x_\eta & x_\zeta & x_\tau \\ y_\xi & y_\eta & y_\zeta & y_\tau \\ z_\xi & z_\eta & z_\zeta & z_\tau \\ 0 & 0 & 0 & 1 \end{bmatrix}. \tag{2.4}$$

For a non-singular transformation, its inverse transformation must also exist, and the transformation matrix is

$$J^{-1} = \frac{\partial(\xi,\eta,\zeta,\tau)}{\partial(x,y,z,t)} = \begin{bmatrix} \xi_x & \xi_y & \xi_z & \xi_t \\ \eta_x & \eta_y & \eta_z & \eta_t \\ \zeta_x & \zeta_y & \zeta_z & \zeta_t \\ 0 & 0 & 0 & 1 \end{bmatrix}. \tag{2.5}$$

It should be noted that all the information concerning grid velocity $\overrightarrow{v_g} = (x_t, y_t, z_t)$ is related with $(\xi_t, \eta_t, \zeta_t)$ by

$$\begin{cases} \xi_t = -\overrightarrow{v_g} \times \nabla \xi \\ \eta_t = -\overrightarrow{v_g} \times \nabla \eta \\ \zeta_t = -\overrightarrow{v_g} \times \nabla \zeta \end{cases}. \tag{2.6}$$

## 2.2 Space Discretization

A brief review of the SD method is given here for completeness. A more detailed description of this numerical method is available at [22]. In the SD method, two sets of points are given, namely the solution and flux points, as shown in Fig. 1(b). Conservative variables

are defined at the solution points, and then interpolated to flux points to obtain local fluxes. In this study the flux points are selected to be the Legendre-Gauss points plus both end points -1 and 1.

The fluxes are computed at the flux points using Lagrange interpolation polynomials. It should be pointed out that this solution polynomial is only continuous within a standard element, but discontinuous at the cell interfaces. Therefore, for the inviscid flux, a Riemann solver is necessary to compute a common flux on the interface. For a moving boundary problem, since the eigenvalues of the Euler equations are different from those for a fixed boundary problem by the grid velocity, the design of the Riemann solver should consider the grid velocity. Taking the Rusanov flux [22] as an example, the reconstructed fluxes in three directions can be written as

$$
\begin{cases}
\widetilde{F^i} = \dfrac{1}{2}[\widetilde{F_L^i} + \widetilde{F_R^i} - (\left|\overline{V_n} - v_{gn}\right| + \overline{c})\bullet(Q_R - Q_L)\bullet|J|\|\nabla\xi\|]\bullet sign(\vec{n}\bullet\nabla\xi) \\[2mm]
\widetilde{G^i} = \dfrac{1}{2}[\widetilde{G_L^i} + \widetilde{G_R^i} - (\left|\overline{V_n} - v_{gn}\right| + \overline{c})\bullet(Q_R - Q_L)\bullet|J|\|\nabla\eta\|]\bullet sign(\vec{n}\bullet\nabla\eta) \\[2mm]
\widetilde{H^i} = \dfrac{1}{2}[\widetilde{H_L^i} + \widetilde{H_R^i} - (\left|\overline{V_n} - v_{gn}\right| + \overline{c})\bullet(Q_R - Q_L)\bullet|J|\|\nabla\zeta\|]\bullet sign(\vec{n}\bullet\nabla\zeta),
\end{cases} \quad (2.7)
$$

where superscript 'i' indicates the inviscid flux, subscript n indicates the normal direction of the interface. It should be noted that $\xi_t$, $Q\eta_t$ and $Q\zeta_t$ are included in the inviscid fluxes. The reconstruction of the viscous flux can be found in [22].
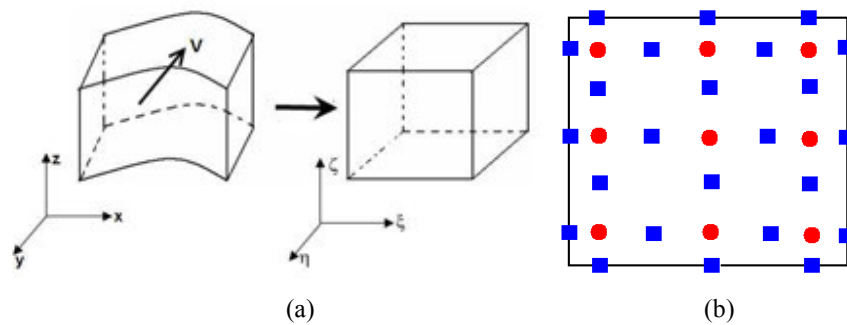


(a)　　　　　　　(b)

**Fig. 1.** (a) Transformation from a moving physical domain to a fixed computational domain; (b) Distribution of solution points (as denoted by circles) and flux points (as denoted by squares) in a standard quadrilateral element for a third-order SD scheme.

### 2.3 Geometric Conservation Law (GCL)

The GCL for the metrics of the transformation from the physical domain to the computational one can be expressed as

$$
\begin{cases}
\dfrac{\partial}{\partial \xi}(|J|\xi_x) + \dfrac{\partial}{\partial \eta}(|J|\eta_x) + \dfrac{\partial}{\partial \zeta}(|J|\zeta_x) = 0 \\[2mm]
\dfrac{\partial}{\partial \xi}(|J|\xi_y) + \dfrac{\partial}{\partial \eta}(|J|\eta_y) + \dfrac{\partial}{\partial \zeta}(|J|\zeta_y) = 0 \\[2mm]
\dfrac{\partial}{\partial \xi}(|J|\xi_z) + \dfrac{\partial}{\partial \eta}(|J|\eta_z) + \dfrac{\partial}{\partial \zeta}(|J|\zeta_z) = 0 \\[2mm]
\dfrac{\partial |J|}{\partial t} + \dfrac{\partial}{\partial \xi}(|J|\xi_t) + \dfrac{\partial}{\partial \eta}(|J|\eta_t) + \dfrac{\partial}{\partial \zeta}(|J|\zeta_t) = 0.
\end{cases}
\tag{2.8}
$$

It is obvious that the first three formula of the GCL only depend on the accuracy of the space discretization, while the last one is related to the time evolution of the moving grid. Since the spatial metrics are computed exactly, the first three equations are automatically satisfied. If the mesh undergoes rigid-body motion without deformation, $|J|$ is independent of time. Due to the discretization error, the time dependent GCL may not be strictly satisfied if one does not pay attention to how the mesh velocity is computed. However, for a dynamic mesh, spurious flows can be induced if the GCL is not strictly enforced. Therefore, GCL is a critical element for dynamic meshes.

In the present study, the GCL error in the numerical simulation is canceled by adding a source term to the N-S equations in the computational domain. In [17-19], the enforcement of GCL is achieved by using the same time integration form for the Jacobian as the conservative variables. An extra equation for the Jacobian needs to be solved iteratively. However, the present approach calculates the Jacobian directly, and then eliminates the errors generated by the disagreements between Jacobian and the corresponding grid velocity through a source term. Herein, treatments of the GCL are introduced separately for explicit and implicit schemes due to their different characteristics.

### Explicit Scheme

The semi-discrete form of the N-S equation in the computational domain reads

$$\frac{\partial \widetilde{Q}}{\partial t} = R\ (\widetilde{Q}^{n}) = -(\frac{\partial \widetilde{F}}{\partial \xi} + \frac{\partial \widetilde{G}}{\partial \eta} + \frac{\partial \widetilde{H}}{\partial \zeta}). \tag{2.9}$$

The equation is solved with a multi-stage strong-stability-preserving (SSP) Runge-Kutta scheme.

The following equation is obvious by the chain rule,

$$\frac{\partial \widetilde{Q}}{\partial t} = \frac{\partial |J| Q}{\partial t} = |J| \frac{\partial Q}{\partial t} + Q \frac{\partial |J|}{\partial t} \tag{2.10}$$

Substitute the last formula of Equations (2.8) into Equation (2.10), we obtain

$$\frac{\partial \widetilde{Q}}{\partial t} = |J| \frac{\partial Q}{\partial t} - Q \left[ \frac{\partial}{\partial \xi}(|J|\xi_t) + \frac{\partial}{\partial \eta}(|J|\eta_t) + \frac{\partial}{\partial \zeta}(|J|\zeta_t) \right] \tag{2.11}$$

Thus Equation (2.9) is changed to the following form,

$$\begin{aligned}
\frac{\partial Q}{\partial t} &= \frac{1}{|J|} \left\{ -\left( \frac{\partial \widetilde{F}}{\partial \xi} + \frac{\partial \widetilde{G}}{\partial \eta} + \frac{\partial \widetilde{H}}{\partial \zeta} \right) + Q \left[ \frac{\partial}{\partial \xi}(|J|\xi_t) + \frac{\partial}{\partial \eta}(|J|\eta_t) + \frac{\partial}{\partial \zeta}(|J|\zeta_t) \right] \right\} \\
&= \frac{1}{|J|} \left\{ -\left( \frac{\partial \widetilde{F}}{\partial \xi} + \frac{\partial \widetilde{G}}{\partial \eta} + \frac{\partial \widetilde{H}}{\partial \zeta} \right) + source \right\}
\end{aligned} \tag{2.12}$$

where

$$source = Q \left[ \frac{\partial}{\partial \xi}(|J|\xi_t) + \frac{\partial}{\partial \eta}(|J|\eta_t) + \frac{\partial}{\partial \zeta}(|J|\zeta_t) \right]. \tag{2.13}$$

Note that $\frac{\partial \widetilde{F}}{\partial \xi} + \frac{\partial \widetilde{G}}{\partial \eta} + \frac{\partial \widetilde{H}}{\partial \zeta}$ contains a term as $Q \left[ \frac{\partial}{\partial \xi}(|J|\xi_t) + \frac{\partial}{\partial \eta}(|J|\eta_t) + \frac{\partial}{\partial \zeta}(|J|\zeta_t) \right]$. It is clear that GCL is satisfied strictly as this term will be canceled by the 'source' term when $Q$ is a constant (i.e. the free stream flow). The benefits of this method are that the source term is easy to compute and implement for the original solver for stationary grids and the calculation of $\partial |J| / \partial t$ can be avoided, which might generate additional errors and increase the computational cost.

**Implicit Scheme**

At each cell 'c', using the backward Euler scheme for the time derivative,

$$\frac{\widetilde{Q_c}^{n+1} - \widetilde{Q_c}^{n}}{\Delta t} - \left[ R_c(\widetilde{Q}^{n+1}) - R_c(\widetilde{Q}^{n}) \right] = R_c(\widetilde{Q}^{n}), \tag{2.14}$$

further performing the Taylor expansion and keeping the first-order term, we obtain

$$R_c(\widetilde{Q}^{n+1}) - R_c(\widetilde{Q}^n) = \frac{\partial R_c}{\partial \widetilde{Q}_c}\Delta\widetilde{Q}_c + \sum_{nb \neq c}\frac{\partial R_c}{\partial \widetilde{Q}_{nb}}\Delta\widetilde{Q}_{nb}, \qquad (2.15)$$

where $\Delta\tilde{Q}_c = \tilde{Q}_c^{n+1} - \tilde{Q}_c^n$, 'nb' indicates all the neighboring cells contributing to the residual of cell 'c'.

Combining (2.14) and (2.15), we obtain

$$(\frac{I}{\Delta t} - \frac{\partial R_c}{\partial \widetilde{Q}_c})\Delta\widetilde{Q}_c - \sum_{nb \neq c}\frac{\partial R_c}{\partial \widetilde{Q}_{nb}}\Delta\widetilde{Q}_{nb} = R_c(\widetilde{Q}^n). \qquad (2.16)$$

However, it is expensive in memory to store the full LHS implicit Jacobian matrices. Therefore, a preconditioned LU-SGS scheme is adopted in the development of the implicit scheme. Herein, we just introduce a preconditioning matrix as

$$D = (\frac{I}{\Delta t} - \frac{\partial R_c}{\partial \widetilde{Q}_c}), \qquad (2.17)$$

and the iterative scheme becomes

$$D\Delta\widetilde{Q}_c^{(k+1)} = (\frac{I}{\Delta t} - \frac{\partial R_c}{\partial \widetilde{Q}_c})\Delta\widetilde{Q}_c^{(k+1)} = R_c(\widetilde{Q}^n) + \sum_{nb \neq c}\frac{\partial R_c}{\partial \widetilde{Q}_{nb}}\Delta\widetilde{Q}_{nb}^*, \qquad (2.18)$$

where superscript $(k+1)$ is an iterative index, and $*$ indicates the most recently updated solutions. It should be noted that $\Delta\tilde{Q}_c^{(k+1)}$ can be written as

$$\Delta\widetilde{Q}_c^{(k+1)} = \widetilde{Q}_c^{(k+1)} - \widetilde{Q}_c^n = (\widetilde{Q}_c^{(k+1)} - \widetilde{Q}_c^{(k)}) + (\widetilde{Q}_c^{(k)} - \widetilde{Q}_c^n), \text{ with } \widetilde{Q}_c^{(k)} = \widetilde{Q}_c^*. \qquad (2.19)$$

Since we do not want to store the matrices $\partial R_c / \partial \tilde{Q}_{nb}$, (2.18) is further manipulated as follows.

$$R_c(\widetilde{Q}^n) + \sum_{nb \neq c}\frac{\partial R_c}{\partial \widetilde{Q}_{nb}}\Delta\widetilde{Q}_{nb}^* = R_c(\widetilde{Q}_c^n, \{\widetilde{Q}_{nb}^n\}_{nb \neq c}) + \sum_{nb \neq c}\frac{\partial R_c}{\partial \widetilde{Q}_{nb}}\Delta\widetilde{Q}_{nb}^*$$

$$\approx R_c(\widetilde{Q}_c^n, \{\widetilde{Q}_{nb}^*\}_{nb \neq c}) \approx R_c(\widetilde{Q}_c^*, \{\widetilde{Q}_{nb}^*\}_{nb \neq c}) - \frac{\partial R_c}{\partial \widetilde{Q}_c}\Delta\widetilde{Q}_c^* \qquad (2.20)$$

$$= R_c(\widetilde{Q}^*) - \frac{\partial R_c}{\partial \widetilde{Q}_c}\Delta\widetilde{Q}_c^* \left( or \quad R_c(\widetilde{Q}^*) - \frac{\partial R_c}{\partial \widetilde{Q}_c}\Delta\widetilde{Q}_c^{(k)} \right)$$

In (2.20), note that both approximations can be obtained using the first-order Taylor series expansion. Combining (2.18-20), we obtain

$$D(\widetilde{Q_c}^{(k+1)} - \widetilde{Q_c}^{(k)}) = \left( \frac{I}{\Delta t} - \frac{\partial R_c}{\partial \widetilde{Q_c}} \right)(\widetilde{Q_c}^{(k+1)} - \widetilde{Q_c}^{(k)}) = R_c(\widetilde{Q}^*) - \frac{\Delta \widetilde{Q_c}^*}{\Delta t}, \qquad (2.21)$$

Since matrix *D* merely serves as a preconditioner, the accuracy of the iteration will be determined by the right-hand side (RHS) of the equation (2.21).

Note that

$$\frac{\partial \widetilde{F}}{\partial \xi} = \frac{\partial \left[ |J|(Q\xi_t + F\xi_x + G\xi_y + H\xi_z) \right]}{\partial \xi}$$
$$= Q \frac{\partial |J|\xi_t}{\partial \xi} + |J|\xi_t \frac{\partial Q}{\partial \xi} + \frac{\partial \left[ |J|(F\xi_x + G\xi_y + H\xi_z) \right]}{\partial \xi}, \qquad (2.22)$$

which is contained in $R(\tilde{Q})$.

Thus, the GCL is introduced in the RHS as follows.

$$\left( \frac{I}{\Delta t} - \frac{\partial R_c}{\partial \widetilde{Q_c}} \right)(\widetilde{Q_c}^{(k+1)} - \widetilde{Q_c}^{(k)}) = R_c(\widetilde{Q}^*) - \frac{\Delta \widetilde{Q_c}^*}{\Delta t} + Q_c^* \left( \frac{\Delta |J|^*}{\Delta t} + \frac{\partial}{\partial \xi}(|J|^* \xi_t^*) + \frac{\partial}{\partial \eta}(|J|^* \eta_t^*) + \frac{\partial}{\partial \zeta}(|J|^* \zeta_t^*) \right)$$

$$(2.23)$$

It should be noted that in the above equation the discrete form of $\Delta |J|^*/\Delta t$ is exactly the same as $\Delta \tilde{Q}_c^* /\Delta t$. This consistency can help minimize the errors induced by discretization schemes. For example, the second-order backward difference scheme (BDF2) for the two derivatives can be written as below,

$$\frac{\Delta \widetilde{Q_c}^*}{\Delta t} = \frac{3\widetilde{Q_c}^* - 4\widetilde{Q_c}^n + \widetilde{Q_c}^{n-1}}{2\Delta t}, \quad \frac{\Delta |J|^*}{\Delta t} = \frac{3|J|^* - 4|J|^n + |J|^{n-1}}{2\Delta t} \qquad (2.24)$$

## 2.4  General Grid Deformation Strategies

In order to solve problems with moving grids, it is necessary to design a grid moving algorithm. As the first step, the boundary motion of the physical domain is specified according to the physical problem. Then traditionally two methods can be used to manipulate the rest of the mesh nodes. The first one is to use the algebraic procedure to smooth the whole field [5,17-19,30]. Another approach is to solve differential equations (usually elliptic, like equations of linear elasticity) with the specified boundary conditions [21,30]. For the sake of computational efficiency, an algebraic methodology is performed in the present study, which has been widely used by other researchers [17-19].

The first implementation of the algebraic method is to make the whole physical domain perform a rigid-body motion. Obviously, this approach cannot handle relative motions among several components. Another implementation is to use blending functions to reconstruct the whole physical domain. In the present study, a fifth-order polynomial blending function proposed in [19],

$$r_5(s) = 10s^3 - 15s^4 + 6s^5, s \in [0,1] \tag{2.25}$$

is adopted. It is obvious that $r_5'(0) = r_5'(1) = 0$, which can generate a smooth variation at both end points during the mesh reconstruction. Herein, '$s$' is a normalized arc length, which reflects the 'distance' between the present node and the moving boundaries. Specifically, $s=0$ means that the present node will move with the moving boundary, while $s=1$ means that the present node will not move. Therefore, for any motion (transition, rotation), the change of the position vector $\vec{P}$ is

$$\Delta \vec{P}_{present} = (1 - r_5)\Delta \vec{P}_{rigid} . \tag{2.26}$$

After these manipulations, a new set of mesh nodes can be calculated based on $\Delta \vec{P}$. In the present study, for the deformable grid approach, in order to maintain the grid quality near the wall boundaries, rigid motions are enforced in the vicinity of the wall boundaries. The outer boundaries far from the wall are specified as stationary reference. Between the rigidly displaced grid and the stationary grid, the blending function (2.25) is used to interpolate and smooth the grid motion.

It should be mentioned that the same smoothing method can also be used in problems with two or more objects with relative motions. In the present study, a tandem airfoil problem is investigated using this approach, as will be discussed in the next section. In that case, the change of the position vector $\vec{P}$ can be written as

$$\begin{aligned} \Delta \vec{P}_{present} &= \Delta \vec{P}_{rigid1}, \quad if \quad s_1 = 0 \\ \Delta \vec{P}_{present} &= \Delta \vec{P}_{rigid2}, \quad if \quad s_2 = 0 \\ \Delta \vec{P}_{present} &= \frac{s_2^n}{s_1^n + s_2^n}\left[1 - r_5(s_1)\right]\Delta \vec{P}_{rigid1} + \frac{s_1^n}{s_1^n + s_2^n}\left[1 - r_5(s_2)\right]\Delta \vec{P}_{rigid2}, \quad otherwise \end{aligned} \tag{2.27}$$

and it is made sure that there is no region with both $s_1 = 0$ and $s_2 = 0$.

Another point is that if '$s$' in the blending function (2.25) is set to be 0 at any grid point,

then a rigidly moving grid approach is achieved. In this case, the whole domain will have the same motion. Generally speaking, a rigid grid is only suitable for simple motions of one object. For the case of multiple objects with relative motions, it will generate overset cells. From a numerical perspective, the Jacobian of the transformation from the physical domain to the computational domain will be the same all the time, and theoretically this will introduce less error when performing simulations, as Jacobian needs to be calculated only once. On the other hand, a deformable grid is desirable in more general cases. But extra efforts are needed to calculate the changing Jacobian as the grid evolves.

It is clear that for systems with complex relative motions, the algebraic algorithm for the grid motion can be hard to design. However, for many cases this method enjoys its remarkable simplicity and efficiency. Several examples will be shown in the next section.

## 3. Numerical Results

### 3.1 Accuracy Study Using an Isentropic Vortex Propagating Problem

In order to verify that the SD method can preserve its high-order accuracy for deformable meshes, a 2D Euler vortex propagation case is performed in the present study. SSP third-order Runge Kutta (SSP-RK3) time integration is used for this study. The definition of the isentropic vortex and its evolution process can be described as [7]

$$u(r) = \frac{U'_{max}}{b} r e^{\frac{1}{2}(1-\frac{r^2}{b^2})}, \; \rho(r) = (1-\frac{1}{2}(\gamma-1)U'^2_{max} e^{1-\frac{r^2}{b^2}})^{1/(\gamma-1)}, \; p(r) = (1-\frac{1}{2}(\gamma-1)U'^2_{max} e^{1-\frac{r^2}{b^2}})^{\gamma/(\gamma-1)},$$

and

$$\begin{pmatrix} \rho(x,y,t) \\ u(x,y,t) \\ v(x,y,t) \\ p(x,y,t) \end{pmatrix} = \begin{pmatrix} 0 \\ U_0 \\ V_0 \\ 0 \end{pmatrix} + \begin{pmatrix} \rho(r) \\ -u(r)\sin\theta \\ u(r)\cos\theta \\ p(r) \end{pmatrix},$$

where $u(r), \rho(r), p(r)$ are the velocity, density and pressure distribution of the vortex respectively; $U_0$ and $V_0$ are the advection velocities of the main stream in x and y directions; $r = \sqrt{(x-U_0 t)^2 + (y-V_0 t)^2}$ is the radial distance from the vortex center; b is a constant.

The isentropic vortex was originally centered at (0,0), with the initial condition given by

$(U_0, V_0) = (0.5,0)$, $U'_{max} = 0.5U_0$, $b = 0.2$. The physical domain of this problem is set to be $[-2,2] \times [-2,2]$ with one cell in z direction. The grid deformation strategy follows [13], which analytically defines the grid motion as

$$\vec{x}(t) = \vec{x}(t) + d\vec{x}(t)$$

with

$$dx(t) = A_x L_x dt / t_{\max} \sin(f_n t) \sin(f_x x) \sin(f_y y)$$
$$dy(t) = A_y L_y dt / t_{\max} \sin(f_n t) \sin(f_x x) \sin(f_y y)$$

for 2D problems. Herein, $A_{x,y}$ is the amplitude in x and y directions; $L_{x,y}$ and $t_{max}$ depict the reference length and time; $dt$ is the time step, and

$$f_n = n_t \pi / t_{\max}, \quad f_x = n_x \pi / L_x, \quad f_y = n_y \pi / L_y.$$

The motion control parameters of the deformable grid are set as $L_x = L_y = 4$, $t_{max} = 0.1$ and $n_x = n_y = 2$, $n_t = 1$ and $A_x = A_y = 0.2$. Since at $t = 0.1$ the grid has the largest deformation, the errors are analyzed at that instance. In order to ensure that the time integration errors have no effects on the accuracy analyses, a fixed time step is chosen as $\Delta t = 5 \times 10^{-5}$. Pressure coefficient (defined as $C_p = (p - p_\infty)/(0.5\rho U_\infty^2)$) distribution of the vortex is displayed in Fig. 2(a) at $t = 0.1$. From Fig. 2(b), it is obvious that the analytical result agrees well with the numerical one. Results of the grid refinement study are displayed in Fig. 3, which demonstrate the accuracy of the SD method for the deformable domain. The errors are measured with both $L_2$ and $L_\infty$ norms, and an optimal convergence has been achieved in all cases. It is also found that the schemes with and without GCL for the isentropic vortex propagation tests almost obtain the same error values and accuracy. However, for the free stream preservation test, it is obvious from Fig. 4 that for both explicit (SSP-RK3) and implicit (BDF2) schemes, if the GCL is not enforced, the error level can reach up to nine orders larger than machine zero. But with a GCL compliant scheme, machine zero can be achieved. In this test, the 4th order scheme is used on the grid with 19×19×1 cells, and the errors are computed at $t = 0.1$ as well.

(a)                                                    (b)
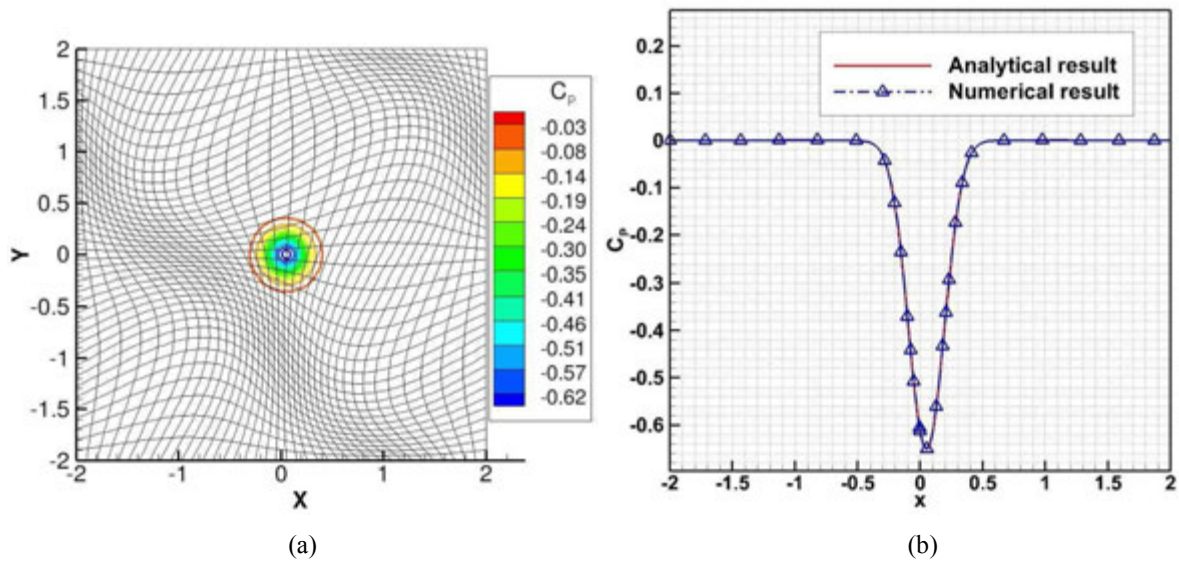
**Fig. 2.** (a) Pressure coefficient distribution and grid deformation; (b) comparison between numerical and analytical solutions of pressure coefficient along y=0 at t=0.1. The solid line denotes the analytical result, and the dash-dot line with triangles indicates the numerical result.



(a)                                                    (b)
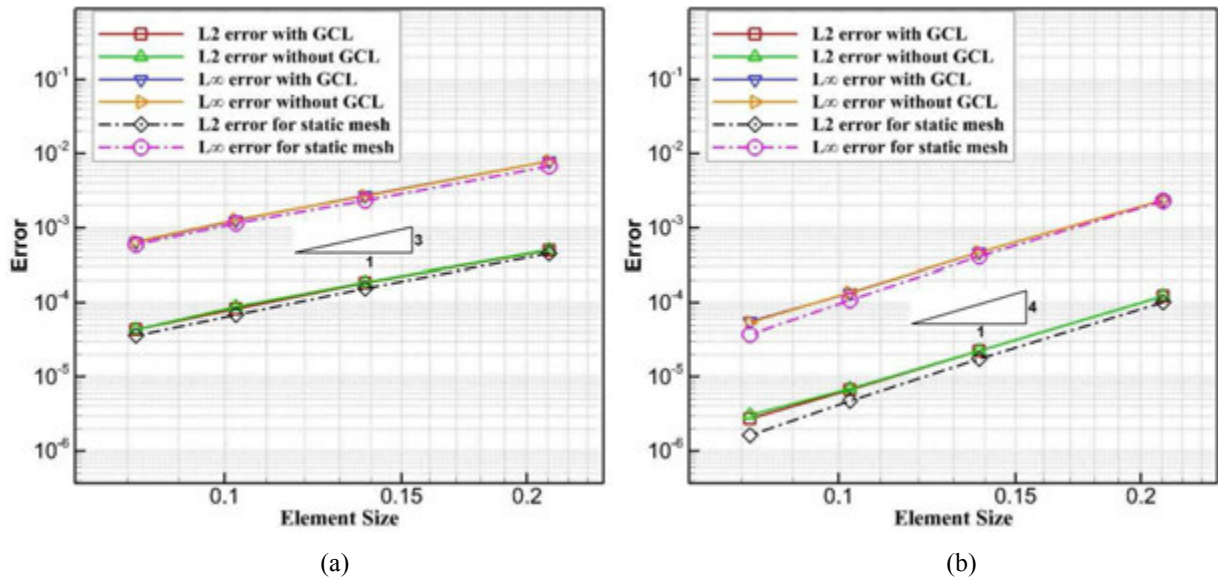
**Fig. 3.** The convergence of the vortex propagation problem using the deformable grid with and without GCL correction, as well as for the stationary grid. Figure (a) and (b) displays results from the 3$^{rd}$-order and 4$^{th}$-order SD methods respectively. In both cases, four mesh sizes are used and error representations in both 2-norm (as denoted by $L_2$) and infinity-norm (as denoted by $L_\infty$) are given.
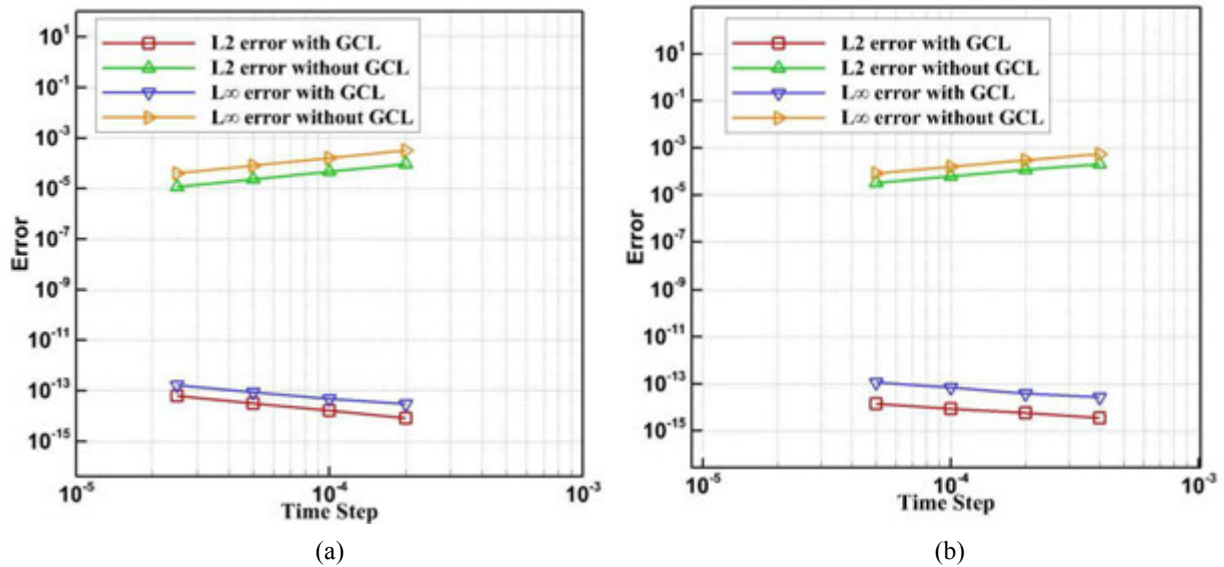
**Fig. 4.** The convergence of the free stream preservation test using the deformable grid with and without GCL correction. Results from the 4th-order SD method with (a) explicit SSP-RKS and (b) implicit BDF2 time integration schemes are displayed. In both cases, four time steps are used and error representations in both 2-norm (as denoted by $L_2$) and infinity-norm (as denoted by $L_\infty$) are given.

### 3.2 Bio-inspired Flow Simulations

Recently, there is a growing interest in the study of bio-inspired flows in the fluid dynamics community. One of the major objectives is to investigate the wake structures after flapping airfoils or wings [1,2,6,10,15,16,20,28,29,35]. The reason is that based on the evolution of these wake structures, the thrust and lift generation mechanism in agile flight can be clearly revealed. As mentioned before, such flows are unsteady vortex dominated flows. In order to resolve the subtle vortex structures, a high-order method is necessary, as 1st and 2nd order flow solvers may dissipate the unsteady vortices quickly. Moreover, these problems all involve moving boundaries. Therefore, several numerical simulations of the flapping-related motions are carried out to examine the performance of the high-order SD method for deformable meshes. Unless otherwise noted, the default numerical scheme used in the simulations is the 3rd order SD scheme. For the two dimensional simulations, the implicit BDF2 time integration is used; and for the three dimensional simulations, the explicit SSP-RK3 time integration is employed. For all the simulations presented in this section, the free stream Mach number is chosen as 0.1.

*3.2.1 Flat Plate Pitch-up Process*

A series of canonical unsteady experimental studies on the flat plate pitch-up problem was conducted in [15,16]. This problem is also studied using the high-order SD method. The aim of the study is to investigate the aerodynamic responses of maneuvering flights, such as perching. The main features of these problems can be generalized as high-frequency and high-amplitude pitching processes, which can be used to verify the efficiency of the SD method for deformable meshes. In order to compare the numerical results with the experimental ones, the functions and parameters used in the present study are defined to be consistent with the experiment.

The maximum pitching angle $\alpha_m$ is set to be $40^o$, and $\alpha$ is computed according to

$$\alpha(T) = \alpha_m \frac{G(T)}{Max(G(T))},$$

with a smoothing function defined in [6] as

$$G(T) = \ln\left[\frac{\cosh(a(T-T_1))\cosh(a(T-T_4))}{\cosh(a(T-T_2))\cosh(a(T-T_3))}\right],$$

where $a$ is a function shape parameter, which is set to be 11.0, $T_1 = \Delta T_s$, $T_2 = T_1 + \Delta T_{pu}$, $T_3 = T_2 + \Delta T_h$ and $T_4 = T_3 + \Delta T_{pd}$ as shown in Fig. 5. Herein, $T$ is a non-dimensional time with respect to $C/U_\infty$, where '$C$' stands for the chord length. The start-up interval $\Delta T_s$ is set to be 1.0, the reduced pitch rate $K = (C\alpha_m/\Delta T_{pu,d})/2U_\infty$ is specified as 0.2, and the hold interval $\Delta T_h$ is set to be 0.05. The Reynolds number based on the plate chord length is 10,000. The non-dimensional time step used for the simulations is $\Delta t U_\infty/C = 7.5 \times 10^{-5}$.

Fig. 6 shows the details of the deformable grid and the rigidly displaced grid. The grid has 77×78×1 cells, and the minimum cell size normalized by the plate chord length in the transverse direction is 0.0015. The numerical results for two instances during the pitch-up process, namely $tU_\infty/C = 1.8725$ (corresponding pitch angle $20^o$) and $tU_\infty/C = 2.745$ (corresponding pitch angle $40^o$), are compared with the experimental results. From Fig. 7 and 8, it is obvious that the computed instantaneous vorticity and velocity fields agree well with the experimental data. The corresponding force histories for both deformable and rigidly moving grids are displayed in Fig. 9. Note that the results with different grid deformation

algorithms are nearly identical.
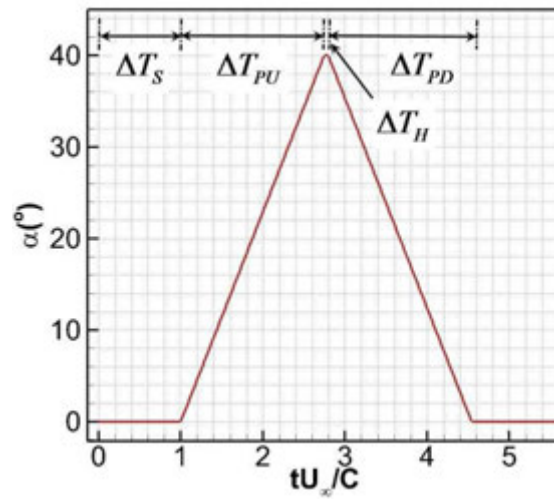


**Fig. 5.** Pitching angle evolution during the hold, pitch-up, hold and pitch-down process.
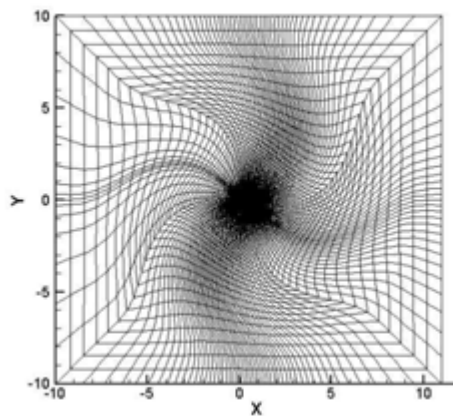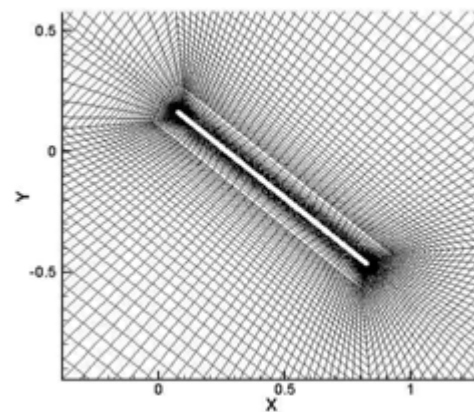


| (a) | (b) |
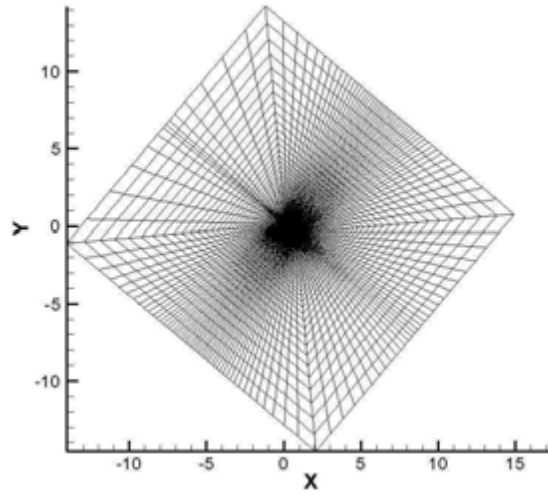
(c)

**Fig. 6.** (a) Overview of the deformable grid; (b) close-up view of the deformable grid near the moving boundary; (c) overview of the rigidly moving grid.



*a. Experimental results (courtesy of OL [15]). From left to right: flow visualization with dye; u velocity contour (PIV); vorticity contour in the spanwise direction (PIV).*
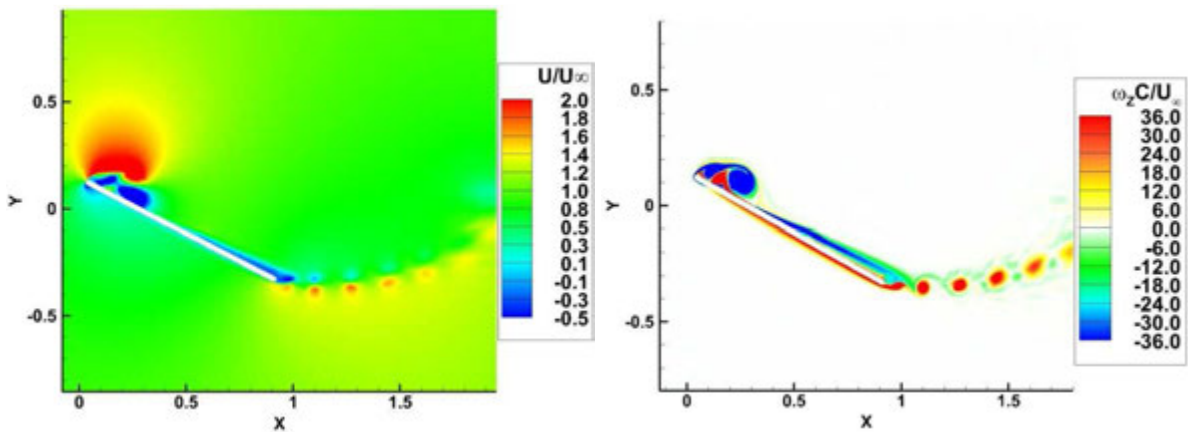


*b. Numerical results with deformable grids. Left: u velocity contour ($u/U_\infty$); right: vorticity contour in the*

*spanwise direction.*
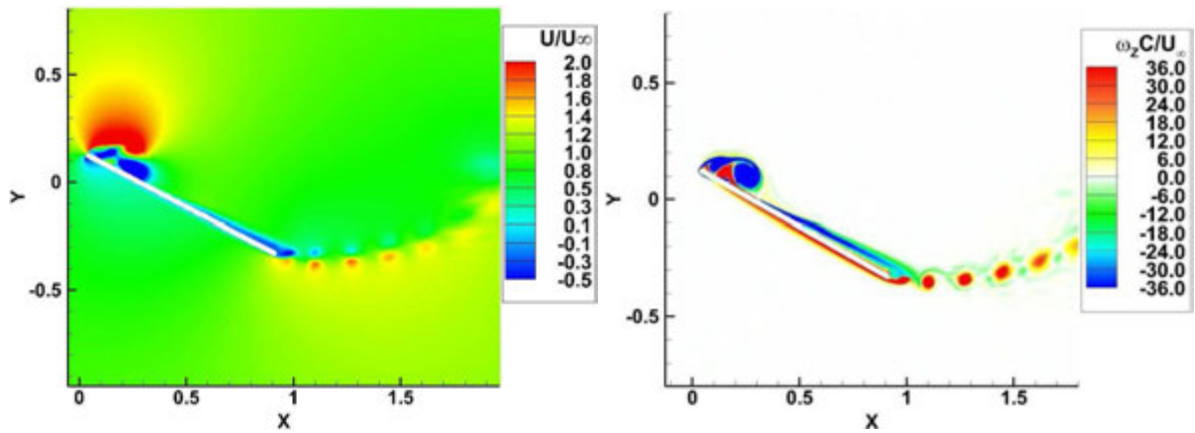


*c. Numerical results with rigidly moving grids. Left: u velocity contour; right: vorticity contour in the spanwise direction.*

**Fig. 7.** Comparison between numerical and experimental results for Re=10000, k=0.2, $\alpha = 20°$ when $tU_\infty/C = 1.8725$.
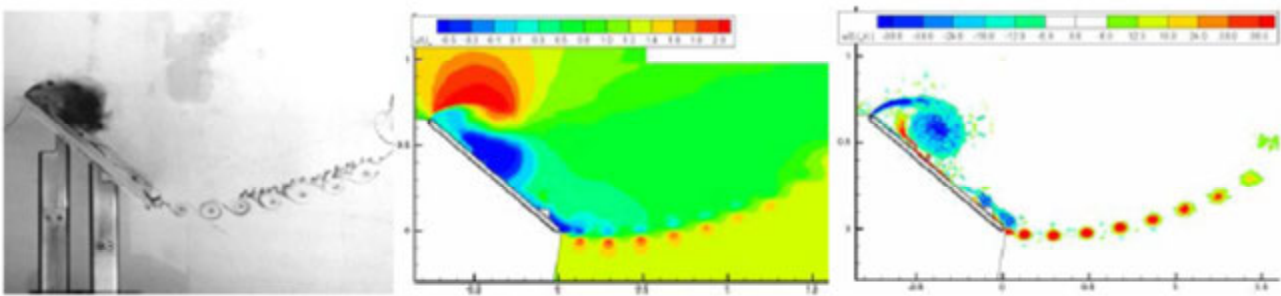


*a. Experimental results (courtesy of OL [15]). From left to right: flow visualization with dye; u velocity contour (PIV); vorticity contour in the spanwise direction (PIV).*
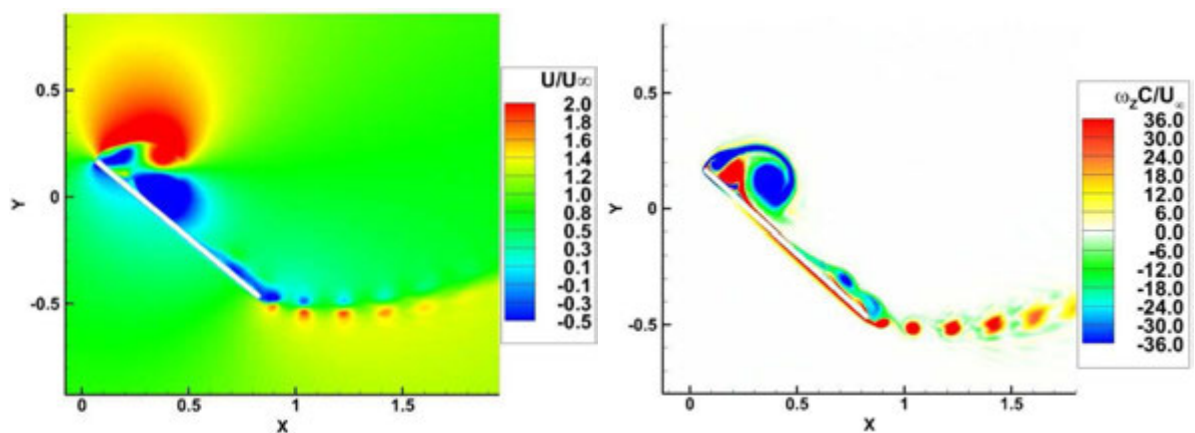


*b. Numerical results with deformable grids. Left: u velocity contour ($u/U_\infty$); right: vorticity contour in the*

*spanwise direction.*
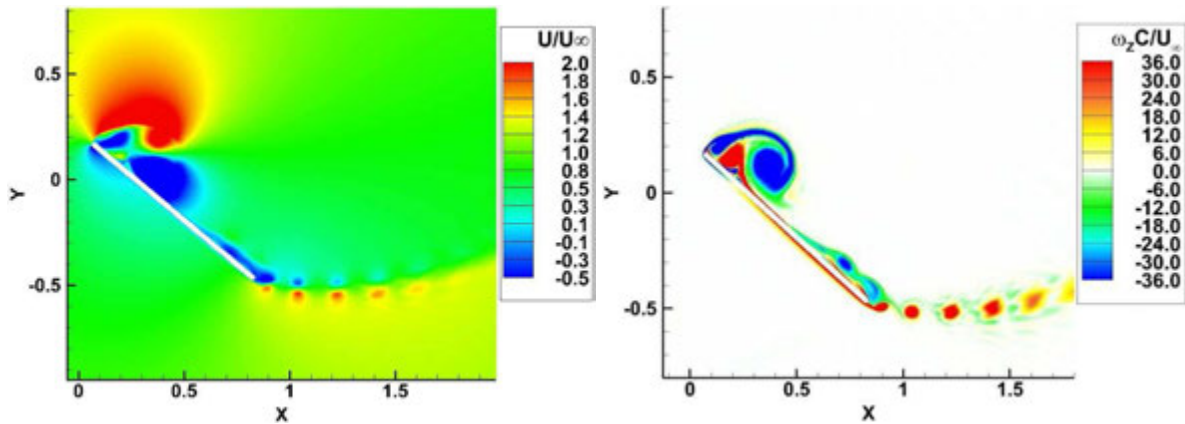


*c. Numerical results with rigidly moving grids. Left: u velocity contour; right: vorticity contour in the spanwise direction.*

**Fig. 8.** Comparison between numerical and experimental results for Re=10000, k=0.2, $\alpha = 40°$ when $tU_\infty/C = 2.745$.



(a)         (b)
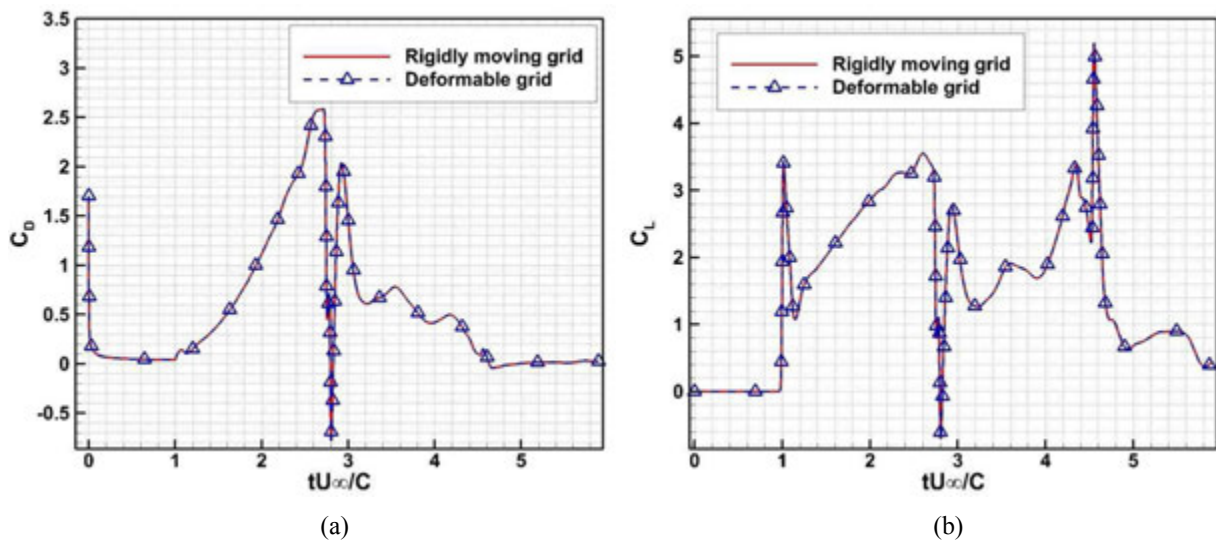
**Fig. 9.** (a) Drag coefficient history and (b) lift coefficient history for Re=10000, k=0.2, calculated using both the rigidly moving grid (as denoted by the solid line) and the deformable grid (as denoted by the dash-dot line with triangles).

### 3.2.2 Flow over a Sinusoidally Pitching Airfoil

An experimental investigation of the flow over a NACA-0012 airfoil performing a pitching motion with small amplitude and high reduced frequency has been conducted in [2]. The aim of the study is to find the critical point at which the von Karman vortex street turns

into a reverse von Karman street and to study the parameter dependencies of the thrust generation during the pitching motion. Following this experimental study, a numerical research is completed with the same parameter setting. And some cases are verified both with rigidly moving and deformable grid strategies.

In the present study, the airfoil performs a pitching motion expressed as

$$\alpha(t) = \alpha_m + \alpha_0 \sin(\omega t + \phi), \ \omega = 2\pi f$$

where $\alpha_m$ is the mean angle of attack, $\alpha_0$ is the amplitude of the pitching angle, $\phi$ is the initial phase. Also, the reduced frequency $k$ and the Strouhal number $St$ are defined respectively as

$$k = \frac{\omega C}{2U_\infty}, \ St = \frac{fA}{U_\infty},$$

where $C$ is the chord length of the airfoil, $A$ is the pitching amplitude. The Reynolds number based on the airfoil chord length for all the simulations in this section is 12,600. The non-dimensional time step used for the two dimensional simulations is $\Delta t U_\infty/C = 1 \times 10^{-4}$; while that for the three dimensional simulations is $\Delta t U_\infty/C = 1 \times 10^{-5}$.

For the rigidly moving grid approach, the computational grid moves with the body and is updated using

$$\begin{cases} x_{present} - x_c = (x_{former} - x_c)\cos(\Delta\alpha) - (y_{former} - y_c)\sin(\Delta\alpha) \\ y_{present} - y_c = (x_{former} - x_c)\sin(\Delta\alpha) + (y_{former} - y_c)\cos(\Delta\alpha) \end{cases}$$

where $(x_c, y_c)$ is the pitching center, and $\Delta\alpha = \alpha_0(\sin(\omega(t + dt) + \phi_0) - \sin(\omega t + \phi_0))$.

The deformable grid and the rigidly moving grid at maximum displacements for the St=0.33 case are displayed in Fig. 10. There the grid with 341×47×1 cells for the two dimensional simulations and that with 341×47×10 cells for the three dimensional simulations are shown. The minimum cell size normalized by the airfoil chord length in the transverse direction is 0.001 and that in the spanwise direction for the three dimensional simulations is 0.02. A grid refinement study has been performed in [35] to determine this grid setup. The initial conditions for all simulations on the dynamic grids in the present section are set as the steady solutions of the flow fields under the same Reynolds number (Re=12600) and inlet Mach number (Ma=0.1). The effects of initial conditions on the bio-inspired flow simulations are discussed in [35], and it is found that the present initial conditions can best imitate the

general experimental setups. The convergence history of the steady flow over the stationary NACA 0012 airfoil and the pressure coefficient ($C_p$) contour are shown in Fig. 11.

The phase-averaged vorticity field from the experiment [2] and the corresponding instantaneous vorticity fields from the numerical simulations with different grid deformation algorithms are displayed in Fig. 12. In addition, the experimental and numerical results for the time-averaged vorticity and velocity fields are shown in Fig. 13. The numerical results are found to agree well with the experimental results. Thrust and lift coefficient histories for both deformable and rigidly moving grids are plotted in Fig. 14. According to [2], the mean thrust coefficient for the case Re=12600, k=11.5, St=0.19 is around 0.024. In the present study, the mean thrust coefficient is calculated to be 0.031, and it is obtained by averaging the data in the continuous four cycles after twenty-four cycles. In addition, an interesting phenomenon discovered in the numerical simulation is that if the pitching amplitude is further increased, which means that the Strouhal number is increased, an asymmetric wake structure appears during the pitching motion. This was first reported in [10] for the plunging motion and has been experimentally studied in [29]. The vorticity fields with both deformable and rigidly moving grid are described in Fig. 15. The initial phase $\phi$ is set to be $180^o$. A three dimensional simulation is then conducted using the same parameters as that of the two dimensional simulations, except that in the spanwise direction, periodic boundary conditions are specified. From Fig. 15(c), (d) and Fig. 16, it can be found that results from the 3D simulation are almost the same as those from the 2D simulations. This demonstrates that under the flow conditions specified in the present study, the flow is laminar and 2D simulations can predict the flow features well. The vortex structures in Fig. 15(d) are indicated by Q-criterion, which is described by

$$Q = \frac{1}{2}(R_{ij}R_{ij} - S_{ij}S_{ij}) = \frac{1}{2}\frac{\partial u_i}{\partial x_j}\frac{\partial u_j}{\partial x_i},$$

where $R_{ij} = \frac{1}{2}(\frac{\partial u_i}{\partial x_j} - \frac{\partial u_j}{\partial x_i})$ is the angular rotation tensor, and $S_{ij} = \frac{1}{2}(\frac{\partial u_i}{\partial x_j} + \frac{\partial u_j}{\partial x_i})$ is the rate-of-strain tensor. It also can be discovered from Fig. 16(a) that the thrust generation process appears certain unsteady features accompanying with the asymmetric wake structures. Again, it can be found from Fig. 16 that the numerical results do not depend on the grid deformation

algorithms.

(a)

(b)

(c)

(d)
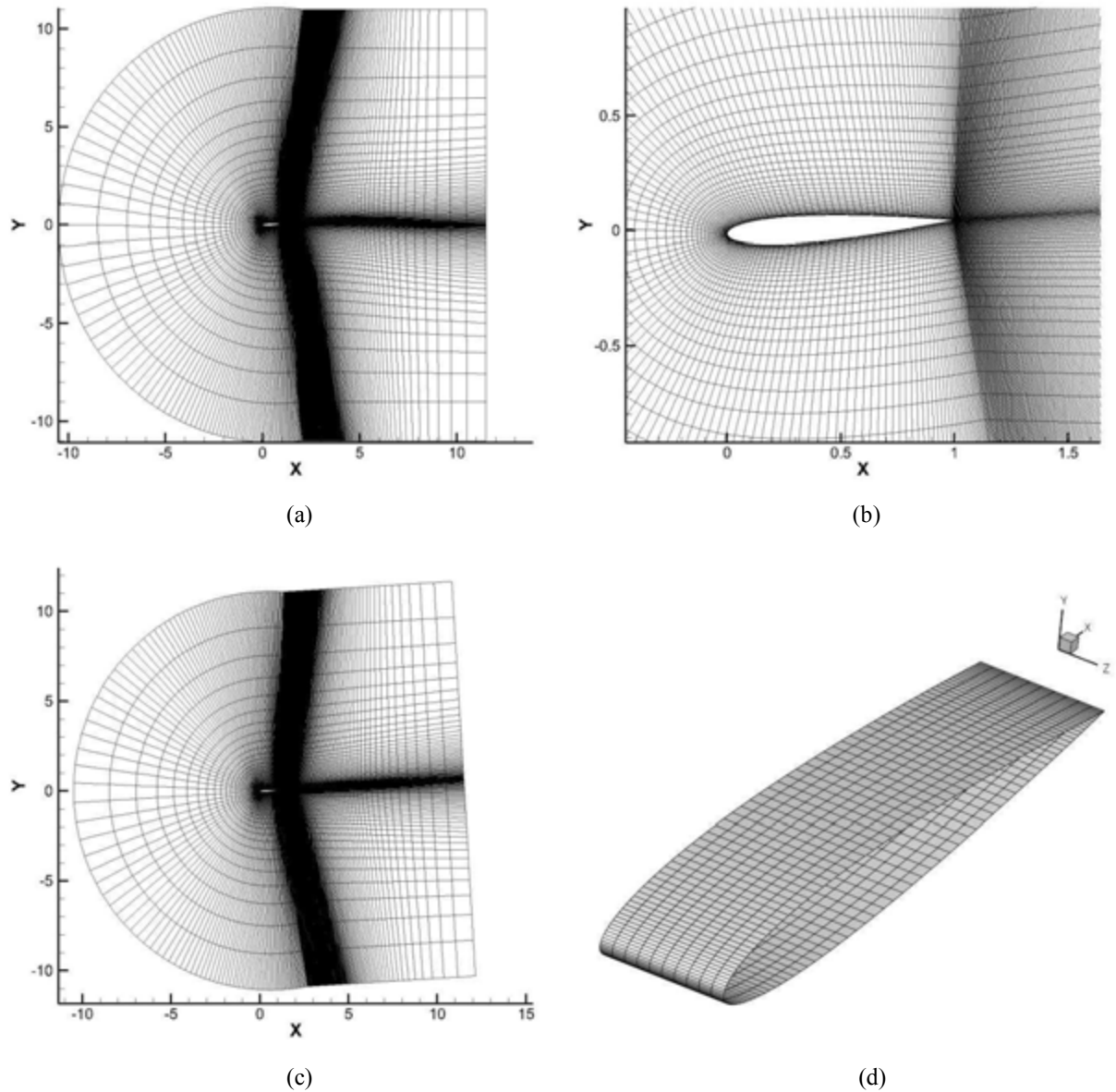
**Fig. 10.** Grids used for the simulations of the sinusoidally pitching airfoil. (a) Overview of the deformable grid; (b) close-up view of the deformable grid near the moving boundary; (c) overview of the rigidly moving grid; (d) airfoil surface grid for the 3D simulations.

(a)                                                        (b)
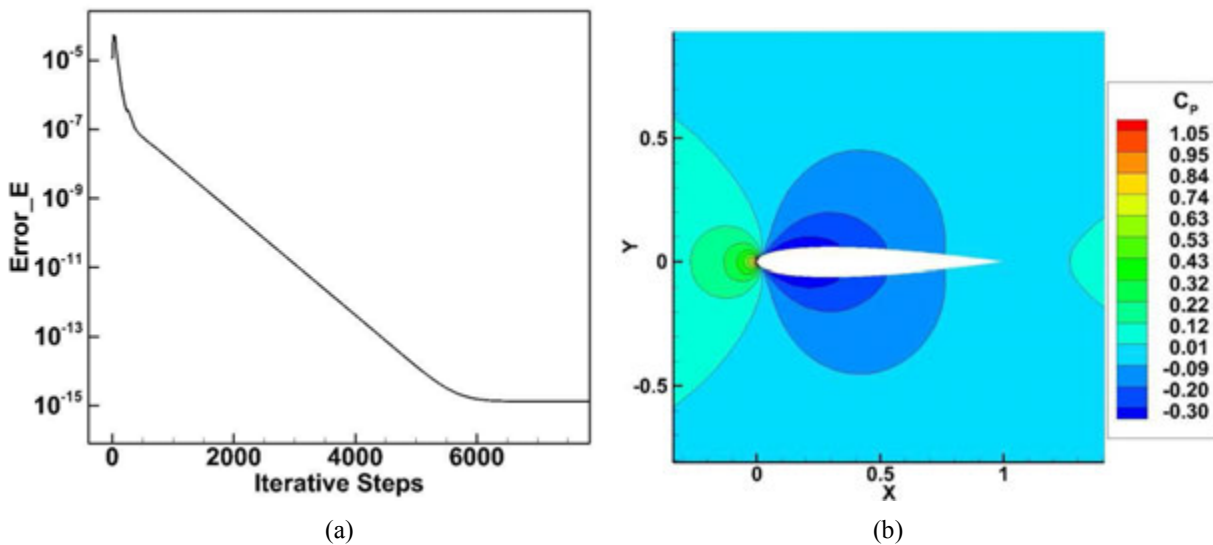
**Fig. 11.** (a) Convergence history of the energy error for the steady solution of the flow over a stationary NACA0012 airfoil with implicit (LU-SGS) time integration; (b) pressure coefficient contours for the converged steady flow.



(a)



(b)                                                        (c)
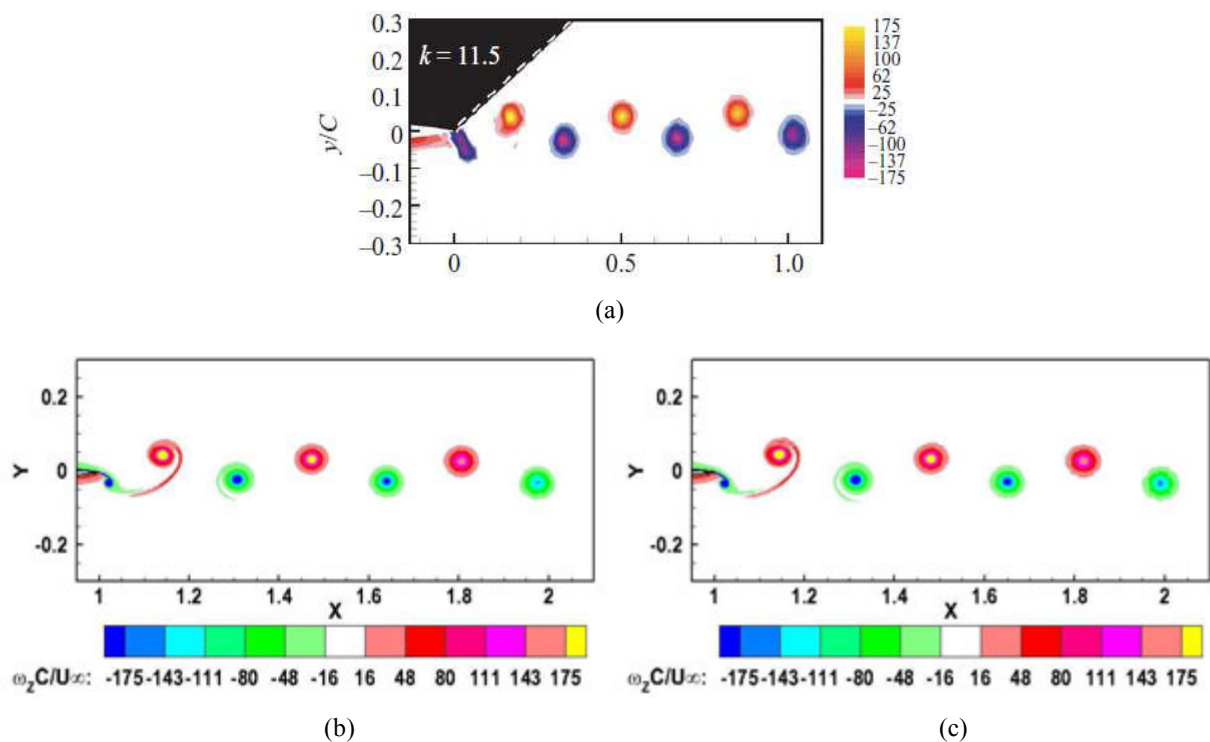
**Fig. 12.** Vorticity field for Re=12600, k=11.5, St=0.19. (a) Phase-averaged experimental results (courtesy of Bohl and Koochesfahani [2]); (b) Instantaneous numerical results with deformable grid; (c) Instantaneous numerical results with rigidly moving grid.
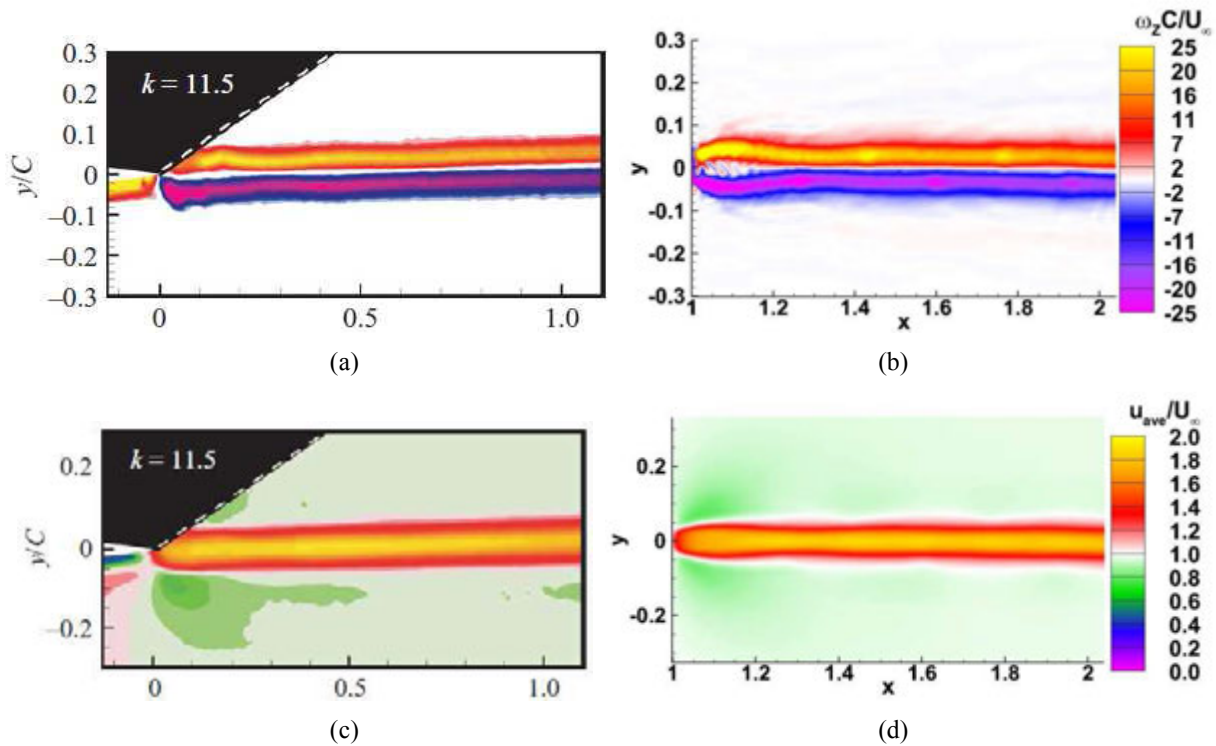
**Fig. 13.** Averaged flow fields for Re=12600, k=11.5, St=0.19. (a) vorticity field, experimental results, (courtesy of Bohl and Koochesfahani [2]); (b) vorticity field, numerical results; (c) u velocity field, experimental results, (courtesy of Bohl and Koochesfahani [2]); (d) u velocity field, numerical results.
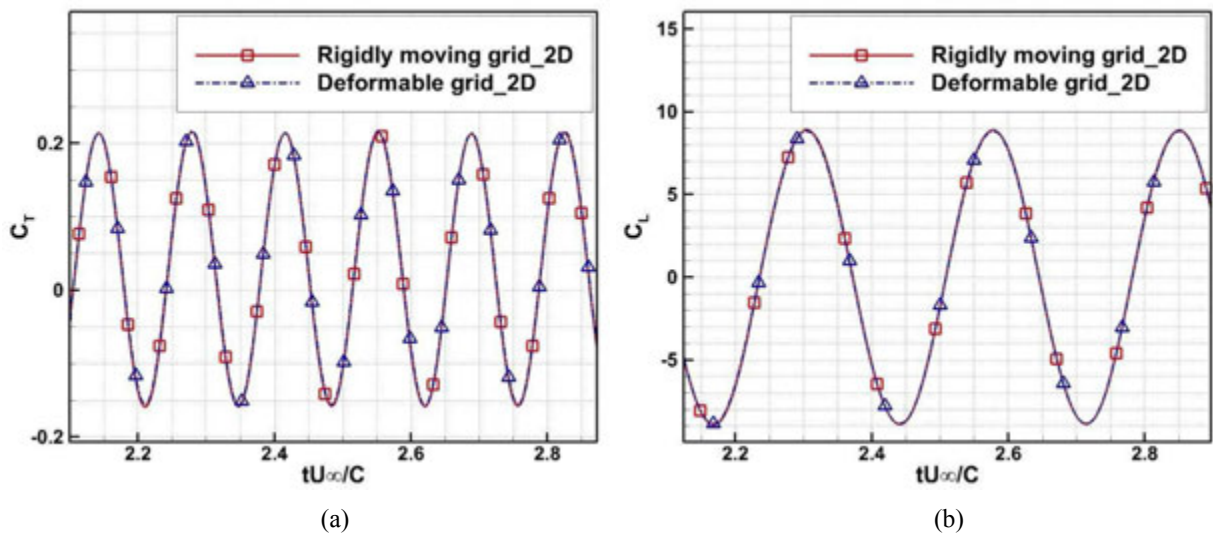


**Fig. 14.** (a) Thrust coefficient history and (b) lift coefficient history for Re=12600, k=11.5, St=0.19, calculated using both the rigidly moving grid (as denoted by the solid line with squares) and the deformable grid (as denoted by the dash-dot line with triangles).
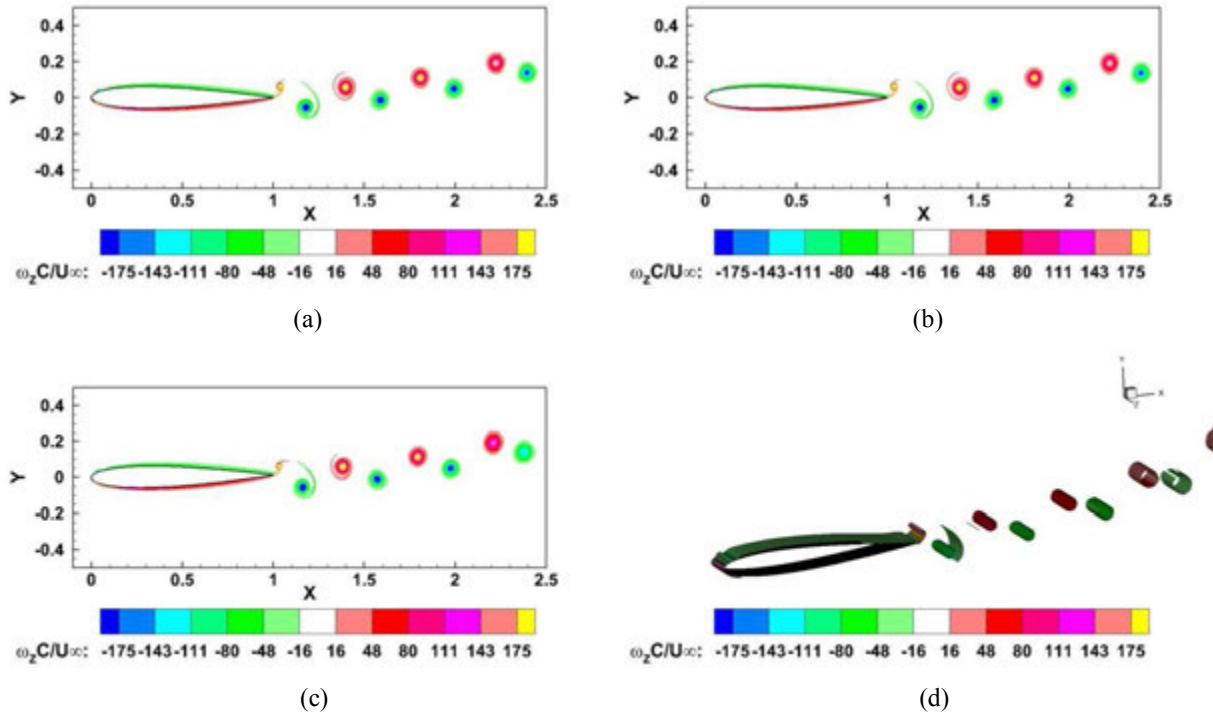
**Fig. 15.** Instantaneous spanwise vorticity field for Re=12600, k=11.5, St=0.33. (a) 2D simulation with the deformable grid; (b) 2D simulation with the rigidly moving grid; (c) 3D simulation with the rigidly moving grid; (d) Iso-surface of Q colored by the spanwise vorticity from the 3D simulation results.



(a)

(b)
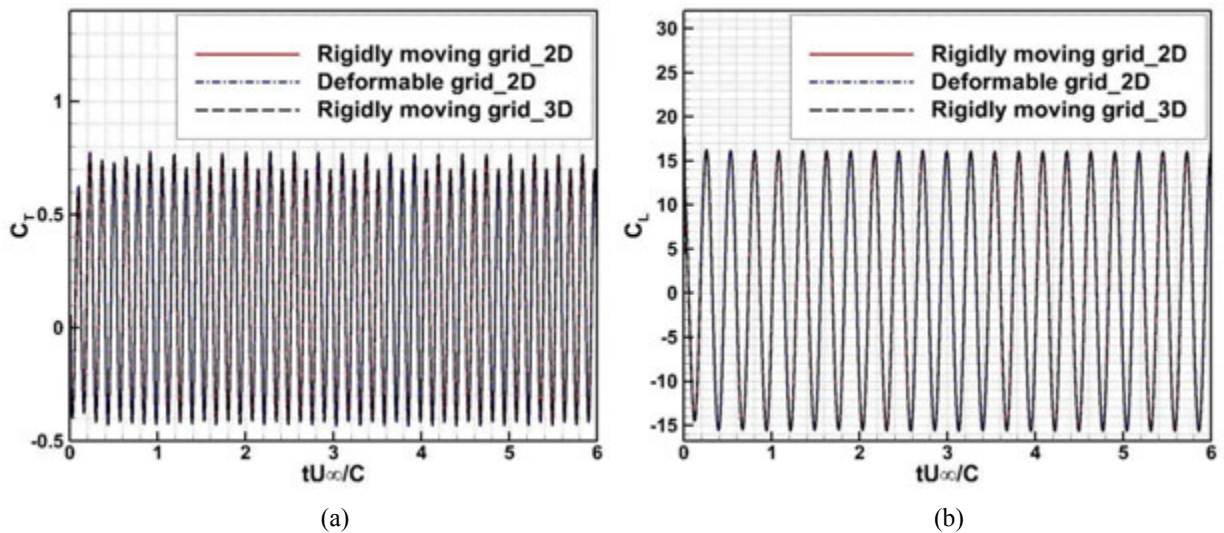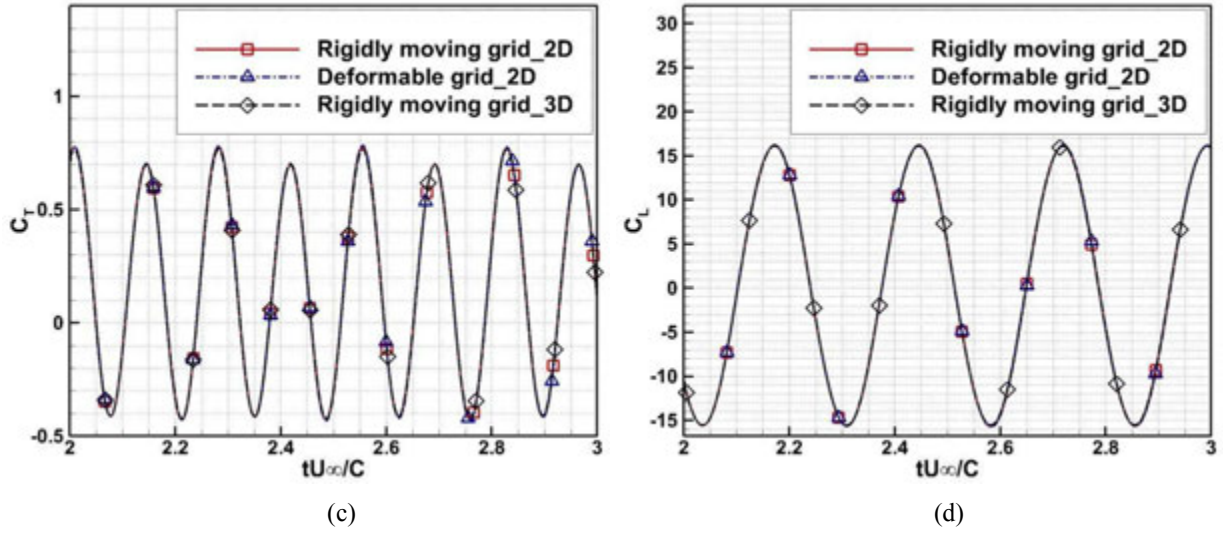
**Fig. 16.** (a) Thrust coefficient convergence history and (b) lift coefficient convergence history for Re=12600, k=11.5, St=0.33, for 2D simulations using the rigidly moving grid (as denoted by the solid line with squares) and the deformable grid (as denoted by the dash-dot line with triangles) and 3D simulations using rigidly moving grid (as denoted by the dash line with diamonds). (c) and (d) are the corresponding close-up views of (a) and (b).

### 3.2.3 Flow over Tandem Airfoils with Inverse Initial Plunging Phases

In order to enhance the thrust or lift generation and increase the propulsive efficiency, the tandem airfoil configuration has been studied by some researchers [1,20]. In these problems, the two airfoils have relative motions, which can be utilized to verify the grid deformation strategy for the SD method. Two flat plates performing plunging motions are studied here. The Reynolds number based on the plate chord length is 10,000. The motions of the two plates are specified as follows.

$$\text{Fore plate:} \quad y = h\sin(\omega t + \phi_1)$$

$$\text{Hind plate:} \quad y = h\sin(\omega t + \phi_2)$$

where $h/C = 0.2$, the reduced frequency $k = 1.5$, $\phi_1 = 0^o$ and $\phi_2 = 180^o$. The non-dimensional time step used for the simulations is $\Delta t U_\infty / C = 2 \times 10^{-4}$.

The deformable grid is displayed in Fig. 17. In order to compare the performances of high-order methods and their low-order counterparts, two sets of grids with almost the same degrees of freedom (DOFs) for the 3$^{rd}$ and 2$^{nd}$ order schemes are used in the simulations. A

grid with 46,270 cells (185,080 DOFs) is designed for the 2$^{nd}$ order scheme; while another grid with 20,056 cells (180,504 DOFs) is designed for the 3$^{rd}$ order scheme. The computed vorticity fields from both 3$^{rd}$ and 2$^{nd}$ order accuracy schemes are shown in Fig. 18, and remarkable differences of small vortex structures near the moving wall boundaries can be observed for different accuracy approaches. Further, Fig. 19 displays the different aerodynamic force convergence histories for methods of different accuracy. The 2$^{nd}$ order scheme shows certain quasi-steady features after several cycles, which is not found from the results of the 3$^{rd}$ order scheme. This can be explained as follows. Due to the relatively high numerical dissipation, the 2$^{nd}$ order scheme can only capture the large vortex structures as seen from Fig. 18. As a comparison, the 3$^{rd}$ order scheme can resolve fine vortex structures near the wall boundaries with the same DOFs. These observations further demonstrate the necessity of high-order methods in vortex dominated flows.



(a)                    (b)
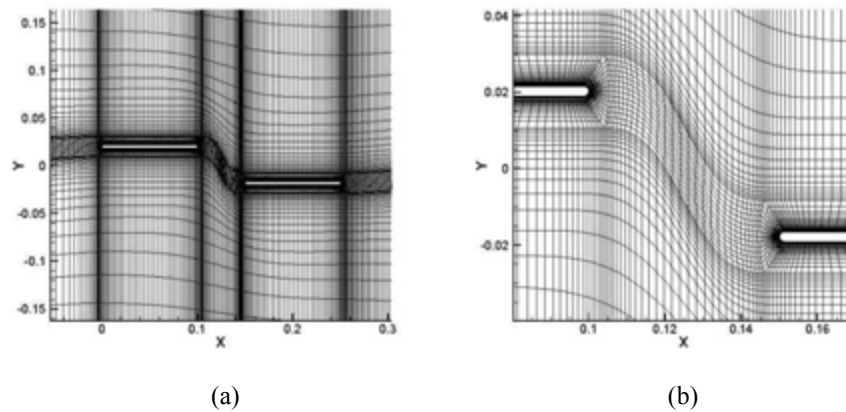
**Fig. 17.** (a) Overview of the deformable grid; (b) close-up view of the deformable grid between the two moving boundaries.
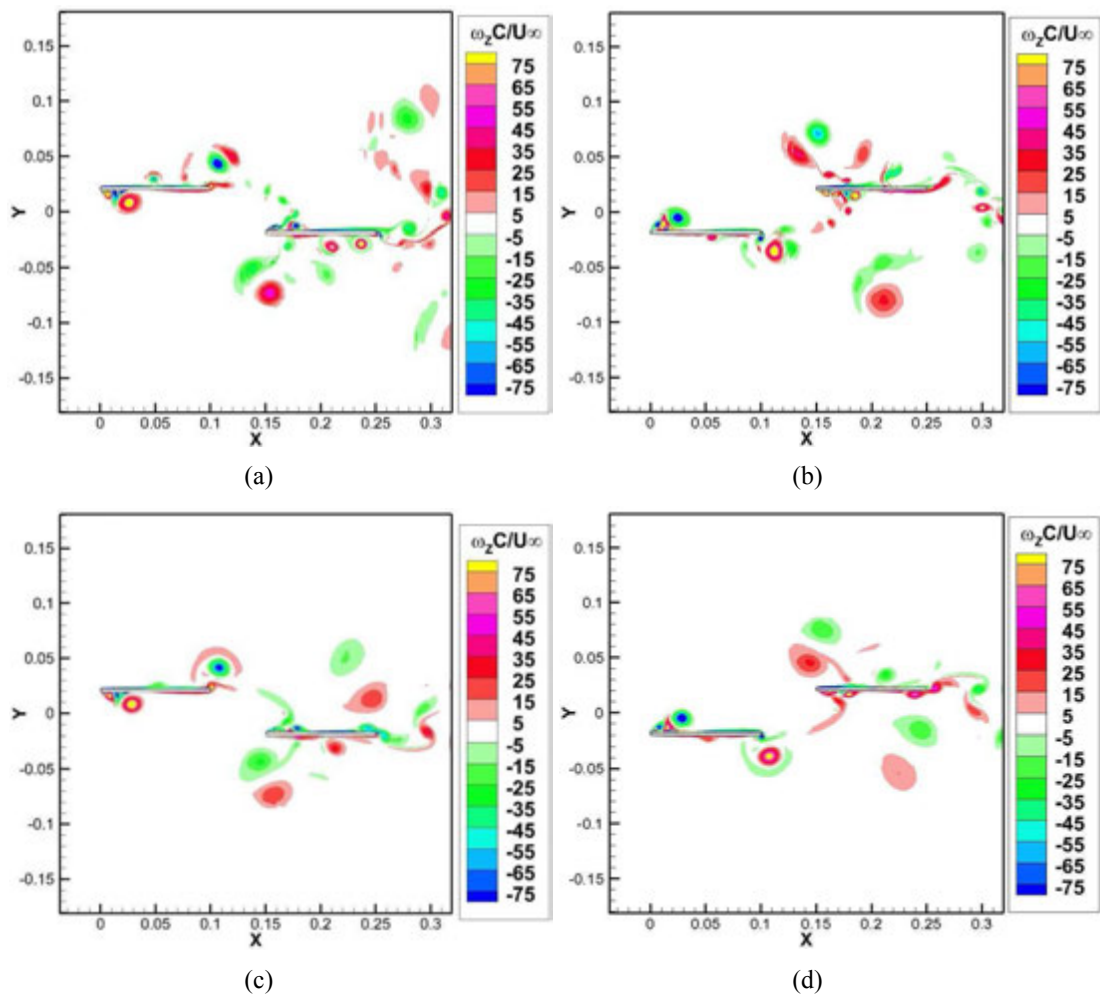
**Fig. 18.** Instantaneous vorticity fields of a tandem airfoil configuration. (a) and (c) display the vorticity fields calculated at the phase of the fore plate up and hind plate down position using the 3$^{rd}$ order and 2$^{nd}$ order accuracy schemes respectively; (b) and (d) display the vorticity fields calculated at the phase of the fore plate down and hind plate up position using the 3$^{rd}$ order and 2$^{nd}$ order accuracy schemes respectively.

|                 |                 |
|:---------------:|:---------------:|
| (a)             | (b)             |
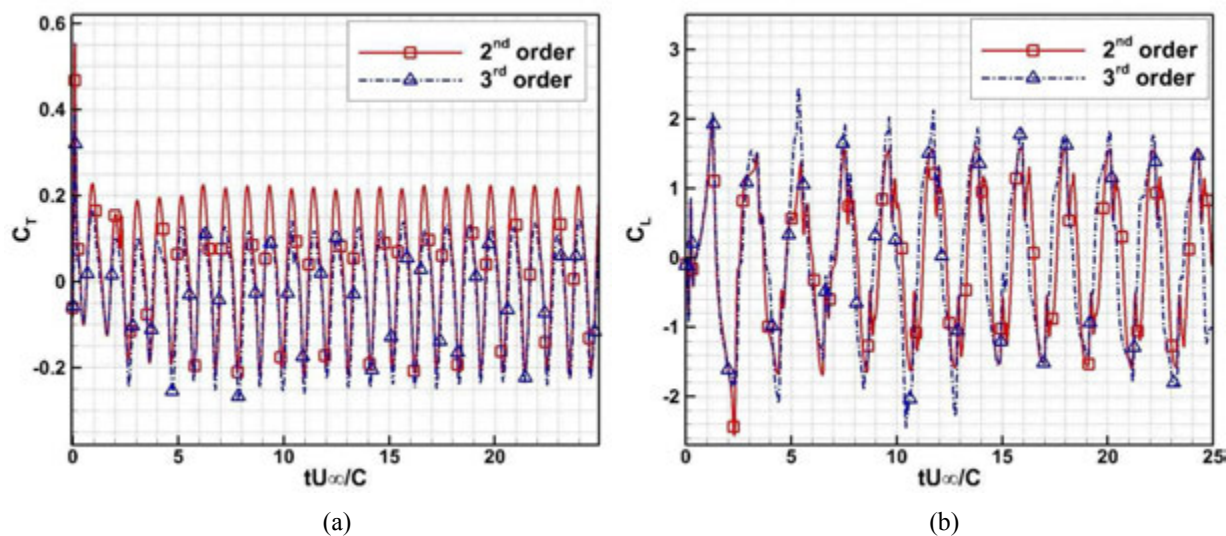
**Fig. 19.** (a) Thrust coefficient convergence history and (b) lift coefficient convergence history calculated using both the 3rd order scheme (as denoted by the dash-dot line with triangles) and the 2nd order scheme (as denoted by the solid line with squares).

## 4. Conclusions

A high-order spectral difference method has been extended to solve compressible Navier-Stokes equations on deformable meshes. Since the present method is based on unstructured grids, it can handle complex geometries. Moreover, the differential form of the SD method makes the implementation straightforward even for high-order curved boundaries. Because a time-dependent transformation from the physical domain to the computational one has been made in the application of the method, the Geometric Conservation Law (GCL) has been carefully considered during the process and implemented for both the explicit and implicit time integration methods. It has been demonstrated that the developed algorithm preserved the high-order accuracy and works efficiently for several bio-inspired flow problems. Numerical tests clearly show that the high-order method with low numerical dissipation can resolve much more elaborate vortex structures than the low-order method, and can then help better illuminate the underlying physics of the vortex-dominated flow.

## References

[1] I. Akhtar, R. Mittal, G. V. Lauder and E. Drucker, Hydrodynamics of a biologically inspired

tandem flapping foil configuration. Theor. Comput. Fluid Dyn., 21: 155–170, 2007.

[2] D. G. Bohl, M. M. Koochesfahani, MTV measurements of the vertical field in the wake of an airfoil oscillating at high reduced frequency, J. Fluid Mech. (2009), vol. 620, pp. 63-88.

[3] B. Cockburn and C.-W. Shu, TVB Runge-Kutta local projection discontinuous Galerkin finite element method for conservation laws II: general framework. Math. Comput., 52:411–435, 1989.

[4] J. Donea, Arbitrary Lagrangian-Eulerian finite element methods, Computational methods for transient analysis (A84-29160 12-64). Amsterdam, North-Holland, 473-516,1983.

[5] L. Dubuc, F. Cantariti, M. Woodgate, B. Gribben, K. J. Badcock and B. E. Richards,A grid deformation technique for unsteady flow computations. Int. J. Numer. Meth. Fluids, 32: 285–311,2000.

[6] J. D. Eldredge, C. J. Wang and M. V. OL, A computational study of a canonical pitch-up, pitch-down wing maneuver. AIAA paper, 2009-3687.

[7] F. Q. Hu, X. D. Li, D. K. Lin, Absorbing boundary conditions for nonlinear Euler and Navier-Stokes equations based on the perfectly matched layer technique, J. Comput. Phys. (2008), vol. 227, pp. 4398-4424.

[8] H. T. Huynh. A flux reconstruction approach to high-order schemes including discontinuous Galerkin methods. AIAA Paper, 2007-4079, 2007.

[9] A. Jameson, A proof of the stability of the spectral difference method for all orders of accuracy. J. Sci. Comput., doi: 10.1007/s10915-009-9339-4, 2010.

[10] K. D. Jones, C. M. Dohring, and M. F. Platzer, Experimental and computational investigation of the Knoller-Betz effect, AIAA J. (1998), vol. 36, No.7, pp. 1240-1246.

[11] D. A. Kopriva and J. H. Kolias. A conservative staggered-grid Chebyshev multi-domain method for compressible flows. J.Comput.Phys.,125(1):244–261, 1996.

[12] Y. Liu, M. Vinokur, Z. J. Wang. Discontinuous spectral difference method for conservation laws on unstructured grids, J. Comput. Phys. (2006), vol. 216, pp. 780–801.

[13] D. J. Mavriplis, C. R. Nastase, On the geometric conservation law for high-order discontinuous Galerkin Discretizations on dynamically deforming meshes, AIAA paper, 2008-778.

[14] G. May, A. Jameson, A spectral difference method for the Euler and Navier–Stokes equations(2006), AIAA Paper No.2006–304.

[15] M. V. OL, The high-frequency, high-amplitude pitch problem: airfoils, plates and wings. AIAA paper, 2009-3686.

[16] M. V. OL , A. Altman, J. D. Eldredge, D. J. Garmann and Y. H. Lian, AIAA paper, Résumé of the AIAA FDTC low Reynolds number discussion group's canonical cases. 2010-1085.

[17] K. Ou, A. Jameson, On the temporal and spatial accuracy of spectral difference method on moving deformable grids and the effect of geometric conservation law, AIAA paper, 2010-5032, 2010.

[18] K. Ou, CH. Liang and A. Jameson, A high-order spectral difference method for the Navier-Stokes equations on unstructured moving deformable grids. AIAA Paper, 2010-541, 2010.

[19] P. O. Persson, J. Peraire, J. Bonet, Discontinuous Galerkin solution of the Navier-Stokes equations on deformable domains, Computer Methods in Applied Mechanics and Engineering (2009), vol. 198, pp. 1585-1595.

[20] M. F. Platzer, K. D. Jones, J. Young, J. C. S. Lai, Flapping-wing aerodynamics: progress and challenges, AIAA J. (2008), vol. 46, No.9, pp. 2136-2149.

[21] K. Stein, T. Tezduyar and R. Benney, Mesh moving techniques for fluid-structure interactions with large displacements. J. Appl. Mech., 70(1):58-63,2003.

[22] Y. Z. Sun, Z. J. Wang, Y. Liu, High-order multidomain spectral difference method for the Navier-Stokes equations on unstructured hexahedral grids, Commun. Comput. Phys. (2006), vol. 2, No. 2, pp. 310-333.

[23] Y. Z. Sun, Z. J. Wang, Y. Liu, Efficient implicit non-linear LU-SGS approach for compressible flow computation using high-order spectral difference method, Commun. Comput. Phys. (2009), vol. 5, No. 2-4, pp. 760-778.

[24] J. Tannehill, D. Anderson and R. Pletcher, Computational fluid mechanics and heat transfer, (second edition), Taylor & Francis, 1997.

[25] P. D. Thomas, C. K. Lombard, Geometric conservation law and its application to flow computations on moving grids, (1979), AIAA J. vol. 17, pp. 1030-1037.

[26] K. Van den Abeele,C. Lacor, and Z. J. Wang. On the stability and accuracy of the spectral difference method. J.Sci.Comput.,37(2):162–188,2008.

[27] M. R. Visbal, D. V. Gaitonde, On the use of high-order finite-difference schemes on curvilinear and deforming meshes, J. comput. Phys. (2002), vol. 181, pp. 155-185.

[28] M. R. Visbal, High-fidelity simulation of transitional flows past a plunging airfoil(2009), AIAA Paper, No. 2009-391.

[29] K. D. von Ellenrieder, S. Pothos, PIV measurement of the asymmetric wake of a two dimensional heaving hydrofoil, Exp. Fluids (2007), vol. 43, No. 5.

[30] T. Wuilbaut, Algorithmic developments for a multi-physics framework, PhD. Thesis, 2008.

[31] Z. J. Wang, High-order methods for the Euler and Navier Stokes equations on unstructured grids, Progress in Aerospace Science (2007), vol. 43, pp. 1-41.

[32] Z. J. Wang, Spectral(finite)volume method for conservation laws on unstructured grids: Basic formulation. J. Comput. Phys., 178:210–251,2002.

[33] Z. J. Wang, Y. Liu, G. May, A. Jameson, Spectral difference method for unstructured grids II: extension to the Euler equations. J. Sci. Comput. (2007), vol. 32, pp. 45–71.

[34] Z. J. Wang, Y. Sun, C. Liang and Y. Liu, Extension of the SD method to viscous flow on unstructured grids. In Proceedings of the 4th international conference on computational fluid dynamics, Ghent, Belgium, July 2006.

[35] M. L. Yu, H. Hu and Z. J. Wang, A numerical study of vortex-dominated flow around an oscillating airfoil with high-order spectral difference method. AIAA Paper, 2010-726, 2010.

# CHAPTER 3. Experimental and Numerical Investigations on the Asymmetric Wake Vortex Structures around an Oscillating Airfoil

A paper published in the 50th AIAA ASM conference proceedings

Meilin Yu, Hui Hu and Z. J. Wang

## Abstract

Wake structures behind a sinusoidally pitching NACA0012 airfoil have been studied with both experimental and numerical approaches. The results from Particle Image Velocimetry (PIV) measurements and those from the high-order unstructured dynamic grid based spectral difference (SD) compressible Navier-Stokes (NS) solver agree well with each other. Two types of wake transition processes, namely the transition from a drag-indicative wake to a thrust-indicative wake and that from the symmetric wake to the asymmetric wake are experimentally investigated. Asymmetric wake phenomena have been emphasized in the study. The deflected wake is found to appear at approximately Strouhal number 0.31 and reduced frequency 15.1 for the pitching amplitude 5$^\text{o}$. As the Strouhal number increases, the dipole mode of the vortex pair becomes more apparent, which is considered to be a vital element to form the asymmetric wake. Besides, the dependency of the deflective directions of the asymmetric wake on other parameters, e. g. initial phase angle, reduced frequency, has been analyzed both experimentally and numerically.

## Nomenclature

$AoA$ = angle of attack

$a$ = speed of sound

$C_L$ = lift coefficient

$C_T$ = thrust coefficient

$c$ = chord length

| | | |
|---|---|---|
| $E$ | = | total energy |
| $F, G$ | = | vectors of fluxes in the physical domain |
| $\tilde{F}, \tilde{G}$ | = | vectors of fluxes in the computational domain |
| $i, j$ | = | index of coordinates in x, y direction |
| $J$ | = | Jacobian matrix |
| $K$ | = | reduced frequency |
| $M$ | = | Mach number |
| $\dot{m}$ | = | mass flow rate |
| $p$ | = | non-dimensional pressure |
| $Q, \tilde{Q}$ | = | vectors of conservative variables in the physical and computational domains |
| $Re$ | = | Reynolds number based on the chord length |
| $r_5$ | = | fifth-order polynomial blending function |
| $St$ | = | Strouhal number |
| $s$ | = | normalized arc length |
| $t, \tau$ | = | time in the physical and computational domain |
| u,v | = | non-dimensional velocity in x, y direction |
| $\vec{v}_g$ | = | grid velocity |
| $x, y$ | = | non-dimensional Cartesian coordinates in the physical domain |
| $\alpha$ | = | pitch angle of the airfoil |
| $\xi, \eta$ | = | Cartesian coordinates in the computational domain |
| $\rho$ | = | non-dimensional density |
| $\phi$ | = | phase angle |
| $\omega_z$ | = | spanwise (z) vorticity |

## 1. Introduction

Bird-sized and insect-sized Micro-Air-Vehicles (MAVs) have opened up new opportunities for surveillance missions. Their miniaturized size and versatile functionality offers a significant advantage over conventional approaches in high-density or bio-

harmful environments. MAVs can be designed with fixed, rotary or flapping wings. Among them, the flapping wing motion, which has been widely used by natural flyers, is attractive due to its high efficiency and excellent maneuverability. It is observed that in natural flights within the Reynolds number range of $10^3$ to $10^5$, a thrust can be generated from flapping motions due to the generation of the reverse von Karman vortex street behind the flapping wing. However, it is challenging to fully understand the aerodynamics exhibited by natural flapping wing flyers considering the intricacies behind them. Therefore, it is reasonable to simplify the complicated system by substituting it with appropriate models at different complexity levels. With these simplified models, one can study the underlying physics behind the bio-inspired unsteady flow piece by piece and in turn, to apply them in the design of MAVs. Readers who are interested in these topics can refer to two comprehensive reviews by Shyy et al. [1,2].

Among all research directions, wake structure analyses have attracted much attention, as the evolution of the vortex street reveals the flapping wing dynamics. Myriads of experiments and numerical simulations have been carried out for both two dimensional (2D) and three dimensional (3D) wake structure analyses. Koochesfahani [3] studied the wake patterns for a pitching NACA0012 airfoil with the small pitching amplitude but relatively large pitching frequency through the dye visualization and laser Doppler velocimetry (LDV) measurement. They concluded that the wake pattern can be controlled by adjusting the frequency, amplitude and the shape of the oscillation wave form. In a successive work, Bohl and Koochesfahani [4] studied the flow over a sinusoidally pitching NACA0012 airfoil of various reduced frequencies using molecular tagging velocimetry (MTV). In that research, they reported the transition point to change from a von Karman vortex street to a reverse von Karman vortex street for the pitching motion with small pitching amplitude ($2^o$) but relatively large reduced frequency. Through the linear stability analyses of the wake structures, Triantafyllou et al. [5] obtained the optimal wake width based Strouhal number for oscillating foils in the range 0.25 to 0.35. Anderson et al. [6] experimentally confirmed that the propulsion efficiency at the optimal Strouhal number 0.3-0.4 can be up to 87%. Based on the numerical studies of a heaving

airfoil, Wang [7] also obtained that the optimal Strouhal number is around 0.3 and showed certain criteria to achieve the optimal performance. Lai and Platzer [8] experimentally studied the wake features after a plunging NACA0012 airfoil, and confirmed that a plunging foil could generate a jet-like wake structure. Further, based on the dye visualization, they showed schematically the processes for the generations of different wake patterns. Later, extensive numerical simulations have been performed by Young and Lai [9], focusing on the relationships between flow features and the aerodynamic parameters. Godoy-Diana et al. [10] experimentally studied the aerodynamic parameter dependency of the transition from the drag-generation wake to the thrust-generation one for a teardrop like pitching foil based on the wake visualization and displayed the parameter map for different wake types. Compared with 2D wake structures, 3D wake patterns are more complex and fewer results are reported. Ellenrieder et al. [11] analyzed the Strouhal number and plunge/pitch phase lag effects on the wake vortex structures behind a translating finite-span wing through dye visualizations. Dong et al. [12] numerically confirmed that the performance of a low-aspect-ratio flapping foil is closely related to the wake vortex evolutions. Besides, from the aspect of the optimal vortex formation, Dabiri [13] displayed the ubiquitous existence of this phenomenon in the biological propulsion and suggested that the optimal Strouhal number could be one consequence of the optimal vortex formation process. Therefore, it is still an open question to specify whether aerodynamic parameters other than the present popular ones, such as Strouhal number, reduced frequency and advanced ratio, etc. exist, which can better describe the flapping systems, and to resolve the dependency of the bio-inspired flow on these aerodynamic parameters.

Investigating the wake visualization results from experiments and numerical simulations, researchers found an interesting asymmetric wake vortex shedding mode which deserves to be further studied. The key problem originated from the asymmetric wake phenomenon can be stated like this. Intuitively, if an axis-symmetric airfoil oscillates around the balancing position of zero angle of attack (AoA) using a symmetric motion algorithm, e.g. sinusoidal pitch or plunge, the wake direction should always

follow the stream wise direction. This is true under the small Strouhal number as has been confirmed by many experimental and numerical results [3,4,6,7,9,10]. However, it is found that as the Strouhal number increases, a deflected wake can be observed behind an oscillating foil. It is an open question to answer the originality of the asymmetric wake. Furthermore, since the deflected wake is usually accompanied with larger thrust and lift generation, it seems that to fully understand the characteristics of this phenomenon might be vital for the design and control of MAVs. As reported by Jones et al. [14], a deflected wake occurs generally with a relative larger wake width based Strouhal number (around 0.48). Beside, during the experiment, they found that the direction of the deflected wake pattern can alter somewhat arbitrarily due to some reasons that were not clear. Through a numerical simulation with an inviscid panel code, the asymmetric wake can be predicted in their research. Platzer et al. [15] suggested that for flow with large Strouhal numbers, a viscous flow solver is necessary to provide a complete picture of the occurrence of the deflected wake structure. Lewin and Haj-Hariri [16] used an incompressible viscous flow solver to study the aerodynamic parameter dependency of thrust generation for a heaving airfoil. From their research, wake patterns are categorized in detail, and deflected wakes those can alter directions are reported. The possible reason can be attributed to the intensive interactions between leading edge vortices (LEVs) and trailing edge vortices (TEVs). Heathcote and Gursul [17] found that the period of the jet switching during their experiment is two orders of magnitude greater than the plunging period of the foil. They also showed that the jet switching period closely depends on the Strouhal number and the stiffness of the airfoil. Godoy-Diana et al. [10] showed the watershed for the symmetric reverse von Karman vortex street and the asymmetric jet-like wake in a frequency-amplitude map. From the diagram, the authors concluded that asymmetric wake patterns can even fall into the optimal Strouhal number region. Later, Godoy-Diana et al. [18] modeled the asymmetric wake phenomenon by using a dipole model, which has been termed as a dual mode in Jone et al.'s [14] work. A similar approach has been used to model the asymmetric wake for a semi-infinite vortex array by Yu et al. [19]. Ellenrieder and Pothos [20] experimentally verified the onset of the deflected wake and the

corresponding flow features. They claimed that when Strouhal number exceeds 0.434, a deflected wake will appear for a plunging NACA0012 airfoil. Liang et al. [21] numerically found that the deflective angle decreases when the Reynolds number decreases for a fast plunging airfoil. As suggested by some researchers, the 3D counterpart of the 2D asymmetric wake might be the two jet-like wake patterns behind a free-end finite-span wing, as shown in Ref. 0. Recently, Hu et al. [22] have experimentally verified that for a fixed-root wing, the two jet-like wake patterns can also be observed. Whether these flow structures can be related to the 2D asymmetric wake pattern still needs more investigations.

Obviously, the aforementioned unsteady bio-inspired flows are dominated by moving vortices, which play a critical role in the wake pattern analyses. As 1$^{st}$ and 2$^{nd}$ order flow solvers may dissipate the unsteady vortices, a high-order dynamic grid based spectral difference (SD) method is used in tackling these unsteady vortex-dominated flows. As the high order method means possible high cost, an efficient high-order method needs to be developed for the bio-inspired flow simulations. The SD method [23,24] is used in the present study to make compromise between these two competing factors.. It has been demonstrated that the dynamic grid based SD method works well for the bio-inspired flows. The basic approach to achieve high-order accuracy in the SD method is to use a high degree polynomial to approximate the exact solution in a local element (a standard cell). However, unlike the discontinuous Galerkin (DG) method [25] and spectral volume (SV) method [26], the SD method is in differential form, which is efficient and simple to implement. Furthermore, the SD method can use larger time steps than the DG type method, which might make it more competitive for the potential engineering use. Recently, all kinds of high-order methods have been used for the bio-inspired flows. Visbal [27] has successfully utilized a high-order method (a compact finite-difference approach) to simulate the flow field around a SD7003 airfoil. Persson et al. [28] have developed a dynamic DG method for a finite-span wing simulation and compared the results with other numerical methods. Liang et al. [21] have successfully used SD method for a plunging NACA0012 airfoil simulation. In their research, the asymmetric wake has

been reported under large Strouhal number and the relationship between the deflected direction and Reynolds number has been studied. Several potential applications for SD method in the bio-inspired flow have been reported by Yu et al. [24]. They also discovered that the asymmetric wake phenomena can appear under Strouhal number 0.33 with no leading edge separation. Ou et al. [29] developed a 3D SD solver for the finite-span flapping wing simulations, and verified the effectiveness of the method for the bio-inspired flow simulations.

Based on the above discussions, the present paper endeavors to further study the conditions for the occurrence of the deflected wake and how these conditions affect the dynamic behaviors of the deflected wake. The remaining paper is organized as follows. In section 2 and 3, the experimental setup and the numerical method will be introduced. The numerical simulation setup is also specified in section 3. Then experimental and numerical results are displayed in section 4. Two wake transition processes are discussed there and the asymmetric wake phenomenon is analyzed through both experimental and numerical approaches. Finally, conclusions are summarized in section 5.

## 2. Experimental Setup

The experimental study was performed in a closed-circuit low-speed wind tunnel located in the Aerospace Engineering Department of Iowa State University. A plexiglass-walled test section is mounted on this wind tunnel, and the interior dimensions of the test section are of 2.5m × 0.3m × 0.3m. The tunnel has a 40:1 contraction section upstream of the test section and has honeycombs, screen structures and a cooling system installed ahead of the contract section. A uniform incoming flow with low turbulent intensity can then be provided for the test section. For the present study, the free stream velocity for the test section is maintained at 0.5m/s.

The NACA0012 airfoil used in the present study has a chord length of 4 inch and spanwise length of 11.5 inch. The airfoil model was manufactured with an in-house 3D printer. A linkage mechanism, which is driven by a servo-controlled DC motor, is used to

provide the sinusoidal pitching motion $\alpha = \alpha_0 cos(\omega t + \phi_0)$ of the airfoil as shown in Fig. 1(a). The experimental setup for the phase-lock PIV measurement is schematically displayed in Fig. 1(b). During the experiment, the flow was seeded with 1-5 micro-meter oil droplets. A double-pulsed Nd:YAG laser (NewWave Research Solo) adjusted on the second harmonic and emitting two laser pulses at a wavelength of 532 nm at a repetition rate of 2Hz was used to illuminate the wake region behind the airfoil via the reflection of a mirror mounted under the test section. The laser sheet was created from a laser beam by inserting a set of spherical and cylindrical lenses between the laser and mirror. The laser sheet was positioned near the middle span of the airfoil and had a thickness of approximately 1mm. A high-resolution 12-bit ($1,600 \times 1,200$ pixel) CCD camera (PCO 1600, CookeCorp) was used for PIV image acquisition. The time sequence for the trigger of laser and camera was controlled by the Digital Delay Generator (Berkeley Nucleonics, Model 565). For the phase-lock measurement, the delay generator was linked to a digital pulse generator to provide a trigger signal. A tachometer is used to capture the phase information and supply the signal to the digital pulse generator.

For the post processing, instantaneous PIV velocity vectors were obtained by using a frame to frame cross-correlation technique involving successive frames of patterns of particle images in an interrogation window of 32×32 pixels with an effective overlap of 50% of the interrogation windows. The spanwise vorticity was then calculated from the velocity field.
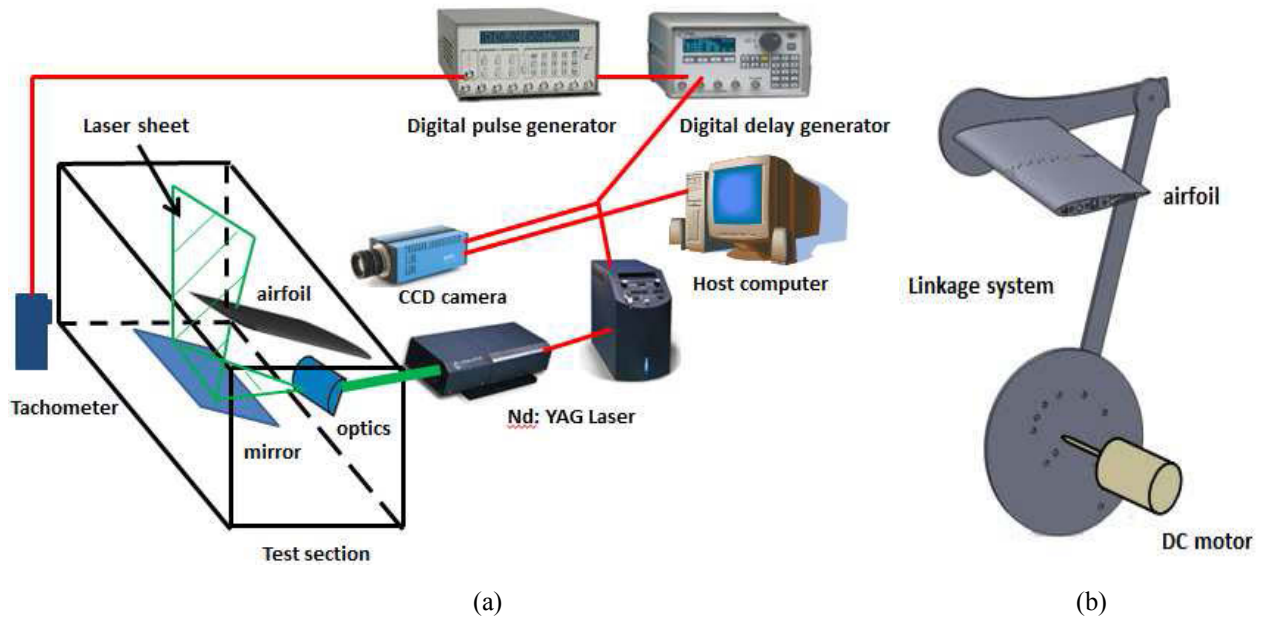
**Figure 1.** Sketch of (a) the experimental setup for the PIV measurement and (b) the linkage system used to generate a sinusoidal pitching motion for the airfoil.

## 3. Numerical Method

### 3.1 Governing Equations

Numerical simulations are performed with an unsteady compressible Navier-Stokes solver using dynamic unstructured grid based high-order spectral difference (SD) method developed in Ref. 0. The 2D unsteady compressible Navier-Stokes equations in conservation form read,

$$\frac{\partial Q}{\partial t} + \frac{\partial F}{\partial x} + \frac{\partial G}{\partial y} = 0. \tag{1}$$

Herein, $Q = (\rho, \rho u, \rho v, E)^T$ are the conservative variables, and $F, G$ are the total fluxes including both the inviscid and viscous flux vectors, i.e., $F = F^i - F^v$ and $G = G^i - G^v$, which takes the following form

$$F^i = \begin{Bmatrix} \rho u \\ p + \rho u^2 \\ \rho u v \\ u(E + p) \end{Bmatrix}, \; G^i = \begin{Bmatrix} \rho v \\ \rho u v \\ p + \rho v^2 \\ v(E + p) \end{Bmatrix}, \tag{2}$$

$$F^v = \left\{ \begin{array}{c} 0 \\ \tau_{xx} \\ \tau_{yx} \\ u\tau_{xx} + v\tau_{yx} + \frac{\mu C_{pre}}{P_r} T_x \end{array} \right\}, \quad G^v = \left\{ \begin{array}{c} 0 \\ \tau_{xy} \\ \tau_{yy} \\ u\tau_{xy} + v\tau_{yy} + \frac{\mu C_{pre}}{P_r} T_y \end{array} \right\}$$

In Eq. (2), $\rho$ is the fluid density, $u$ and $v$ are the Cartesian velocity components, $p$ is the pressure, and $E$ is the total energy, $\mu$ is dynamic viscosity, $C_{pre}$ is the specific heat at constant pressure, $P_r$ is the Prandtl number, and $T$ is the temperature. The stress tensors in Eq.(2) take the following form

$$\tau_{xx} = 2\mu\left(u_x - \frac{u_x + v_y}{3}\right), \qquad \tau_{yy} = 2\mu\left(v_y - \frac{u_x + v_y}{3}\right),$$

$$\tau_{xy} = \tau_{yx} = \mu(v_x + u_y) \tag{3}$$

On assuming that the fluid obeys the perfect gas law, the pressure is related to the total initial energy by $E = \frac{p}{\gamma-1} + \frac{1}{2}\rho(u^2 + v^2)$ with a constant ratio of the specific heats $\gamma$, which closes the solution system.

To achieve an efficient implementation, a time-dependent coordinate transformation from the physical domain $(t, x, y)$ to the computational domain $(\tau, \xi, \eta)$, as shown in Fig. 2(a), is applied on Eq. (1), which is

$$\frac{\partial \tilde{Q}}{\partial \tau} + \frac{\partial \tilde{F}}{\partial x} + \frac{\partial \tilde{G}}{\partial y} = 0, \tag{4}$$

where

$$\begin{cases} \tilde{Q} = |J|Q \\ \tilde{F} = |J|(Q\xi_\tau + F\xi_x + G\xi_y). \\ \tilde{G} = |J|(Q\eta_\tau + F\eta_x + G\eta_y) \end{cases} \tag{5}$$

Herein, $\tau = t$ and $(\xi, \eta) \in [-1,1]^2$, are the local coordinates in the computational domain. In the transformation shown above, the Jacobian matrix $J$ takes the following form

$$J = \frac{\partial(x, y, t)}{\partial(\xi, \eta, \tau)} = \begin{pmatrix} x_\xi & x_\eta & x_\tau \\ y_\xi & y_\eta & y_\tau \\ 0 & 0 & 1 \end{pmatrix}. \tag{6}$$

It should be noted that the grid velocity $\vec{v_g} = (x_t, y_t)$ is related with $(\xi_\tau, \eta_\tau)$ by

$$\begin{cases} \xi_\tau = -\vec{v_g} \cdot \nabla\xi \\ \eta_\tau = -\vec{v_g} \cdot \nabla\eta \end{cases} \tag{7}$$

### 3.2 Space Discretization

The SD method is used for the space discretization. In the SD method, two sets of points are given, namely the solution and flux points, as shown in Fig. 2(b). Conservative variables are defined at the solution points (SPs), and then interpolated to flux points to calculate local fluxes. In the present study, the solution points are chosen as the Chebyshev-Gauss quadrature points. A weak instability for the choice of the flux points in the original SD method was found independently by Van den Abeele, et al. [30,31] and Huynh [32]. Huynh [32] further found that the use of Legendre-Gauss quadrature points as flux points results in a stable SD method. It is then proved mathematically in Ref. 0 that the adoption of the Legendre-Gauss quadrature points as the flux points can ensure the stability of the SD method. Therefore, the flux points are selected to be the Legendre-Gauss points with both end points as -1 and 1.

Then on using Lagrange polynomials we reconstruct all the fluxes at the flux points. It should be pointed out that this reconstruction is only continuous within a standard element, but discontinuous on the cell interfaces. Therefore, for the inviscid flux, a Riemann solver is necessary to reconstruct a common flux on the interface. Since the eigenvalues of the Euler equations with moving boundaries are different from those with fixed boundaries due to the grid velocity, the design of the Riemann solver should consider the grid velocity. Furthermore, since the flow regime for flapping flight is almost incompressible and the present governing equations are compressible Navier-Stokes equations, the Riemann solver should provide good performance at low Mach numbers. The AUSM+-up Riemann solver [34] for all speed is selected for the present simulation and is proved to behave well at low Mach numbers. The procedure to reconstruct the common fluxes for the AUSM+-up Riemann solver can be specified as follows.

Suppose the face normal of arbitrary interface denotes as $\vec{n}$, then the interface mass

flow rate $\dot{m}_{1/2}$ reads

$$\dot{m}_{1/2} = a_{1/2} M_{1/2} \begin{cases} \rho_L & if\ M_{1/2} > 0 \\ \rho_R & otherwise \end{cases}, \tag{8}$$

where the subscript '1/2' stands for the interface, $a$ and $M$ are speed of sound and Mach number respectively. It should be noted that the grid velocity has been included in the interface Mach number $M$. The numerical normal fluxes $\tilde{F}^i$ and $\tilde{G}^i$ can then be specified as

$$\begin{cases} \tilde{F}^i = \left( \dot{m}_{1/2} \begin{cases} \psi_L & if\ \dot{m}_{1/2} > 0 \\ \psi_R & otherwise \end{cases} + P_{1/2} \right) |J| |\nabla\xi| sign(\vec{n} \cdot \nabla\xi) \\ \tilde{G}^i = \left( \dot{m}_{1/2} \begin{cases} \psi_L & if\ \dot{m}_{1/2} > 0 \\ \psi_R & otherwise \end{cases} + P_{1/2} \right) |J| |\nabla\eta| sign(\vec{n} \cdot \nabla\eta) \end{cases} \tag{9}$$

where $\psi = (1, u, v, (E+p)/\rho)^T$, $P = \left(0, pn_x, pn_y, pv_{g,n}\right)^T$, with $n_x$, $n_y$ and $v_{g,n}$ specifying the face normal components in $x$ and $y$ direction and the grid velocity in the face normal direction respectively. The superscript 'i' indicates the inviscid flux. The reconstruction of the viscous flux is based on a simple average of the 'left' and 'right' fluxes. The detailed reconstruction procedures are well stated in previous work [0].



(a)　　　　　　　　(b)
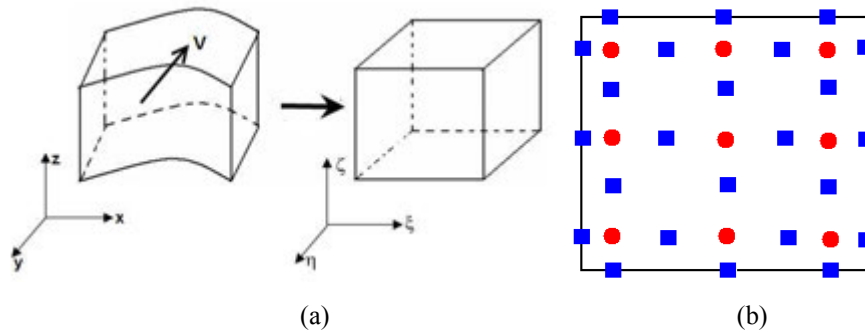
**Figure 2.** (a) Transformation from a moving physical domain to a fixed computational domain; (b) Distribution of solution points (circles) and flux points (squares) in a standard quadrilateral element for a third-order accurate SD scheme.

## 3.3 Grid Deformation Strategy and Simulation Parameters

A snapshot of the deformation grid is displayed in Fig. 2. Herein, the pitching motion of the airfoil is controlled by a cosine algorithm described as

$$\alpha(t) = \alpha_m + \alpha_0 \cos(\omega t + \phi_0), \omega = 2\pi f \tag{10}$$

where $\alpha_m$ is the mean angle of attack, $\alpha_0$ is the amplitude of the pitching angle, and $\phi_0$ is the initial phase of the airfoil.

The rigid-body motion for the wall can be expressed as

$$\begin{cases} x_{present} - x_c = (x_{former} - x_c)\cos(\Delta\alpha) - (y_{former} - y_c)\sin(\Delta\alpha) \\ y_{present} - y_c = (x_{former} - x_c)\sin(\Delta\alpha) + (y_{former} - y_c)\cos(\Delta\alpha) \end{cases} \tag{11}$$

where $(x_c, y_c)$ is the pitching center, and $\alpha = \alpha_0 \cos(\omega t + \phi_0)$.

Then by using a fifth-order polynomial blending function proposed in Ref. 0,

$$r_5(s) = 10s^3 - 15s^4 + 6s^5, s \in [0,1] \tag{12}$$

the motion of the boundary is interpolated to the whole inner grids. More details for the grid deformation strategy used in this study can be found in Ref. 0.

The chord length based Reynolds number ($R_e = \rho U_\infty C/\mu$) for the experiment is 3,340. The Strouhal number ($S_t$), which is the ratio of the characteristic velocity of the flapping wing to the free stream velocity, defined by $S_t = 2fA/U_\infty$, varies from 0.1 to 0.37 for the experimental study and some higher Strouhal numbers out of the aforementioned range are also tested in the numerical study. The reduced frequency ($K$), which is a measure of flapping frequency with respect to the intrinsic frequency of the flow over the airfoil, defined by $K = 2\pi f c/U_\infty$, varies from 5.0 to 17.6 in the experiments and some higher values are also used in the numerical simulations. Note that the parameter variation range is large for both the experimental and numerical studies. In the present study H-refinement (grid refinement) and p-refinement studies were conducted at first to determine the suitable grid and numerical accuracy. Based on the investigations, a 3rd order accurate scheme with a medium mesh was chosen as shown in Fig. 3. Details about these studies can be found in the Ref. 0.

(a)                                                   (b)
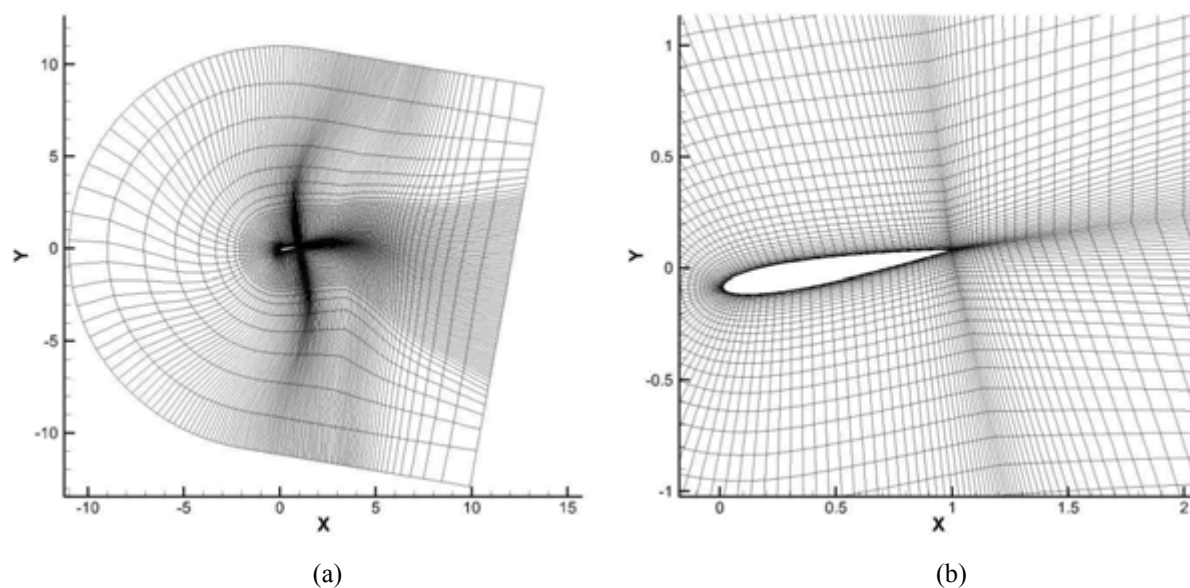
**Figure 3.** Snapshot of the deformable grid. (a) is an overview of the grid and (b) is a close-up view near the wall boundary.

## 4. Results and Discussions

Both experimental and numerical results on wake structures behind a pitching NACA0012 airfoil are analyzed in this section. The schematic of the geometry and kinematics of the NACA0012 airfoil is shown in Fig. 4. The comparison between numerical and experimental spanwise vorticity fields at $S_t = 0.31$, $K = 15.1$ and the pitching amplitude $\alpha_0 = 5^o$ is shown in Fig. 5. The velocity vectors at six downstream locations are displayed in Fig. 5 as well. It is clear that numerical results bare good visual agreements with the experimental results. Other validation of the numerical results against experimental data with different flow conditions and airfoil kinematics is available at Ref. 0.

The vorticity decay profiles of the first two vortices from both experiments and numerical simulations, as indicated with the dashed line in Fig. 6, are compared with each other. Note that in this study the assemble average of the magnitude of the vorticity $|\omega|$ which is not smaller than 50% $|\omega|_{max}$ in a domain centered at the point with $|\omega|_{max}$ is used as a measure of the vortex strength. $|\omega_0|$ is defined as the vortex strength of the vortex nearest to the airfoil trailing edge at the phase angle $\phi = 0^o$ based on the

aforementioned definition. From the comparison it is observed that the vorticity decay of the numerical results follows a power law, while that of the experimental results follows an error function curve. This implies that in the experiment the vortex near the airfoil trailing edge exhibits a lower decaying rate than the numerical simulations. The vortex decay profile discrepancies between the numerical and experimental results may be due to wall effects of the wind tunnel.

### 4.1 Experimental Results on the Wake Vortex Structure Transition Process

In this section, two types of wake vortex structure transitions processes are displayed for the pitching amplitude $\alpha_0 = 5^o$, namely the transition from a drag-indicative wake to a thrust-indicative wake, and the transition from a symmetric thrust-indicative wake to an asymmetric (deflective) thrust/lift-indicative wake. The asymmetric wake phenomenon in the present study is categorized as follows. The oscillating airfoil's shape and kinematics are symmetric with respect to a baseline. For the pitching motion, the baseline is the horizontal line passing through the axis of symmetry of the NACA0012 airfoil with a zero AoA, as shown in Fig. 4. It is found that the center line of the wake vortex street generated by the pitching motion has a deflective angle with respect to the baseline. This is why it is called the asymmetric wake phenomenon. As discussed in the first section, this phenomenon is counterintuitive in the sense that both the geometric and dynamic parameters of the airfoil are symmetric about the baseline but the wake vortex street can be asymmetric with respect to the base line as the Strouhal number and reduced frequency increase. The wake symmetry breakdown mechanism will be explained shortly.

#### 4.1.1 Wake Transition from a Drag-Indicative Type to a Thrust-Indicative Type

The wake transition from a drag-indicative type to a thrust-indicative type has been reported by many researchers for plunging or pitching airfoils. Herein, this typical transition process is reproduced for the pitching NACA12 airfoil and serves as a verification of the present experimental setup.

The vorticity fields behind the oscillating airfoil at four phases(i.e. $0^o, 90^o, 180^o$ and

$270^o$ ) during the wake transition process from a drag-indicative type to a thrust-indicative type, are shown in Figs. 7-9. The corresponding velocity vectors for each phase are also plotted in these figures. Note that only a quarter of the total vectors are displayed here for clarity. From Fig. 7, it is clear that the vortex row with negative vorticity is on top of the vortex row with positive vorticity, resulting in a momentum deficit between the two rows. These vortex configurations form a drag-indicative wake. The Strouhal number and the reduced frequency for this case are 0.1 and 5.0 respectively. When the Strouhal number and the reduced frequency increase to 0.12 and 5.7 respectively, a 'neutral' wake appears. It features that the vortices with alternating signs are almost aligned along a straight line as shown in Fig. 8. A thrust-indicative wake is generated when the Strouhal number and the reduced frequency further increase to 0.29 and 13.8 respectively. From Fig. 9, it is obvious that the vortex row with positive vorticity is on top of the vortex row with negative vorticity, resulting in a momentum surplus between the two rows. Note that all vortices in these three cases are equally spaced in the streamwise direction.

The time-averaged velocity fields and spanwise vorticity fields for these three cases are shown in Fig. 10. The three different wake types can be clearly distinguished from the time-averaged velocity fields. Also, it is observed that when the geometric and kinematic parameters of the airfoil are symmetric about the baseline, the drag-indicative wakes are also symmetric about the same baseline.

### 4.1.2 *Wake Transition from a Thrust-Indicative Type to a Thrust/Lift-Indicative Type*

The wake transition processes from the symmetric thrust-indicative type to the asymmetric thrust/lift-indicative type are displayed in Figs. 9, 11 and 12 with the spanwise vorticity fields. Note that the wake in Fig. 11 is slightly deflected from the baseline. The Strouhal number and the reduced frequency for this case are 0.31 and 15.1 respectively. From the figure it is also found that the two vortices shed in one pitching cycle have the tendency to move closer with each other. The Strouhal number of this transition point is smaller than the proposed threshold $S_t = 0.434$ of the deflected wake in Ref. 0. The reasons might be attributed to that the threshold proposed in Ref. 0 is for a

plunging airfoil oscillating at a lower reduced frequency ($\approx 6.3$). It becomes more apparent that when the Strouhal number and the reduced frequency reach up to 0.37 and 17.6 respectively, 'dipole' like vortex structures appear as shown in Fig. 12, and the dipole is made up of the two vortices with different signs shed in one pitching cycle.

The corresponding time-averaged velocity and spanwise vorticity fields are shown in Fig. 13. From the time-averaged velocity field it is clear that for the case with $S_t = 0.31$ and $K = 15.1$, the wake slightly goes up and for the case with $S_t = 0.37$ and $K = 17.6$ the wake has a large deflective angle with the baseline. Also note that jet-like wakes can be observed from the time-averaged velocity and vorticity fields.

## 4.2 Experimental and Numerical Results on the Deflective Wake Phenomenon

One of questions floating around in the discussions is: Can the deflective direction of the wake be changed? If so, which factors will determine the deflective direction? As reviewed in the introduction part, different researchers found different features of the asymmetric wake. Some found that the deflective direction of the wake can change during one shoot of the experiment [17] or the numerical simulation [16]; some found that the deflective direction of the wake may alternate somewhat arbitrarily in the experiment [14]; some confirmed that the wake deflective direction is determined by the initial conditions of the numerical simulations [19,21]. In the present studies, different features of the asymmetric wakes have been found. The results are displayed as below.

### 4.2.1 Deflective Direction

From the experimental study, it is found that the deflection of the asymmetric wake is not sensitive to the airfoil geometry, airfoil mounting method, linkage system, or airfoil motion, but is sensitive to the alignment of the wind tunnel. At this point, it is still unclear what determines the wake deflective direction, but the reflective direction had very good repeatability in duplicated experiments. Wakes with different deflective directions were captured in the experiments. The vorticity fields for two wakes with opposite deflective angles at $S_t = 0.33$ and $K = 15.7$ are shown in Fig. 14. It appeared that the asymmetric

wake was sensitive to some unknown disturbances from the alignment of the wind tunnel, and these unknown disturbances are amplified when the aerodynamic parameters, like the Strouhal number and the reduced frequency, exceed certain range (here $S_t = 0.31$ and $K = 15.1$). And the amplified disturbances may induce the deflective direction of the wake.

The wake deflective directions in the numerical simulations are found to be determined by the initial pitching directions of the airfoil. The spanwise vorticity fields with the initial phases $\phi_0 = 0^o$ and $180^o$ are shown in Fig. 15. The Strouhal number and the reduced frequency for this case are 0.75 and 18.0 respectively. From the results shown in Fig. 15, it is found that the asymmetric wakes with different initial phases can have different deflected angles. Meanwhile, since the initial phases chosen in these two cases make the initial positions of the airfoil symmetric to the horizontal axis of the airfoil, the wake shown at the same time is anti-symmetric. It can be inferred that the thrust coefficient histories should be the same for the two cases, while the lift coefficient histories should be of the same absolute values but the opposite signs. This has been confirmed by the thrust and lift histories shown in Fig. 16.

Note that from Fig. 15 and 16, when the wake is deflected upward, it will induce a low pressure region on the top surface of the airfoil, which could result in a positive lift. This has previously been reported by Cleaver et al. [36]. Since leading edge vortices (LEVs) appear in this case, they will bring in disturbances into the flow fields. Whether or not these disturbances are major factors to trigger the asymmetric wake still needs to be further examined. The results for the spanwise vorticity fields with the initial phases $\phi_0 = 0^o$ and $180^o$ at $R_e = 12,600$, $S_t = 0.33$, $K = 23.0$ and $\alpha_0 = 2^o$ are shown in Fig. 17. It is clearly observed that even if there exists no LEVs, the asymmetric wake can occur. This has been reported by the same authors in Ref. 24. Therefore, it is quite possible that the asymmetric wake phenomenon is intrinsically an inviscid phenomenon and the vortex dynamics will dominate the formation of the vortex street structure, although at high Strouhal numbers LEVs will introduce large disturbances to the wake structures and even affect the vortex structures [16].

*4.2.2 Reduced Frequency and Strouhal Number Effects*

As discussed in Ref. 0, the threshold of the asymmetric wake could vary with the Strouhal number and the reduced frequency. Here three cases at the same Strouhal number (0.31) but different reduced frequencies(i.e. 15.1, 7.5 and 5.0) are numerically studied. The pitching amplitudes for these three cases are $5^o$, $10^o$ and $15^o$ respectively. From the spanwise vorticity fields and the corresponding time-averaged velocity fields displayed in Fig. 18, it is found that the asymmetric wake is more apparent for the case with a larger reduced frequency. The deflective point for the case with $K = 15.1$ is roughly two-chord length downstream of the airfoil. This point is shifted to the position which is about three-chord length downstream of the airfoil for the case with $K = 7.5$. However, it is hard to distinguish the deflective point for the case with $K = 5.0$ even after five-chord length downstream of the airfoil. These phenomena can be explained as follows. At the same Strouhal number, the vortex streets should have similar configurations (i.e. the ratio between the distance of the two vortex rows and the distance of the adjacent two vortices with opposite sign of vorticity). However, if the reduced frequency is large, the strength of the shedding vortices will become large and the distance between the adjacent two vortices shed in one pitching cycle becomes small. This increases the chance for the interaction between these two vortices. Therefore, for the flow with a large reduced frequency, the vortices with different signs shed in one pitching cycle have the tendency to form a dipole mode and then change the configuration of the whole vortex street. If the reduced frequency is small, the strength of the shedding vortices will become small and the distance between the adjacent two vortices shed in one pitching cycle becomes large. Both effects will reduce the chance for the formation of the asymmetric wake.

The thrust and lift coefficient histories are displayed in Fig. 19. It is clear that with the present parameters, a relatively large reduced frequency is beneficial for the thrust generation. An interesting observation of the lift generation is that although an asymmetric wake is generated after the oscillating airfoil, almost no net lift is generated.

This might be attributed to the fact that the deflective angle of the asymmetric wake is so small that its effects on the aerodynamic force are not apparent.

Note that all the three cases discussed above in this section have thrust-indicative wakes, as the Strouhal number is fixed at 0.31, which falls into the 'thrust-indicative' wake type[0,0]. Here three cases at the same reduced frequency (15.1) but different Strouhal numbers (i.e. 0.19, 0.31 and 0.41) are further studied to illuminate the effects of the Strouhal number on the wake structures. The normalized spanwise vorticity fields for Strouhal number 0.19 and 0.41 are displayed in Fig. 20 and that for Strouhal number 0.31 is shown in Fig. 18 (a). When the Strouhal number equals 0.19, even though that the reduced frequency is large, the wake is almost of the 'neutral' type and symmetric about the baseline (horizontal line). From Fig. 21, it is confirmed that under this condition no net thrust and lift is generated. But when the Strouhal number increases to 0.41, an apparent asymmetric 'thrust/lift-indicative' wake appears. From the thrust and lift coefficient histories shown in Fig. 21, it is clear that both net thrust and lift are generated. The direction of the net lift is upwards, which aligns with the wake direction. This further validates the analyses of the correlations between the lift direction and the wake direction in section B. 1. On comparing the aerodynamic force histories for the fixed Strouhal number as shown in Fig. 19 and those for fixed reduced frequency as shown in Fig. 21, it is concluded that the aerodynamic force is more sensitive to the change of Strouhal number than that of the reduced frequency. Interestingly, based on the vorticity fields shown in Figs. 18 and 20, it seems that the asymmetric wake phnomenon is affected more by the Strouhal number as well.

## 5. Conclusions

PIV measurements have been performed for the wake structure analyses behind a sinusoidally pitching NACA0012 airfoil. A high-order unstructured dynamic grid based SD compressible solver has been used to study the same wake structures. The experimental and numerical results agree qualitatively with each other. Two types of wake

transition processes (i.e. the transition from a drag-indicative wake to a thrust-indicative wake and that from the symmetric wake to the asymmetric wake) are experimentally studied. Using the present geometric and dynamic parameters, the wake transition point from the drag-indicative type to the thrust-indicative type is found to be $S_t = 0.12$; the transition point from the symmetric type to the asymmetric type is at $S_t = 0.31$. The asymmetric wake is believed to be closely related to the formation of a dipole-like vortex pair shed in one pitching cycle and can be treated as an inviscid phenomenon. In numerical simulations, the deflective angle of the asymmetric wake is determined by the initial phase angle, whereas in the experiments, what determines the wake deflective direction is still unclear at this point. The reduced frequency and the Strouhal number will affect the strength of the shedding vortices and further affect the formation of the asymmetric wake. Based on the present cases studied, both aerodynamic forces and the asymmetric wake structures are more sensitive to the Strouhal number than the reduced frequency.

## References

[1] W. Shyy, M. Berg and D. Ljungqvist, Flapping and flexible wings for biological and micro air vehicles, Prog. Aerosp. Sci. (1999), vol.35, iss.5, pp.455-505.

[2] W. Shyy, H. Aono, S. K. Chimakurth, P. Trizila, C. K. Kang, C. E. S. Cesnik and H. Liu, Recent progress in flapping wing aerodynamics and aeroelasticity, Prog. Aerosp. Sci. (2010), vol.46, iss.7, pp.284-327.

[3] M. M .Koochesfahani, Vortical patterns in the wake of an oscillating airfoil, AIAA J. (1989), vol. 27, pp. 1200-1205.

[4] D. G. Bohl and M. M. Koochesfahani, MTV measurements of the vertical field in the wake of an airfoil oscillating at high reduced frequency, J. Fluid Mech. (2009), vol. 620, pp. 63-88.

[5] G. S. Triantafyllou, M. S. Triantafyllou and M. A. Grosenbaugh, Optimal thrust development in oscillating foils with application to fish propulsion, Journal of Fluids and Structures (1993), vol.7, pp.205-224.

[6] J. M. Anderson, K. Streitlien, D. S. Barrett and M. S. Triantafyllou, Oscillating foils of high propulsive efficiency. J. Fluid Mech., 360, 41 (1998).

[7] Z. Jane Wang, Vortex shedding and frequency selection in flapping flight, J. Fluid Mech. (2000), vol.410, pp.323-341.

[8] J. C. S. Lai and M. F. Platzer, Jet Characteristics of a plunging airfoil, AIAA J. (1999), vol.37, No.12, pp.1529-1537.

[9] J. Young and J. C. S. Lai, Oscillating frequency and amplitude effects on the wake of a

plunging airfoil, AIAA J. (2004), vol.42, No.10, pp. 2042-2052.

[10] R. Godoy-Diana, J. Aider, J. E. Wesfreid, Transition in the wake of a flapping foil, Physical Review E (2008), vol. 77.

[11] K. D. von Ellenrieder, K. Parker, and J. Soria, Flow structures behind a heaving and pitching finite-span wing, J. Fluid Mech. (2003), vol. 490, pp. 129-138.

[12] H. Dong, R. Mittal and F. M. Najjar, Wake topology and hydrodynamic performance of low aspect ratio flapping foils, J. Fluid Mech. (2006), vol. 566, pp. 309-343.

[13] J. O. Dabiri, Optimal vortex formation as a unifying principle in biological propulsion, Annu. Rev. of Fluid Mech. (2009), vol.41, pp.17-33.

[14] K. D. Jones, C. M. Dohring, and M. F. Platzer, Experimental and computational investigation of the Knoller-Betz effect, AIAA J. (1998), vol. 36, No.7, pp. 1240-1246.

[15] M. F. Platzer, K. D. Jones, J. Young and J. C. S. Lai, Flapping-wing aerodynamics: progress and challenges, AIAA J. (2008), vol. 46, No.9, pp. 2136-2149.

[16] G. C. Lewin, H. Haj-Hariri, Modeling thrust generation of a two-dimensional heaving airfoil in a viscous flow, J. Fluid Mech. (2003), vol.492, pp.339-362.

[17] S. Heathcote and I. Gursul, Jet switching phenomenon for a periodically plunging airfoil, Physics of Fluids (2007), vol.19.

[18] R. Godoy-Diana, C. Marais, J. Aider and J. E. Wesfreid , A model for the symmetry breaking of the reverse Benard–von Karman vortex street produced by a flapping foil, J. Fluid Mech., vol. 622, pp. 23-32, 2009.

[19] M. L. Yu, H. Hu and Z. J. Wang, A numerical study of vortex-dominated flow around an oscillating airfoil with high-order spectral difference method. AIAA Paper, 2010-726.

[20] K. D. von Ellenrieder and S. Pothos, PIV measurement of the asymmetric wake of a two dimensional heaving hydrofoil, Exp. Fluids (2007), vol. 43, No. 5.

[21] C. L. Liang, K. Ou, S. Premasuthan, A. Jameson and Z. J. Wang, High-order accurate simulations of unsteady flow past plunging and pitching airfoils, Computer & Fluids (2010), vol.40, pp.236-248.

[22] H. Hu, L. Clemons, and H. Igarashi, An experimental study of the unsteady vortex structures in the wake of a root-fixed flapping wing, Exp. Fluids, vol.51, No.2, 2011, pp347–359.

[23] Y. Z. Sun, Z. J. Wang and Y. Liu, High-order multidomain spectral difference method for the Navier-Stokes equations on unstructured hexahedral grids, Commun. Comput. Phys. (2006), vol. 2, No. 2, pp. 310-333.

[24] M. L. Yu, Z. J. Wang and H. Hu, A high-order spectral difference method for unstructured dynamic grids, Computers & Fluids, 2011, Vol.48, No. 1, 2011, pp.84-97.

[25] B. Cockburn and C.-W. Shu, TVB Runge-Kutta local projection discontinuous Galerkin finite element method for conservation laws II: general framework. Math. Comput., 52:411–435, 1989.

[26] Z. J. Wang, Spectral(finite)volume method for conservation laws on unstructured grids: Basic formulation. J. Comput. Phys. (2002), 178:210–251.

[27] M. R. Visbal, High-fidelity simulation of transitional flows past a plunging airfoil, AIAA Paper, No. 2009-391.

[28] P. O. Persson, D. J. Willis and J. Peraire, The numerical simulation of flapping wings at low Reynolds numbers, AIAA Paper, 2010-724.

[29] K. Ou, P. Castonguay and A. Jameson, 3D flapping wing simulation with high order spectral difference method on deformable mesh, AIAA Paper, 2011-1316.

[30] K. Van den Abeele and C. Lacor. An accuracy and stability study of the 2D spectral volume method. J. Comput. Phys., 226(1):1007–1026, 2007.

[31] K. Van den Abeele,C. Lacor, and Z. J. Wang. On the stability and accuracy of the spectral difference method. J.Sci.Comput.,37(2):162–188,2008.

[32] H. T. Huynh. A flux reconstruction approach to high-order schemes including discontinuous Galerkin methods. AIAA Paper, 2007-4079.

[33] A. Jameson, A proof of the stability of the spectral difference method for all orders of accuracy. J. Sci. Comput., doi: 10.1007/s10915-009-9339-4, 2010.

[34] M. S. Liu, "A sequel to AUSM, Part 2: AUSM+-up for all speeds," J. Comput. Phys. (2006), vol. 214, pp.137–170.

[35] P. O. Persson, J. Peraire and J. Bonet, Discontinuous Galerkin solution of the Navier-Stokes equations on deformable domains, Computer Methods in Applied Mechanics and Engineering (2009), vol. 198, pp. 1585-1595.

[36] D. J. Cleaver, Z. Wang and I. Gursul, Vortex mode bifurcation and lift force of a plunging airfoil at low Reynolds numbers, AIAA Paper, 2010-390.
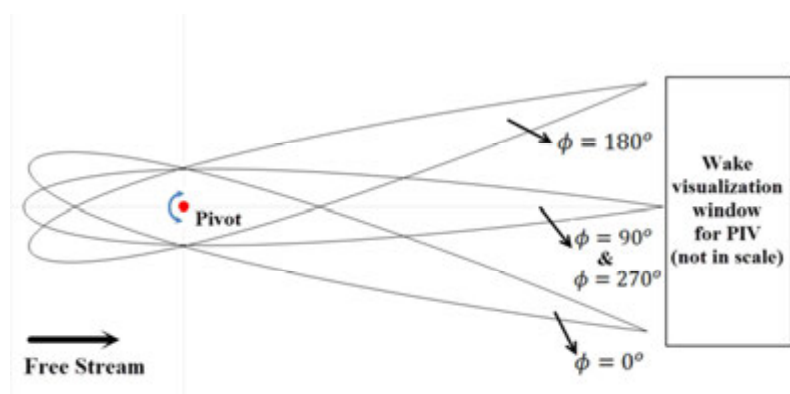
**Figure 4.** Schematic of the pitching kinematic of the NACA0012 airfoil.



(a)  (b)
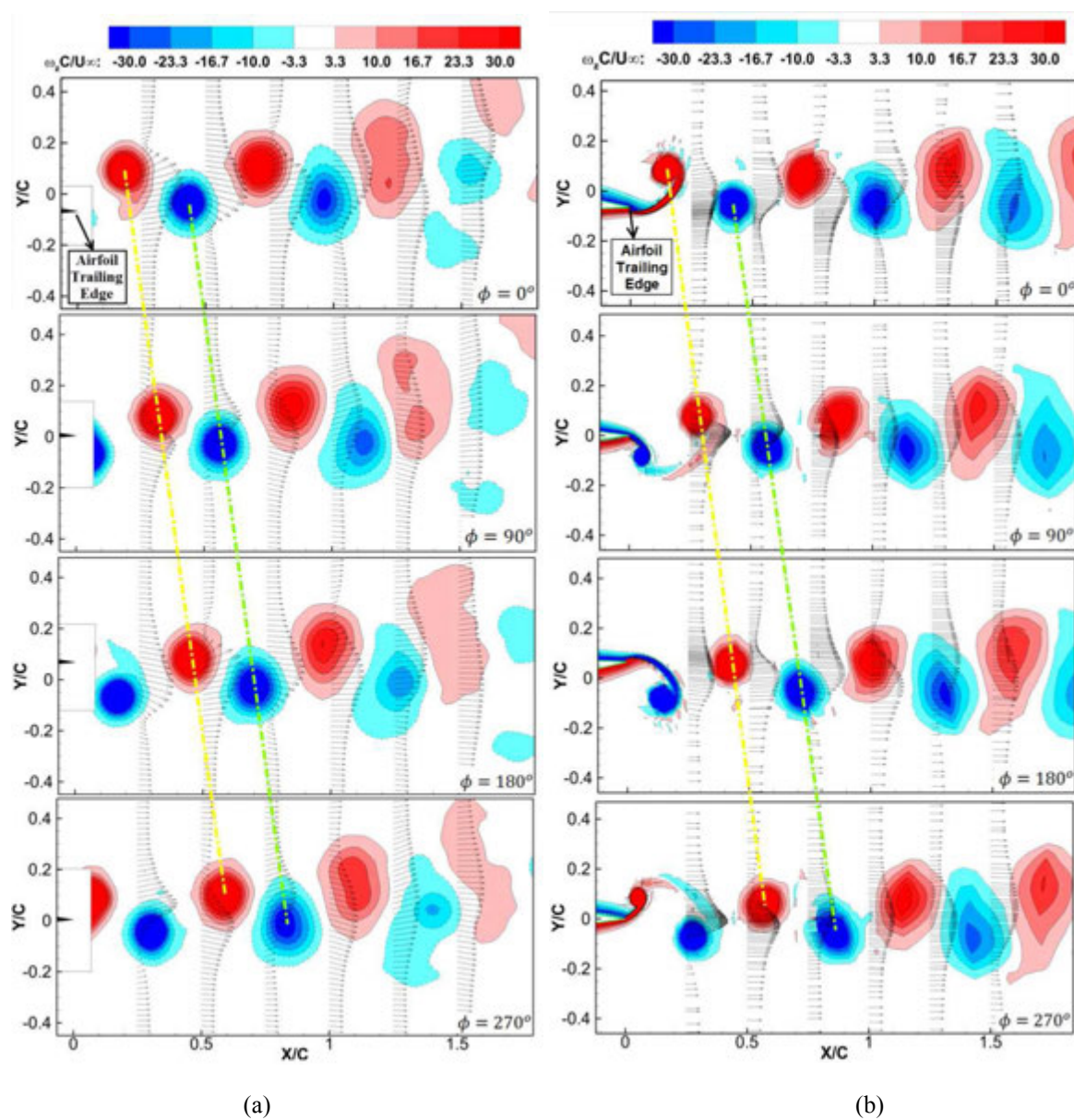
**Figure 5.** Comparison between the phase-locked spanwise vorticity fields from PIV (a) and the instantaneous numerical vorticity fields (b) with $S_t = 0.31$, $K = 15.1$ and the pitching amplitude $\alpha_0 = 5^o$ at the same phase.
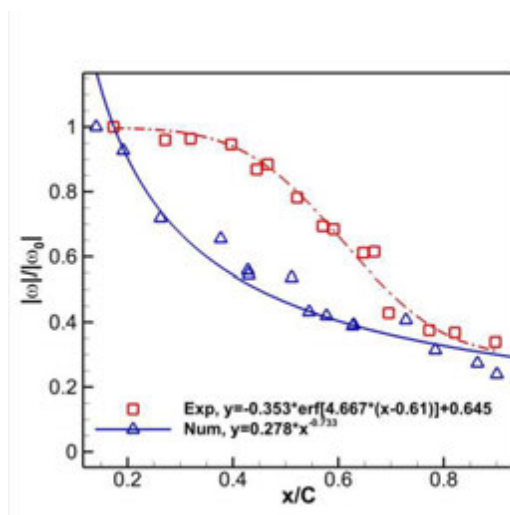


**Figure 6.** The vortex strength decay in the wake versus downstream distance in both experiments and numerical simulations with $S_t = 0.31$, $K = 15.1$ and the pitching amplitude $\alpha_0 = 5^o$. The decay profile for the numerical simulations follows the power law while that for the experiments falls into an error function curve.
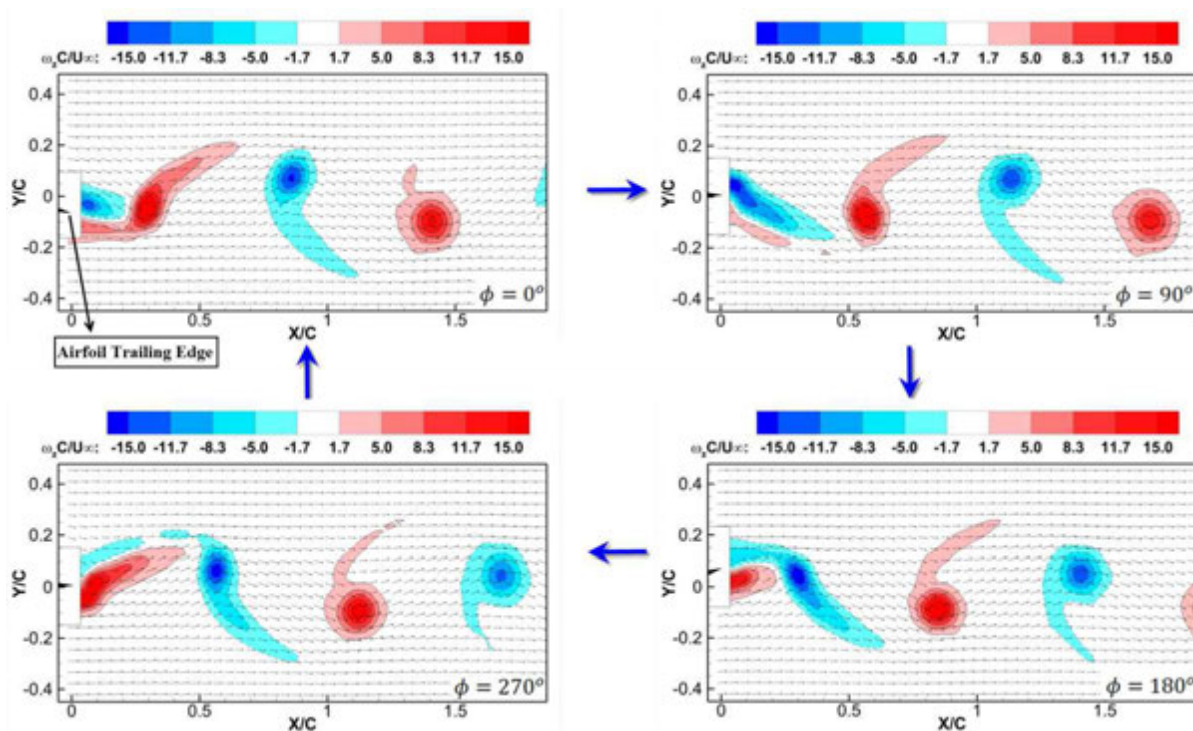
**Figure 7.** Phase-locked spanwise vorticity fields from PIV with $S_t = 0.1$, $K = 5.0$ and the pitching amplitude $\alpha_0 = 5^o$ at four different phases, namely $0^o$, $90^o$, $180^o$ and $270^o$.



**Figure 8.** Phase-locked spanwise vorticity fields from PIV with $S_t = 0.12$, $K = 5.7$ and the pitching

amplitude $\alpha_0 = 5^o$ at four different phases, namely $0^o$, $90^o$, $180^o$ and $270^o$.



**Figure 9.** Phase-locked spanwise vorticity fields from PIV with $S_t = 0.29$, $K = 13.8$ and the pitching amplitude $\alpha_0 = 5^o$ at four different phases, namely $0^o$, $90^o$, $180^o$ and $270^o$.

**Figure 10.** Time-averaged velocity (up) and vorticity (down) fields from the PIV measurements with the pitching amplitude $\alpha_0 = 5^o$. (a) $S_t = 0.1$, $K = 5.0$; (b) $S_t = 0.12$, $K = 5.7$; (c) $S_t = 0.29$, $K = 13.8$.
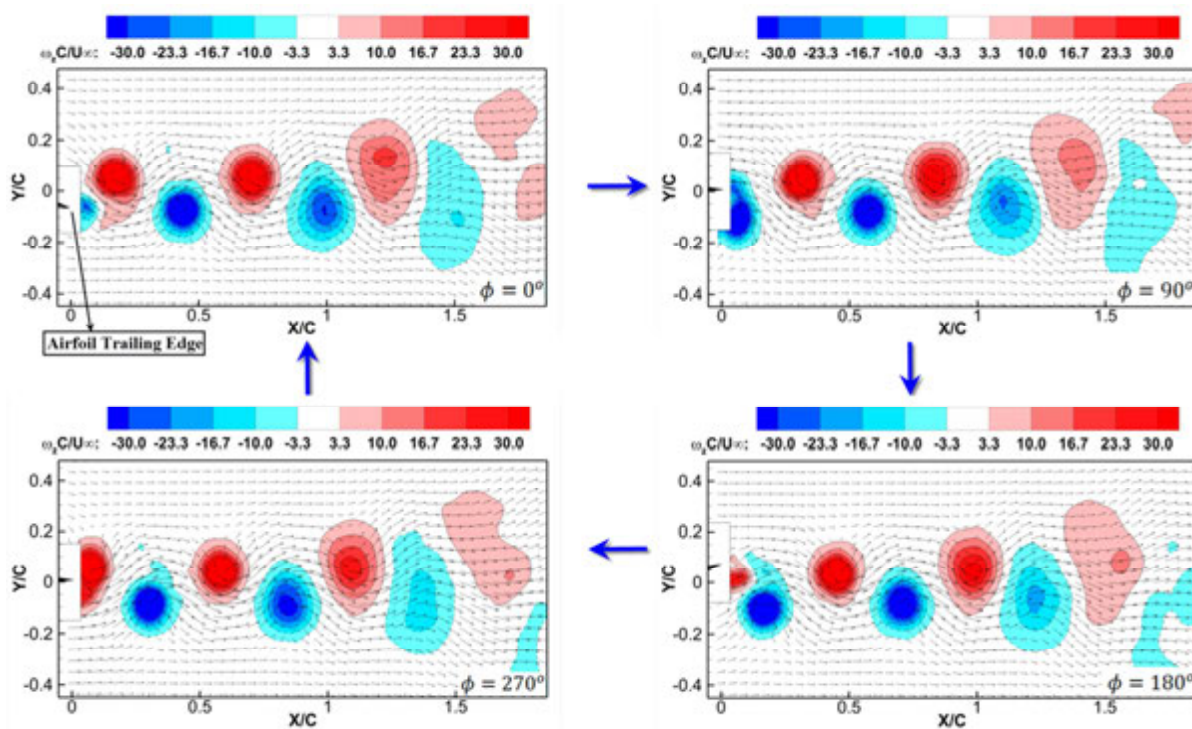


**Figure 11.** Phase-locked spanwise vorticity fields from PIV with $S_t = 0.31$, $K = 15.1$ and the pitching amplitude $\alpha_0 = 5^o$ at four different phases, namely $0^o$, $90^o$, $180^o$ and $270^o$.

**Figure 12.** Phase-locked spanwise vorticity fields from PIV with $S_t = 0.37$, $K = 17.6$ and the pitching amplitude $\alpha_0 = 5°$ at four different phases, namely 0°, 90°, 180° and 270°.
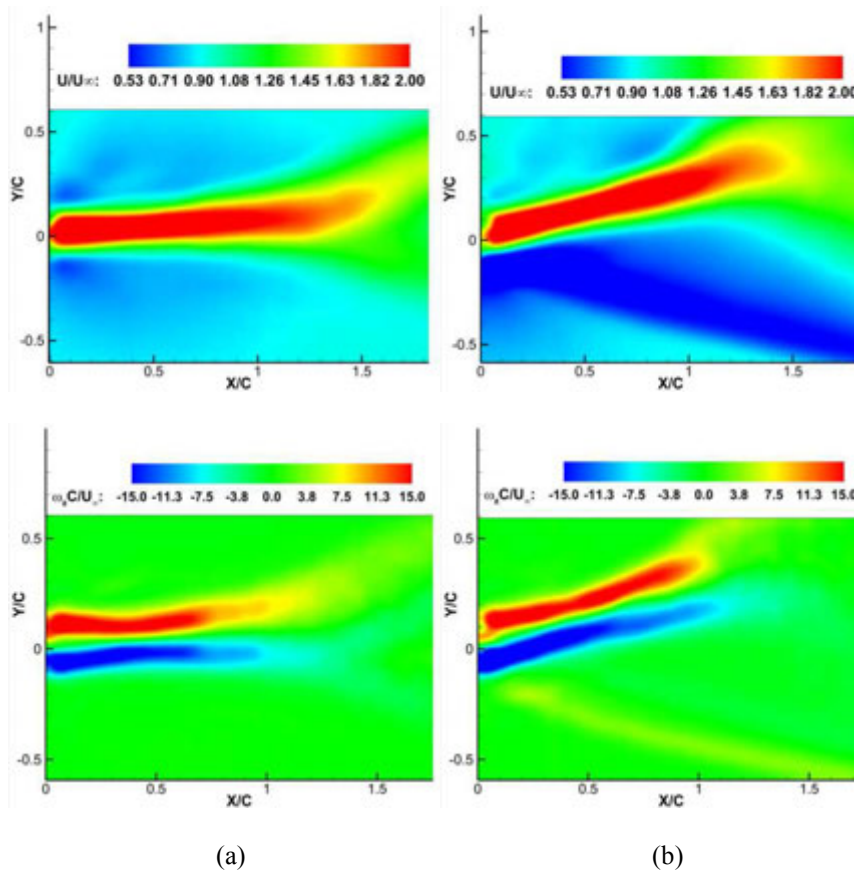


(a)                (b)

**Figure 13.** Time-averaged velocity (up) and vorticity (down) fields from the PIV measurements with the pitching amplitude $\alpha_0 = 5^o$. (a) $S_t = 0.31$, $K = 15.1$; (b) $S_t = 0.37$, $K = 17.6$.



| (a) | (b) |
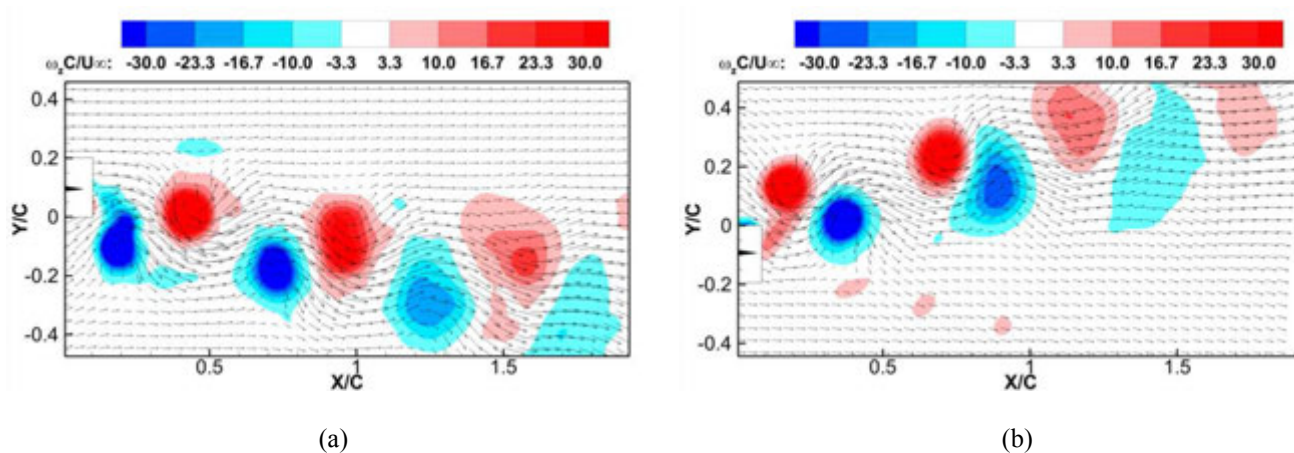
**Figure 14.** Phase-locked spanwise vorticity fields from PIV for two asymmetric wakes with different deflective directions at $S_t = 0.37$, $K = 17.6$ and the pitching amplitude $\alpha_0 = 5^o$.



| (a) | (b) |
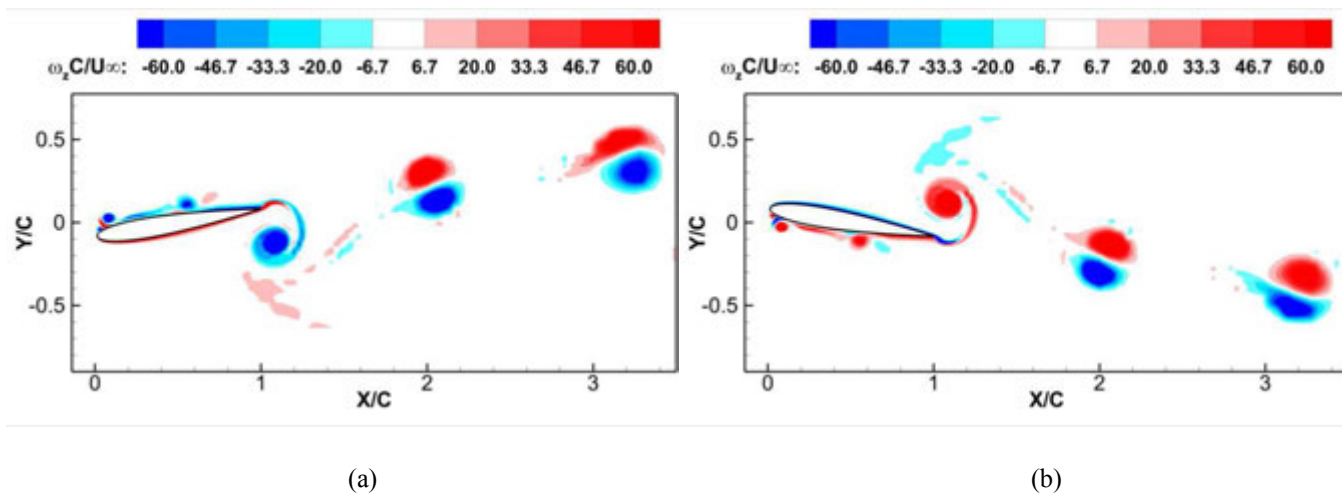
**Figure 15.** Spanwise vorticity fields from numerical simulations with $S_t = 0.75$, $K = 18.0$ and the pitching amplitude $\alpha_0 = 10^o$ at the same time. The initial phase angles are (a) $\phi_0 = 180^o$ and (b) $\phi_0 = 0^o$.

(a)                                                                              (b)
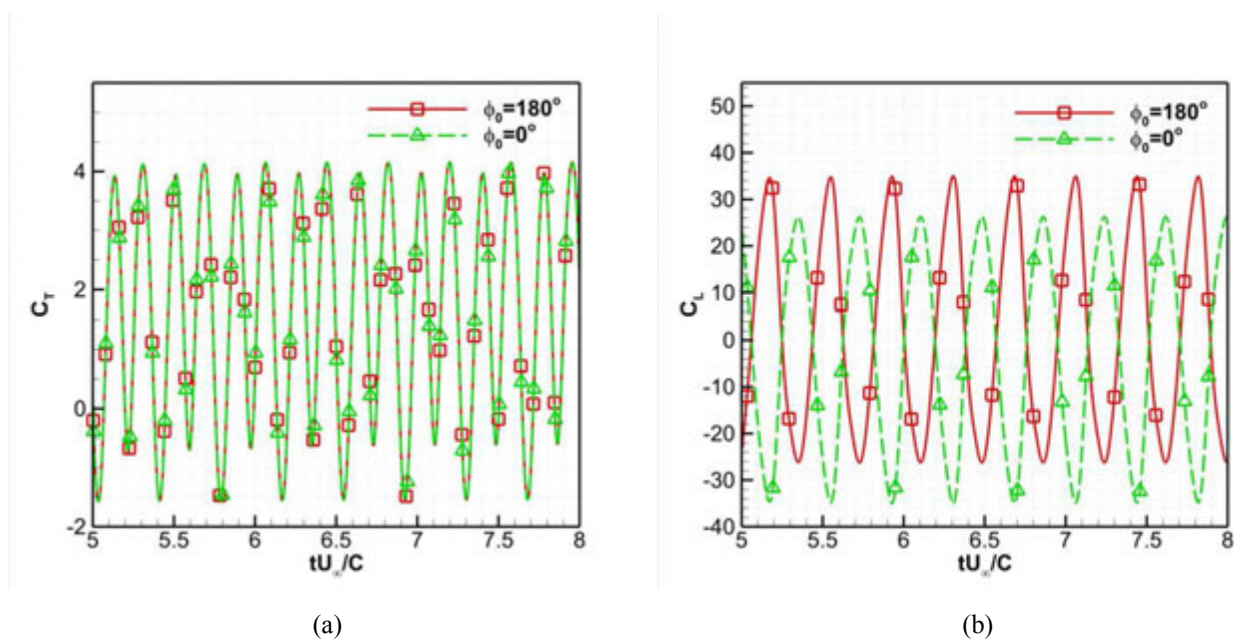
**Figure 16.** Aerodynamic force coefficient histories for the pitching airfoil with $S_t = 0.75$, $K = 18.0$ and the pitching amplitude $\alpha_0 = 10^o$ and different initial phase angles $0^o$ and $180^o$. (a) Thrust coefficient histories; (b) lift coefficient histories.





(a)                                                                              (b)
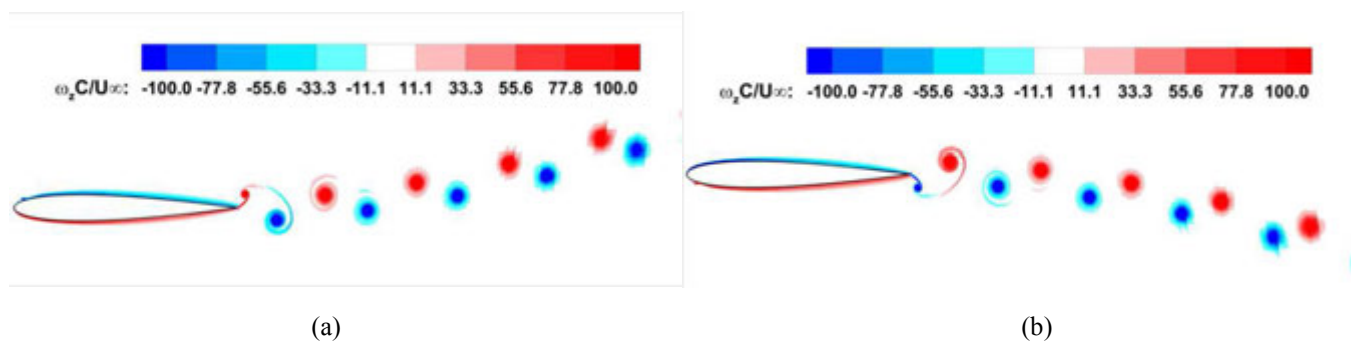
**Figure 17.** Spanwise vorticity fields from numerical simulations with Re = 12,600, $S_t = 0.3$, $K = 23.0$ and the pitching amplitude $\alpha_0 = 2^o$ at the same time. The initial phase angles are (a) $\phi_0 = 180^o$ and (b) $\phi_0 = 0^o$.
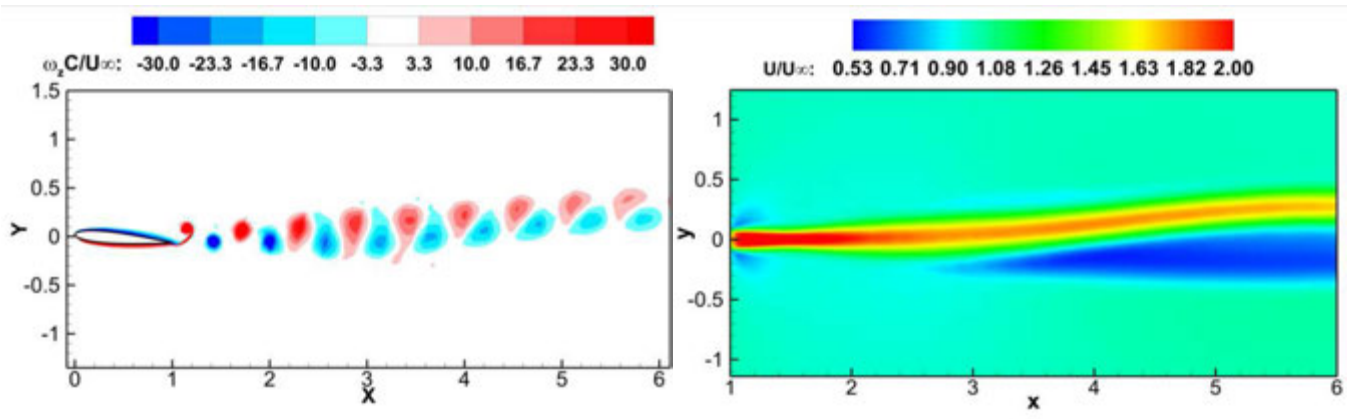
(a)
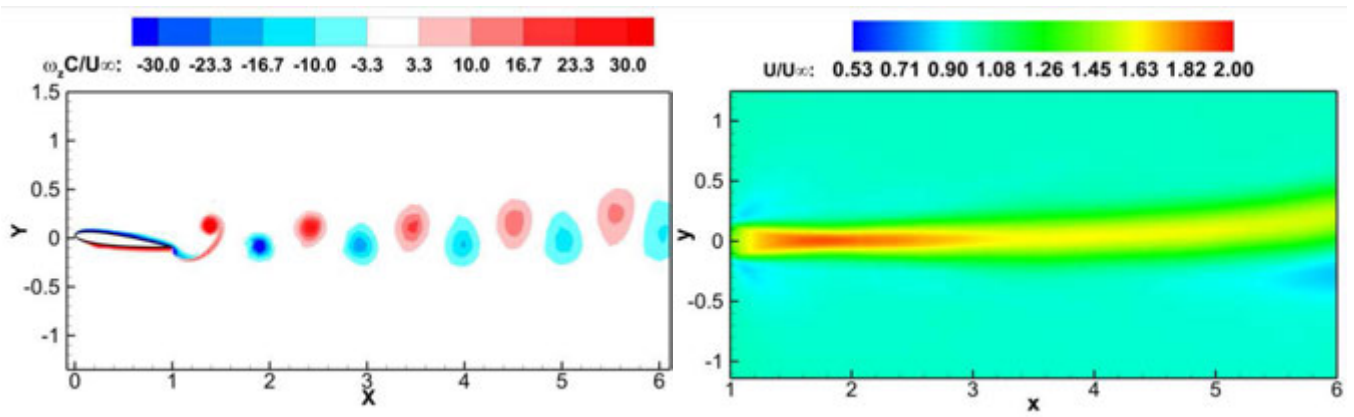


(b)
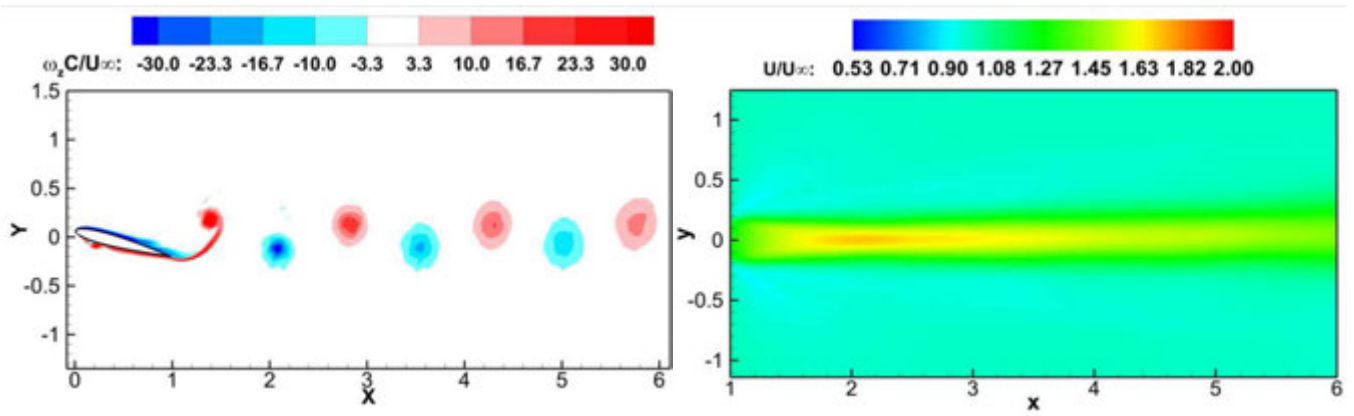


(c)

**Figure 18.** Instantaneous spanwise vorticity fields and time-averaged velocity fields with $S_t = 0.31$. (a) $K = 15.1$ and the pitching amplitude $\alpha_0 = 5^o$; (b) $K = 7.5$ and the pitching amplitude $\alpha_0 = 10^o$; (c) $K = 5$ and the pitching amplitude $\alpha_0 = 15^o$. The phase angle for the three vorticity fields is $0^o$.
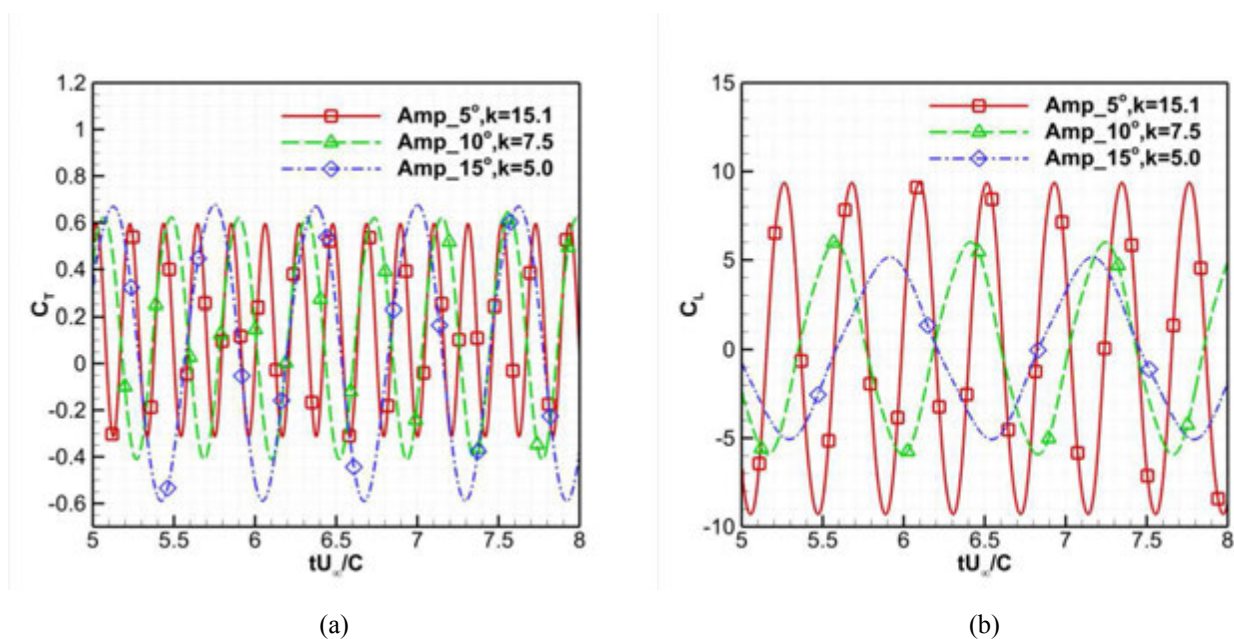
**Figure 19.** Aerodynamic force coefficient histories for the pitching airfoil with $S_t = 0.31$ but different reduced frequencies and pitching amplitudes. (a) Thrust coefficient histories; (b) lift coefficient histories.
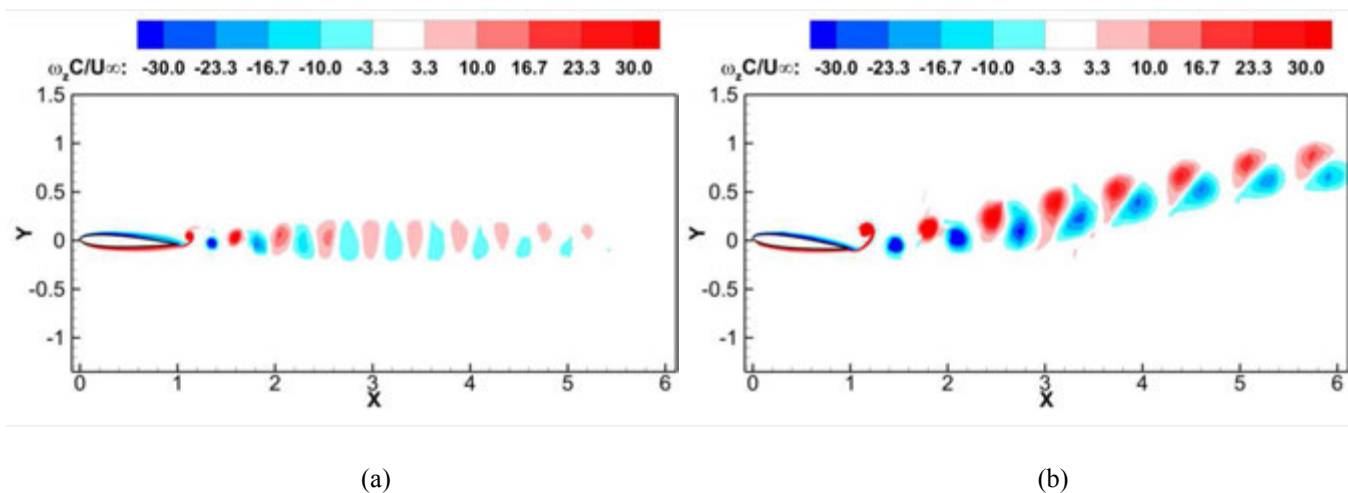


**Figure 20.** Instantaneous spanwise vorticity fields with $K = 15.1$. (a) $S_t = 0.19$ and the pitching amplitude $\alpha_0 = 3^o$; (b) $S_t = 0.41$ and the pitching amplitude $\alpha_0 = 6.5^o$. The phase angle for both vorticity fields is $0^o$.
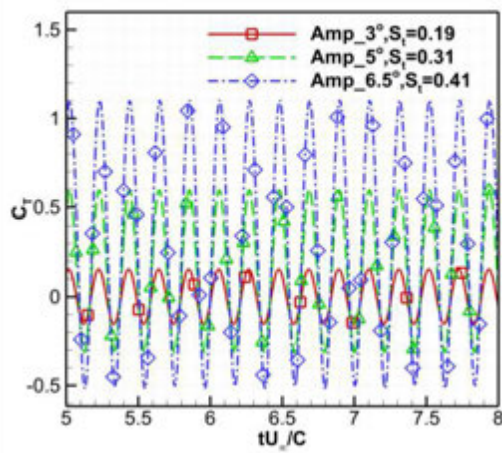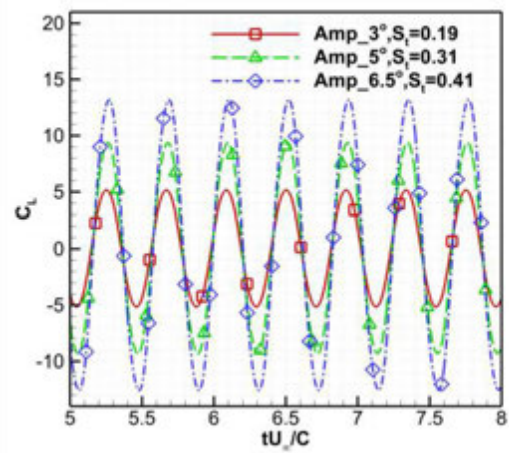
(a)                                                            (b)

**Figure 21.** Aerodynamic force coefficient histories for the pitching airfoil with K = 15.1 but different Strouhal numbers and pitching amplitudes. (a) Thrust coefficient histories; (b) lift coefficient histories.

# CHAPTER 4. Airfoil Thickness Effects on the Thrust Generation of Plunging Airfoils

A paper published in Journal of Aircraft

Meilin Yu, Z. J. Wang and Hui Hu

## Abstract

A numerical study was conducted to investigate the effects of airfoil thickness on the thrust generation of plunging airfoils and to assess the contributions of pressure and viscous forces in flapping propulsion. A series of NACA symmetric airfoils with thickness ratio ranging from 4.0% to 20.0% of the airfoil chord length were used in the present study to undertake a same sinusoid plunging motion at a low Reynolds number of $Re$ =1,200 with the plunging Strouhal number $Str$ = 0.45 and reduced frequency $k$ = 3.5. It was found that the thickness of the airfoils would affect the evolution of the unsteady vortex structures around the plunging airfoils significantly, even though the airfoils were set to undertake the same plunging motion. The different behaviors of the unsteady vortex structures shedding from the airfoils with different thickness cause dramatic changes to the resultant aerodynamic force acting on the plunging airfoils. For a thick plunging airfoil with its thickness ratio greater than 9.0%, pressure force was found to play a dominate role in the thrust generation, and viscous force would be almost negligible and contribute mainly to drag production. It confirms that traditional inviscid model of Knoller–Betz effect (i.e., ignoring viscous effect) can be used to explain many phenomena associated with flapping propulsion. A new finding of the present study is the substantial contribution of viscous force to the thrust generation for thin plunging airfoils (i.e., the thickness ratio less than 8.0%). Viscous force was found to become thrust producing, instead of drag producing, and play a non-negligible role in the thrust generation for the thin airfoils (i.e., viscous force would produce up to 20.5% of the total thrust for NACA0004 airfoil in the present study). The role change of viscous force in the thrust generation of the plunging airfoils was found to be closely related to the variations of the dynamics of the unsteady vortex structures around the plunging airfoils.

# 1. Introduction

Micro-Air-Vehicles (MAVs) have been one of the most active research topics in aerospace engineering community in recent years. The miniaturized aircraft is expected to open up new opportunities for surveillance-like missions, especially in hazardous environments inaccessible to ground vehicles. Among different MAV designs, flapping-wing-based designs stand out with high efficiency and excellent maneuverability, as demonstrated by the natural fliers such as birds and insects. It has long been realized that steady-state aerodynamics does not accurately account for the aerodynamic forces produced in flapping flight. This has prompted extensive studies to elucidate the fundamental mechanism of flapping flight to produce enough aerodynamic forces needed for propulsion and maneuvering. Knoller [1] and Betz [2] are among the first to propose an invisid theory, which is known as the Knoller–Betz effect, to explain why a flapping wing can generate thrust in flapping motion. Katzmayr [3] provided the first experimental verification of the Knoller–Betz effect by placing a stationary wing into a sinusoidally oscillating airflow. Ober [4] provided additional theoretic explanations and calculations to confirm Katzmayr's experimental results. Much progress has been made since then to uncover the underlying physics of flapping propulsion [5-15].

While many important findings have been derived through those previous studies, much work is still needed for a better understanding of flapping propulsion for the optimum design of flapping-wing-based MAVs. For example, while birds and insects flap their thin wings to fly (i. e., wing thickness is only a few percent of the chord length), much thicker airfoils (airfoil thickness > 10% of chord length) were usually used in previous studies to reveal the underlying physics of flapping flight [6-12]. Although numerous experimental and numerical studies have been conducted recently to investigate the effects of kinematic parameters of flapping motions, such as the flapping frequency, amplitude and phase difference between plunging and pitching motions, on the thrust generation and propulsive efficiency, the influence of airfoil thickness on flapping propulsion has not yet been fully explored [10]. Furthermore, while the inviscid model of Knoller–Betz effect (i.e., ignoring viscous effect) has been used widely to explain many phenomena associated with flapping propulsion [8-

10], the role of viscous force in flapping propulsion is still poorly understood. Many fundamental questions, such as "are viscous effects negligible for flapping propulsion under all conditions?" and "while viscous force is known to be usually drag producing, can it ever make a positive contribution to the thrust generation in flapping propulsion?", still remain to be answered.

In this short paper, we report a numerical study to investigate the effects of airfoil thickness on the thrust generation of plunging airfoils and to assess the contribution of viscous force to the thrust generation in flapping propulsion. A series of commonly-used symmetric NACA airfoils with thickness ranging from 4% to 20% of the chord length were used to undertake the same plunging motion at a low Reynolds number of Re = 1,200. The behaviors of the unsteady vortex structures around the plunging airfoils and the resultant aerodynamic forces acting on the plunging airfoils were compared quantitatively in order to reveal the underlying physics related to flapping propulsion. The contribution of viscous force on the thrust generation in flapping propulsion was also examined in detail based on the quantitative comparison.

## 2. Numerical Method and Studied Parameters

In the present study, a high-order spectral difference (SD) method with dynamic unstructured grids was used for the numerical simulation. The governing equations for the fluid flow are the unsteady Navier-Stokes equations in a conservation form, which can be expressed as,

$$\frac{\partial Q}{\partial t} + \frac{\partial F}{\partial x} + \frac{\partial G}{\partial y} + \frac{\partial H}{\partial z} = 0. \tag{1}$$

Herein, $Q = (\rho, \rho u, \rho v, \rho w, E)^T$ are the conservative variables, $\rho$ is the fluid density, $u, v$ and $w$ are the Cartesian velocity components, and $E$ is the total initial energy. $F$, $G$, $H$ are the total fluxes including both the inviscid and viscous flux vectors, i.e., $F = F^i - F^v$, $G = G^i - G^v$ and $H = H^i - H^v$. Detailed formulas for the fluxes can be found in Yu et al. [15]. With the assumption that the fluid obeys the perfect gas law, the pressure is related to the total initial energy by $E = \frac{p}{\gamma - 1} + \frac{1}{2}\rho(u^2 + v^2 + w^2)$, which closes the solution system.

To achieve an efficient implementation, a time-dependent coordinate transformation from

the physical domain $(t, x, y, z)$ to the computational domain $(\tau, \xi, \eta, \zeta)$ is applied on Eq. (1), which is

$$\frac{\partial \tilde{Q}}{\partial \tau} + \frac{\partial \tilde{F}}{\partial x} + \frac{\partial \tilde{G}}{\partial y} + \frac{\partial \tilde{H}}{\partial z} = 0, \qquad (2)$$

where

$$\begin{cases} \tilde{Q} = |J| Q \\ \tilde{F} = |J| \left( Q\xi_\tau + F\xi_x + G\xi_y + H\xi_z \right) \\ \tilde{G} = |J| \left( Q\eta_\tau + F\eta_x + G\eta_y + H\eta_z \right) \\ \tilde{H} = |J| \left( Q\zeta_\tau + F\zeta_x + G\zeta_y + H\zeta_z \right) \end{cases} \qquad (3)$$

Herein, $\tau = t$ and $(\xi, \eta, \zeta) \in [-1,1]^3$, are the local coordinates in the computational domain. In the transformation shown above, the Jacobian matrix $J$ takes the following form

$$J = \frac{\partial(x, y, z, t)}{\partial(\xi, \eta, \zeta, \tau)} = \begin{pmatrix} x_\xi & x_\eta & x_\zeta & x_\tau \\ y_\xi & y_\eta & y_\zeta & y_\tau \\ z_\xi & z_\eta & z_\zeta & z_\tau \\ 0 & 0 & 0 & 1 \end{pmatrix}. \qquad (4)$$

Note that the grid velocity $\overrightarrow{v_g} = (x_t, y_t, z_t)$ is related with $(\xi_\tau, \eta_\tau, \zeta_\tau)$ by

$$\begin{cases} \xi_\tau = -\overrightarrow{v_g} \cdot \nabla\xi \\ \eta_\tau = -\overrightarrow{v_g} \cdot \nabla\eta \\ \zeta_\tau = -\overrightarrow{v_g} \cdot \nabla\zeta \end{cases} . \qquad (5)$$

In the present study H-refinement (grid refinement) and p-refinement studies were conducted at first to determine the suitable grid and numerical accuracy. Based on the investigations, a 3rd order accurate scheme with a medium mesh was chosen. A time refinement study was also performed to determine a reasonable non-dimensional time step as $\Delta t \cdot C / V_\infty = 8 \times 10^{-6}$, where $C$ is the chord length and $V_\infty$ the free stream velocity. Further information about the implementation of the method described above for the numerical simulation of the unsteady flows around flapping airfoils as well as the validation of the simulation results against experimental data is available in reference [15].

The airfoils used in the present study are a series of symmetric NACA airfoils, i.e., NACA0004, NACA0006, NACA0009, NACA0012 and NACA0020 airfoils. The airfoils were set to undertake a plunging motion, which can be expressed as $y = A sin(2\pi f t)$, where $f$ is the flapping frequency, $A$ is the plunging amplitude. The Reynolds number ($Re$) based on the airfoil chord length, $C$, and the free stream velocity, $V_\infty$, was set to be 1,200 for the

present study, i.e., $Re=\rho V_\infty C/\mu$=1,200, which is well within the insect flight regime. Strouhal number, $Str = 2fA/V_\infty$, and reduced frequency, $k = 2\pi fC/V_\infty$, are the most commonly used non-dimensional parameters to characterize the kinematics of flapping airfoils/wings. In the present study, the Strouhal number of the plunging airfoils was chosen to be 0.45, i.e., $Str =$ 0.45. The reduced frequency of the plunging motion was set to be 3.5, i.e., $k$ =3.5. It has been suggested that the wake flow downstream of a flapping airfoil/wing can be characterized as drag producing, neutral, or thrust-producing depending on the flapping frequency and stroke amplitude [6-14]. Based on the findings of the previous work of Jones et al. [8] and Lewin & Haj-Hariri [12], with the kinematic parameters used in the present study, the wake flows downstream the plunging airfoils should be thrust-producing, which was confirmed by the numerical simulation results of the present study.

## 3. Results and Discussions

Figure 1 and Figure 2 display the typical behaviors of the unsteady vortex structures around a thick airfoil (e.g., NACA0020) and a thin airfoil (e.g., NACA0004) in a plunging cycle. The flow pattern around the plunging airfoils at such a relatively large Strouhal number (i.e., $Str=0.45$) was found to be featured mainly by the periodic shedding of Leading Edge Vortice (LEVs) and Trailing Edge Vortices (TEVs) as well as the interactions among LEVs, TEVs and plunging airfoils, which agrees with those reported by Lewin & Haj-Hariri [12]. It is clearly observed that, even though the airfoils were set to undertake the same plunging motion, the evolutions of the unsteady LEVs and TEVs around the plunging airfoils were found to vary significantly due to the thickness differences of the airfoils. As shown in Fig. 1, for the thick airfoil case, the LEVs shed from the airfoil leading edge traveled downstream along with the free stream continuously, and then interacted with the TEVs further downstream. Similar behavior of the LEVs was also reported by Ashraf et al. [10] in their study of the vortex structures around a plunging NACA0012 airfoil. However, for the thin airfoil (e.g. NACA0004) as shown in Fig. 2, instead of traveling downstream along with the free stream continuously, the LEVs over the lower (or upper) surface of the airfoil stayed close to the airfoil leading edge during the entire down strokes (or upstrokes) of the plunging

motion. After being stretched seriously, the LEVs were found to move against the free stream around the sharp airfoil leading edge, and shift to the upper (or lower) side of the airfoil during the subsequent upstrokes (or down strokes). Such phenomena were also found by Lewin and Haj-Hariri [12] and were named as LEV circumnavigation. Associated with the different behaviors of the LEVs around thick and thin airfoils, the flow patterns and the resultant aerodynamic forces acting on the plunging airfoils were also found to vary dramatically.

Figure 3 shows the pressure distributions and velocity vector fields (only 2% of the vectors were shown) around NACA0020 and NACA0004 airfoils at the same plunging phase angle of $\Phi = 180$ deg. It can be found that, for a thick airfoil such as NACA0020, corresponding to the rolling up of the LEVs on the airfoil upper (or lower) surface during the down strokes (or upstrokes) of the plunging motion, a region with relatively low pressure was found on the airfoil upper (or lower) surface near the airfoil leading edge as shown in Fig. 3(a), which is favorable for the thrust generation. The region with relatively low pressure was found to separate from the airfoil surface and move downstream as the LEVs shed from the airfoil leading edge and travel downstream. However, for a thin airfoil as shown in Fig. 3(b), associated with the LEV circumnavigation described above, low pressure regions were found to exist on both the upper and lower surfaces, and the low pressure regions would remain near the airfoil leading edge during almost the whole plunging cycle. Furthermore, the LEV circumnavigation was also found to induce strong reversed flows on both the upper and lower surfaces near the leading edge of the thin airfoils. Corresponding to the strong reversed flows near the airfoil leading edge, the viscous force acting on the upper and lower surfaces of the thin airfoil could actually be thrust-producing, instead of being drag-producing. The interesting finding can be revealed more quantitatively in the analysis of the resultant aerodynamic forces acting on the plunging airfoils.

Based on the distributions of pressure and viscous forces on the surfaces of the plunging airfoils, the resultant aerodynamic forces acting on the plunging airfoils in the term of thrust coefficient, $C_T = Thrust/(0.5\rho V_\infty^2 S)$, were determined. Figure 4 shows the histories of the thrust coefficients of the five plunging airfoils investigated in the present study. It is clear that, while the thrust coefficients of the plunging airfoils were found to fluctuate greatly in

each plunging cycles, the fluctuating amplitude of the thrust coefficients decreases as the thickness of the plunging airfoil decreases. While all the airfoils were set to undertake the same periodic plunging motion, only the thrust coefficients of the thicker airfoils (e.g., NACA0020 and NACA0020 airfoils) were found to be periodic, as expected. The thrust coefficients of the thinner airfoils (e.g., NACA0004 and NACA0006 airfoils) were found to become aperiodic even though the plunging motion of the airfoils is periodic. The aperiodic behavior of the flow field around a plunging airfoil was also reported by Lewin & Haj-Hariri [12] with an elliptical airfoil plunging at a similar Strouhal numbers (e.g., *Str* ≈ 0.48) as that of the present study. It should also be noted that, for the thicker airfoils (e.g., NACA0012 or NACA0020), while the resultant aerodynamic force acting on the plunging airfoils were found to be thrust producing for most of the time in each plunging cycles (i.e., thrust coefficient being positive), the resultant aerodynamic force could also become drag producing (i.e., thrust coefficient becoming negative) at some phase angles. However, the thrust coefficients of the thinner airfoils (e.g., NACA0004 or NACA0006) were found to be positive almost in the entire plunging cycles, indicating that almost no drag was experienced by the thinner airfoils during the plunging motion. This is believed to be closely related to the LEV circumnavigation to maintain low pressure regions and reverse flows near the leading edges of the thinner airfoils.

In order to assess the role of viscous force in the thrust generation of flapping propulsion, the total thrusts acting on the plunging airfoils were decomposed into two parts, i.e., one part contributed from pressure force ($T_p = \int p n_x ds$) and the other from the viscous force ($T_v = \int (\sigma_{xx} n_x + \sigma_{xy} n_y + \sigma_{xz} n_z) ds$, where $\sigma$ denotes the viscous stress). Figure 5 shows the comparisons of the total thrust coefficients (i.e., considering the contributions from both pressure and viscous forces) and the thrust coefficients based on the contribution from pressure force only (i.e., ignoring the viscous forces) for NACA0020 and NACA0004 airfoils. The profiles in solid lines represent the total thrust coefficients, and the profiles in dashed lines indicate the results based on the contribution from pressure force only. The differences between the solid and dashed lines would represent the contribution of viscous force on the thrust generation. It can be seen clearly that, compared with viscous force, pressure force was found to play a dominant role in the thrust generation of flapping

propulsion. It is also observed that, the differences between the solid and dashed lines were found to become larger for the thinner airfoil (e.g., NACA0004), compared with those for the thicker airfoil case (e.g., NACA0020). This indicates that the effects of viscous force on the thrust generation in flapping propulsion would become stronger for the thinner airfoils.

In order to reveal the contribution of viscous force on the thrust generation of the plunging airfoils more clearly and quantitatively, the averaged total thrust coefficients of the plunging airfoils, $<C_T>$, and the contributions from pressure force, $<C_{T\_P}>$, and viscous force, $<C_{T\_V}>$, over plunging cycles were calculated. As revealed clearly from the results listed in Table 1, the averaged thrust coefficients of the plunging airfoils vary significantly as the airfoil thickness changes. With the plunging kinematic parameters and the airfoil thickness range used in the present study, a thicker airfoil was found to generate a larger averaged thrust when undertaking a same plunging motion. The finding was found to agree with the conclusion reported by Ashraf et al. [10]. The results shown in Table 1 also confirmed that pressure force would play a dominant role in the thrust generation of flapping propulsion. For the thicker airfoils (e.g., NACA0012 and NAC0020 airfoils), viscous force was found to be mainly drag producing, and its effect was found to be very small (~ 2.0%), which is negligible. The finding can be used to explain why the traditional inviscid model of Knoller–Betz effect (i.e., ignoring the viscous effect) can be used to explain many phenomena associated with flapping propulsion. The drag-producing nature of viscous force for thick airfoils was found to agree with the results reported in Wang (2000). More interestingly, as revealed from the results given in Table 1, viscous force becomes thrust producing, instead of drag producing, for the thinner airfoils (e.g., NACA0006 and NACA0004). The contribution of viscous force to the thrust generation in flapping flight was found to become more and more substantial as the thickness of the plunging airfoil decreases (i.e., 13.6% for NACA0006 and up to 20.5% for NACA0004). This is believed to be closely related to the existence of reverse flows near the leading edges on both sides of the airfoil surfaces during almost whole plunging cycles for the thinner airfoils, as shown clearly in Fig. 3.

## 4. Conclusions

A numerical study was conducted to investigate the effects of airfoil thickness on the thrust

generation of plunging airfoils and to assess the contribution of viscous force to flapping propulsion.  A series of commonly-used NACA symmetric airfoils were used in the present study to undertake a same plunging motion at a low Reynolds number of $Re$ =1,200 with the plunging Strouhal number $Str$ = 0.45 and reduced frequency $k$ = 3.5.  It was found that, even though the airfoils were set to undertake the same plunging motion, the evolutions of the vortex structures around the plunging airfoils and the resultant aerodynamic forces acting on the airfoils could vary dramatically due to the difference in airfoil thickness.

While the Leading Edge Vortices (LEVs) of the thicker airfoils (e.g., > 9.0% thickness ratio for the present study) were found to shed periodically and travel downstream along with the free stream continuously, LEV circumnavigation was found for the thinner airfoils (e.g., < 9.0% thickness ratio) with LEVs stretched and remaining near the airfoil leading edges for most of time in the plunging cycles.  Associated with the LEV circumnavigation, low pressure regions and reverse flows were found to remain near the leading edge on both sides of the airfoils during almost whole plunging cycles for the thinner airfoils.  The different behaviors of the LEVs for the thick and thin airfoils can affect the resultant aerodynamic force acting on the plunging airfoils dramatically.  While the thrust generation of the plunging airfoils with larger thickness was found to be periodic as expected, the thrust generation of the thin airfoils can become aperiodic even though the plunging motion is periodic.

The present study also revealed that, pressure force plays a dominate role in the thrust generation of the plunging airfoils. As expected, viscous force contributes mainly to drag production, and its effect is almost negligible for the airfoils with relatively large thickness, which explains why the traditional inviscid model of Knoller–Betz effect (i.e., ignoring the viscous effect) can be used to explain many phenomena associated with flapping propulsion. Another important finding of the present study is the substantial contribution of viscous force to the thrust generation for thin airfoils. The viscous force was found to become thrust producing, instead of drag producing, and play a non-negligible role in the thrust generation for the thin airfoils (i.e., producing up to 20.5% of the total thrust for NACA0004 airfoil in the present study).  The role change of viscous force in the thrust generation of the plunging airfoils was found to be closely related to the dynamics of the unsteady vortex structures

around the plunging airfoils.

Note that in the present study, the reduced frequency is defined as $k = 2\pi f C/V_\infty$ based on the chord length $C$. Since the airfoil thickness effects on the aerodynamic performances are the main interest in the short paper, it makes sense to define the reduced frequency based on the airfoil thickness. Then it is clear that if we want to keep the reduced frequency the same for all airfoils, the thinner airfoil must maneuver with a larger frequency. Under such conditions, if the Strouhal number is kept the same for all airfoils, the thinner airfoil will plunge with a smaller plunging amplitude. These cases can be interesting and will be compared and analyzed in future publications.

## Acknowledgment

# References

[1] Knoller, R., "Die gesetze des luftwiderstandes. Flug- und Motortechnik," Vol. 3, No.21, 1909, pp.1–7.

[2] Betz, A., "Ein beitrag zur erklaerung des segelfluges. Zeitschrift fuer Flugtechnik und Motorluftschiffahrt," Vol.3, 1912, pp.269–270.

[3] Katzmayr, R., "Effect of periodic changes of angle of attack on behavior of airfoils," NACA Technical Report TM 147, 1922.

[4] Ober, S., "Note on the Kaztmayreffect on airfoil drag," NACA TR TN 214, 1925.

[5] von Karman T. and Burgers, J. M., "Aerodynamic Theory: A General Review of Progress", Vol. 2. 1935.

[6] Koochesfahani, M. M .,"Vortical patterns in the wake of an oscillating airfoil," AIAA J., Vol. 27, 1989, pp.1200-1205.

[7] Dickinson, M. H., Lehmann, F. O., and Sane, S. P., "Wing rotation and the aerodynamic basis of insect flight," Science, Vol. 284, 1999, pp. 1954-1960.

[8] Jones K. D., Dohring, C. M., and Platzer, M. F., "Experimental and computational investigation of the Knoller-Betz effect," AIAA J., Vol. 36, No.7, 1998, pp. 1240-1246.

[9] Platzer, M. F., Jones, K. D., Young, J. and Lai, J. C. S., "Flapping-wing aerodynamics: progress and challenges," AIAA J., Vol. 46, No.9, 2008, pp. 2136-2149.

[10] Ashraf, M.A., Yong, J., and Lai J.C.S., "Reynolds number, thickness and camber effects on flapping airfoil propulsion," Journal of Fluids and Structures, Vol. 27, 2011, pp145-160.

[11] Wang, Z. J., "Vortex shedding and frequency selection in flapping flight," J. Fluid Mech. Vol.410, 2000, pp.323-341.

[12] Lewin, G. C., and Haj-Hariri, H., "Modeling thrust generation of a two-dimensional heaving airfoil in a viscous flow," J. Fluid Mech., Vol.492, 2003, pp.339-362.

[13] Shyy, W., Lian, Y., Tang, J., Viieru, D., and Liu, H., "Aerodynamics of Low Reynolds Number Flyers," Cambridge University Press, 2008.

[14] Hu, H., Clemons L., and Igarashi, H., "An Experimental Study of the Unsteady Vortex Structures in the Wake of a Root-Fixed Flapping Wing," *Experiments in Fluids,* Vol.51, No.2, 2011, pp347–359.

[15] Yu M. L., Wang, Z. J., and Hu, H., "A high-order spectral difference method for unstructured dynamic grids," Computers and Fluids, Vol. 48, 2011, pp. 84-97.
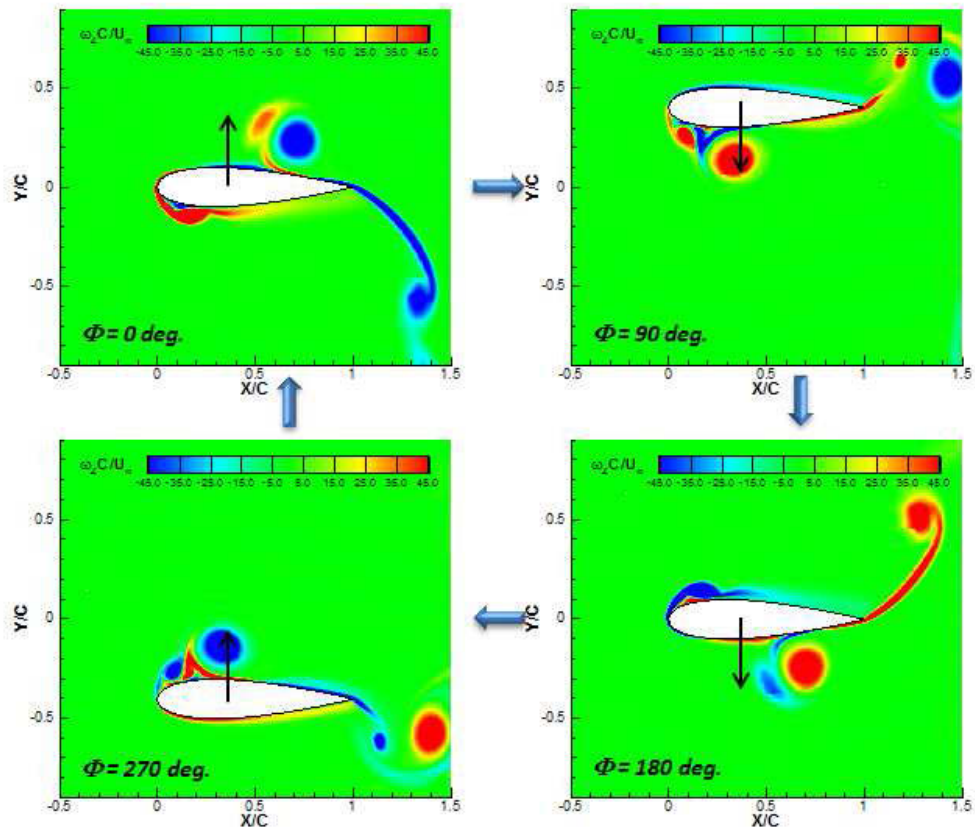
**Fig. 1.** Evolution of the unsteady vortex structures around NACA0020 airfoil in a plunging cycle.
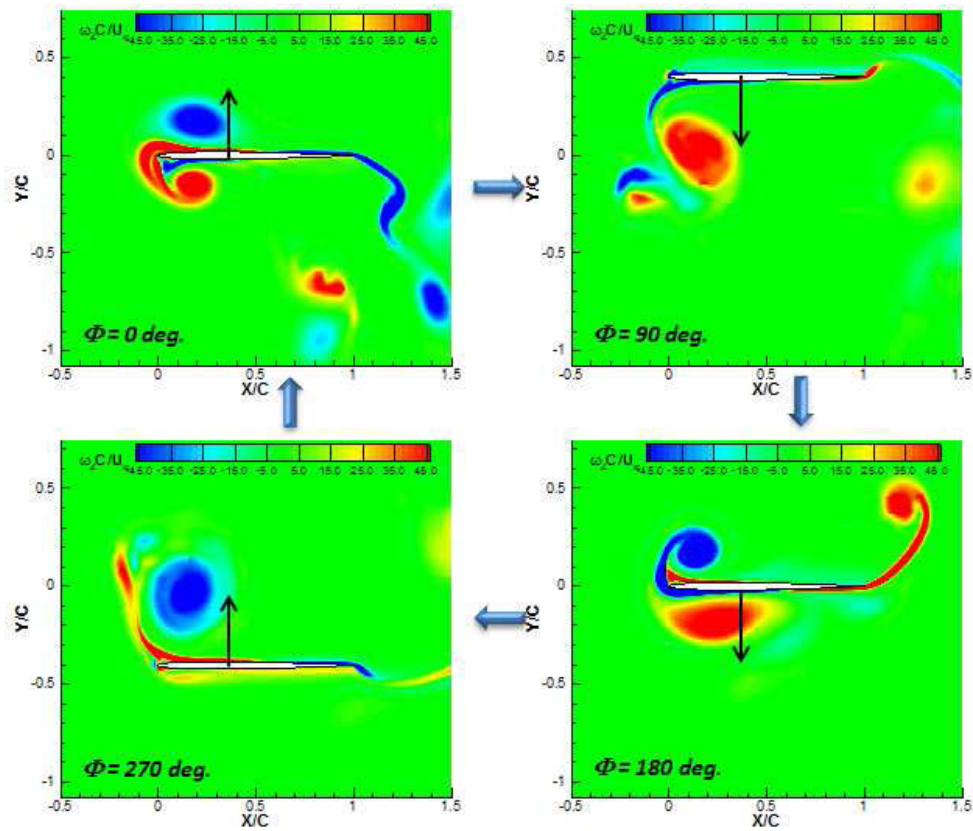
**Fig. 2.** Evolution of the unsteady vortex structures around NACA0004 airfoil in a plunging cycle.
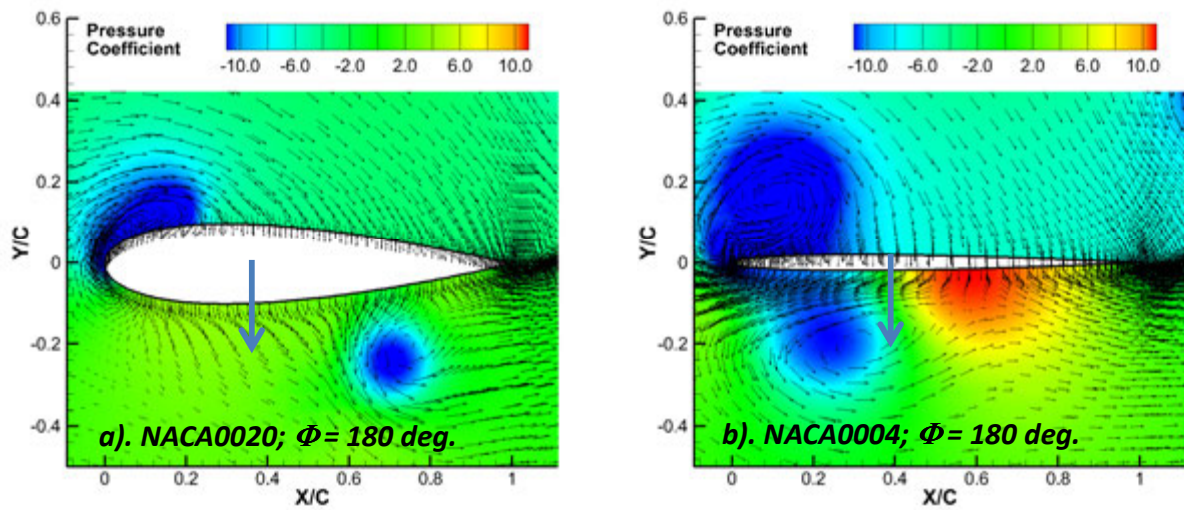
**Fig. 3**: Comparison of the pressure distributions and velocity fields around NACA0020 and NACA0004 airfoils at the phase angle of Φ = 180 deg. in the plunging motion.
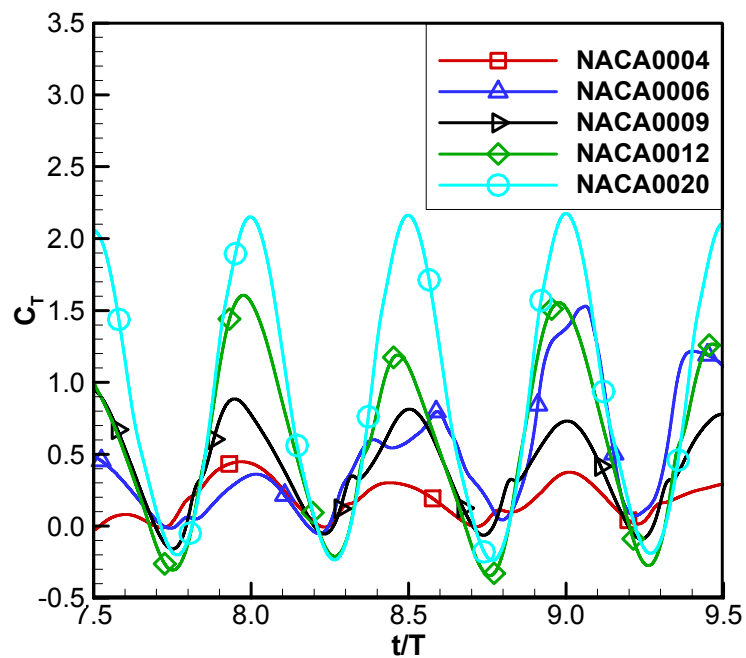


**Fig. 4.** Histories of the thrust coefficients of the NACA symmetrical airfoils in plunging motion.
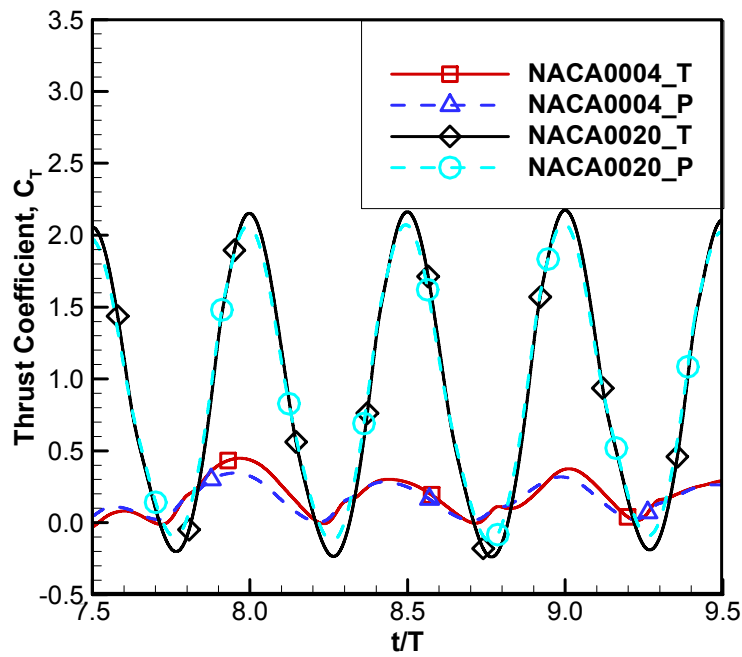
**Fig. 5**. Comparison of the total thrust coefficients of the plunging airfoils and the contributions from pressure force only.

**Table 1:** Averaged total thrust coefficients $< C_T >$ and the contributions from the pressure force $< C_{T\_P} >$ and viscous force $< C_{T\_v} >$

| Airfoil | $< C_T >$ | $< C_{T\_P} >$ | $<C_{T\_V} >$ | $<C_{T-V}>/< C_T >$ |
|---------|-----------|----------------|---------------|---------------------|
| **NACA0004** | 0.261 | 0.208 | 0.053 | 20.5% |
| **NACA0006** | 0.384 | 0.332 | 0.052 | 13.6% |
| **NACA0009** | 0.410 | 0.421 | -0.011 | -2.6% |
| **NACA0012** | 0.573 | 0.584 | -0.011 | -1.9% |
| **NACA0020** | 0.920 | 0.937 | -0.017 | -1.9% |

# CHAPTER 5. A High-Fidelity Numerical Study of Kinematics and Airfoil Thickness Effects on the Thrust Generation of Oscillating Airfoils

A paper published in the 42nd AIAA Fluid Dynamics Conference and Exhibit

Meilin Yu, Z. J. Wang and Hui Hu

## Abstract

High-fidelity numerical simulations with the spectral different (SD) method are performed to investigate the flow over a series of oscillating NACA 4-digit airfoils. Kinematics and airfoil thickness effects on the aerodynamic performances are highlighted. It is found that the combined plunging and pitching motion can outperform the pure plunging or pitching motions by sophisticatedly adjusting the airfoil gestures during the oscillation stroke. Also, the leading edge vortices (LEVs) manipulation during the gesture adjustment will vary with the airfoil thickness. The thin airfoil (NACA0006) better manipulates LEVs than the thick airfoil (NACA0030) does in our cases, and there exists an optimal thickness for large thrust generation with reasonable propulsive efficiency. At the same Strouhal number (0.3), the trends of the airfoil thickness effects on the thrust generation and propulsive efficiency are similar for the investigated reduced frequencies, namely 1 and 3.5. For all airfoil thicknesses, relatively low reduced frequency is conducive to the thrust production and propulsive efficiency. As the Strouhal number increases to 0.45, larger thrust can be generated with the same kinematics, but the propulsive efficiency will suffer if the kinematics is not optimal for the chosen aerodynamic parameters.

## Nomenclature

| | |
|---|---|
| $AOA$ | = angle of attack |
| $a$ | = speed of sound |
| $C_P$ | = pressure coefficient, $(p - p_\infty)/(0.5\rho U_\infty^2)$ |
| $C_p$ | = specific heat at constant pressure |
| $\langle C_{power} \rangle$ | = time averaged power coefficient, |

$$-\frac{1}{T}\int_{t_0}^{t_0+T}\left[Lift(t)\dot{y}(t) + Moment(t)\dot{\theta}(t)\right]dt/(0.5\rho U_\infty^3 C)$$

$C_T$      = thrust coefficient, $Thrust/(0.5\rho U_\infty^2 C)$

$\langle C_T \rangle$      = time averaged thrust coefficient, $\frac{1}{T}\int_{t_0}^{t_0+T} C_T(t)dt$

$\langle C_{T\_P} \rangle$      = time averaged thrust coefficient calculated from the pressure force

$\langle C_{T\_v} \rangle$      = time averaged thrust coefficient calculated from the viscous force

$C$      = chord length

$E$      = total energy

$F, G$      = vectors of fluxes in the physical domain

$\tilde{F}, \tilde{G}$      = vectors of fluxes in the computational domain

$f$      = oscillation frequency

$H_0$      = plunging amplitude

$i, j$      = index of coordinates in x, y direction

$J$      = Jacobian matrix

$k$      = reduced frequency, $2\pi f C/U_\infty$

$Ma$      = Mach number

$Ma_\infty$      = Mach number of the free stream

$\dot{m}$      = mass flow rate

$n_x, n_y$      = face normal components in $x$, $y$ direction, respectively

$Pr$      = Prandtl number

$p$      = pressure

$p_\infty$      = pressure of the free stream

$Q, \tilde{Q}$      = vectors of conservative variables in the physical and computational domains

$Re$      = Reynolds number based on the chord length, $\rho U_\infty C/\mu$

$Str$      = Strouhal number, $2fH_0/U_\infty$

$t, \tau$      = time in the physical and computational domain

$u, v$      = non-dimensional velocities in $x$, $y$ direction

$\vec{v}_g$      = grid velocity

$x, y$      = non-dimensional Cartesian coordinates in the physical domain

$x_\tau, x_\xi, x_\eta,$      = metrics coefficients of the time-dependent coordinate transformation

$y_\tau, y_\xi, y_\eta$

| | |
|---|---|
| $\gamma$ | = ratio of specific heats |
| $\langle \Delta p \rangle$ | = averaged pressure differences in the streamwise direction, |
| | $\int_{\partial \Omega} p\,dS \Big/ \text{(Frontal Area)}$ |
| $\eta_{power}$ | = propulsive efficiency, $\langle C_T \rangle / \langle C_{Power} \rangle$ |
| $\theta$ | = pitching angle of the airfoil |
| $\theta_0$ | = pitching amplitude |
| $\mu$ | = dynamic viscosity |
| $\xi, \eta$ | = Cartesian coordinates in the computational domain |
| $\rho$ | = density |
| $\tau_{ij}$ | = viscous stress tensors, $i, j$ can be $x$ or $y$ |
| $\phi$ | = phase lag between pitching and plunging motions |

## 1. Introduction

Unsteady flapping-wing aerodynamics has witnessed great prosperity in the last three decades. This prosperity is not only attributed to the human being's continuous curiosity on the effective propulsion exhibited by fascinating nature flyers, but also is due to the increasing interest in the design of Micro Air Vehicles (MAVs), which have been considered to have the potential to open up new opportunities for surveillance-like missions and to revolutionize the sensing and information gathering technologies in the near future. A large amount of experimental and computational research has been conducted on flapping-wing related topics and many comprehensive reviews and book chapters [1, 2, 3, 4, 5, 6, 7, 8] have systematically summarized these works from different aspects. Although great progress has been made on the unsteady flapping-wing aerodynamics due to the appearance of advanced flow diagnostic technologies and the development of high-fidelity computational fluid dynamics (CFD), a more thorough understanding which can reliably guide the design and control of MAVs suitable for different environmental surroundings is still needed.

It is well known that flapping motions can effectively generate thrust at low Reynolds and Mach numbers. The explanation for the thrust generation with oscillating airfoils was given

by Knoller [9] and Betz [10] independently based on the inviscid assumption and the effective angle of attack (AOA) concept. This was experimentally confirmed by Katzmayr [11] through mounting a stationary wing in an oscillating flow. After that, von Karman and Burgers [12] showed a thought-provoking way to explain the thrust or drag production by checking momentum surfeit or deficit in the wake based on the wake vortices orientation and location. This has gradually become a qualitative principle to judge whether an oscillating mechanism generate thrust or drag. Moreover, some interesting wake vortices phenomena have been discovered and studied by many researchers and their impact on the aerodynamic performance of the oscillating foils/wings have been discussed. Freymuth [13] experimentally documented the vortex street of the thrust-indicative type for pure plunging or pitching motion of NACA0015 airfoil. Koochesfahani [14] found that the wake pattern after a pitching airfoil can be controlled by adjusting the pitching frequency, amplitude and the shape of the oscillation wave. After that, Triantafyllou *et al*. [15] found that the optimal thrust development in oscillating foils can occur at Strouhal number ranging from 0.25 to 0.35 by performing stability analyses of measured average velocity profiles. Jones *et al*. [16] used the water-tunnel experiments and inviscid flow simulations to study the evolution of wake structures behind a plunging airfoil. A comprehensive classification of wake types was summarized in their results. Lai and Platzer [17] further studied the jet characteristics behind a plunging NACA0012 airfoil with the dye flow visualization and laser Doppler velocimetry (LDV) measurements. Wang [18] confirmed that the optimal flapping was closely related to the interaction between leading edge vortices (LEVs) and trailing edge vortices (TEVs) for the pure plunging motion. Lewin and Haj-Hariri [19] numerically classified the wake patterns behind a plunging airfoil and discussed the LEVs' effects on the wake pattern and propulsive efficiency. Young and Lai [20] studied different types of wake structures behind a plunging airfoil and the associated aerodynamic forces. They found that the aerodynamic forces relied more on the dynamic behaviors of LEVs while the wake structures were mainly controlled by the TEVs. Recently, Schnipper *et al*. [21] performed a systematic study on the wake patterns behind a pitching foil in the vicinity of the drag-thrust transition region in order to reveal the connection between wake structures and aerodynamic force generation. As a continuation of previous work, Bohl and Koochesfahani [22] studied the wake structures

behind a sinusoidally pitching NACA0020 airfoil of various reduced frequencies using molecular tagging velocimetry (MTV).

All the aforementioned studies on wake structures are tied to simple airfoil kinematics, namely pure plunging or pitching motions, and relatively large airfoil thickness ratio. As reported by many researchers, a combined plunging and pitching motion is a more elaborate modeling of the flapping wing kinematics. Jones and Platzer [23] argued that the combined plunging and pitching motion could adjust the effective angle of attack (AOA) of the airfoil, enhancing the thrust generation or power extraction performance. Anderson et al. [24] experimentally examined the propulsive performance of a NACA0012 airfoil with a combined plunging and pitching motion, and showed the parameters for optimal thrust production. Isogai et al. [25] concluded from their results of a NACA0012 airfoil undergoing combined pitching and plunging motion that a high propulsive efficiency could be obtained when pitching lead plunging by 90 degrees and no apparent leading edge separation appears. Similarly, Tuncer and Platzer [26] found that high propulsive efficiency came with an attached flow over the full period of the oscillatory cycle for a NACA0012 airfoil. Note that in both cases the free stream Mach number was 0.3, which may be a bit large for the flapping wing simulations. Ramamurti and Sandberg [27] used a finite element incompressible flow solver to study an oscillating NACA0012 airfoil and invesigated the effect of the phase difference between pitching and plunging motions on the thrust generation and propulsive efficiency. Kang et al. [28] used a Reynolds-Averaged Navier-Stokes (RANS) approach to study the flow over an oscillating SD7003 airfoil, and discussed the effects of turbulence model on the prediction of flow features.

There is a growing awareness in this community that the airfoil thickness can affect thrust generation and propulsive efficiency. Lentink and Gerritsma [29] compared the performances of several plunging airfoils with different thickness at Reynolds number 150, and concluded that airfoils with larger thickness could generate greater thrust than the airfoils with small thickness. An et al. [30] found that thickness ratio was a crucial parameter for thrust production and their results indicated that there existed an optimal thickness ratio for the thrust generation at Reynolds number 185. Ashraf et al. [31] systematically studied the thickness effects on the propulsive performances of flapping airfoils at different Reynolds

numbers ranging from 200 to $2 \times 10^6$. They found that for low Reynolds numbers, thin airfoils outperformed thick airfoils, while for high Reynolds numbers there existed an optimal thickness for the thrust production and propulsive efficiency. These results were different from Cebeci et al.'s [32] conclusion based on an unsteady panel code simulation that thickness had a negligible effect on the propulsive efficiency. This might be due to the fact that the inviscid analysis could not handle the dynamic behaviors of LEVs, which play a vital role in the aerodynamic performance evaluation.

Numerical simulations continue to be a powerful tool in the flapping-wing community. Moreover, high order CFD methods appear to be more accurate than their low order counterparts for simulations of vortex-dominated flow [33]. Some recent work on the numerical simulations of bio-inspired flow with high-order methods has provided impressive results for the community and demonstrated the potential of the high-order numerical simulation in unsteady flapping-wing aerodynamics. Visbal et al. [34, 35] successfully utilized a high-order method (a compact finite-difference approach) to simulate the flow field around a SD7003 airfoil. Persson et al. [36] developed a dynamic Discontinuous Galerkin (DG) method for a finite-span wing simulation and compared the results with other numerical methods. Liang et al. [37] used a 2D spectral difference (SD) method for a plunging NACA0012 airfoil simulation. Several applications for 2D and 3D SD method in the bio-inspired flow have been reported by Yu et al. [38].Their results demonstrated the effectiveness of the dynamic unstructured grid based SD method for some challenging bio-inspired flow simulations. Ou et al. [39] recently developed a 3D SD solver for the finite-span flapping wing simulations. Results from their research showed the potential of using high order methods as an efficient tool for the full scale flapping wing aerodynamics studies.

Although all nature flyers use complex 3D wing kinematics in the flapping flight, some intrinsic principles of unsteady aerodynamics do fall into the 2D frameworks and understanding these basic physics can help researchers make progress on the study of the 3D flapping-wing aerodynamics. Therefore, this study is restricted to 2D flapping-wing simulations and possible 3D work will be presented in future publications. The remainder of this paper is organized as follows. In Section II, the dynamic unstructured grid based SD method is introduced. The implementation of the AUSM[+]-up Riemann solver [40] for all

speeds is then introduced and the simulation parameters are presented at the end of this section. Numerical results are displayed and discussed in section III. Section IV briefly concludes this work.

## 2. Numerical Method and Simulation Parameters

### 2.1 Governing Equations

Numerical simulations are performed with an unsteady compressible Navier-Stokes (N-S) solver using dynamic unstructured grid based high-order SD method developed in [38, 41]. The 2D unsteady compressible N-S equations in conservation form read,

$$\frac{\partial Q}{\partial t} + \frac{\partial F}{\partial x} + \frac{\partial G}{\partial y} = 0. \tag{1}$$

Herein, $Q = (\rho, \rho u, \rho v, E)^T$ are the conservative variables, and $F, G$ are the total fluxes including both the inviscid and viscous flux vectors, i.e., $F = F^i - F^v$ and $G = G^i - G^v$, which takes the following form

$$F^i = \left\{ \begin{array}{c} \rho u \\ p + \rho u^2 \\ \rho uv \\ u(E + p) \end{array} \right\}, \; G^i = \left\{ \begin{array}{c} \rho v \\ \rho uv \\ p + \rho v^2 \\ v(E + p) \end{array} \right\},$$

$$F^v = \left\{ \begin{array}{c} 0 \\ \tau_{xx} \\ \tau_{yx} \\ u\tau_{xx} + v\tau_{yx} + \frac{\mu C_p}{Pr} T_x \end{array} \right\}, \; G^v = \left\{ \begin{array}{c} 0 \\ \tau_{xy} \\ \tau_{yy} \\ u\tau_{xy} + v\tau_{yy} + \frac{\mu C_p}{Pr} T_y \end{array} \right\} \tag{2}$$

In Eq. (2), $\rho$ is the fluid density, $u$ and $v$ are the Cartesian velocity components, $p$ is the pressure, and $E$ is the total energy, $\mu$ is dynamic viscosity, $C_p$ is the specific heat at constant pressure, $Pr$ is the Prandtl number, and $T$ is the temperature. The stress tensors in Eq. (2) take the following form

$$\tau_{xx} = 2\mu \left( u_x - \frac{u_x + v_y}{3} \right), \tau_{yy} = 2\mu \left( v_y - \frac{u_x + v_y}{3} \right), \tau_{xy} = \tau_{yx} = \mu(v_x + u_y) \tag{3}$$

On assuming that the perfect gas law is obeyed, the pressure is related to the total initial energy by $E = \frac{p}{\gamma - 1} + \frac{1}{2}\rho(u^2 + v^2)$ with constant γ, which closes the solution system.

To achieve an efficient implementation, a time-dependent coordinate transformation from the physical domain $(t, x, y)$ to the computational domain $(\tau, \xi, \eta)$, as shown in Fig. 1. (a), is applied to Eq. (1). And we obtain

$$\frac{\partial \tilde{Q}}{\partial \tau} + \frac{\partial \tilde{F}}{\partial x} + \frac{\partial \tilde{G}}{\partial y} = 0, \tag{4}$$

where

$$\begin{cases} \tilde{Q} = |J|Q \\ \tilde{F} = |J|\left(Q\xi_\tau + F\xi_x + G\xi_y\right). \\ \tilde{G} = |J|\left(Q\eta_\tau + F\eta_x + G\eta_y\right) \end{cases} \tag{5}$$

Herein, $\tau = t$ and $(\xi, \eta) \in [-1,1]^2$, are the local coordinates in the computational domain. In the transformation shown above, the Jacobian matrix $J$ takes the following form

$$J = \frac{\partial(x, y, t)}{\partial(\xi, \eta, \tau)} = \begin{pmatrix} x_\xi & x_\eta & x_\tau \\ y_\xi & y_\eta & y_\tau \\ 0 & 0 & 1 \end{pmatrix}. \tag{6}$$

Note that the grid velocity $\vec{v_g} = (x_t, y_t)$ is related with $(\xi_\tau, \eta_\tau)$ by

$$\begin{cases} \xi_\tau = -\vec{v_g} \cdot \nabla\xi \\ \eta_\tau = -\vec{v_g} \cdot \nabla\eta \end{cases}. \tag{7}$$

## 2.2 Space Discretization

The SD method is used for the space discretization. In the SD method, two sets of points are given, namely the solution and flux points, as shown in Fig. 1. (b). Conservative variables are defined at the solution points (SPs), and then interpolated to flux points to calculate local fluxes. In this study, the solution points are chosen as the Chebyshev-Gauss quadrature points. It has been proved in [42] that the adoption of the Legendre-Gauss quadrature points as the flux points can ensure the stability of the SD method. Therefore, the flux points are selected to be the Legendre-Gauss points with end points as -1 and 1.

Then using Lagrange polynomials, we reconstruct all the fluxes at the flux points. It is worth to point out that this reconstruction is continuous within a standard element, but discontinuous on the cell interfaces. Therefore, for the inviscid flux, a Riemann solver is

necessary to reconstruct a common flux on the interface. For a moving boundary problem, since the eigenvalues of the Euler equations are different from those for a fixed boundary problem by the grid velocity, the design of the Riemann solver should consider the grid velocity. Furthermore, since the flow regime for flapping flight is almost incompressible and the present governing equations are compressible N-S equations, the Riemann solver should provide good performance at low Mach numbers. The AUSM$^+$-up Riemann solver [40] for all speed is selected for the present simulation and is proved to behave well at low Mach numbers. The procedure to reconstruct the common fluxes for the AUSM$^+$-up Riemann solver can be specified as follows.

Denote the face normal of arbitrary interface as $\vec{n}$. Then the interface mass flow rate $\dot{m}_{1/2}$ reads

$$\dot{m}_{1/2} = a_{1/2} Ma_{1/2} \begin{cases} \rho_L & if\ Ma_{1/2} > 0 \\ \rho_R & otherwise \end{cases}, \tag{8}$$

where the subscript '1/2' stands for the interface, $a$ and $Ma$ are speed of sound and Mach number respectively. Note that the grid velocity has been included in the interface Mach number $Ma$. The numerical normal fluxes $\tilde{F}^i$ and $\tilde{G}^i$ can then be specified as

$$\begin{cases} \tilde{F}^i = \left( \dot{m}_{1/2} \begin{cases} \psi_L & if\ \dot{m}_{1/2} > 0 \\ \psi_R & otherwise \end{cases} + P_{1/2} \right) |J| |\nabla \xi| sign(\vec{n} \cdot \nabla \xi) \\ \tilde{G}^i = \left( \dot{m}_{1/2} \begin{cases} \psi_L & if\ \dot{m}_{1/2} > 0 \\ \psi_R & otherwise \end{cases} + P_{1/2} \right) |J| |\nabla \eta| sign(\vec{n} \cdot \nabla \eta) \end{cases} \tag{9}$$

where $\psi = (1, u, v, (E+p)/\rho)^T$, $P = \left(0, pn_x, pn_y, pv_{g,n}\right)^T$, with $n_x$, $n_y$ and $v_{g,n}$ specifying the face normal components in $x$ and $y$ direction and the grid velocity in the face normal direction respectively. Note that in the implementation of the dynamic grid based Riemann solver, the last term of the flux needs to be corrected by $v_{gn}p_{L/R}$ times by the corresponding metrics, where $v_{gn} = x_t n_x + y_t n_y$ is the surface grid velocity and $p_{L/R}$ is the surface pressure. The superscript '$i$' indicates the inviscid flux and the subscripts '$L$' and '$R$' denote the left and right states on the cell interface. The reconstruction of the viscous flux is based on the average of the 'left' and 'right' fluxes. The detailed reconstruction procedures can be found in [41].

### 2.3 Simulation Parameters

In this study, the kinematics of the airfoil is specified as follows.

$$\text{Plunging motion: } y = H_0 sin(2\pi ft);$$

$$\text{Pitching motion: } \theta = \theta_0 sin(2\pi ft + \phi).$$

Herein, $y$ and $\theta$ are the plunging displacement and pitching angle of the airfoil respectively, $C$ is the chord length of the airfoil, and $H_0$ is the plunging amplitude, $f$ is the oscillation frequency, $\theta_0$ is the pitching amplitude, and $\phi$ is the phase lag between pitching and plunging motions. In view of the optimal thrust generation conditions suggested in [24], the pivot point for the pitching motion is located at the one-third chord length from the leading edge and $\phi$ is fixed at $75^o$. The sketch of the airfoil kinematics is displayed in Fig. 2.

The aerodynamic parameters are specified as follows. The Reynolds number ($Re$) based on the airfoil chord length and the free stream velocity is $Re = \rho U_\infty C/\mu = 1,200$, well within the insect flight regime. According to the optimal Strouhal number suggested in [15], the Strouhal number $Str$ (a measure of the characteristic velocity of the object with respect to the free stream velocity) based on the plunging amplitude $H_0$ is chosen as 0.3. The reduced frequency $k$ (a measure of flapping frequency with respect to the intrinsic frequency of the flow over the airfoil) is assigned as 3.5 or 1.0. As reported by many researchers, the inlet Mach number $Ma_\infty$ is crucial for the aerodynamic performance of a flapping wing if a compressible solver is adopted for the simulation. In the present study, $Ma_\infty$ is set to be 0.05, which is in accordance with the value specified in [20].

## 3. Results and Discussions

The performance of the developed solver for low Mach number flow is firstly tested by computing the steady inviscid flow over a NACA0012 airfoil at $Ma_\infty = 0.05$ and zero angle of attack (AOA) with a $3^{rd}$ order accurate scheme and an implicit LU-SGS time integration [38] on a coarse mesh. The residual convergence history, pressure coefficient ($C_P$) contour, and the Mach number ($Ma$) contour are displayed in Fig. 3. (a)-(c) respectively. Then a steady viscous flow over the NACA0012 airfoil at $Re = 5,000$, $Ma_\infty = 0.05$ and zero AOA is simulated with the same scheme on the same mesh. The residual convergence history, pressure coefficient ($C_p$) contour, and the Mach number contour ($Ma$) are displayed in Fig. 3.

(d)-(f) respectively. From Fig. 3 it is obvious that both the Euler and N-S solvers work well at low Mach number as no oscillation of the flow field is observed. Then H-refinement (grid refinement) and p-refinement studies are conducted to determine the suitable grid and numerical accuracy for the present study. The time histories of the thrust for the oscillating NACA0006 airfoil with the combined plunging and pitching motions at $Str = 0.3, k = 3.5$ are shown in Fig. 4. It is found that the time histories of thrust coefficient $C_T$ for the 3rd order scheme with both coarse and fine grids and the 4th order scheme with the coarse grid agree well with each other, while for the 2nd order scheme with the coarse mesh, the curve shows marked deviation. Based on these observations, a 3rd order accurate scheme with a coarse mesh is chosen.

### 3.1 Thickness Effects with Different Kinematics

Three kinds of oscillation motions are studies, namely the pure plunging motion, the pure pitching motion and the combined plunging and pitching motion. The time histories of the thrust coefficient for NACA0006 and NACA0030 with different oscillation motions at $Str = 0.3, k = 1$ are displayed in Fig. 5. Note that here the combined motion is a linear superposition of the plunging and pitching motions as stated in Section II.C. But from Fig. 5, it is clear that the aerodynamic force generated from the combined motion is not the linear superposition of the aerodynamic forces generated from the plunging and pitching motion. This is also confirmed by the time averaged thrust coefficients as shown in Table 1. This can be attributed to the nonlinear effects of the unsteady vortex flow. Specifically, from both the instantaneous and time averaged thrust coefficients it is found that both airfoils only generate drag when pure pitching motion is adopted. This infers that the pitching motion is not powerful enough to generate thrust in present cases. Instead, the plunging motion plays a major role in generating thrust. However, for pure plunging motion the averaged thrust generated by both airfoils, especially NACA0006, appears to be small, as shown in Table 1. Before moving forward, we introduce the concept of 'frontal area', which is defined as the projection of the airfoil in the free stream direction as shown in Fig. 2. Obviously, when the airfoil is parallel to the free stream, the frontal area is nothing but the airfoil thickness. From Table 1 we find that the drastic change in the thrust coefficient from the pure plunging

motion to the combined motion is mainly due to the change in pressure force. This can be explained as follows. When a suitable pitching motion is added to the plunging motion, the frontal area can be effectively adjusted to enhance the thrust generation from pressure force. Thus, the performance in terms of thrust generation is significantly improved with the combined flapping motion.

The above discussions can be further verified by examining the flow fields. The instantaneous vorticity and pressure fields for NACA0006 with different oscillation motions are shown in Fig. 6 and 7; while those for NACA0030 are shown in Fig. 8 and 9. The flow visualizations are extracted at four different phases, namely $0$, $\pi/2$, $\pi$ and $3\pi/2$, based on the plunging cycle. From the comparisons of the flow fields with different kinematics for a certain airfoil, it is clear that at phases $0$ and $\pi$, with the combined motion, the pitching motion can adjust the gesture of the plunging airfoil to better maneuver the LEVs and meanwhile provide a larger frontal area to enhance the pressure force contribution on the thrust generation. Note that as the kinematics is not optimized here, the combined motion does not entirely eliminate the formation of the LEVs. And the propulsive efficiency might not have reached the maximum value in the studied cases.

By comparing the time histories of the thrust coefficient in Fig. 5 and time averaged thrust coefficients in Table 1, it is found that NACA0006 can generate larger thrust than NACA0030 under the combined motion. But for the pure plunging motion, NACA0030 outperforms NACA0006. It seems that the pitching motion did not help significantly enhance the aerodynamic performance of the plunging NACA0030 airfoil, but it extensively increases the thrust generation of NACA0006. The inferior performance of the NACA0006 airfoil with pure plunging motion can be attributed to the small frontal area. Specifically, if we assume that the averaged pressure differences $\langle \Delta p \rangle$ in the streamwise direction are the same for both NACA0006 and NACA0030 airfoils, the time averaged pressure dominated thrust coefficient $\langle C_{T\_P} \rangle$ of NACA0030 should be five times (the ratio beween the thicknesses of the NACA0030 and NACA0006 airfoils) of that of NACA0006. However, from the results it is observed that the time averaged pressure dominated thrust coefficient $\langle C_{T\_P} \rangle$ of the NACA0030 airfoil is only twice, but not five times of that of the NACA0006 airfoil. This is largely due to the performance degradation of the NACA0030 airfoil. As can be observed

from Fig. 8 (i) and (k), at phases 0 and $\pi$, the LEVs are almost entirely located in the rearward part of the airfoil. This will induce a low pressure region there and hinder the thrust generation.

The reason that the pitching motion does not intensively enhance the thrust generation of the plunging NACA0030 airfoil can be given as follows. On examining Fig. 8. (a) and (c), it is observed that although the pitching motion helps enlarge the frontal area of the plunging NACA0030 airfoil at phases 0 and $\pi$, e.g. $t/T = 3$ and 3.5 in Fig. 5. (b), the LEVs is still located in the rearward part of the airfoil. This vortex configuration does not contribute much to the thrust generation. Moreover, at phases $\pi/2$ and $3\pi/2$, e.g. $t/T = 3.25$ and 3.75, the airfoil with the combined motion experiences larger drag peak than that with the plunging motion as displayed in Fig. 5. (b). This is due to the interaction between the propagating LEVs and the forming TEVs during the plunging stroke. Specifically, in the combined motion, parts of the TEVs are trapped on the trailing edge as shown in Fig. 8. (b) and (d), inducing a low pressure region there as shown in Fig. 9. (b) and (d). However, in the plunging motion, the TEVs are not trapped on the trailing edge, as displayed in Fig. 8. (j) and (l). Thus there does not exist a low pressure region in the rearward part of the airfoil.

The better performance of the NACA0006 airfoil with the combined motion can be attributed to the LEVs dynamics as well. From Figs. 6 and 7, it is observed that for the NACA0006 airfoil the pitching motion can better control the LEVs and ensure that the low pressure region is located in the forward part of the airfoil at phases 0 and $\pi$, and no low pressure region is located in the rearward part of the airfoil at phases $\pi/2$ and $3\pi/2$. From Fig. 5. (a), it is found that in contrast to NACA0030, the NACA0006 airfoil with the combined motion does not experience larger drag peak than that with the plunging motion. This is due to the fact that no TEVs are trapped on the trailing edge for both the combined and plunging motions.

### 3.2 Thickness Effects at Different Reduced Frequencies and Strouhal Numbers

As aforementioned, a suitable combined motion can enhance the aerodynamic performances of the oscillating airfoil. In this section, the kinematics of the airfoils is chosen as a combined motion with the pitching motion leading the plunging motion by $75^o$. The

thickness effects with different reduced frequencies but the same Strouhal number are compared at first. The flow fields, namely the spanwise vorticity fields and the corresponding pressure fields of NACA0020 at $Str = 0.3$ and $k = 1$ are displayed in Fig. 10. Note that the flow fields of NACA0012 are similar to those of NACA0006, and are not shown for conciseness. By comparing the flow fields of NACA0006 (Fig. 6. (a)-(d)), NACA0020 (Fig. 10. (a)-(d)) and NACA0030 (Fig. 8. (a)-(d)), it is observed that at $Str = 0.3$ and $k = 1$, as the airfoil becomes thicker, at the end of the plunging strokes, i.e. at phases $\pi/2$ and $3\pi/2$, more parts of the forming TEVs will be trapped on the trailing edge of the airfoil, inducing an low pressure region on the rearward part of the airfoil. This process results in larger drag peaks at phases $\pi/2$ and $3\pi/2$ on thicker airfoils as shown in Fig. 11. Moreover, it is also observed from the vorticity fields that as the airfoil thickness increases, the LEVs will be pushed further towards the trailing edge of the airfoil. This degrades the positive control of the pitching motion on thrust generation during the plunging motion. The pressure coefficient $C_P$ distributions on different phases are displayed in Fig. 12. From this figure it is clear that the pressure distributions on the NACA0006 and NACA0012 airfoils are similar to each other, while those on other airfoils departure from them a lot, especially on the surface with LEVs. At phases $0$ and $\pi$, it is found that a low pressure region with large suction peaks exists on the forward part of the NACA0006 or NACA0012 airfoil. But for thick airfoils, the low pressure regions with small suction pressure spread out almost over the entire surface. As aforementioned, the pressure distribution features of NACA0006 and NACA0012 are beneficial for the thrust generation, but the same is not true for NACA0020 and NACA0030. At phases $\pi/2$ and $3\pi/2$, it is observed that on the suction surfaces, thicker airfoils experience larger suction pressure, while on the pressure surfaces, thick airfoils experience excessive pressure on the forward part and wide-spread suction pressure on the rearward part. All these features dramatically increase the drag on thick airfoils at phases $\pi/2$ and $3\pi/2$.

Similar trends can be concluded for the oscillating airfoils using a combined motion at $Str = 0.3$ and $k = 3.5$. However, there exist some distinct aerodynamic features for these cases with present parameters. From the flow fields shown in Figs. 13-15, it is found that for thin airfoils, the wake vortices formed during the upstroke or downstroke consist of two vortices of the same sign. One of the vortices is from LEVs while the other is from TEVs.

For thick airfoils, only one vortex is shed during the upstroke or downstroke. However at $Str = 0.3$ and $k = 1$, the wake vortices shed during the upstroke or downstroke consist of two vortices of the opposite sign. It is also observed that the LEVs formed at the beginning of a certain cycle are shed off from the airfoil at the end of the cycle. However at $Str = 0.3$ and $k = 1$, the LEVs formed at the beginning of a certain stroke are shed off from the airfoil at the end of the stroke. Note that one stroke corresponds to half the oscillating cycle. From the surface pressure distributions displayed in Fig. 16, it is found that there exist distinct differences in pressure distributions on the forward part of airfoils with different thicknesses at phases 0 and $\pi$. But at phases $\pi/2$ and $3\pi/2$, the pressure distributions are similar for all airfoils. These features suggest that at $Str = 0.3$ and $k = 3.5$, the thrust peaks of oscillating airfoils with different thicknesses will exhibit apparent differences but the drag peaks will not be of large discrepancy. The time histories of thrust coefficients shown in Fig. 11. (b) confirm the above analyses. The differences of aerodynamic features between the cases at $k = 1$ and 3.5 are inherently related to the dynamics of LEVs as discussed before.

The propulsive efficiency and time averaged thrust coefficient $\langle C_T \rangle$ for several NACA 4-digit airfoils at $Str = 0.3, k = 1$ and 3.5 are displayed in Fig. 17. (a). Following the work in [31, 23], the propulsive efficiency is defined as

$$\eta_{Power} = \frac{\langle C_T \rangle}{\langle C_{Power} \rangle},$$

where $\langle C_{Power} \rangle$ is the time averaged power coefficient. From Fig. 17. (a), it is found that thin airfoils perform well for thrust generation and can achieve relatively high propulsive efficiency at both $k = 1$ and 3.5, $Str = 0.3$. The variation trends of the time-averaged thrust coefficient and propulsive efficiency versus the airfoil thickness are similar at $k = 1$ and 3.5. For the same airfoil thickness, both the time-averaged thrust coefficient and propulsive efficiency are larger at lower reduced frequency than that at higher reduced frequency. From the time histories of thrust coefficient for NACA0006 with different reduced frequencies shown in Fig. 17. (b), it is obvious that during one oscillating cycle, the airfoil with small reduced frequency experiences larger thrust but less drag compared with that with large reduced frequency. Also, the pressure force dominates the thrust/drag generation. In Fig. 17. (b) the variation of the frontal area normalized by its maximum value is plotted as well. It is

clear that when the frontal area reaches a maximum, the airfoil experiences a thrust peak; when the frontal area reaches a minimum, the airfoil experiences a drag peak. Thus, for thin airfoils, the flapping motion skillfully manipulates the pressure force on the airfoil to enhance the thrust generation and weaken the drag generation.

The vorticity fields around the NACA0006 airfoil at $k = 3.5, Str = 0.45$ are displayed in Fig. 18. Note that the kinematics at $Str = 0.45$ is the same as that at $Str = 0.3$. Comparing the vorticity fields with those shown in Fig. 13. (a)-(d), it is found that as the Strouhal number increases, the vortex structures of the flow field do not change much. The time histories of the thrust coefficient for the two cases at $k = 3.5, \ Str = 0.3$ and $0.45$ are shown in Fig. 19. The time averaged thrust coefficients and propulsive efficiencies are 0.249 and 27.9% at $k = 3.5, \ Str = 0.3$, and 0.779 and 24.1% at $k = 3.5, \ Str = 0.45$. In a word, the propulsive efficiency is traded off against the thrust generation.

## 4. Conclusions

A dynamic unstructured grid based high-order spectral difference compressible Navier-Stokes solver is adopted in the present study to perform high-fidelity simulations on the flow fields over several oscillating airfoils with different thickness ratios. It is found that the combined plunging and pitching motion can outperform the pure plunging and pitching motions by sophisticatedly adjusting the airfoil gestures during the oscillation stroke. However, the LEVs manipulation during the gesture adjustment will vary with the airfoil thickness ratio. For the present aerodynamic and kinematic parameters, thin airfoils outperform thick airfoils. Furthermore, at the same Strouhal number (0.3), reduced frequency can dramatically affect the aerodynamic performance because of different LEVs' behaviors associated with different reduced frequencies. The trends of the thickness effects on the thrust generation and propulsive efficiency are similar for the studied two reduced frequencies, namely 1 and 3.5. For all airfoil thicknesses, relatively low reduced frequency is conducive to the thrust production and propulsive efficiency. As the Strouhal number increases to 0.45, larger thrust can be generated with the same kinematics, but the propulsive efficiency will suffer if the kinematics is not optimal for the chosen aerodynamic parameters.

# References

[1] S. Ho, H. Nassef, N. Pornsinsirirak, Y. C. Tai and C. M. Ho, "Unsteady aerodynamics and flow control for flapping wing flyers," *Progress in Aerospace Sciences,* vol. 39, no. 8, pp. 635-681, 2003.

[2] M. F. Platzer, K. D. Jones, J. Young and J. C. S. Lai, "Flapping-wing aerodynamics: progress and challenges," *AIAA J.,* vol. 46, no. 9, pp. 2136-2149, 2008.

[3] K. V. Rozhdestvensky and V. A. Ryzhov, "Aerohydrodynamics of flapping-wing propulsors," *Progress in Aerospace Sciences,* vol. 39, no. 8, pp. 585-633, 2003.

[4] W. Shyy, H. Aono, S. Chimakurthi, P. Trizila, C. Kang, C. Cesnik and H. Liu, "Recent progress in flapping wing aerodynamics and aeroelasticity," *Progress in Aerospace Sciences,* vol. 48, no. 7, pp. 284-327, 2010.

[5] W. Shyy, M. Berg and D. Ljungqvist, "Flapping and flexible wings for biological and micro air vehicles," *Progress in Aerospace Sciences,* vol. 35, no. 5, pp. 455-505, 1999.

[6] W. Shyy, Y. Lian, J. Tang, D. Viieru and H. Liu, Aerodynamics of low Reynolds number flyers, New York: Cambridge Univ. Press, 2008.

[7] M. S. Triantaflyllou, A. H. Techet and F. S. Hover, "Review of experimental work in biomimetic foils," *IEEE Journal of Oceanic Engineering,* vol. 29, no. 3, pp. 585-594, 2004.

[8] Z. J. Wang, "Dissecting insect flight," *Annu. Rev. Fluid Mech.,* vol. 37, no. 1, pp. 183-210, 2005.

[9] R. Knoller, "Die Gesetze des Luftwiderstandes," *Flug- und Motortechnik (Wien),* vol. 3, no. 21, pp. 1-7, 1909.

[10] A. Betz, "Ein Beitrag zur Erklaerung des Segelfluges," *Zeitschrift fur Flugtechnik und Motorluftschiffahrt,* vol. 3, pp. 269-272, 1912.

[11] R. Katzmayr, "Effect of periodic changes of angle of attack on behavior of airfoils," *National Advisory Committee for Aeronautics,* 1922.

[12] T. Von Karman and J. M. Burgers, *Aerodynamic Theory: A General Review of Progress,* vol. 2, 1935.

[13] P. Freymuth, "Propulsive vortical signature of plunging and pitching airfoils," *AIAA J.,* vol. 26, pp. 881-883, 1988.

[14] M. M. Koochesfahani, "Vortical patterns in the wake of an oscillating airfoil," *AIAA J.,* vol. 27, pp. 1200-1205, 1989.

[15] G. S. Triantaflyllou, M. S. Triantaflyllou and M. A. Grosenbaugh, "Optimal thrust development in oscillating foils with application to fish propulsion," *Journal of Fluids and Structures,* vol. 7, pp. 205-224, 1993.

[16] K. D. Jones, C. M. Dohring and M. F. Platzer, "Experimental and computational investigation of the Knoller–Betz effect," *AIAA J.,* vol. 36, pp. 1240-1246, 1998.

[17] J. C. S. Lai and M. F. Platzer, "Jet characteristics of a plunging airfoil," *AIAA J.,* vol. 37, pp. 1529-1537, 1999.

[18] Z. J. Wang, "Vortex shedding and frequency selection in flapping flight," *J. Fluid Mech.,* vol. 410, pp. 323-341, 2000.

[19] G. C. Lewin and H. Haj-Hariri, "Modeling thrust generation of a two-dimensional heaving airfoil in a viscous flow," *J. Fluid Mech.,* vol. 492, pp. 339-362, 2003.

[20] J. Young and J. C. S. Lai, "Oscillation frequency and amplitude effects on the wake of a plunging airfoil," *AIAA J.,* vol. 42, pp. 2042-2052, 2004.

[21] T. Schnipper, A. Andersen and T. Bohr, "Vortex wakes of a flapping foil," *J. Fluid Mech.,* vol. 633, pp. 411-423, 2009.

[22] D. G. Bohl and M. M. Koochesfahani, "MTV measurements of the vertical field in the wake of an airfoil oscillating at high reduced frequency," *J. Fluid Mech.,* vol. 620, pp. 63-88, 2009.

[23] K. D. Jones and M. F. Platzer, "Numerical computation of flapping-wing propulsion and power extraction," in *AIAA Paper 97-0826*, 1997.

[24] J. M. Anderson, K. Streitlien, D. S. Barrett and M. S. Triantafyllou, "Oscillating foils of high propulsive efficiency," *J. Fluid Mech.,* vol. 360, pp. 41-72, 1998.

[25] K. Isogai, Y. Shinmoto and Y. Watanabe, "Effects of dynamic stall on propulsive efficiency and thrust of flapping airfoil," *AIAA J.,* vol. 37, pp. 1145-1151, 1999.

[26] I. H. Tuncer and M. F. Platzer, "Computational study of flapping airfoil aerodynamics," *Journal of Aircraft,* vol. 37, pp. 514-520, 2000.

[27] R. Ramamurti and W. Sandberg, "Simulation of flow about flapping airfoils using finite element incompressible flow solver," *AIAA J.,* vol. 39, pp. 253-260, 2001.

[28] C. K. Kang, H. Aono, P. Trizila, Y. Baik, J. M. Rausch, L. Bernal, M. V. Ol and W. Shyy, "Modeling of pitching and plunging airfoils at Reynolds number between $1\times10^4$ and $6\times10^4$," in *AIAA Paper 2009-4100*, 2009.

[29] D. Lentink and M. Gerritsma, "Influence of airfoil shape on performance in insect flight," in *AIAA Paper 2003-3447*, 2003.

[30] S. An, J. Maeng and C. Han, "Thickness effect on the thrust generation of heaving airfoils," *Journal of Aircraft,* vol. 46, pp. 216-222, 2009.

[31] M. A. Ashraf, J. Young and J. C. S. Lai, "Reynolds number, thickness and camber effects on flapping airfoil propulsion," *Journal of Fluids and Structures,* vol. 27, pp. 145-160, 2011.

[32] T. Cebeci, M. Platzer, H. Chen, K. C. Chang and J. P. Shao, Analysis of low-speed unsteady airfoil flows, Horizons Publishing Inc., 2004.

[33] Z. J. Wang, "High-order methods for the Euler and Navier Stokes equations on unstructured grids," *Progress in Aerospace Science,* vol. 43, pp. 1-41, 2007.

[34] M. R. Visbal, "High-fidelity simulation of transitional flows past a plunging airfoil," in *AIAA Paper 2009-391*, 2009.

[35] M. R. Visbal, R. E. Gordnier and M. C. Galbraith, "High fidelity simulations of moving and flexible airfoils at low Reynolds number," *Experiments in Fluids,* vol. 46, pp. 903-922, 2009.

[36] P. O. Persson, D. J. Willis and J. Peraire, "The numerical simulation of flapping wings at low Reynolds numbers," in *AIAA Paper 2010-72*, 2010.

[37] C. L. Liang, K. Ou, S. Premasuthan, A. Jameson and Z. J. Wang, "High-order accurate simulations of unsteady flow past plunging and pitching airfoils," *Computer & Fluids,* vol. 40, pp. 236-248, 2010.

[38] M. L. Yu, Z. J. Wang and H. Hu, "A high-order spectral difference method for unstructured dynamic grids," *Computer & Fluids,* vol. 48, pp. 84-97, 2011.

[39] K. Ou, P. Castonguay and A. Jameson, "3D flapping wing simulation with high order spectral difference method on deformable mesh," in *AIAA Paper 2011-1316*, 2011.

[40] M. S. Liu, "A sequel to AUSM, Part 2: AUSM+-up for all speeds," *J. Comput. Phys.,* vol. 214, pp. 137-170, 2006.

[41] Y. Z. Sun, Z. J. Wang and Y. Liu, "High-order multidomain spectral difference method for the Navier-Stokes equations on unstructured hexahedral grids," *Commun. Comput. Phys.,* vol. 2, pp.

310-333, 2006.

[42] A. Jameson, "A proof of the stability of the spectral difference method for all orders of accuracy," *J. Sci. Comput.,* vol. 45, pp. 348-358, 2010.
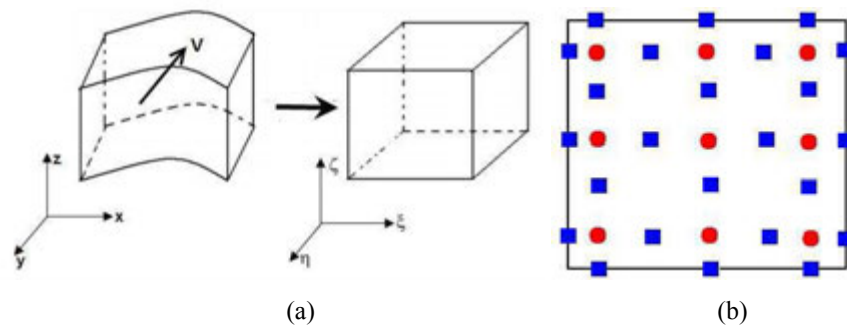
**Fig. 1.** (a) Transformation from a moving physical domain to a fixed computational domain; (b) Distribution of solution points (as denoted by circles) and flux points (as denoted by squares) in a standard quadrilateral element for a third-order SD scheme.
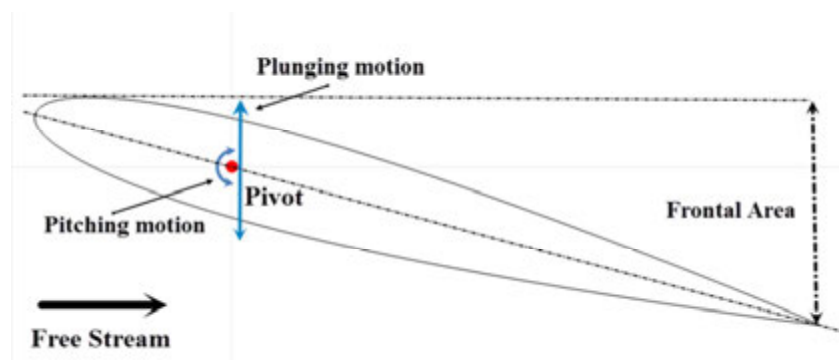


**Fig. 2.** Sketch of the kinematics of the NACA0012 airfoil.
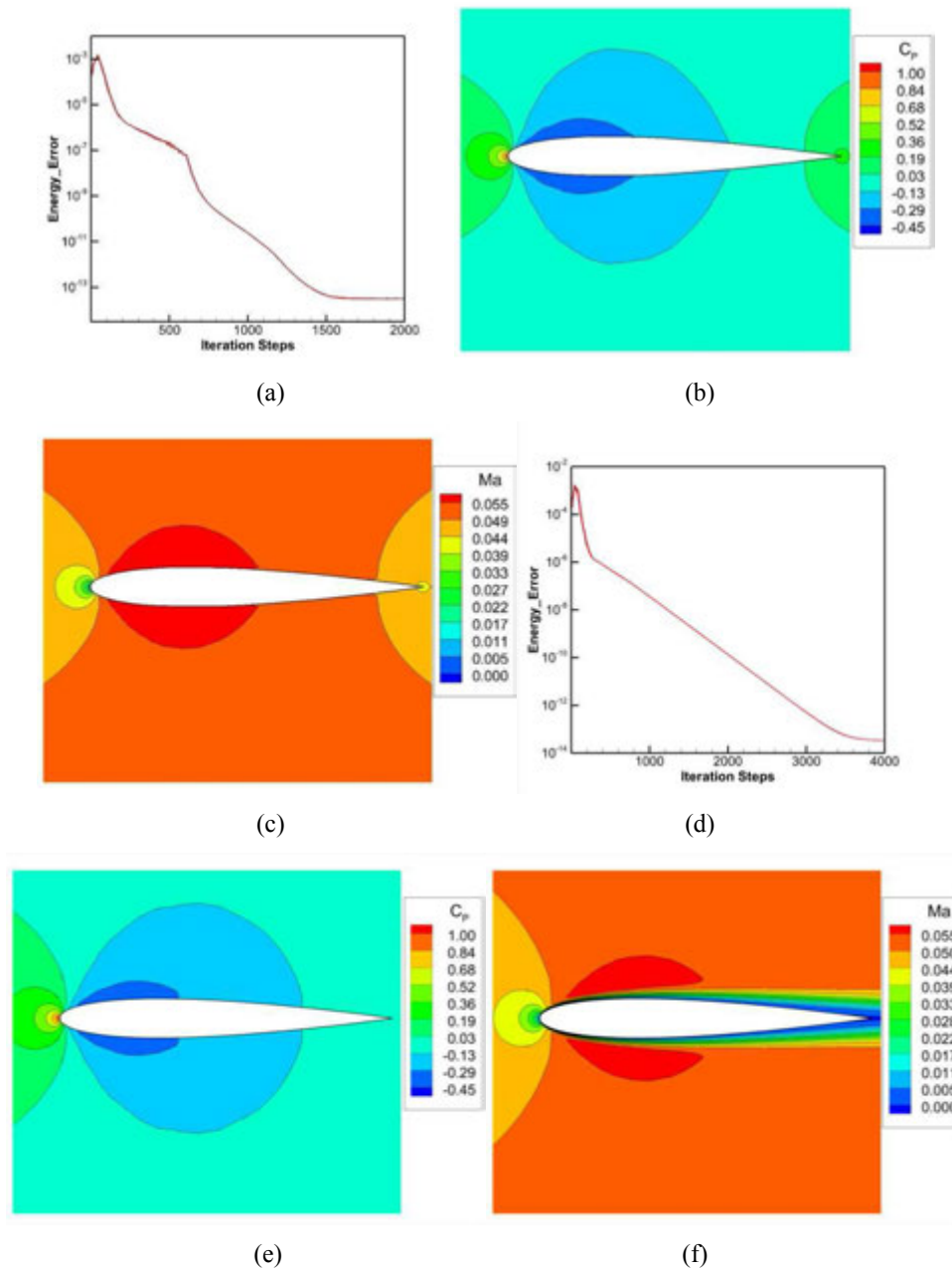
**Fig. 3.** (a) Convergence history of the energy residual for the steady solution of the inviscid flow over a stationary NACA0012 airfoil with implicit (LU-SGS) time integration at $Ma_\infty = 0.05$; (b) pressure coefficient contours for the converged steady inviscid flow; (c) Mach number contours for the converged steady inviscid flow; (d) Convergence histories of the energy residual of the steady solution of the viscous flow over a stationary NACA0012 airfoil with implicit (LU-SGS) time integration at $Re = 5,000$, $Ma_\infty = 0.05$; (e) pressure coefficient contours of the converged steady viscous flow; (f) Mach number contours of the converged steady viscous flow.
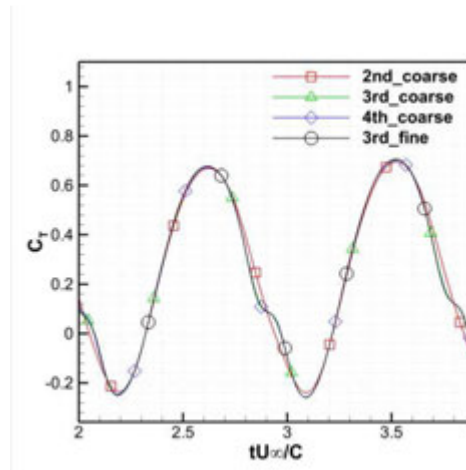
**Fig. 4.** *hp* refinement study for the flow over NACA0006 airfoil with the combined plunging and pitching motion at $Str = 0.3, k = 3.5$.



<table>
<tr><td>(a)</td><td>(b)</td></tr>
</table>
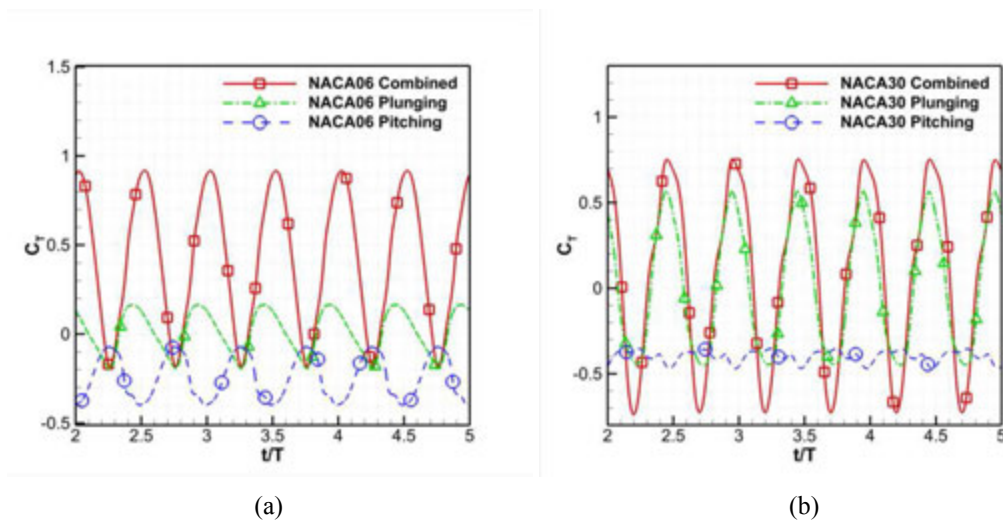
**Fig. 5.** Time histories of the thrust coefficients for the NACA0006 (a) and NACA0030 (b) airfoils with different motions at $Str = 0.3, k = 1$.

| | NACA0006 | | | NACA0030 | | |
|---|---|---|---|---|---|---|
| | Plu. | Pit. | Com. | Plu. | Pit. | Com. |
| $\langle C_T \rangle$ | 0.0085 | -0.240 | 0.418 | 0.020 | -0.399 | 0.105 |
| $\langle C_{T\_P} \rangle$ | 0.032 | -0.198 | 0.453 | 0.056 | -0.327 | 0.166 |
| $\langle C_{T\_v} \rangle$ | -0.0235 | -0.042 | -0.035 | -0.036 | -0.075 | -0.061 |

**Table 1.** Time averaged thrust coefficients for the NACA0006 and NACA0030 airfoils with different motions at $Str = 0.3, k = 1$. $\langle C_T \rangle$ denotes the total time averaged thrust coefficient; $\langle C_{T\_P} \rangle$ denotes the time averaged thrust coefficient based on the contribution from the pressure force; $\langle C_{T\_v} \rangle$ denotes the time averaged thrust coefficient based on the contribution from the viscous force.



(a)  (b)

(c)  (d)

(e)  (f)
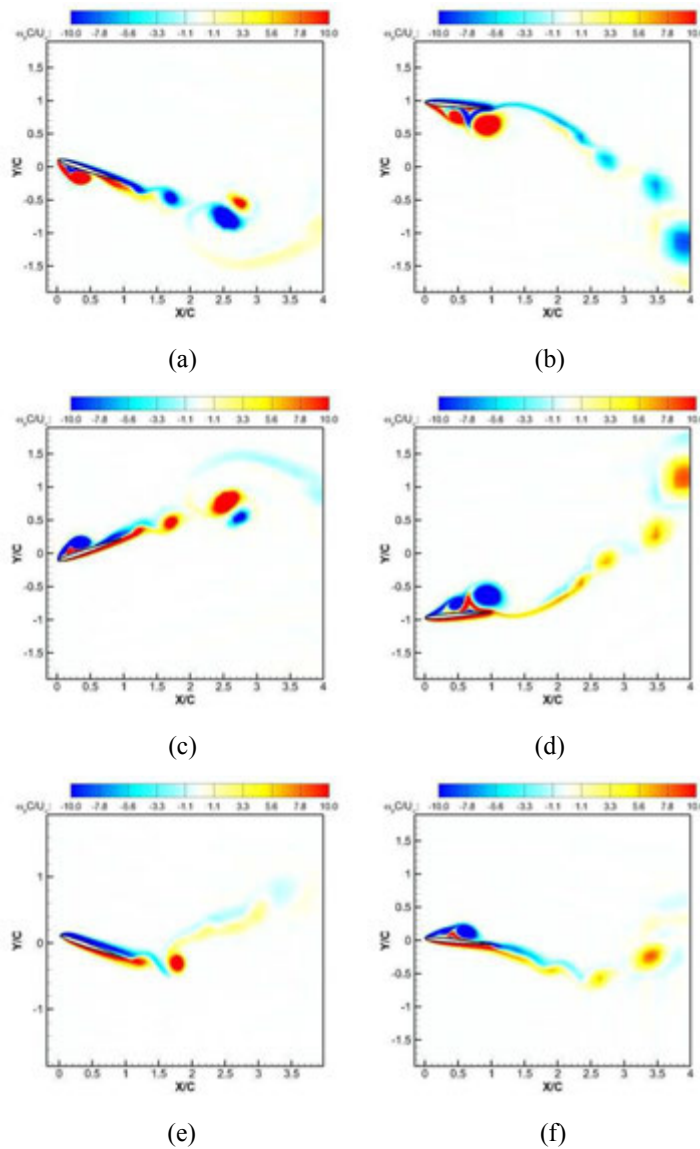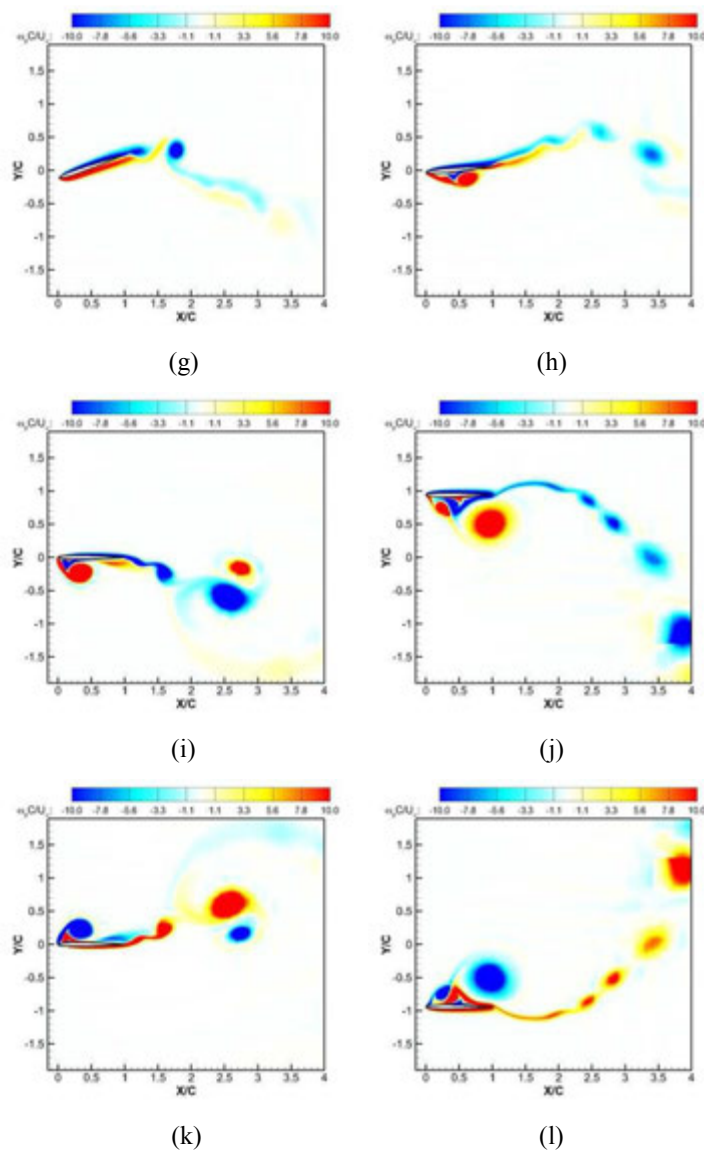
**Fig. 6.** Vorticity fields for the NACA0006 airfoil with different motions at $Str = 0.3, k = 1$. (a)-(d) combined plunging and pitching motion at phases $0, \pi/2, \pi, 3\pi/2$ respectively; (e)-(h) pitching motion at phases $0, \pi/2, \pi, 3\pi/2$ respectively; (i)-(l) plunging motion at phases $0, \pi/2, \pi, 3\pi/2$ respectively.
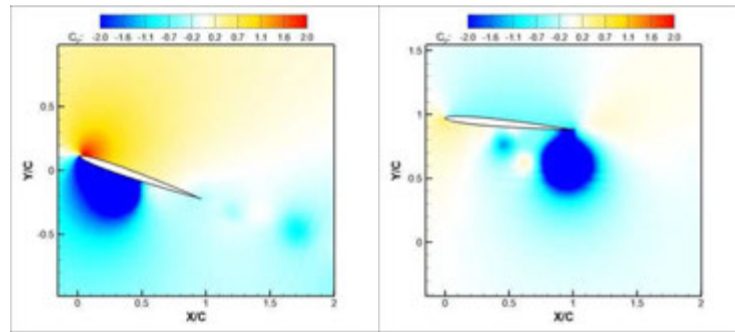
(a)　　　　　　　　　　(b)
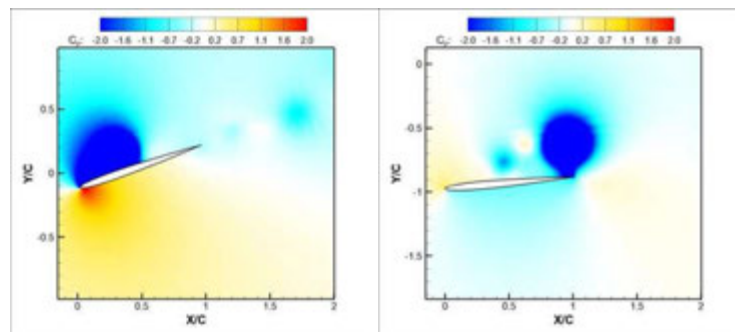
(c)　　　　　　　　　　(d)
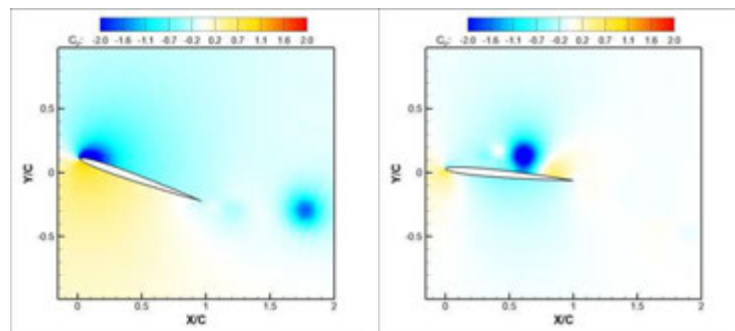
(e)　　　　　　　　　　(f)
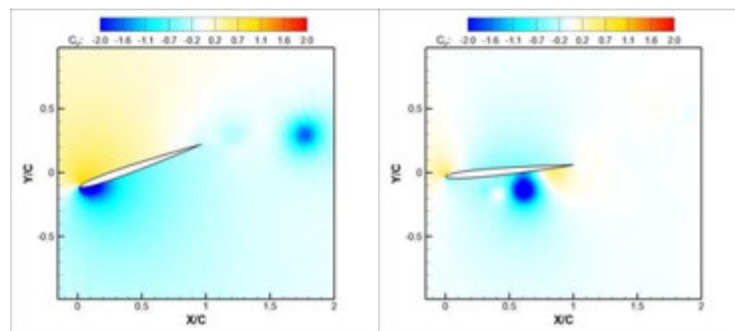
(g)　　　　　　　　　　(h)
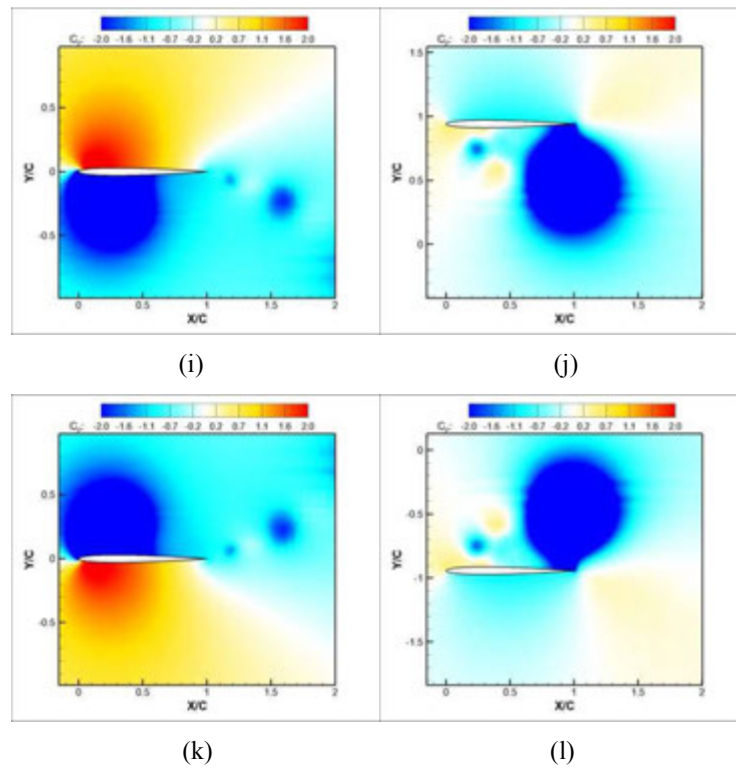
**Fig. 7.** Pressure fields for the NACA0006 airfoil with different motions at $Str = 0.3, k = 1$. (a)-(d) combined plunging and pitching motion at phases $0, \pi/2, \pi, 3\pi/2$ respectively; (e)-(h) pitching motion at phases $0, \pi/2, \pi, 3\pi/2$ respectively; (i)-(l) plunging motion at phases $0, \pi/2, \pi, 3\pi/2$ respectively.

(c)

(d)

(e)

(f)

(g)

(h)

(i)

(j)

(k)                              (l)
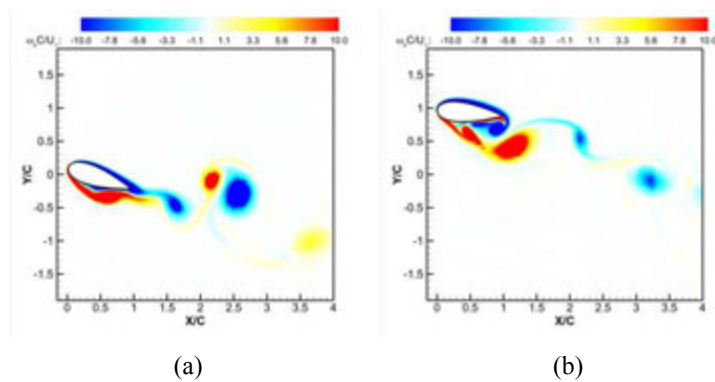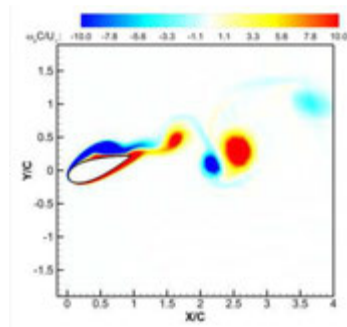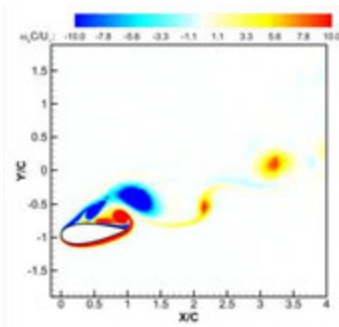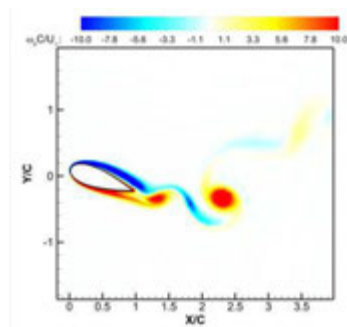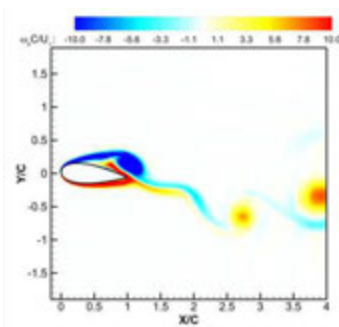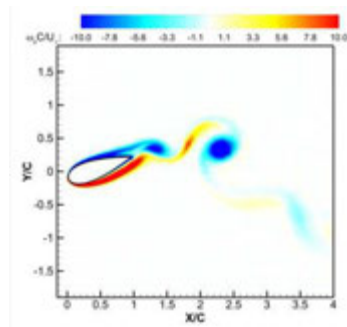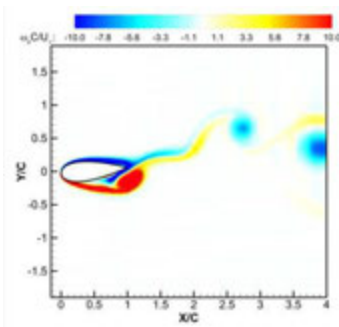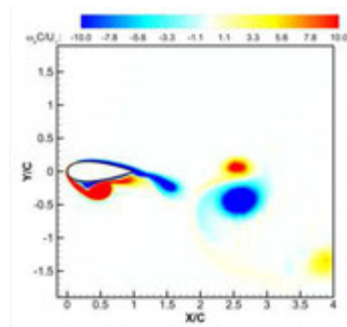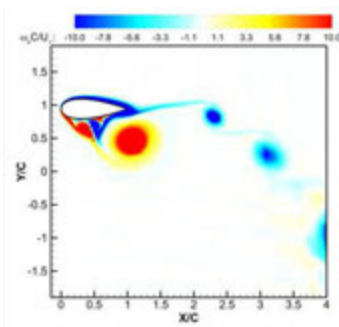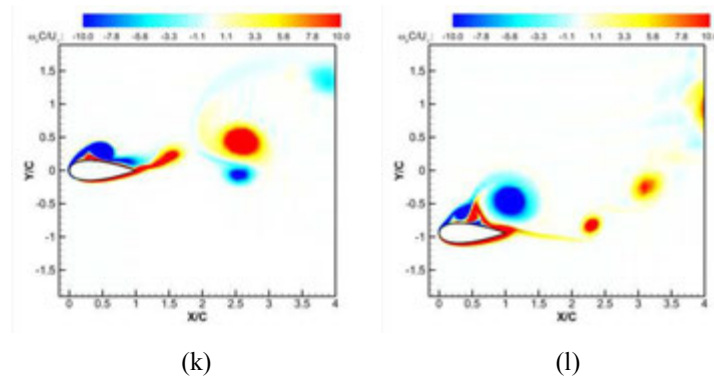
**Fig. 8.** Vorticity fields for the NACA0030 airfoil with different motions at $Str = 0.3, k = 1$. (a)-(d) combined plunging and pitching motion at phases $0, \pi/2, \pi, 3\pi/2$ respectively; (e)-(h) pitching motion at phases $0, \pi/2, \pi, 3\pi/2$ respectively; (i)-(l) plunging motion at phases $0, \pi/2, \pi, 3\pi/2$ respectively.



(a)                              (b)



(c)                              (d)

(e)

(f)

(g)

(h)

(i)

(j)

(k)

(l)
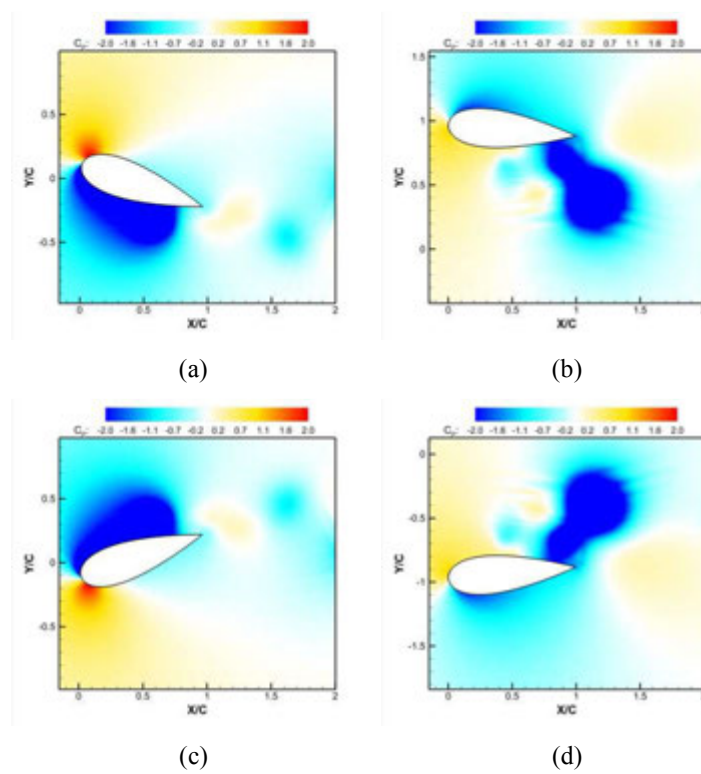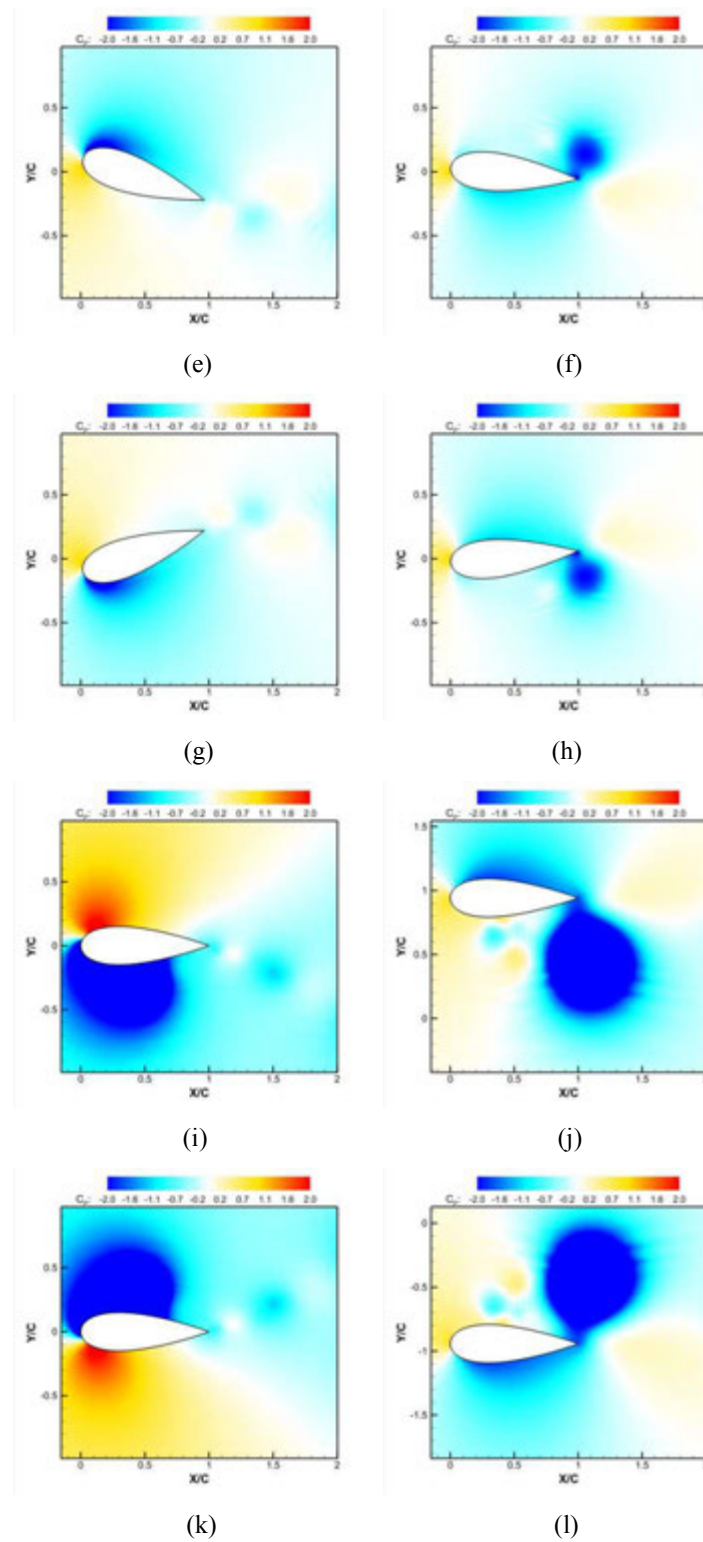
**Fig. 9.** Pressure fields for the NACA0030 airfoil with different motions at $Str = 0.3, k = 1$. (a)-(d) combined plunging and pitching motion at phases $0, \pi/2, \pi, 3\pi/2$ respectively; (e)-(h) pitching motion at phases

$0, \pi/2, \pi, 3\pi/2$ respectively; (i)-(l) plunging motion at phases $0, \pi/2, \pi, 3\pi/2$ respectively.



(a)



(b)



(c)



(d)



(e)



(f)



(g)



(h)
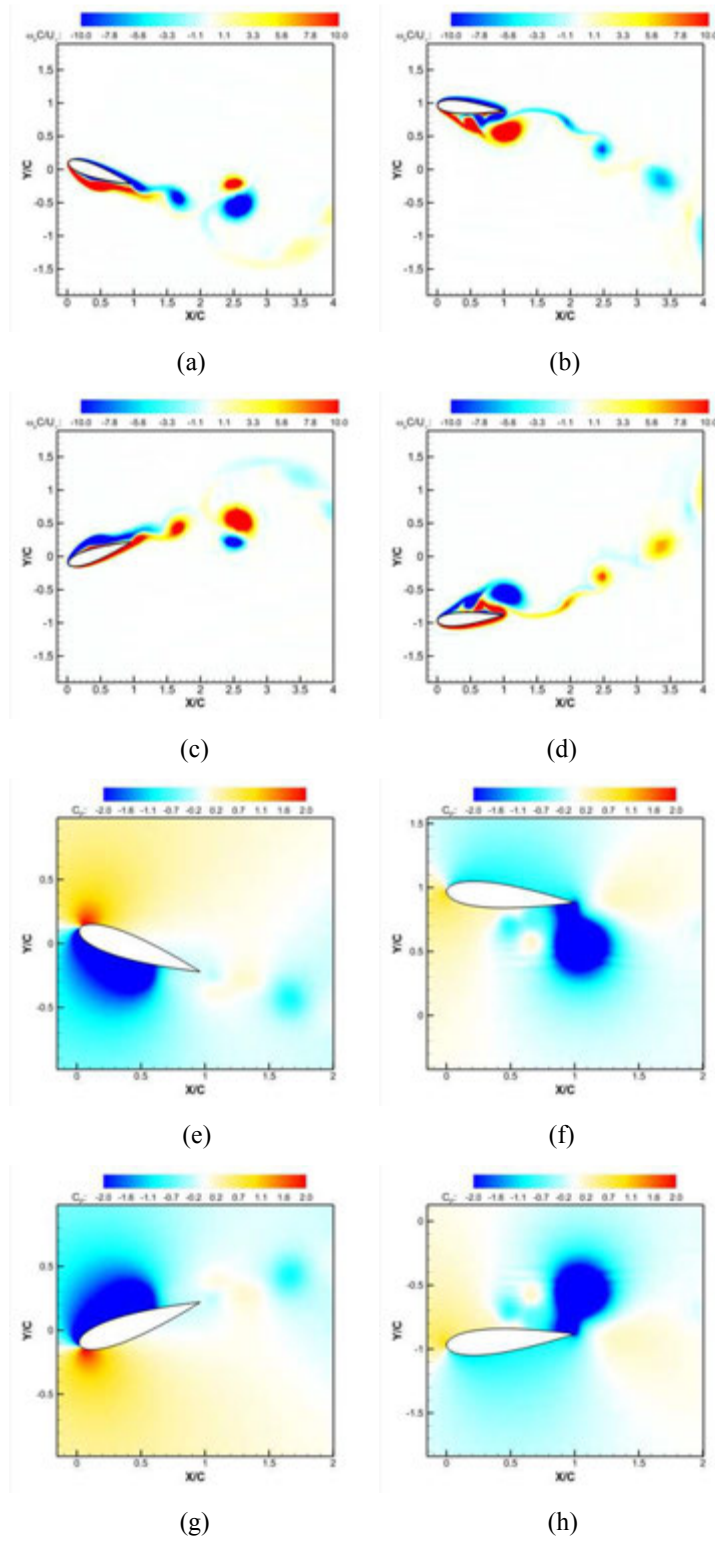
**Fig. 10.** Vorticity and pressure fields for the NACA0020 airfoil with the combined motion at $Str = 0.3, k = 1$. (a)-(d) vorticity fields at phases $0, \pi/2, \pi, 3\pi/2$ respectively; (e)-(h) pressure fields at phases $0, \pi/2, \pi, 3\pi/2$ respectively.



(a)                                              (b)
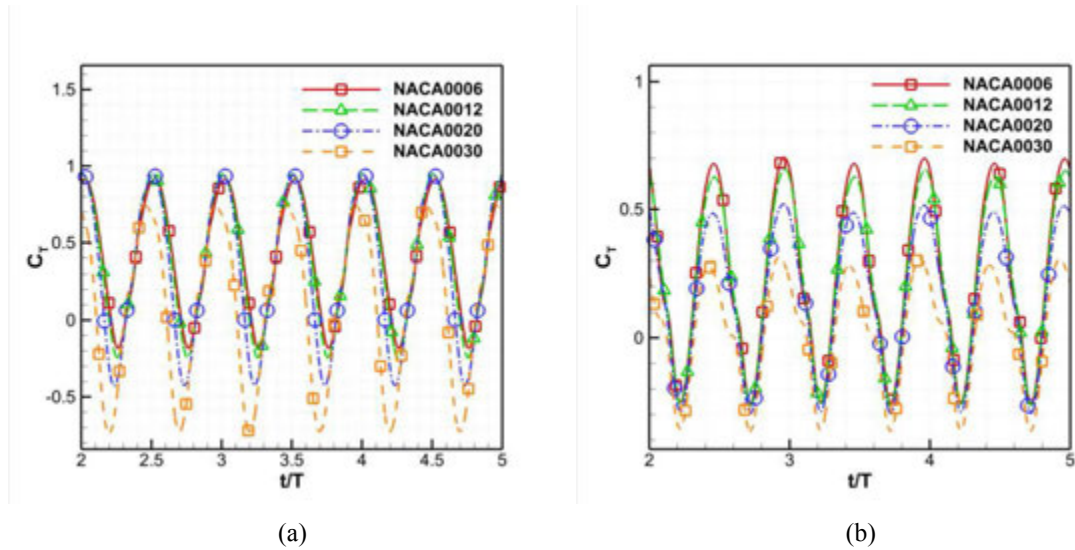
**Fig. 11.** Time histories of the thrust coefficients for a series of NACA 4-digit airfoils with the combined plunging and pitching motion at (a) $Str = 0.3, k = 1$, and (b) $Str = 0.3, k = 3.5$.



(a)                                              (b)
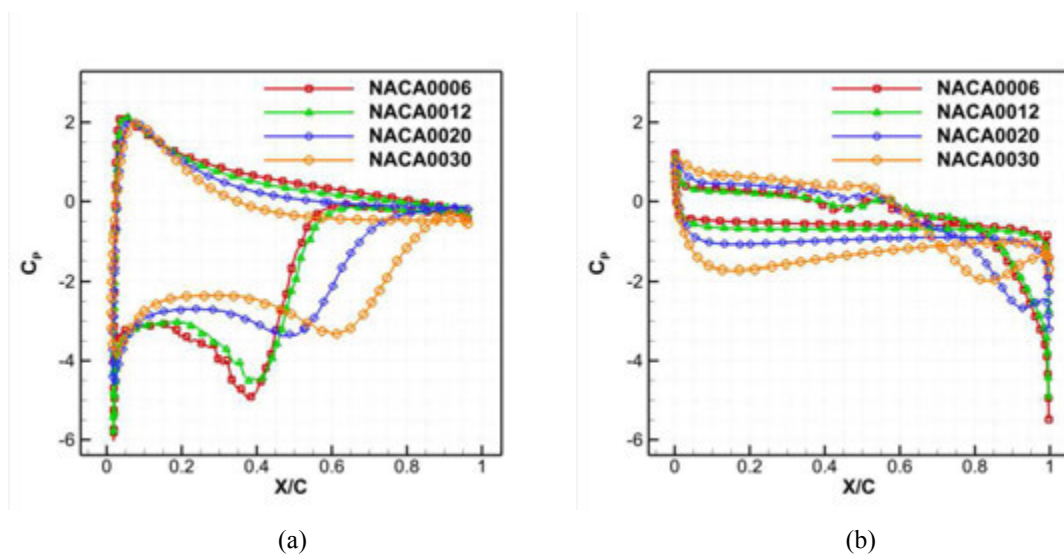
**Fig. 12.** Surface pressure coefficienct $C_P$ distributions for a series of NACA 4-digit airfoils with the combined motion at $Str = 0.3, k = 1$. (a) phases: 0 and $\pi$; (b) phases: $\pi/2$ and $3\pi/2$.

(a)                                    (b)

(c)                                    (d)

(e)                                    (f)

(g)                                    (h)

**Fig. 13.** Vorticity and pressure fields for the NACA0006 airfoil with the combined motion at $Str = 0.3, k = 3.5$ . (a)-(d) vorticity fields at phases $0, \pi/2, \pi, 3\pi/2$ respectively; (e)-(h) pressure fields at phases

$0, \pi/2, \pi, 3\pi/2$ respectively.



(a)                              (b)

(c)                              (d)

(e)                              (f)

(g)                              (h)
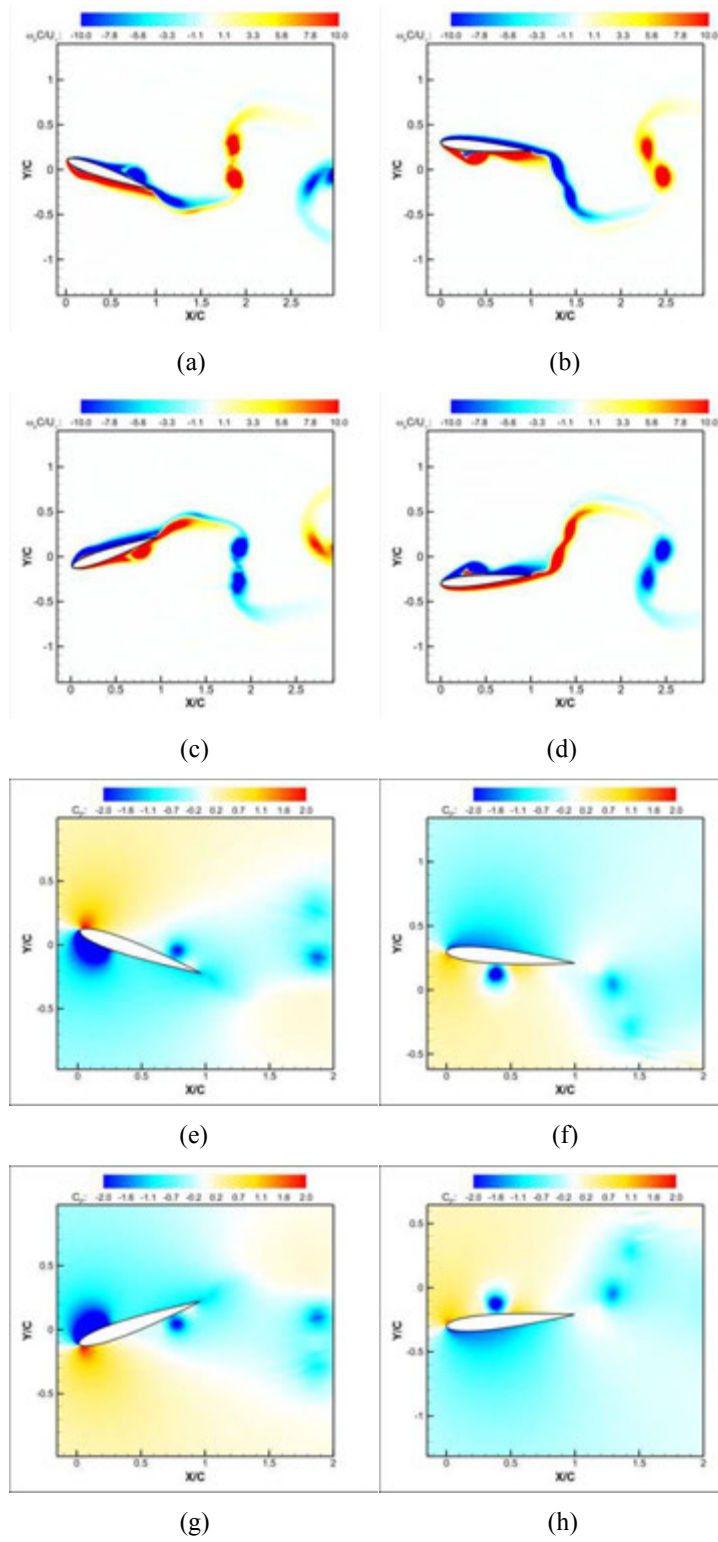
**Fig. 14.** Vorticity and pressure fields for the NACA0012 airfoil with the combined motion at $Str = 0.3, k = 3.5$ . (a)-(d) vorticity fields at phases $0, \pi/2, \pi, 3\pi/2$ respectively; (e)-(h) pressure fields at phases $0, \pi/2, \pi, 3\pi/2$ respectively.



(a)                                                         (b)

(c)                                                         (d)

(e)                                                         (f)

(g)                       (h)
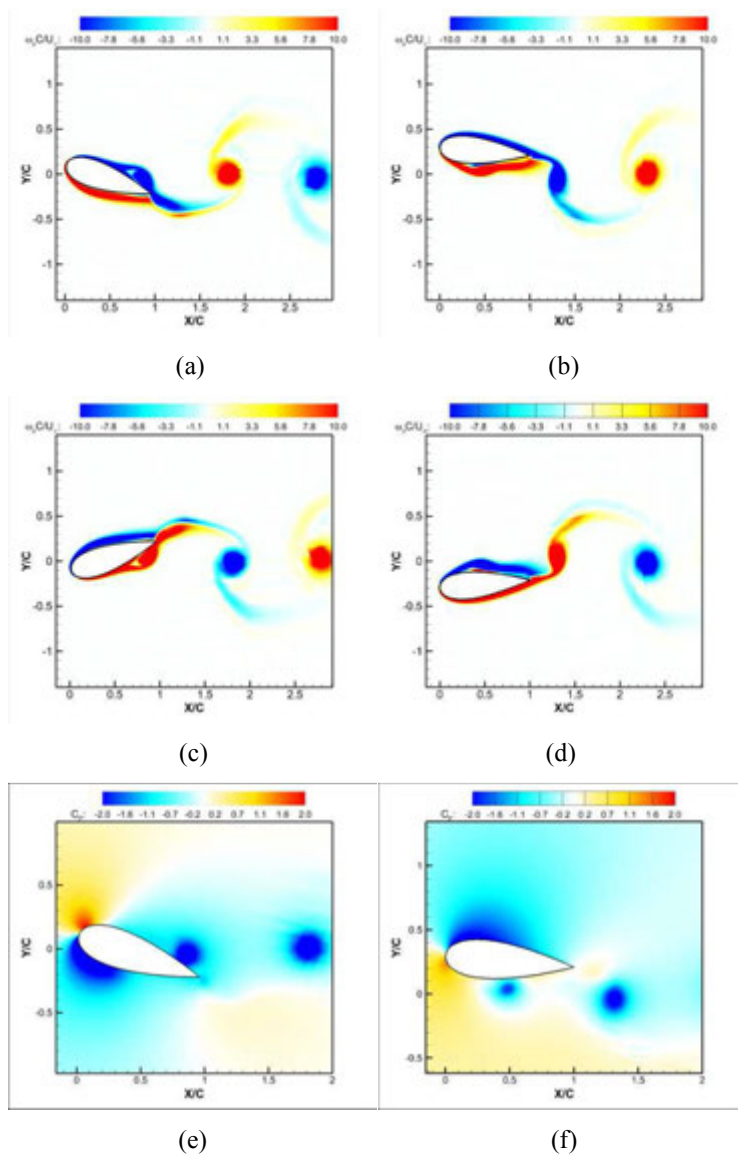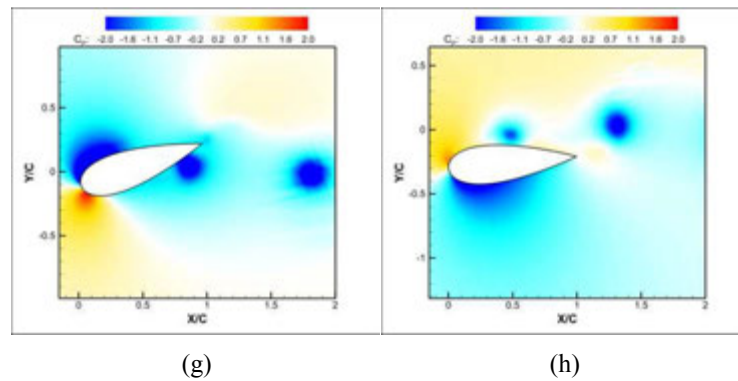
**Fig. 15.** Vorticity and pressure fields for the NACA0030 airfoil with the combined motion at $Str = 0.3, k = 3.5$ . (a)-(d) vorticity fields at phases $0, \pi/2, \pi, 3\pi/2$ respectively; (e)-(h) pressure fields at phases $0, \pi/2, \pi, 3\pi/2$ respectively.



(a)                       (b)
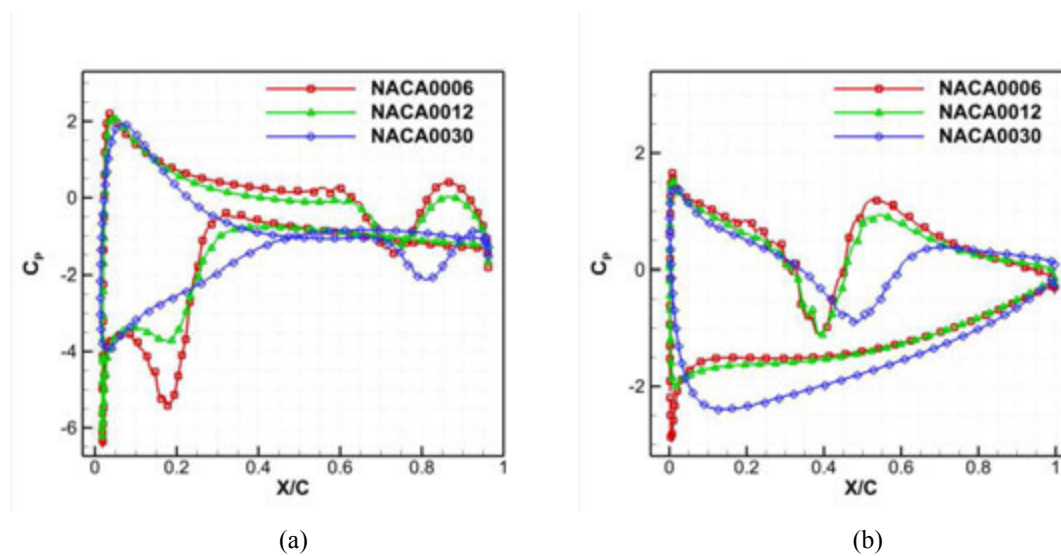
**Fig. 16.** Surface pressure coefficienct $C_P$ distributions for a series of NACA 4-digit airfoils with the combined motion at $Str = 0.3, k = 3.5$. (a) phases: 0 and $\pi$; (b) phases: $\pi/2$ and $3\pi/2$.

(a)                                                    (b)
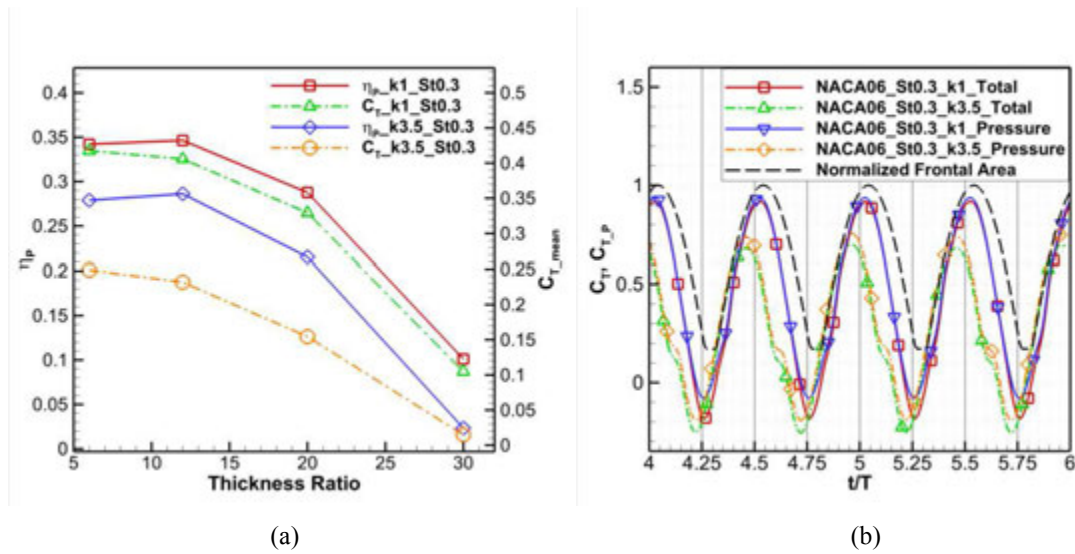
**Fig. 17.** (a) Time averaged thrust coefficients and propulsive efficiencies for a series of NACA 4-digit airfoils; (b) Time histories of the thrust coefficients for the NACA0006 with combined plunging and pitching motions at different reduced frequencies 1 and 3.5. '_Total' means that the thrust is calculated from both pressure and viscous forces; and '_Pressure' means that the thrust is calculated only from the pressure forces.



(a)                                                    (b)

(c)                                                    (d)
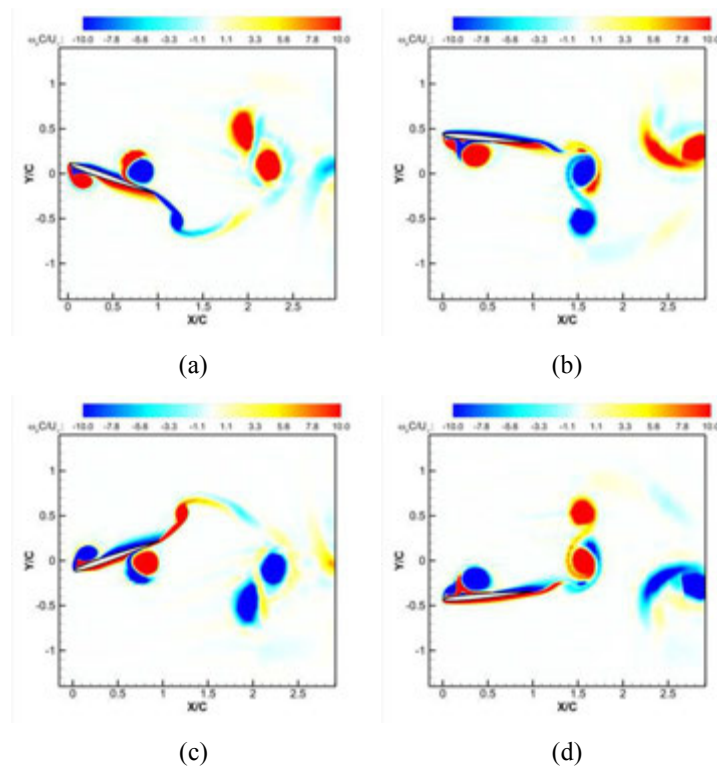
**Fig. 18.** Vorticity fields for the NACA0006 airfoil with the combined motion at $Str = 0.45, k = 3.5$. (a)-(d) vorticity fields at phases $0, \pi/2, \pi, 3\pi/2$ respectively.
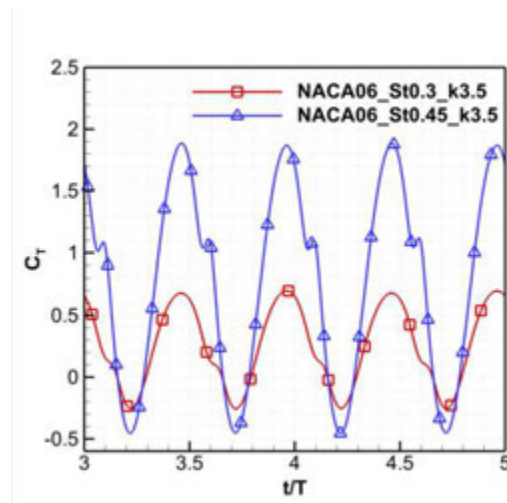
**Fig. 19.** Time histories of the thrust coefficients for the NACA0006 airfoil with the combined motion at $Str = 0.3, k = 3.5$ and $Str = 0.45, k = 3.5$.

# CHAPTER 6. High-Fidelity Optimization of Flapping Airfoils for Maximum Propulsive Efficiency

A paper submitted to the 51$^{st}$ AIAA ASM conference proceedings

Meilin Yu, Z. J. Wang and Hui Hu

## 1. Introduction

Unsteady flapping-wing aerodynamics has attracted considerable research efforts in the past years partially due to the increased interest in designing Micro Air Vehicles (MAVs) for a variety of missions, including reconnaissance and surveillance, targeting and sensing. Comprehensive reviews [1, 2, 3, 4, 5, 6, 7, 8] are available for the latest progress in this area, but there are still many missing pieces to this puzzle. One of them is to find flapping wing kinematics with maximum efficiency and adequate aerodynamics performance for MAV flight.

Flapping motions can effectively generate thrust at low Reynolds and Mach numbers, and many research efforts have been devoted to shed light on the mechanism of efficient flapping flight. Jones and Platzer [9] argued that the combined plunging and pitching motion of flapping flight could adjust the effective angle of attack (AOA) of the airfoil, thus enhancing the thrust generation or power extraction performance. Anderson *et al.* [10] experimentally examined the propulsive performance of a NACA0012 airfoil with a combined plunging and pitching motion, and showed the parameters for an optimal thrust production. Isogai *et al.* [11] concluded from their results for a NACA0012 airfoil undergoing combined pitching and plunging mot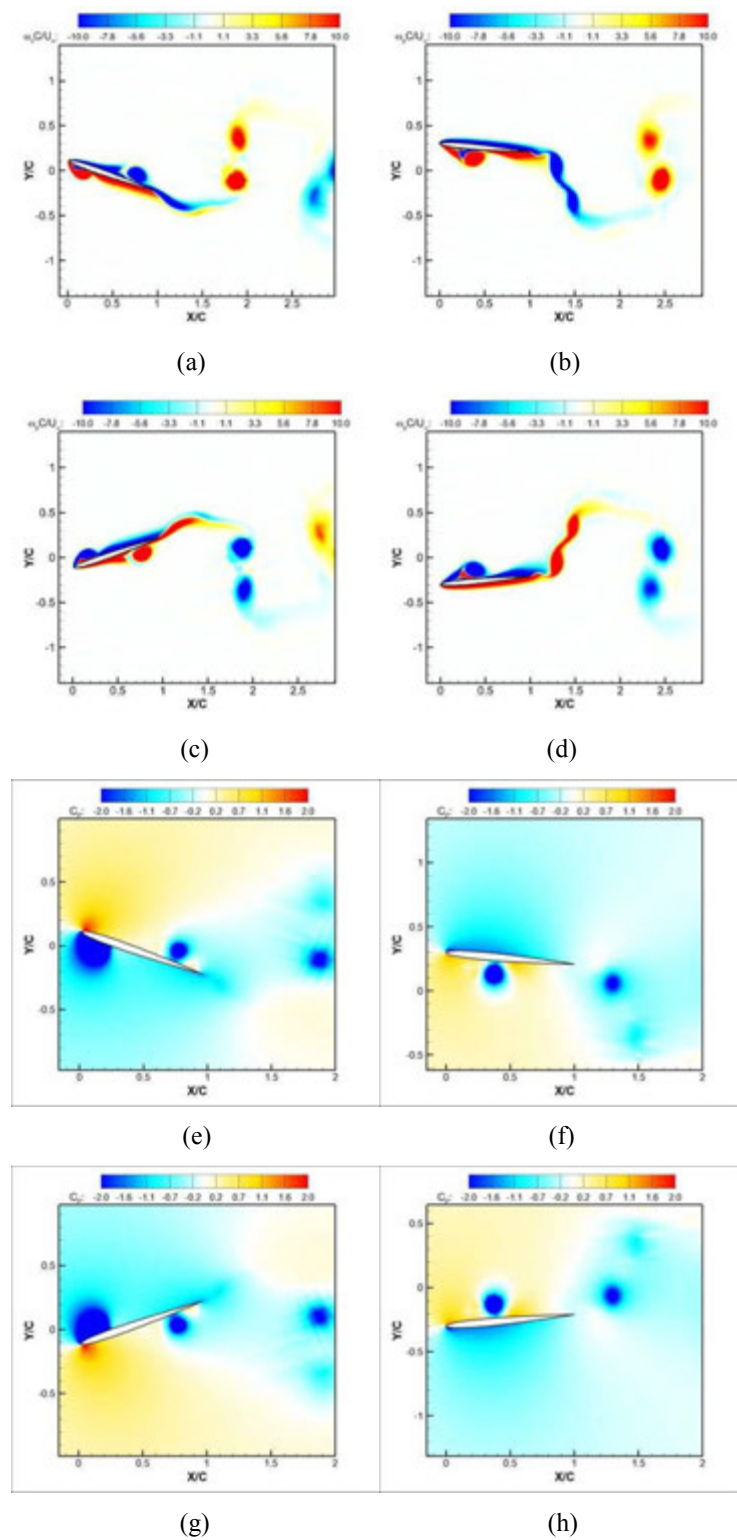ion that a high propulsive efficiency could be obtained when the pitching lead plunging by 90 degrees and no apparent leading edge separation appeared. At the same time, Tuncer and Platzer [12] similarly found that high propulsive efficiency came with an attached flow over the full period of the oscillation cycle for an NACA0012 airfoil. Note that in both cases the free stream Mach number was 0.3, which may be a bit large for the flapping wing simulations. Ramamurti and Sandberg [13] used a finite element incompressible flow solver to study an oscillating NACA0012 airfoil and investigated the effect of the phase difference between pitching and plunging motions on the thrust generation and propulsive

efficiency. Kang *et al*. [14] used a Reynolds-Averaged Navier-Stokes (RANS) approach to study the flow over an oscillating SD7003 airfoil and examined the effects of turbulence model on the prediction of flow features.

Also, there has been long-standing research interest in optimizing the kinematics of a flapping wing to achieve optimal aerodynamic performance (lift, lift to drag ratio, thrust, propulsive efficiency, power consumption, etc.) in different scenarios. Jones [15] calculated the optimum load distribution along the wing for a given wing-root bending momentum during the pure flapping motion, and found that the optimum loading was able to generate thrust more efficiently compared with an elliptic loading, which was suggested to be optimal for steady flight. Hall and Hall [16] computed the optimal circulation distribution along the span of flapping wings in fast forward flight using a 1D integral solution for small-amplitude motions and vortex-lattice techniques for large-amplitude motions. Ito [17] utilized vortex lattice method in conjunction with a hybrid optimization algorithm combining genetic algorithm and sequential quadratic programming to optimize the flapping wing motion. Vortex lattice model was also adopted by other research groups [18, 19] as a suitable compromise between computational cost and accuracy, but it might fail to provide appropriate level of complexity of the motion when viscous effects became non-negligible [18]. In addition, Hamdaoui *et al.* [20] optimized the efficient flapping kinematics using a multi-objective evolutionary algorithm coupled with flapping flight physics models.

The growing sophistication of computation hardware and simulation tools now allows for direct coupling between optimization algorithms and high-fidelity Navier-Stokes solvers for purpose of flapping motion optimization. Tuncer and Kaya [21] optimized the weighted sum consisted of thrust and propulsive efficiency of an flapping airfoil in combined plunging and pitching motion by coupling gradient-based optimization method with 2D Navier-Stokes solver supporting moving overset grid. Willis *et al.* [22] exploited a collection of computation tools with multiple fidelity level in the design of effective flapping wing vehicles. In 2009, Pesavento and Wang [23] further confirmed that 2D flapping flight can be aerodynamically more efficient than the optimal steady motion. Recently, Culbreth *et al.* [24] presented several optimization results for flapping airfoils and wings obtained from an optimization framework constructed by a gradient-based optimization algorithm and a low-

dissipation kinetic energy preserving (KEP) finite volume Navier-Stokes solver. They found that the maximum propulsive efficiency appeared to occur right before the incipience of leading edge separation.

In the study, we propose to take a cost-effective multi-level optimization approach to provide further insights into flapping motions with maximum propulsive efficiency. At the first stage, a gradient-based optimization algorithm is coupled with a second-order spectral difference (SD) Navier-Stokes solver to search for the optimal kinematics of a NACA0012 airfoil undergoing a combined plunging and pitching motion. Since it is evidenced that high-order methods can be more accurate than the low-order counterparts for simulations of vortex-dominated flows (e.g. bio-inspired flows) [25], at the final stage, a high-order Navier-Stokes solver is used to verify the optimization results and reveal the detailed vortex structures associated with the optimal kinematics of the flapping flight with high-fidelity to help better understand the physics.

The remainder of this paper is organized as follows. In Section II, the optimization framework will be introduced. Some preliminary numerical results are displayed and discussed in section III. Section IV briefly concludes the preliminary work.

## 2. Optimization Framework

### 2.1 Governing Equations

Numerical simulations are performed with an unsteady compressible Navier-Stokes solver using dynamic unstructured grid based high-order spectral difference (SD) method developed in [26]. The 2D unsteady compressible Navier-Stokes equations in conservation form read,

$$\frac{\partial Q}{\partial t} + \frac{\partial F}{\partial x} + \frac{\partial G}{\partial y} = 0. \tag{1}$$

Herein, $Q = (\rho, \rho u, \rho v, E)^T$ are the conservative variables, and $F, G$ are the total fluxes including both the inviscid and viscous flux vectors, i.e., $F = F^i - F^v$ and $G = G^i - G^v$, which takes the following form

$$F^i = \begin{Bmatrix} \rho u \\ p + \rho u^2 \\ \rho uv \\ u(E+p) \end{Bmatrix}, \quad G^i = \begin{Bmatrix} \rho v \\ \rho uv \\ p + \rho v^2 \\ v(E+p) \end{Bmatrix},$$

$$F^v = \begin{Bmatrix} 0 \\ \tau_{xx} \\ \tau_{yx} \\ u\tau_{xx} + v\tau_{yx} + \dfrac{\mu C_p}{Pr} T_x \end{Bmatrix}, \quad G^v = \begin{Bmatrix} 0 \\ \tau_{xy} \\ \tau_{yy} \\ u\tau_{xy} + v\tau_{yy} + \dfrac{\mu C_p}{Pr} T_y \end{Bmatrix}. \tag{2}$$

In Eq. (2), $\rho$ is the fluid density, $u$ and $v$ are the Cartesian velocity components, $p$ is the pressure, and $E$ is the total energy, $\mu$ is dynamic viscosity, $C_p$ is the specific heat at constant pressure, $Pr$ is the Prandtl number, and $T$ is the temperature. The stress tensors in Eq. (2) take the following form

$$\tau_{xx} = 2\mu\left(u_x - \frac{u_x + v_y}{3}\right), \tau_{yy} = 2\mu\left(v_y - \frac{u_x + v_y}{3}\right), \tau_{xy} = \tau_{yx} = \mu\left(v_x + u_y\right). \tag{3}$$

On assuming that the perfect gas law is obeyed, the pressure is related to the total initial energy by $E = \frac{p}{\gamma - 1} + \frac{1}{2}\rho(u^2 + v^2)$ with constant $\gamma$, which closes the solution system.

To achieve an efficient implementation, a time-dependent coordinate transformation from the physical domain $(t, x, y)$ to the computational domain $(\tau, \xi, \eta)$, as shown in Fig. 1. (a), is applied to Eq. (1). And we obtain

$$\frac{\partial \tilde{Q}}{\partial \tau} + \frac{\partial \tilde{F}}{\partial x} + \frac{\partial \tilde{G}}{\partial y} = 0, \tag{4}$$

where

$$\begin{cases} \tilde{Q} = |J|Q \\ \tilde{F} = |J|\left(Q\xi_\tau + F\xi_x + G\xi_y\right). \\ \tilde{G} = |J|\left(Q\eta_\tau + F\eta_x + G\eta_y\right) \end{cases} \tag{5}$$

Herein, $\tau = t$ and $(\xi, \eta) \in [-1,1]^2$, are the local coordinates in the computational domain. In the transformation shown above, the Jacobian matrix $J$ takes the following form

$$J = \frac{\partial(x, y, t)}{\partial(\xi, \eta, \tau)} = \begin{pmatrix} x_\xi & x_\eta & x_\tau \\ y_\xi & y_\eta & y_\tau \\ 0 & 0 & 1 \end{pmatrix}. \tag{6}$$

Note that the grid velocity $\overrightarrow{v_g} = (x_t, y_t)$ is related with $(\xi_\tau, \eta_\tau)$ by

$$\begin{cases} \xi_\tau = -\overrightarrow{v_g} \cdot \nabla \xi \\ \eta_\tau = -\overrightarrow{v_g} \cdot \nabla \eta \end{cases}. \tag{7}$$

## 2.2 Space Discretization

The SD method is used for the space discretization. In the SD method, two sets of points are given, namely the solution and flux points, as shown in Fig. 1. (b). Conservative variables are defined at the solution points (SPs), and then interpolated to flux points to calculate local fluxes. In the present study, the solution points are chosen as the Chebyshev-Gauss quadrature points and the flux points are selected to be the Legendre-Gauss points with end points as -1 and 1. Then using Lagrange polynomials, we reconstruct all the fluxes at the flux points. Note that this reconstruction is continuous within a standard element, but discontinuous on the cell interfaces. Therefore, for the inviscid flux, a Riemann solver is necessary to reconstruct a common flux on the interface. The reconstruction of the viscous flux is based on the average of the 'left' and 'right' fluxes. The detailed reconstruction procedures can be found in [26].
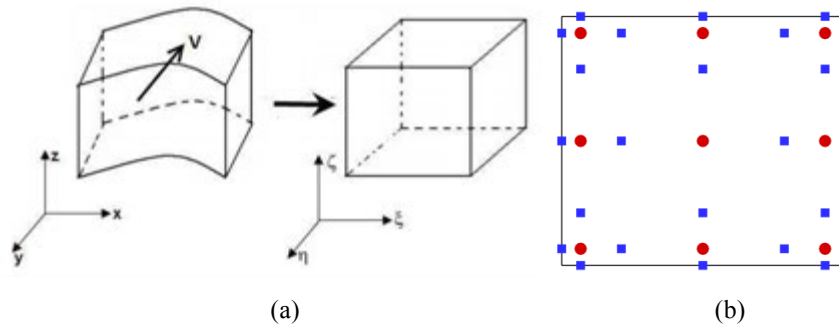


(a)                          (b)

**Fig. 1.** (a) Transformation from a moving physical domain to a fixed computational domain; (b) Distribution of solution points (as denoted by circles) and flux points (as denoted by squares) in a standard quadrilateral element for a third-order SD scheme.

### 2.3 Simulation Parameters

In this study, the kinematics of the airfoil is specified as follows.

$$\text{Plunging motion:} \quad y = hsin(\omega t);$$

$$\text{Pitching motion:} \quad \theta = Asin(\omega t + \phi),$$

where $y$ and $\theta$ are the plunging displacement and pitching angle of the airfoil respectively, $C$ is the chord length, $h$ and $A$ are the plunging and pitching amplitude respectively, $\omega$ is the angular frequency of oscillation and $\phi$ is the phase lag between the plunging and pitching motions.

The aerodynamic parameters are specified as follows. The Reynolds number (Re) based on the airfoil chord length and the free stream velocity is $Re = \rho U_\infty C / \mu = 1,200$, well within the insect flight regime. The Strouhal number $Str$ based on the plunging amplitude $h$ is defined as $Str = 2fh / U_\infty$. The reduced frequency $k$ based on the airfoil chord length $C$ is defined as $k = 2\pi f C / U_\infty$.

### 2.4 Optimization Procedure

For simplicity, we consider an unconstrained optimization problem of the form

$$maximize \ \eta_{power}(\boldsymbol{x}) = \frac{\langle C_T \rangle}{\langle C_{power} \rangle},$$

where $\eta_{power}$ is the propulsive efficiency, $\langle C_T \rangle$ is the time averaged thrust coefficient, $\langle C_{power} \rangle$ is the time averaged power input of the oscillating airfoil, and $\boldsymbol{x}$ denotes the optimization parameters. The unsteady flow solver is used to evaluate the propulsive efficiency $\eta_{power}$.

The Broyden-Fletcher-Goldfarb-Shanno (BFGS) method [27] is adopted for the optimization. It is a quasi-newton algorithm and can achieve a superlinear rate of convergence. The BFGS algorithm is briefly reviewed here for completeness [27].

*Denote the function to be minimized by f (f= $\eta_{power}$ in our case). Give an educated guess of the optimization parameters as $x_0$. Let the convergence tolerance be $\varepsilon > 0$, $s_0 = x_1 - x_0$, and $y_0 = \nabla f_1 - \nabla f_0$. Then, the initial inverse Hessian approximation $H_0$ can be specified as below:*

$$H_0 = \frac{y_0^T s_0}{y_0^T y_0} I .$$

*Let $k = 0$,*

**while $\|\nabla f_k\| > \varepsilon$,**

*Compute line search direction*

$$p_k = -H_k \nabla f_k .$$

*Set $x_{k+1} = x_k + \alpha_k p_k$, where $\alpha_k$ is the line search step length, which satisfies the Wolfe condition,*

$$f(x_k + \alpha_k p_k) \le f(x_k) + c_1 \alpha_k \nabla f_k^T p_k ;$$

$$\nabla f(x_k + \alpha_k p_k)^T p_k \ge c_2 \nabla f_k^T p_k .$$

*Update $s_k$, $y_k$, and $H_{k+1}$ using the following formulas:*

$$s_k = x_{k+1} - x_k$$

$$y_k = \nabla f_{k+1} - \nabla f_k$$

$$H_{k+1} = \left( I - \rho_k s_k y_k^T \right) H_k \left( I - \rho_k y_k s_k^T \right) + \rho_k s_k s_k^T ,$$

*where $\rho_k = 1/\left( y_k^T s_k \right)$.*

*$k = k + 1$*

**end (while)**

Typical values for $c_1$ and $c_2$ in the Wolfe condition suggested in Ref. [27] are $c_1 = 10^{-4}$ and $c_2 = 0.9$.

## 3.  Optimization Results and Discussions

In this section, the NACA0012 and NACA0006 airfoils are used for the optimization. The optimizations are performed for one to four kinematic parameters with the NACA0012 airfoil

and for four kinematic parameters with the NACA0006 airfoil. The convergence criteria $\varepsilon$ is set as $10^{-6}$ in this study.

### 3.1 Results for NACA0012

*3.1.1 Optimization of $x = \phi$ at $Str = 0.3$, $k = 3.5$ and $A = 20^o$*

The initial condition for this case is specified as $\phi = 75^o$. Note that this initial value is chosen based on the suggestions in Ref. [10]. The convergences of the $L_2$ norm of $\nabla\eta$ and $\phi$ are shown in Fig. 2. The optimized phase lag $\phi$ is $87.8^o$ and the propulsive efficiency is 30.8%. Note that the optimal propulsive efficiency is achieved after only six optimization iterations.



<center>(a)                                              (b)</center>
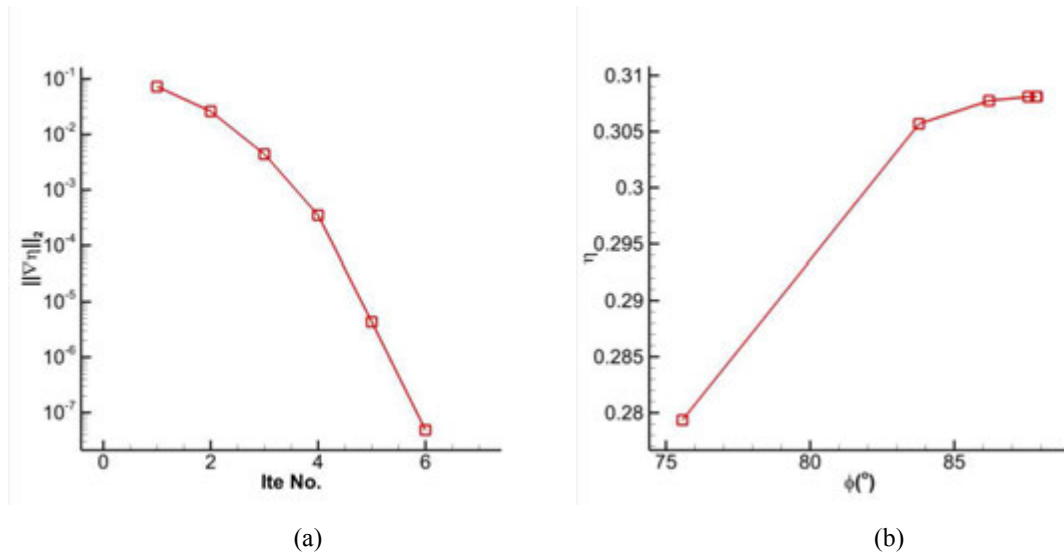
**Fig. 2.** Convergences of (a) the $L_2$ norm of $\nabla\eta$ and (b) the phase lag $\phi$.

*3.1.2 Optimization of $x = (\phi, A)$ at $Str = 0.3$, $k = 3.5$*

The initial conditions for this case are specified as $(\phi, A) = (75^o, 20^o)$. The convergences of the $L_2$ norm of $\nabla\eta$ and $(\phi, A)$ are shown in Fig. 3. The optimized kinematic parameters $(\phi, A)$ are $(89.2^o, 17.9^o)$ and the propulsive efficiency is 31.2%. Note that the optimal propulsive efficiency is achieved after eight optimization iterations.

(a)



(b)                                        (c)
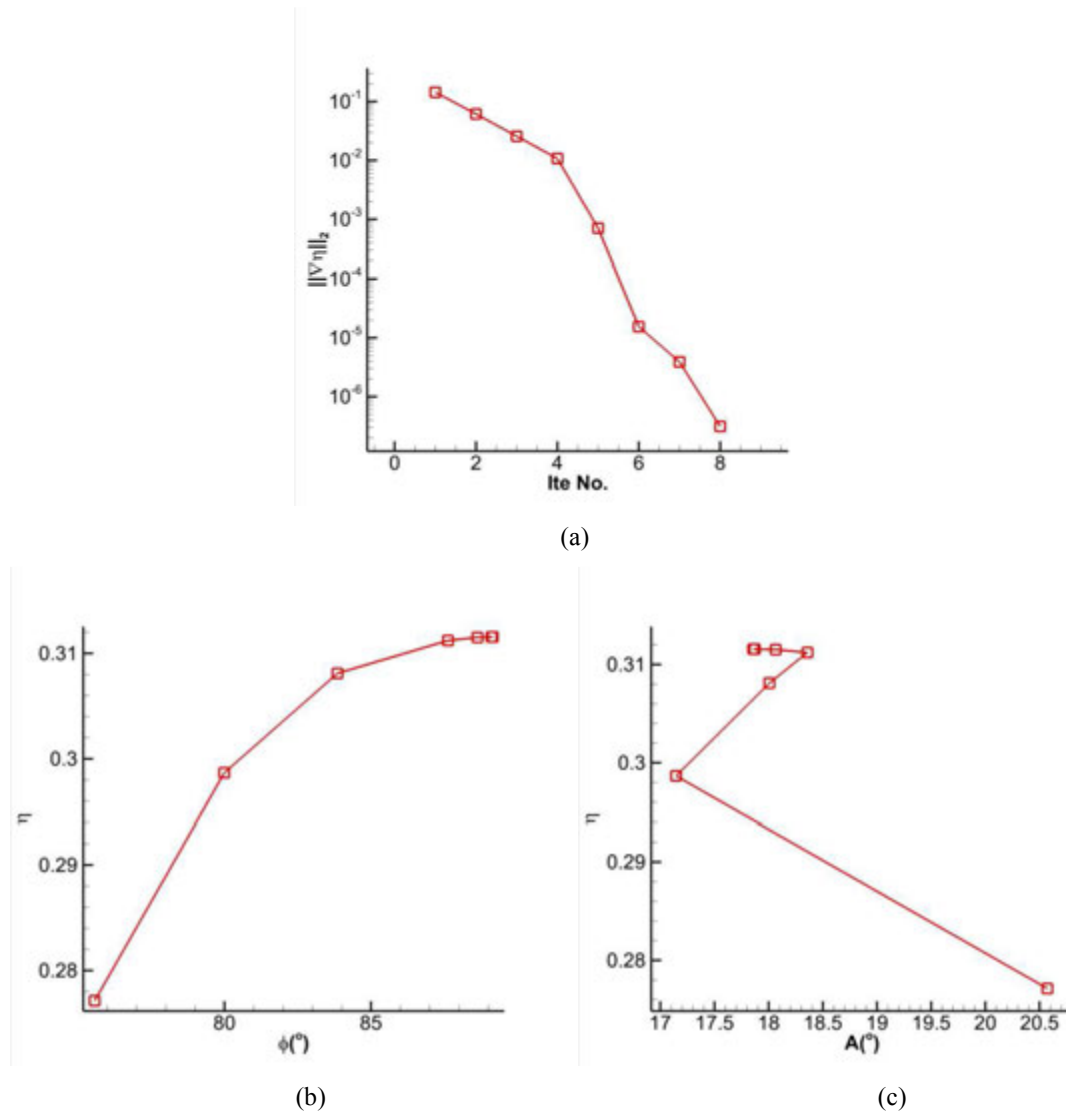
**Fig. 3.** Convergences of (a) the $L_2$ norm of $\nabla\eta$, (b) the phase lag $\phi$ and (c) the pitching amplitude.

### 3.1.3 Optimization of $x = (\phi, A, h)$ at $k = 3.5$ and $k = 1$

The initial conditions for the case at $k = 3.5$ are specified as $(\phi, A, h/C) = (75^o, 20^o, 0.27)$. The convergences of the $L_2$ norm of $\nabla\eta$ and $(\phi, A, h/C)$ are shown in Fig. 4. The optimized kinematic parameters $(\phi, A, h/C)$ are $(84.7^o, 25.9^o, 0.38)$ and the propulsive efficiency is $33.4\%$. Note that the optimal propulsive efficiency is achieved after sixteen optimization iterations.
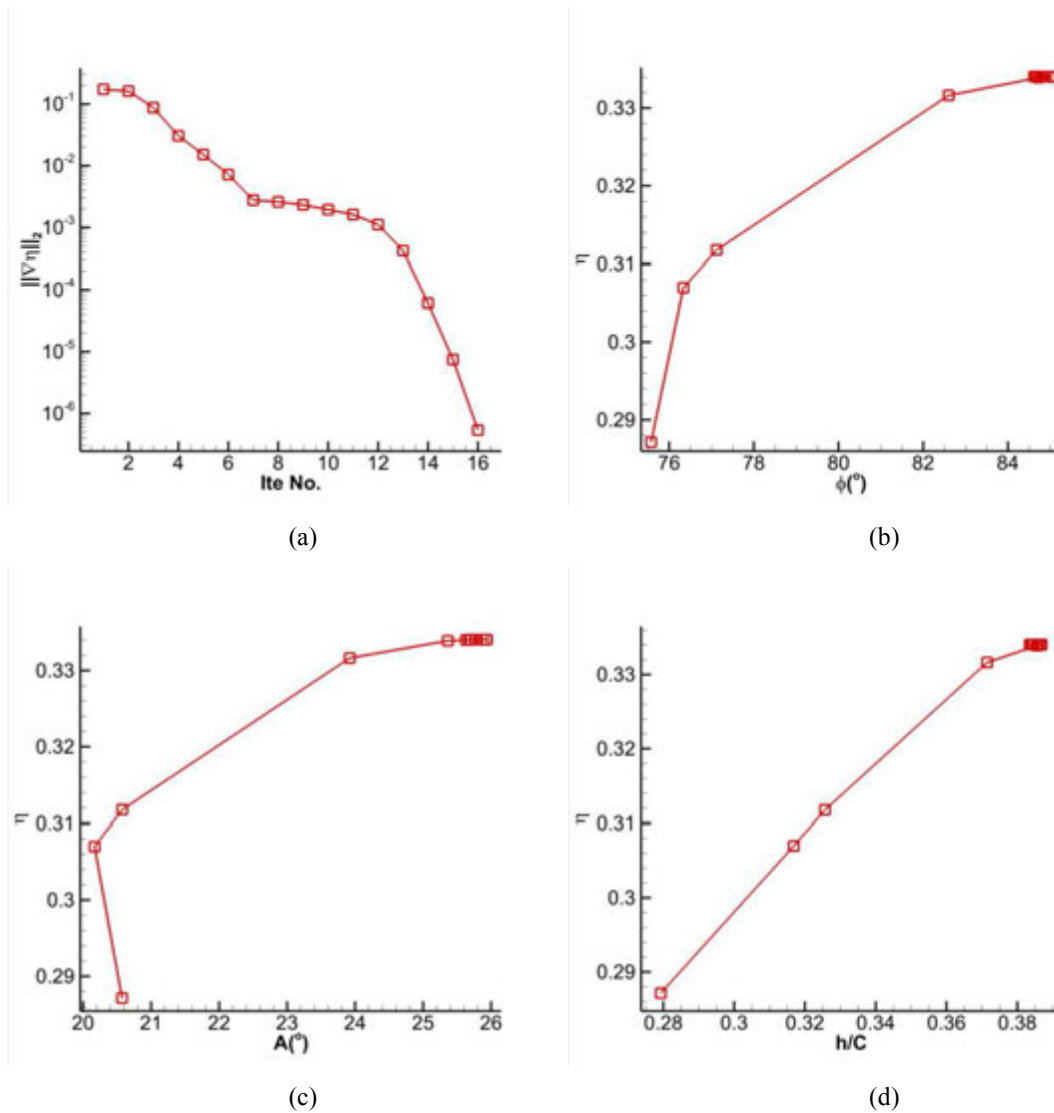
**Fig. 4.** Convergences of (a) the $L_2$ norm of $\nabla\eta$, (b) the phase lag $\phi$, (c) the pitching amplitude and (d) the normalized plunging amplitude at $k = 3.5$.

The initial conditions for the case at $k = 1$ are specified as $(\phi, A, h/C) = (85^o, 45.8^o, 1.5)$. The convergences of the $L_2$ norm of $\nabla\eta$ and $(\phi, A, h/C)$ are shown in Fig. 5. The optimized kinematic parameters $(\phi, A, h/C)$ are $(86.4^o, 49.0^o, 1.66)$ and the propulsive efficiency is 53.3%. In this case, the gradient of the propulsive efficiency $\nabla\eta$ does not converge to the desired error level but the values of $\phi, A, h/C$ converge almost surely towards the local minima. Therefore, the optimization results are reasonable.
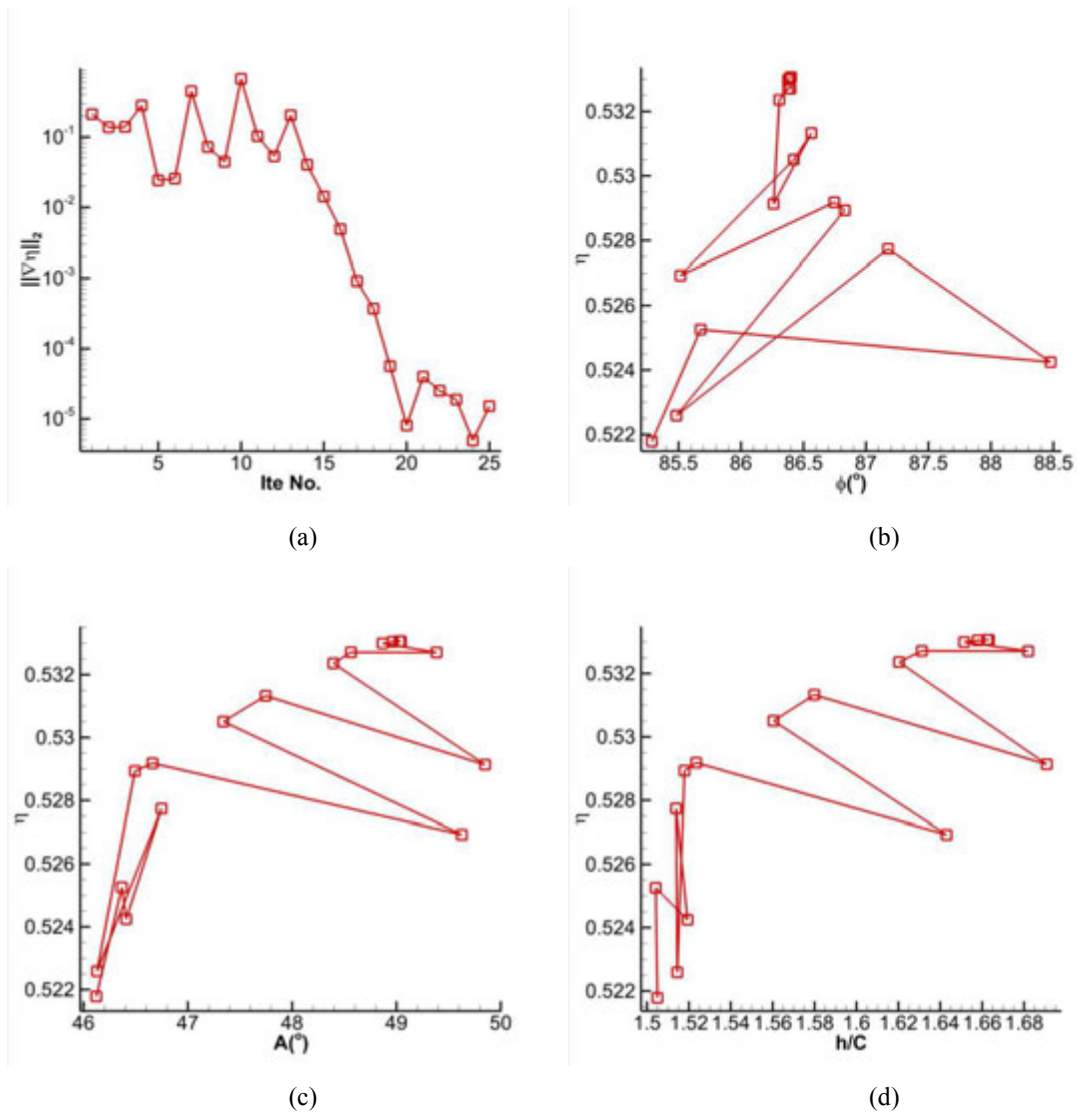
**Fig. 5.** Convergences of (a) the $L_2$ norm of $\nabla\eta$, (b) the phase lag $\phi$, (c) the pitching amplitude and (d) the normalized plunging amplitude at $k = 1$.

### 3.1.4 Optimization of $x = (\phi, A, h, \omega)$

The initial conditions for the case are specified as $(\phi, A, h/C, k) = (85^o, 45.8^o, 1.5, 0.8)$. The convergences of the $L_2$ norm of $\nabla\eta$ and $(\phi, A, h/C)$ are shown in Fig. 6. The optimized kinematic parameters $(\phi, A, h/C, k)$ are $(88.4^o, 41.9^o, 1.57, 0.84)$ and the propulsive efficiency is 53.4%. As in the last case, the gradient of the propulsive efficiency $\nabla\eta$ does not converge to the desired error level but the values of $\phi, A, h/C$ and $k$ converge almost surely towards the local minima. Therefore, the optimization results are reasonable.
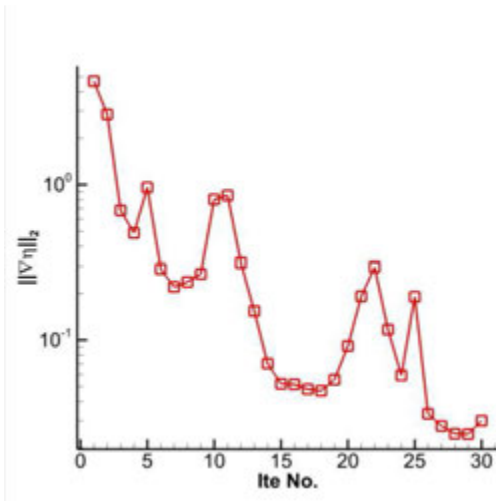
(a)
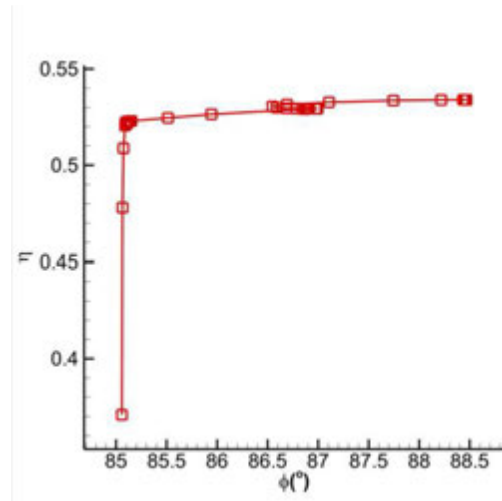
(b)
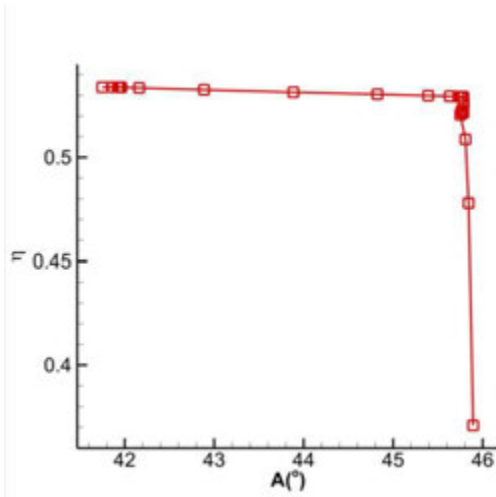
(c)
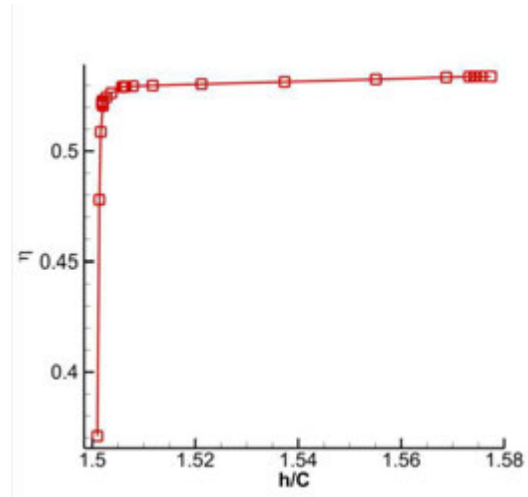
(d)
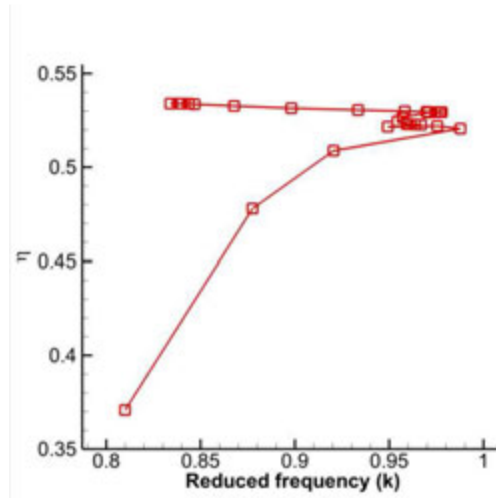
(e)

**Fig. 6.** Convergences of (a) the $L_2$ norm of $\nabla\eta$, (b) the phase lag $\phi$, (c) the pitching amplitude, (d) the normalized plunging amplitude and (e) the reduced frequency.

### 3.1.5 Flow Fields and AerodynamicForces at Optimal Kinematics Parameters

The flow field around the oscillating NACA0012 airfoil with the optimized kinematics $(\phi, A, h/C, k) = (88.4^o, 41.9^o, 1.57, 0.84)$ is simulated using a 3$^{rd}$ order SD scheme. The vorticity fields are displayed in Fig. 7. It is found that large scale leading edge separation only occurs when the airfoil starts to reverse its plunging direction. During most of the oscillation cycle, no leading edge separation shows up. Such kind of flow features may be critical for maintaining the maximum propulsive efficiency, which is also reported in [24].
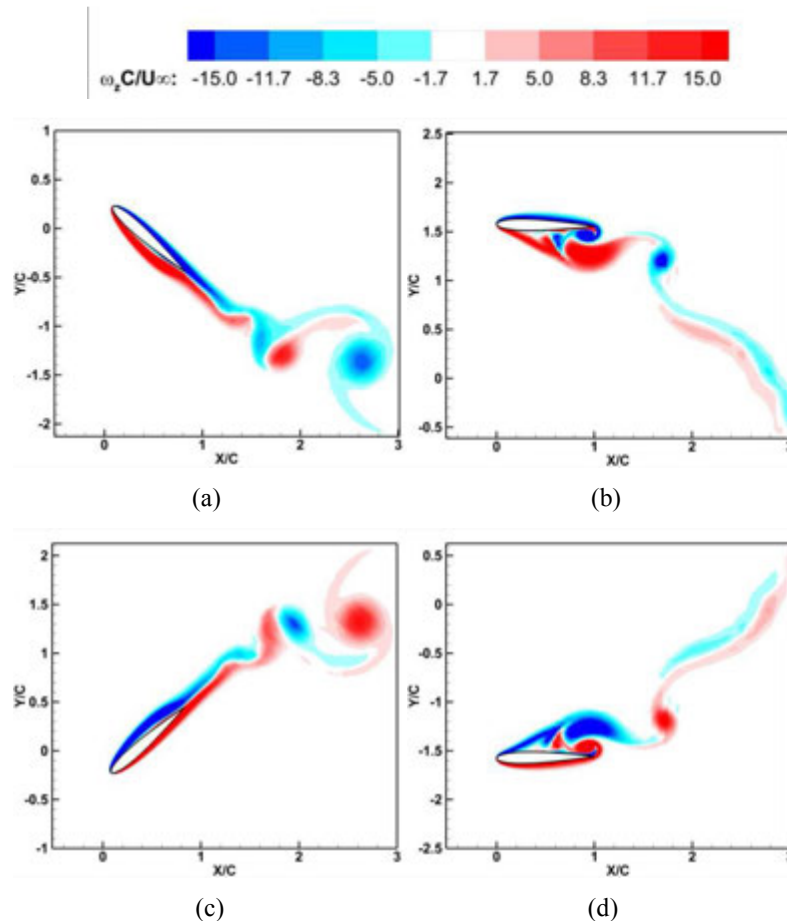


**Fig. 7.** The vorticity fields with optimized kinematics $x = (\phi, A, h/C, k) = (88.4^o, 41.9^o, 1.57, 0.84)$ at different phases from simulations with the 3$^{rd}$ SD scheme for the NACA0012 airfoil. (a) phase 0; (b) phase $\pi/2$; (c) phase $\pi$; (d) phase $3\pi/2$.

### 3.2  Results for NACA0006

On using the same initial conditions of $(\phi, A, h/C, k)$ as shown in 3.1.4, the optimized kinematics parameters for the oscillating NACA0006 airfoil is obtained as $(\phi, A, h/C, k) = (87.0^o, 41.9^o, 1.54, 0.83)$. The maximized propulsion efficiency is $56.9\%$. Similarly to the optimization process of the NACA0012 airfoil, the gradient of the propulsive efficiency $\nabla\eta$ does not converge to the desired error level but the values of $\phi, A, h/C$ and $k$ converge almost surely towards the local minima. The vorticity fields simulated using a 3$^{rd}$ order SD scheme are displayed in Fig. 8. Similar flow features as those from the NACA0012 airfoil can be concluded from the flow fields. The time histories of the thrust and lift forces are shown in Fig. 9. From the results it is found that the absolute peak values of the thrust and lift forces during the oscillation are almost of the same level. Furthermore, although during one stroke of a specific oscillating cycle the aerodynamic forces display certain fluctuation, the force histories are very periodic. This is closely related to the suppression of leading edge separation during the oscillation.



(a)                    (b)

(c)                                    (d)
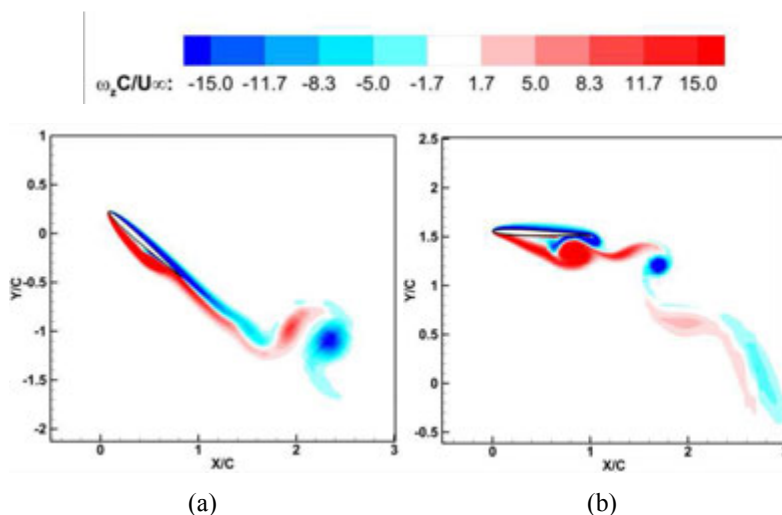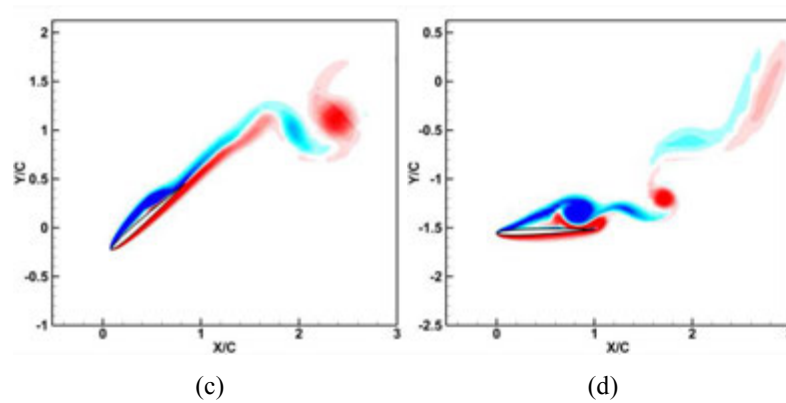
**Fig. 8.** The vorticity fields with optimized kinematics $x = (\phi, A, h/C, k) = (87.0^o, 41.9^o, 1.54, 0.83)$ at different phases from simulations with the 3$^{rd}$ SD scheme for the NACA0006 airfoil. (a) phase 0; (b) phase $\pi/2$; (c) phase $\pi$; (d) phase $3\pi/2$.
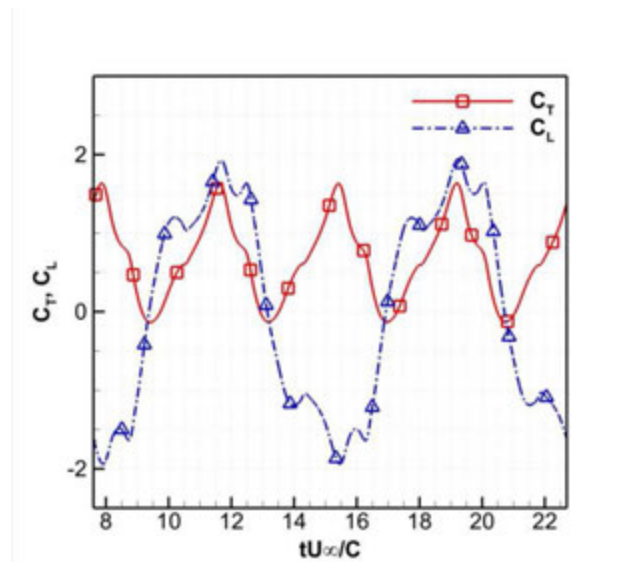


**Fig. 9.** Time histories of the thrust and lift forces with optimized kinematics for the NACA0006 airfoil.

## 4. Conclusions and Future Work

A high order SD scheme based numerical optimization method is proposed to optimize the kinematics of flapping airfoils and provide further insights into flapping motions with maximum propulsive efficiency. A cost-effective multi-level optimization approach is adopted in the development. At the first stage, a gradient-based optimization algorithm is coupled with a second-order SD Navier-Stokes solver to search for the optimal kinematics of

a certain airfoil undergoing a combined plunging and pitching motion. Specifically, the quasi-Newton optimization algorithm BFGS is used to speed up the convergence. Then a high-order SD scheme is used to verify the optimization results and reveal the detailed vortex structures associated with the optimal kinematics of the flapping flight. The proposed optimization procedure is tested for several cases with one to four optimization parameters of flapping NACA0012 and NACA0006 airfoils. The maximum propulsive efficiency for the NACA0012 airfoil can achieve 53.4% and that for the NACA0006 airfoil can be up to 56.9% after four kinematics parameters are optimized, namely, the oscillation frequency, plunging and pitching amplitudes and the phase lag between the plunging and pitching motion. Adjoint based optimization of the flapping wing shape and kinematics for maximum propulsive efficiency will be conducted in the future.

## References

[1] S. Ho, H. Nassef, N. Pornsinsirirak, Y. C. Tai and C. M. Ho, "Unsteady aerodynamics and flow control for flapping wing flyers," *Progress in Aerospace Sciences,* vol. 39, no. 8, p. 635–681, 2003.

[2] M. F. Platzer, K. D. Jones, J. Young and J. C. S. Lai, "Flapping-wing aerodynamics: progress and challenges," *AIAA J.,* vol. 46, no. 9, pp. 2136-2149, 2008.

[3] K. V. Rozhdestvensky and V. A. Ryzhov, "Aerohydrodynamics of flapping-wing propulsors," *Progress in Aerospace Sciences,* vol. 39, no. 8, pp. 585-633, 2003.

[4] W. Shyy, H. Aono, S. Chimakurthi, P. Trizila, C. Kang, C. Cesnik and H. Liu, "Recent progress in flapping wing aerodynamics and aeroelasticity," *Progress in Aerospace Sciences,* vol. 48, no. 7, pp. 284-327, 2010.

[5] W. Shyy, M. Berg and D. Ljungqvist, "Flapping and flexible wings for biological and micro air vehicles," *Progress in Aerospace Sciences,* vol. 35, no. 5, pp. 455-505, 1999.

[6] W. Shyy, Y. Lian, J. Tang, D. Viieru and H. Liu, Aerodynamics of low Reynolds number flyers, New York: Cambridge Univ. Press, 2008.

[7] M. S. Triantaflyllou, A. H. Techet and F. S. Hover, "Review of experimental work in biomimetic foils," *IEEE Journal of Oceanic Engineering,* vol. 29, no. 3, pp. 585-594, 2004.

[8] Z. J. Wang, "Dissecting insect flight," *Annu. Rev. Fluid Mech.,* vol. 37, no. 1, pp. 183-210, 2005.

[9] K. D. Jones and M. F. Platzer, "Numerical computation of flapping-wing propulsion and power extraction," in *AIAA Paper No. 97-0826*, 1997.

[10] J. M. Anderson, K. Streitlien, D. S. Barrett and M. S. Triantafyllou, "Oscillating foils of high propulsive efficiency," *J. Fluid Mech.,* vol. 360, pp. 41-72, 1998.

[11] K. Isogai, Y. Shinmoto and Y. Watanabe, "Effects of Dynamic Stall on Propulsive Efficiency and Thrust of Flapping Airfoil," *AIAA J.,* vol. 37, no. 10, pp. 1145-1151, 1999.

[12] I. H. Tuncer and M. F. Platzer, "Computational study of flapping airfoil aerodynamics," *Journal of Aircraft,* vol. 37, no. 3, pp. 514-520, 2000.

[13] R. Ramamurti and W. Sandberg, "Simulation of flow about flapping airfoils using finite element incompressible flow solver," *AIAA J.,* vol. 39, no. 2, pp. 253-260, 2001.

[14] C. K. Kang, H. Aono, P. Trizila, Y. Baik, J. M. Rausch, L. Bernal, M. V. Ol and W. Shyy, "Modeling of pitching and plunging airfoils at Reynolds number between $1 \times 10^4$ and $6 \times 10^4$," in *AIAA Paper 2009-4100*, 2009.

[15] R. T. Jones, "Wing Flapping with Minimum Energy," NASA Technical Memorandum 81174 , 1980.

[16] K. C. Hall and S. R. Hall, "Minimum induced power requirements for flapping flight," *Journal of Fluid Mechanics,* vol. 323, pp. 285-315, 1996.

[17] K. Ito, "Optimization of Flapping Wing Motion," in *ICAS 2002 CONGRESS*, 2002.

[18] B. K. Stanford and P. S. Beran, "Analytical Sensitivity Analysis of an Unsteady Vortex-Lattice Method for Flapping-Wing Optimization," *Journal of Aircraft,* vol. 47, no. 2, pp. 647-662, 2010.

[19] M. Ghommem, M. R. Hajj, L. T. Watson, D. T. Mook, R. D. Snyder and P. S. Beran, "Deterministic Global Optimization of Flapping Wing Motion for Micro Air Vehicles," in *2010 AIAA ATIO/ISSMO Conference*, 2010.

[20] M. Hamdaoui, J.-B. Mouret, S. Doncieux and P. Sagaut, "Optimization of Kinematics for Birds and UAVs using Evolutionary Algorithms," *World Academy of Science, Engineering and Technology,* vol. 47, pp. 181-192, 2008.

[21] I. H. Tuncer and M. Kaya, "Optimization of Flapping Airfoils for Maximum Thrust and Propulsive Efficiency," *AIAA Journal,* vol. 43, no. 11, pp. 2329-2336, 2005.

[22] D. J. Willis, P.-O. Persson, E. R. Israeli, J. Peraire, S. M. Swartz and K. S. Breuer, "Multifidelity Approaches for the Computational Analysis and Design of Effective Flapping Wing Vehicles," in *AIAA 2008-518*, Reno, Nevada, 2008.

[23] U. Pesavento and Z. J. Wang, "FlappingWing Flight Can Save Aerodynamic Power Compared to Steady Flight," *Physical Review Letters,* vol. 103, pp. 118102-4, 2009.

[24] M. Culbreth, Y. Allaneau and A. Jameson, "High-Fidelity Optimization of Flapping Airfoils and Wings," in *AIAA 2011-3521*, Honolulu, Hawaii, 2011.

[25] Z. J. Wang, "High-order methods for the Euler and Navier Stokes equations on unstructured grids," *Progress in Aerospace Science,* vol. 43, pp. 1-41, 2007.

[26] M. L. Yu, Z. J. Wang and H. Hu, "A high-order spectral difference method for unstructured dynamic grids," *Computer & Fluids,* vol. 48, pp. 84-97, 2011.

[27] J. Nocedal and S. Wright, Numerical optimization, Springer, 2000.

# CHAPER 7. The Effects of Wing Planforms on the Aerodynamic Performance of Thin Finite-Span Flapping Wings

A paper published in the 50th AIAA ASM conference proceedings

Meilin Yu, Z. J. Wang and Hui Hu

## Abstract

A three-dimensional high-order unstructured dynamic grid based spectral difference (SD) Navier-Stokes (N-S) compressible flow solver with low Mach number preconditioning is used to investigate the effects of wing planforms on the aerodynamics performance of the thin finite-span flapping wings in this paper. Two types of wings, namely the rectangular and bio-inspired wings, are simulated and compared. The formation process of the ubiquitous two-jet-like wake patterns behind the finite-span flapping wing is explained at first. Then the effects of the wing planforms on the aerodynamics performance of the finite-span flapping wings are elucidated in terms of the evolutions and dynamic interaction among the leading edge vortices (LEV), trailing edge vortices (TEVs) and the wing tip vortices (TVs). Different types of LEVs have been discovered for different wing planforms with the flapping motion in the vertical direction, resulting in different aerodynamic performances. A combined plunging and pitching motion is then adopted to enhance the thrust production of the flapping wing, and it increases the amount of the thrust production by about thirty times when compared with the flapping motion only in the vertical direction.

### Nomenclature

$AOA$ = angle of attack

$a$ = speed of sound

$AR$ = aspect ratio

| | | |
|---|---|---|
| $C_T$ | = | thrust coefficient |
| $c$ | = | chord length |
| $E$ | = | total energy |
| $F, G, H$ | = | vectors of fluxes in the physical domain |
| $\tilde{F}, \tilde{G}, \tilde{H}$ | = | vectors of fluxes in the computational domain |
| $i, j, k$ | = | index of coordinates in x, y, z direction |
| $J$ | = | Jacobian matrix |
| $K$ | = | reduced frequency |
| $M$ | = | Mach number |
| $\dot{m}$ | = | mass flow rate |
| $\vec{P}$ | = | grid displacement |
| $p$ | = | non-dimensional pressure |
| $Q, \tilde{Q}$ | = | vectors of conservative variables in the physical and computational domains |
| $Re$ | = | Reynolds number based on the chord length |
| $r_5$ | = | fifth-order polynomial blending function |
| $St$ | = | Strouhal number |
| $s$ | = | normalized arc length |
| $t, \tau$ | = | time in the physical and computational domain |
| u,v,w | = | non-dimensional velocity in x, y, z direction |
| $\vec{v}_g$ | = | grid velocity |
| x,y,z | = | non-dimensional Cartesian coordinates in the physical domain |
| $\alpha$ | = | pitch angle of the airfoil |
| $\xi, \eta, \zeta$ | = | Cartesian coordinates in the computational domain |
| $\rho$ | = | non-dimensional density |
| $\phi$ | = | phase angle |
| $\omega_z$ | = | spanwise (z) vorticity |

## 1. Introduction

Research on the bio-inspired flow under low Reynolds number ($10^2$-$10^4$) regimes has increased greatly both in the experiment and computational fluid dynamic (CFD) communities during recent years, encouraged by the design needs of Unmanned Aerial Vehicles (UAVs) and Micro-Air-Vehicles (MAVs). Based on versatile research aims, both two-dimensional (2D) and three-dimensional (3D) unsteady vortex-dominated flows have been studied experimentally and numerically [1]. Among all the topics related to the flapping motion, wing/airfoil shape effects have been emphasized by some researchers [2,3,4]. For the 2D airfoil shape study, Shyy et al. [3] studied different airfoil performances for the low Reynolds number and concluded that airfoil shape can dramatically affect the aerodynamic performance. From the research, they found that thin airfoils with relative large cambers can enjoy better aerodynamic performance than their thick counterparts. Lentink and Gerritsma [2] confirmed that thin airfoils with aft camber perform better under low Reynolds number, compared with traditional thick airfoils. Obviously, airfoils can be treated as a wing with infinite aspect ratio (AR), which cannot reflect the influences of the wing tip vortices over the whole flow field. Therefore, studies of the 3D wing planform effects will help to unfold the 3D wing geometric influences on the vortex interactions, i. e. the wing tip vortices (TVs), leading edge vortices (LEVs) and trailing edge vortices interactions for different wing geometries.

According to the study [5], wings with low ARs (most insects have such kinds of wings [6]) are beneficial for the agile locomotion. Therefore, many studies [1,3,5,7,8,9,10,11] have been concentrated on the aerodynamic performances of low AR wings. It can be found that almost all these studies were focused on the unsteady lift generation of the hovering flight. Ellington et al. [9] first reported that the intense leading edge vortex (LEV) created by dynamic stall is the reason for the high-lift force generation during the hovering flight of the hawkmoth. They also pointed out that the spanwise flow is essential for the stability of such leading edge vortex. However, Birch and Dickinson [7] found that even there does not exist the spanwise flow, the LEV can still be stabilized for the flapping wings of the fruit fly. They confirmed that the downwash effect of the wing tip

vortex can explain the stability of the LEV. In fact, according to Ref. 0, under the regime of high Reynolds numbers, the spanwise flow can enhance the stability of the LEV, while for lower Reynolds numbers, wing tip vortex and wake vorticity play a vital role in prolonging the attachment of the LEV. Recently, Shyy et al. [11] further confirmed that the wing kinematics can greatly affect the wing tip effects on the aerodynamic performance of a low AR wing. For the cruise flight, von Ellenrieder et al. [12] and Parker et al. [13] have studied the 3D vortex structures after a finite-span flapping wing with two free ends. Their research was restricted to the effects of aerodynamic parameters and the wing motion kinemics on the wake structures. In Spentzos et al.'s [4] work, the wing tip effects on the dynamic stall are studied. They confirmed that different wing planforms could have similar flow topology. However, whether these conclusions can be extended generally to flapping wings and how the interaction between the wing tip vortex and the leading/trailing edge vortex affects the thrust/lift generation are still open questions. Here, we focus on the wing tip effects on the vortex flow over a series of low AR (=2.6772) fix-rooted wings with different planforms (namely, rectangular, elliptic, and bionic) during the cruise flight.

Since the phenomena in this study are vortex-dominated flows, high-order methods are needed for the numerical simulations due to their prominent low dissipation features. For the present study, a three-dimensional high-order unstructured dynamic grid based spectral difference (SD) Navier-Stokes (N-S) compressible flow solver was adopted. The spectral difference (SD) method [14] is a recently developed high-order method to solve compressible flow problems on simplex meshes. Its precursor is the conservative staggered-grid Chebyshev multi-domain method [15]. The general formulation of the SD method was first described in Ref. 0 and applied for computational electromagnetic problems. It is then extended to 2D Euler [16] and Navier-Stokes equations [17,18]. After that, Sun et al. [19] implemented the SD method for 3D N-S equations on unstructured hexahedral meshes. Later, a weak instability in the original SD method was found independently by Van den Adeele, et al. [20,21] and Huynh [22]. Huynh [22] further found that the use of Legendre-Gauss quadrature points as flux points results in a stable

SD method. This was later proved by Jameson [23] for the one dimensional linear advection equation. Based on Sun et al.'s [19] work, Yu et al. [24] further developed a Geometric Conservation Law (GCL) compatible SD method for dynamic grids and used it for bio-inspired flow simulations. Liang et al. [25] and Ou et al. [26] have developed dynamic grid based SD method for bio-inspired flow simulation as well.

The paper is further organized as follows. In section 2, the SD method, grid deformation strategy and simulation parameters are briefly introduced. Then numerical results are presented and discussed in section 3. There we explain the formation process of the ubiquitous two-jet-like phenomenon behind the finite-span flapping wing and compare the aerodynamic performances of flapping wings with different wing planforms and kinematics. Finally, conclusions are summarized in section 4.

## 2. Numerical Methods and Simulation Parameters

### 2.1 Governing Equations

A three-dimensional high-order Navier-Stokes (N-S) spectral difference solver for dynamic grids has been used for the present simulation. A brief introduction of the method will be presented here and readers can refer to Ref. 0 for details.

We consider the unsteady compressible Navier-Stokes (N-S) equations in conservation form in the physical domain $(t, x, y, z)$

$$\frac{\partial Q}{\partial t} + \frac{\partial F}{\partial x} + \frac{\partial G}{\partial y} + \frac{\partial H}{\partial z} = 0. \tag{1}$$

Herein, $Q = (\rho, \rho u, \rho v, \rho w, E)^T$ are the conservative variables, $\rho$ is the fluid density, $u, v$ and $w$ are the Cartesian velocity components, and $E$ is the total initial energy. $F, G, H$ are the total fluxes including both the inviscid and viscous flux vectors, i.e., $F = F^i - F^v$, $G = G^i - G^v$ and $H = H^i - H^v$. Detailed formulas for the fluxes can be found in Ref. 0. On assuming that the fluid obeys the perfect gas law, the pressure is related to the total initial energy by $E = \frac{p}{\gamma-1} + \frac{1}{2}\rho(u^2 + v^2 + w^2)$, which closes the solution system.

To achieve an efficient implementation, a time-dependent coordinate transformation from the physical domain $(t, x, y, z)$ to the computational domain $(\tau, \xi, \eta, \zeta)$, as shown in Fig. 1(a), is applied on Eq. (1), which is

$$\frac{\partial \tilde{Q}}{\partial \tau} + \frac{\partial \tilde{F}}{\partial x} + \frac{\partial \tilde{G}}{\partial y} + \frac{\partial \tilde{H}}{\partial z} = 0, \tag{2}$$

where

$$\begin{cases} \tilde{Q} = |J|Q \\ \tilde{F} = |J|\big(Q\xi_\tau + F\xi_x + G\xi_y + H\xi_z\big) \\ \tilde{G} = |J|\big(Q\eta_\tau + F\eta_x + G\eta_y + H\eta_z\big) \\ \tilde{H} = |J|\big(Q\zeta_\tau + F\zeta_x + G\zeta_y + H\zeta_z\big) \end{cases} \tag{3}$$

Herein, $\tau = t$, and $(\xi, \eta, \zeta) \in [-1,1]^3$, are the local coordinates in the computational domain. In the transformation shown above, the Jacobian matrix $J$ takes the following form

$$J = \frac{\partial(x, y, z, t)}{\partial(\xi, \eta, \zeta, \tau)} = \begin{pmatrix} x_\xi & x_\eta & x_\zeta & x_\tau \\ y_\xi & y_\eta & y_\zeta & y_\tau \\ z_\xi & z_\eta & z_\zeta & z_\tau \\ 0 & 0 & 0 & 1 \end{pmatrix}. \tag{4}$$

For a non-singular transformation, its inverse transformation must also exist, and the transformation matrix is

$$J^{-1} = \frac{\partial(\xi, \eta, \zeta, \tau)}{\partial(x, y, z, t)} = \begin{pmatrix} \xi_x & \xi_y & \xi_z & \xi_t \\ \eta_x & \eta_y & \eta_z & \eta_t \\ \zeta_x & \zeta_y & \zeta_z & \zeta_t \\ 0 & 0 & 0 & 1 \end{pmatrix}. \tag{5}$$

It should be noted that all the information concerning grid velocity $\vec{v_g} = (x_t, y_t, z_t)$ is related with $(\xi_\tau, \eta_\tau, \zeta_\tau)$ by

$$\begin{cases} \xi_\tau = -\vec{v_g} \cdot \nabla \xi \\ \eta_\tau = -\vec{v_g} \cdot \nabla \eta \\ \zeta_\tau = -\vec{v_g} \cdot \nabla \zeta \end{cases} \tag{6}$$

## 2.2 Space discretization

The SD method is used for the space discretization. In the SD method, two sets of points are given, namely the solution and flux points, as shown in Fig. 1(b) for a 2D

quadrilateral element. Unknown solutions or degrees of freedom (DOFs) are defined at the solution points (SPs), and fluxes are calculated on flux points (FPs). In the present study, the solution points are chosen as the Chebyshev-Gauss quadrature points. For a $P^{N-1}$ reconstruction, $N$ solution points are needed in 1D and are specified as

$$\xi_s = -\cos\left(\frac{2s-1}{2N}\cdot\pi\right), s = 1,2,\cdots,N \tag{7}$$

It has been proved in Ref. 23 that the adoption of the Legendre-Gauss quadrature points as the flux points can ensure the stability of the SD method. Therefore, the flux points are selected to be the Legendre-Gauss points with end points as -1 and 1. These points are denoted as $\beta_f, f = 0,1,\cdots,N$.

Two sets of Lagrange polynomials based on the solution points and flux points respectively can be specified as follows.

SPs based Lagrange polynomial:

$$L_{s,i}(\xi) = \prod_{s=1,s\neq i}^{N} \frac{\xi-\xi_s}{\xi_i-\xi_s}, i = 1,2,\cdots,N \tag{8}$$

FPs based Lagrange polynomial:

$$L_{f,i}(\beta) = \prod_{f=0,f\neq i}^{N} \frac{\beta-\beta_f}{\beta_i-\beta_f}, i = 0,1,\cdots,N \tag{9}$$

The reconstruction of the SD method is stated briefly as follows. First of all, the inviscid fluxes are reconstructed. Note that the fluxes related to the grid movement are incorporated into the inviscid fluxes, e.g., $\tilde{F}^i = |J|\left(Q\xi_\tau + F^i\xi_x + G^i\xi_y + H^i\xi_z\right)$. The conservative variables $Q_f$ on the flux points are interpolated from the conservative variables $Q_s$ on the solution points via a tensor production of the 1D Lagrange polynomial Eq. (10), which takes the following form

$$Q_f(\xi,\eta,\zeta) = \sum_{k=1}^{N}\sum_{j=1}^{N}\sum_{i=1}^{N} Q_s\left(\xi_i,\eta_j,\zeta_k\right)L_{s,i}(\xi)L_{s,j}(\eta)L_{s,k}(\zeta). \tag{10}$$

Then the fluxes can be reconstructed at the flux points using $Q_f$. Note that this reconstruction is continuous within a standard element, but discontinuous on the cell

interfaces. Therefore, a Riemann flux or common flux needs to be specified on the interface to ensure conservation. Since the flow regime for flapping flight is almost incompressible and the present governing equations are compressible N-S equations, the Riemann solver should retain good performance at low Mach numbers. The AUSM[+]-up Riemann solver [27] for all speed is implemented for the present simulation and is proved to behave well at low Mach numbers. The procedures to reconstruct the common fluxes from the AUSM[+]-up Riemann solver are stated as follows.

Denote the face normal of arbitrary interface by $\vec{n}$, then the interface mass flow rate $\dot{m}_{1/2}$ reads

$$\dot{m}_{1/2} = a_{1/2}M_{1/2}\begin{cases}\rho_L & if\ M_{1/2} > 0 \\ \rho_R & otherwise\end{cases}, \tag{11}$$

where the subscript '1/2' stands for the interface, $a$ and $M$ are speed of sound and Mach number respectively. Note that the grid velocity has been included in the interface Mach number $M$. The numerical normal fluxes $\tilde{F}^i$, $\tilde{G}^i$ and $\tilde{H}^i$ can then be specified as

$$\begin{cases}\tilde{F}^i = \left(\dot{m}_{1/2}\begin{cases}\psi_L & if\ \dot{m}_{1/2} > 0 \\ \psi_R & otherwise\end{cases} + P_{1/2}\right)|J||\nabla\xi|sign(\vec{n}\cdot\nabla\xi) \\ \tilde{G}^i = \left(\dot{m}_{1/2}\begin{cases}\psi_L & if\ \dot{m}_{1/2} > 0 \\ \psi_R & otherwise\end{cases} + P_{1/2}\right)|J||\nabla\eta|sign(\vec{n}\cdot\nabla\eta), \\ \tilde{H}^i = \left(\dot{m}_{1/2}\begin{cases}\psi_L & if\ \dot{m}_{1/2} > 0 \\ \psi_R & otherwise\end{cases} + P_{1/2}\right)|J||\nabla\zeta|sign(\vec{n}\cdot\nabla\zeta)\end{cases} \tag{12}$$

where $\psi = (1, u, v, w, (E + p)/\rho)^T$, $P = (0, pn_x, pn_y, pn_z, pv_{g,n})^T$, with $n_x, n_y, n_z$ and $v_{g,n}$ specifying the face normal components in x, $y$ and z direction and the grid velocity in the face normal direction respectively.

After this, the derivatives of the inviscid fluxes are calculated on the solution points using the following formulas,

$$\frac{\partial\tilde{F}^i}{\partial\xi}(\xi,\eta,\zeta) = \sum_{k=1}^{N}\sum_{j=1}^{N}\sum_{i=0}^{N}\tilde{F}^i(\xi_i,\eta_j,\zeta_k)L'_{f,i}(\xi)L_{s,j}(\eta)L_{s,k}(\zeta)$$

$$\frac{\partial\tilde{G}^i}{\partial\eta}(\xi,\eta,\zeta) = \sum_{k=1}^{N}\sum_{j=0}^{N}\sum_{i=1}^{N}\tilde{G}^i(\xi_i,\eta_j,\zeta_k)L_{s,i}(\xi)L'_{f,j}(\eta)L_{s,k}(\zeta) \tag{13}$$

$$\frac{\partial \widetilde{H}^i}{\partial \zeta}(\xi,\eta,\zeta) = \sum_{k=0}^{N}\sum_{j=1}^{N}\sum_{i=1}^{N}\widetilde{H}^i(\xi_i,\eta_j,\zeta_k)L_{s,i}(\xi)L_{s,j}(\eta)L'_{f,k}(\zeta)$$

Since the viscous fluxes are functions of both the conservative variables $Q$ and their derivatives $\nabla Q$, slightly more involved reconstruction procedures are needed. In the present study, the approach proposed in [28], also known as 'BR1', is adopted. The implementation of this approach in SD is briefly introduced as follows.

Let $\vec{R} = \nabla Q$, and on transforming this formula from the physical domain to the computational domain, we obtain the three components of $\vec{R}$ in the conservation form as

$$R^x = \frac{1}{|J|}\left(\frac{\partial |J|Q\xi_x}{\partial \xi} + \frac{\partial |J|Q\eta_x}{\partial \eta} + \frac{\partial |J|Q\zeta_x}{\partial \zeta}\right)$$
$$R^y = \frac{1}{|J|}\left(\frac{\partial |J|Q\xi_y}{\partial \xi} + \frac{\partial |J|Q\eta_y}{\partial \eta} + \frac{\partial |J|Q\zeta_y}{\partial \zeta}\right). \qquad (14)$$
$$R^z = \frac{1}{|J|}\left(\frac{\partial |J|Q\xi_z}{\partial \xi} + \frac{\partial |J|Q\eta_z}{\partial \eta} + \frac{\partial |J|Q\zeta_z}{\partial \zeta}\right)$$

Then using the conservative variables $Q_f$ on the flux points, the derivatives in Eq. (16) on the solution points can be calculated following the procedure as shown in Eq. (15). Note that the common conservative variables $Q^{com}$ on element interfaces are used in the derivative calculation. In BR1, $Q^{com}$ is the average of the left and right solutions on the interface,

$$Q^{com} = \frac{Q^L + Q^R}{2}. \qquad (15)$$

After this, the gradient of $Q$ is then interpolated back to flux points following the procedure as shown in Eq. (12) and the viscous fluxes can then be calculated on flux points. Again, the gradient of $Q$ from the aforementioned reconstruction is generally discontinuous on the element interface, and BR1 is used to provide a common gradient $\nabla Q^{com}$ on the element interface,

$$\nabla Q^{com} = \frac{\nabla Q^L + \nabla Q^R}{2}. \qquad (16)$$

Thus the viscous fluxes $\tilde{F}^v$, $\tilde{G}^v$, and $\tilde{H}^v$ on flux points are uniquely specified in a local cell, and the flux derivatives on solution points can then be calculated via the approach as shown in Eq. (15).

Once all flux derivatives are available, the DOFs can be updated with either explicit or implicit time integrations.

### 2.3 Dynamic grids strategy

In order to solve problems with moving grids, it is necessary to design a grid moving algorithm. In this study, a blending function approach proposed in Ref. 29 is used to reconstruct the whole physical domain. The fifth-order polynomial blending function reads

$$r_5(s) = 10s^3 - 15s^4 + 6s^5, s \in [0,1] \tag{17}$$

It is obvious that $r_5'(0) = 0$, $r_5'(1) = 0$, which can generate a smooth variation at both end points during the mesh reconstruction. Herein, 's' is a normalized arc length, which reflects the 'distance' between the present node and the moving boundaries. s=0 means that the present node will move with the moving boundary, while s=1 means that the present node will not move. Therefore, for any motion (transition, rotation), the change of the position vector $\vec{P}$ is

$$\Delta\vec{P}_{present} = (1 - r_5)\Delta\vec{P}_{rigid} \tag{18}$$

After these manipulations, a new set of mesh nodes can be calculated based on $\Delta\vec{P}$. It is clear that for systems with complex relative motions, the algebraic algorithm for the grid motion will be hard to design. However, for many cases this method enjoys its remarkable simplicity and efficiency.

### 2.4 Problem statements

Rectangular and bio-inspired flapping wings, as shown in Fig. 2 are studied here. Wing surface grids and streamwise grids on the symmetric plane are also displayed in Fig. 2.

The grid deformation strategy is specified as follows. Suppose that all Lagrangian control points on the flapping wing oscillate only on the plane perpendicular to the spanwise axis. The maximum position of the profile in the plane perpendicular to the chordwise axis is set to be a parabola $h = h_0 r^2$ where $r \in [0,1]$ is the distance from the wing root to the Lagrangian control point normalized by the wing span and $h_0$ is the flapping amplitude of the wingtip. The rigid-body plunging function for one particular position $(x_s, y_s, z_s)$ on the flapping wing is given as follows,

$$x = x_s, z = z_s, y = y_s + h_s\sin(\omega t) \tag{19}$$

where $h_s$ is determined from the aforementioned parabola. Then the blending function Eq. (19) and the motion control function Eq. (20) are used to determine the movement of other grid points. Herein, $\Delta\vec{P}_{rigid}$ is specified as $\Delta y$ on the surface of the flapping wing.

For the combined pitching and plunging motion, the pitching part is controlled as below

$$\begin{pmatrix} x_{present} - x_c \\ y_{present} - y_c \end{pmatrix} = \begin{pmatrix} \cos(\Delta\alpha) & -\sin(\Delta\alpha) \\ \sin(\Delta\alpha) & \cos(\Delta\alpha) \end{pmatrix} \begin{pmatrix} x_{former} - x_c \\ y_{former} - y_c \end{pmatrix} \tag{20}$$

with $y_c = h_{c,s}\sin(\omega t)$ and $\alpha = \alpha_0 cos(\omega t + \phi_0)$. According to the optimal thrust generation conditions suggested by Anderson *et al.* [30], $\phi_0$ is set as 75$^o$. Herein, $\Delta\vec{P}_{rigid}$ is specified as $(\Delta x, \Delta y)$ on the surface of the flapping wing.

The studied finite-span flapping wings have the same wing span, aspect ratio of the planform (defined as the ratio of the square of the wing span to the planform area, $L_{span}^2/Area$) and the kinematic parameters of the flapping motion. In the present study, the Strouhal number ($Str$) of the finite-span flapping wings was selected to be well within the optimal range usually used by flying insects and birds and swimming fishes (i.e., 0.2 < $Str$ < 0.4). For all the simulations during the present study, the Mach number of the free stream is set to be 0.05, under which the flow is almost incompressible. The aspect ratios for all wings are set as 2.6772. The Reynolds number ($Re$) based on the free stream velocity and the averaged chord length (the planform area divided the wing span, $Area/L_{span}$) is 1,200. The reduced frequency ($k$) of the flapping motion is 3.5, and the

Strouhal number ($Str$) of the wingtip, based on the definition in Ref. 31, is 0.38. All these parameters are from the experimental setup stated in Ref. 32. The space discretization accuracy for the simulation is of third order, and the time integration is performed with the explicit three stage TVD Runge-Kutta method [33].
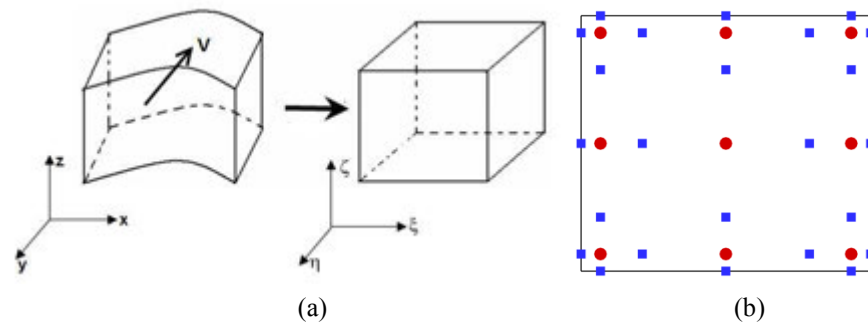


**Figure 1.** (a) Transformation from a moving physical domain to a fixed computational domain; (b) Distribution of solution points (circles) and flux points (squares) in a standard quadrilateral element for a third-order accurate SD scheme.
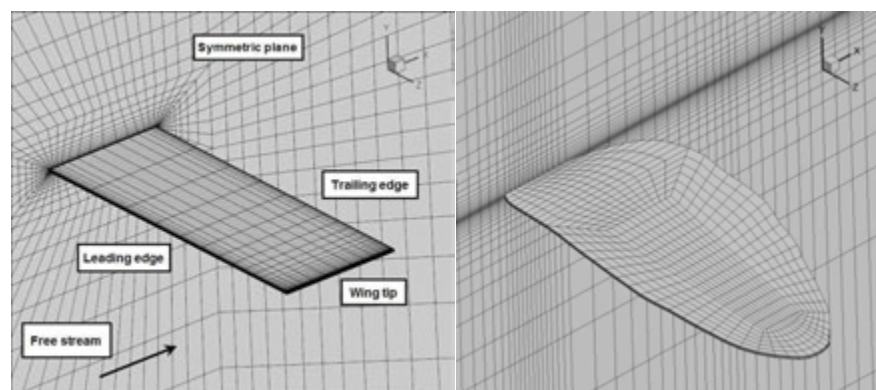


**Figure 2.** Wing surface and root plane meshes for rectangular (left) and bio-inspired (right) wings.

## 3. Numerical Results and Discussions

The comparisons of the instantaneous vorticity distributions from the numerical simulations and those from experimental measurements in the chordwise cross plane at 50%, 75% and 100% wingspan (i.e., wingtip) and the corresponding time-averaged velocity fields are displayed in Fig. 3. Note that the wake structures at 50% wingspan from the numerical simulations bare good visual agreement with the experimental results

at the same position. However, at 75% wingspan and the wingtip, numerical results exhibit more elaborate small vortices structures than the experimental results. From the corresponding time-averaged velocity fields at all three positions as displayed in Fig. 3, it is found that the numerical simulations capture the qualitative features of the wakes indicated by experimental measurements. Specifically, the experimental measurements show a von Karman vortex street type wake at 50% wingspan, which is well captured by the numerical simulations. Although numerical simulations show more elaborate vortices structures at 75% wingspan and the wingtip, the time-averaged results show the similar flow topology as revealed by the experimental results --- jet-like flow structures, which indicates the momentum surplus. Furthermore, these jet-like flow structures are not formed merely by a single inverse von Karman vortex street, but the combination of several inverse von Karman vortex streets (wingtip) or even the mixture of both regular and inverse ones (75% wingspan), which has been reported as bifurcated jets wake pattern in Dong et al.'s [8] study for a free-end finite-span wing. These interesting wake phenomena are considered to be closely tied to the wingtip vortices effects, which will be thoroughly discussed next.



(a)

(b)



(c)
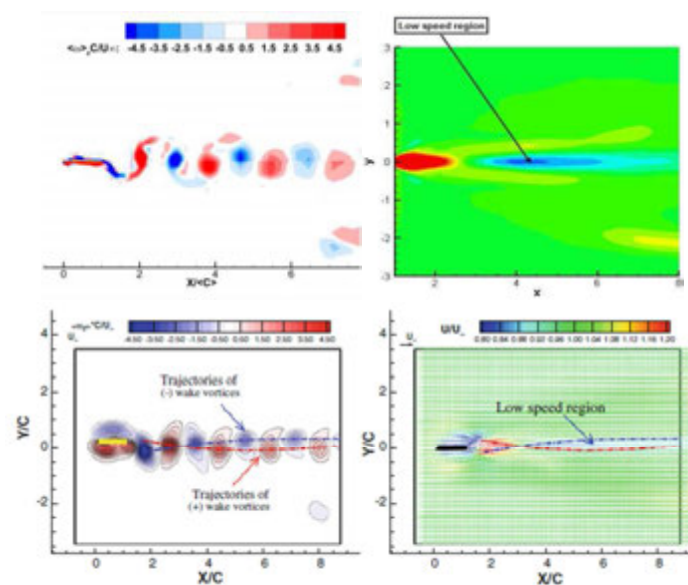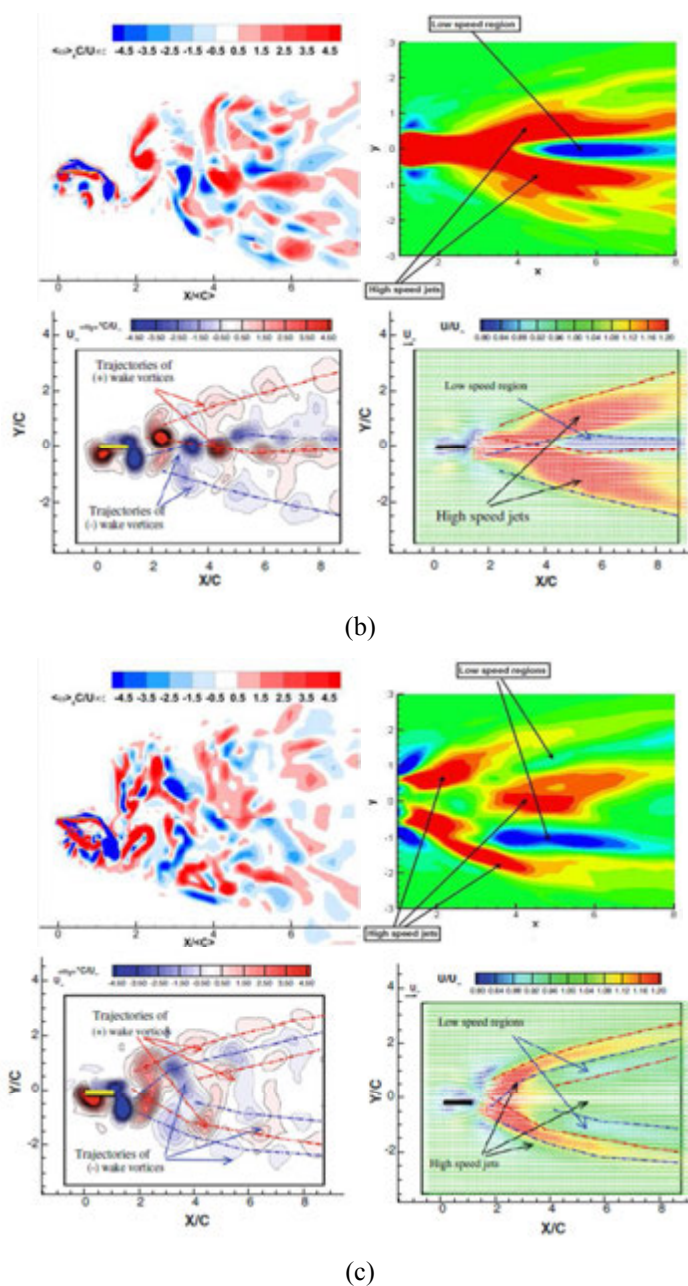
**Figure 3.** Instantaneous vorticity fields and the corresponding time-averaged velocity fields at (a) 50%, (b) 75% wingspan and (c) wingtip for the flapping rectangular wing. Left two columns: numerical results; Right two columns: experimental results (Courtesy of H. Hu, et al.[0]).

### 3.1  Two-Jet-Like Wake Patterns Formation

The wake vortex structures of the flapping rectangular wings from perspective and side views are shown in Fig. 4(a) and (b) respectively. In these figures, the vortex structures

are indicated by the Q-criterion colored with the streamwise velocity. The Q-criterion is a Galilean-invariant vortex criterion, which is defined as follows

$$Q = \frac{1}{2}\left(R_{ij}R_{ij} - S_{ij}S_{ij}\right) = \frac{1}{2}\frac{\partial u_i}{\partial x_j}\frac{\partial u_j}{\partial x_i} \tag{21}$$

where $R_{ij} = \frac{1}{2}\left(\frac{\partial u_i}{\partial x_j} - \frac{\partial u_j}{\partial x_i}\right)$, is the angular rotation tensor, and $S_{ij} = \frac{1}{2}\left(\frac{\partial u_i}{\partial x_j} + \frac{\partial u_j}{\partial x_i}\right)$, is the rate-of-strain tensor. The different vortices have been marked out with rectangular windows or solid arrows which indicate the rotation directions. It is clear from the figures that the complex vortex system around the flapping wing can be decomposed into four parts, namely trailing edge vortices (TEVs), leading edge vortices (LEVs) and tip vortices (TVs), and the entangled vortices (EVs) due to the interactions among TEVs, TVs and LEVs. Similar wake phenomena have been reported by Dong, et al. [8] for free-end finite-span wings except the complex EVs. This might be due to the fact that in the present study a thin wing with shape edges are used for the simulations while in the aforementioned literatures, relatively thick wings are adopted in the simulations.

It has been reported in Ref. 0 that the formation of the two-jet-like wake patterns behind the flapping wing is closely related to the existence of tip vortices. But the reasons for the formation process of the bifurcated jet were not fully analyzed. Herein, a detailed observation of the bifurcated jet effects is shown in Fig. 4(c) for the fixed-root flapping rectangular wing. The figure shows the 3D vorticity fields indicated by the Q-criterion and the spanwise vorticity field at the 75% wingspan. The trajectories of both clockwise (-) and anti-clockwise (+) vortices are also schematically plotted in the figure. Furthermore, the jet bifurcation position is determined by examining the starting point of the two-jet-like wake patterns from the time-averaged velocity fields in Fig. 3. It is observed from the figure that the jet bifurcation occurs when TVs intensively interact with the TEVs and many elaborate small vortices appear in this region.

In order to further examine the physics behind this, a combined flapping and pitching motion with pitch leading plunge 75$^\circ$ is used to reduce the separation from the leading edge and the wingtip, which makes the wake vortex structures much clearer as shown in Fig. 5(a). Note that with this combined motion, the two-jet-like patterns still exists at the

75% wingspan as shown in Fig. 6. From Fig. 5(b), it is obvious that the upper branch of the bifurcated jet is formed by an anti-clockwise vortex row consisting of TEVs and a clockwise vortex row consisting of TVs; while the lower branch of the bifurcated jet is formed by an anti-clockwise vortex row consisting of TVs and a clockwise vortex row consisting of TEVs. The reasons why TVs can contribute to the spanwise vorticity are illustrated in Fig. 5(b). Let's use TVs2, TEVs3 and TVs3 to explain the process. Because of the existence of TVs2, the end part of the TEVs near the wingtip will be dragged gradually from the 'z' direction to the 'y' direction during the flapping stroke, which indicates that certain amount of vorticity in the vertical (y) direction is generated. The induced rotational velocity field is schematically denoted with the blue dashed arrow near the wingtip part of TEVs3. This velocity field will bend the bottom end of TVs3 to TEVs2, and finally TVs3 have a vorticity component in the spanwise direction. It is not hard to examine that this induced vorticity component is negative as denoted with the blue dashed arrow near the bottom part of TVs3. This explains the formation of the spanwise vorticity contribution from the TVs and further elucidates the formation of the two-jet-like wake patterns. Note that the above explanation will also work for the flapping case aforementioned, although the existence of small vortices in that case makes the two-jet-like wake formation process hard to distinguish. Similar explanations can apply to the formation of the wake pattern at the wingtip.
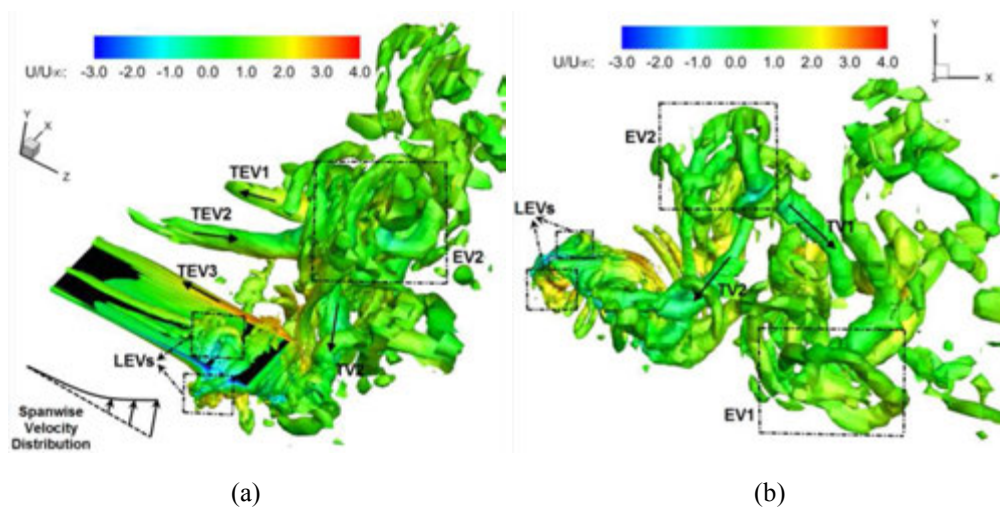


(a)                                              (b)
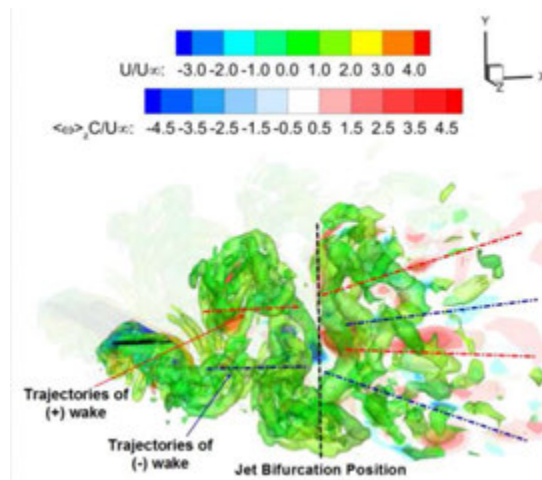
(c)

**Figure 4.** Vortex topology around the flapping rectangular wing. Vortex structures are indicated by the Q-criterion and colored by the streamwise velocity. (a) Perspective view. (b) Side view. (c) Perspective view of the vortex structures near the wingtip region and the spanwise vorticity field of the chordwise cross plane at 75% wingspan.
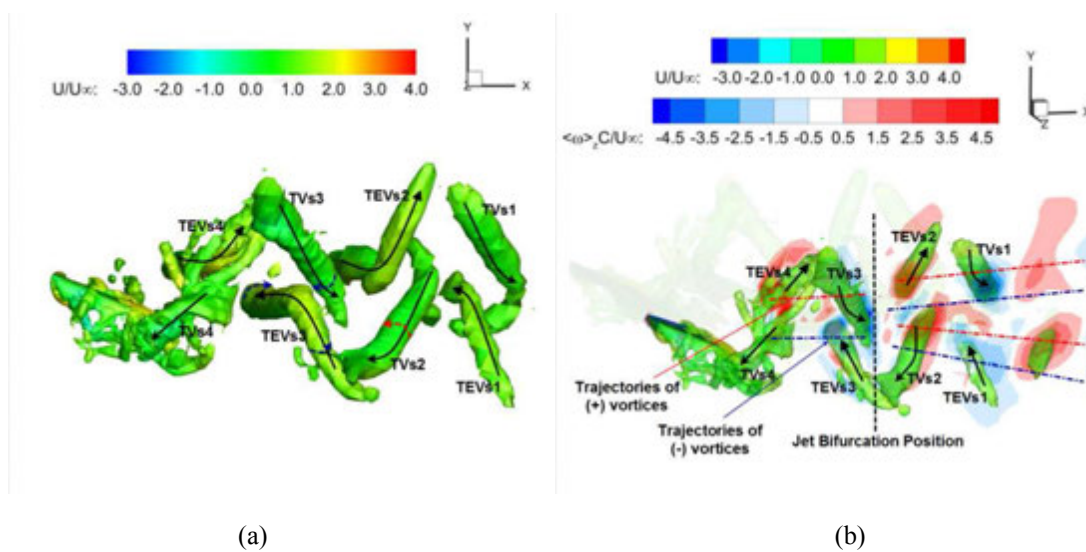


(a)                                      (b)

**Figure 5.** Vortex topology around the rectangular wing with a combined plunging and pitching motion. Vortex structures are indicated by the Q-criterion and colored by the streamwise velocity. (a) Side view. (b) Perspective view of the vortex structures near the wingtip region and the spanwise vorticity field of the chordwise cross plane at 75% wingspan.
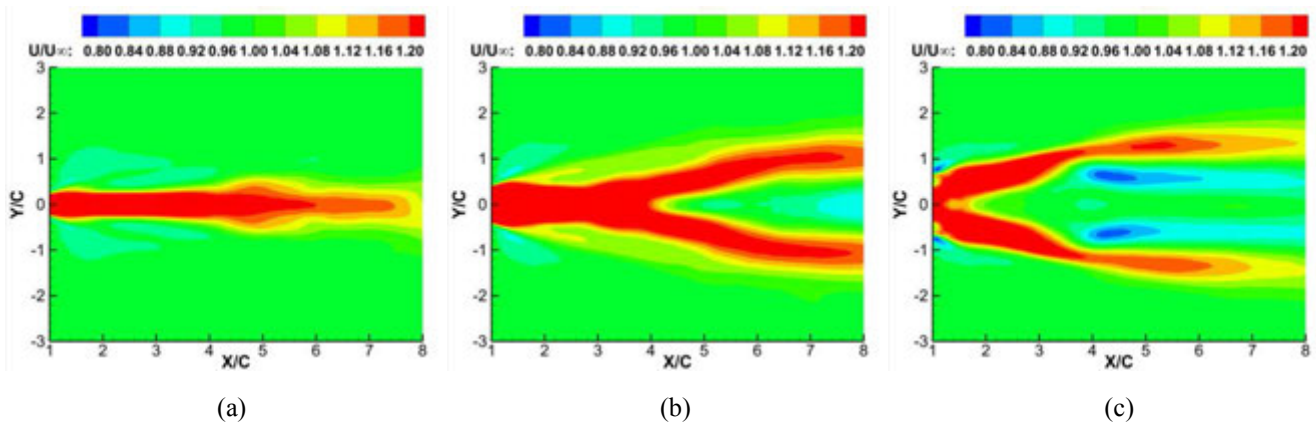
**Figure 6.** Time-averaged velocity fields at (a) 50%, (b) 75% and (c) 100% wingspan for the rectangular wing with a combined plunging and pitching motion.

### 3.2 Aerodynamic Performance Comparisons of Different Wing Planforms

The comparison of thrust coefficient histories for the rectangular and bio-inspired wings with the flapping motion is displayed in Fig. 7(a). The contributions from the pressure force and viscous force for the thrust are shown in Fig. 7(b) and (c). From these figures, it is found that during one flapping cycle the rectangular wing experiences both larger thrust and drag than the bio-inspired wing. These differences mainly come from the contributions from the pressure force. It is also observed that the bio-inspired wing experience less drag from the viscous force (i.e. shear stress). The time-averaged thrust coefficients for these two wings as presented in Table 1. From the table, it is clear that the rectangular wing generates larger thrust than the bio-inspired wing, and for both wings, the pressure force dominates the thrust production. Note that both thrust coefficient histories for the two wings in Fig. 7 display certain small-scale unsteady fluctuations. This can be explained by the rich vortex structures around the flapping wings as shown in Fig. 8. In this figure, the vortex structures indicated by the Q-criterion and colored by the streamwise velocity for the rectangular wing are shown in the upper row. The phases for the four instantaneous flow fields are $0^o, 90^o, 180^o$ and $270^o$ respectively. The corresponding flow fields at the same phases for the bio-inspired wing with the same Q value are displayed in the lower row of Fig. 8. It is found that more small vortex structures are generated around the rectangular wing especially in the wingtip region.

This is due to the relatively sharp tip edge of the rectangular wing and this phenomenon indicates that more flapping energy has been wasted as these small vortices are hard to be efficiently collected to generate thrust. It is also found that the LEVs around the rectangular wing at phases $0^o$ and $180^o$ are stronger than those around the bio-inspired wing. As will be discussed momentarily, at these two phases the flapping wings will experience thrust peaks, which are believed to closely tie to the behaviors of the LEVs. Further, this phenomenon can help to explain the reason why the rectangular wing generates more thrust than the bio-inspired wing does at the present simulation parameters.

As aforementioned, the pressure force dominates the thrust generation in the present cases. Based on careful examinations of the flow fields it is found that the pressure change on the leading and trailing edges of the flapping wings mainly occurs in the regions near the wingtip, indicating that the thrust generation is dominated by the outer 50% regions of the flapping wings. It is obvious that at these regions flapping wings have larger flapping amplitudes and speeds and can result in a local dynamic stall. The associated LEVs can be stabilized by the downwash effects of the TVs and can induce a local low pressure region near the leading edge of the flapping wing. This is beneficial for the thrust production. Since the LEVs of the rectangular wing are more intensively interacting with the leading edge than the bio-inspired wing, a lower pressure region near the wingtip of the rectangular wing makes it experience a larger thrust peak than the bio-inspired wing as observed from the thrust coefficient histories (Fig. 7).

The spanwise vorticity fields and the time-averaged velocity fields of the bio-inspired wing in the chordwise cross plane at 50%, 75% wingspan and wingtip are displayed in Fig. 9. The phases of the flow fields and contour levels are the same as those shown in Fig. 3 for the rectangular wing. Different features of the flow fields can be found by comparing Fig. 9 and 3. At the 50% wingspan, it is clear that the bio-inspired wing has smaller region with velocity deficit than the rectangular wing does. However, at the wingtip, because of the wing shape difference the bio-inspired wing almost does not generate thrust while the rectangular wing still has apparent jet patterns. At the 75%

wingspan, the two-jet-like pattern for the bio-inspired wing has a different shape compared with the rectangular wing, and the high speed region is smaller than the rectangular wing. Since it has been found that the thrust production is mainly determined by the outer 50% regions of the flapping wing, all the discussed wake features for the rectangular and bio-inspired wings show the reasons why the rectangular wing generates more thrust than the bio-inspired wing from the aspect of wake structures.

## 3.3 Aerodynamic Performances for Wings with Combined Plunging and Pitching Motions

Note that according to Table 1 the time-averaged thrust coefficient for the flapping rectangular wing is very small. This can be explained like this. Based on the knowledge that the pressure force dominates the thrust generation, two parameters, namely the effective wing area projection in the streamwise direction and the pressure difference, will determine the output of the thrust during the flapping flight. Since thin wings are adopted in the present study, for the flapping motion in the vertical direction, the wing area projection in the streamwise direction is very small. This is unfavorable to the thrust production. Therefore, it becomes necessary to add certain pitching motion to the flapping motion to enlarge the wing area projection in the streamwise direction. However, the phase lag between the plunging motion and the pitching motion should be carefully designed as this phase lag will affect the adjustment of effective angle of attack (AoA). If this parameter is not assigned properly, the performance of the wing can even degrade. As aforementioned, the phase lag between the plunging motion and the pitching motion is set to be $75^o$ as suggested by Anderson et al. [30].

The histories of the total thrust coefficient and the component contributed by the pressure force for the rectangular wing under combined plunging and pitching motions are displayed in Fig. 10. The corresponding vortex structures indicated by the Q-criterion around the wing are shown in Fig. 11 for four phases, namely $0^o$, $90^o$, $180^o$ and $270^o$. It is concluded that under the combined motions, the flapping wing can generate much larger (about thirty times) thrust than the flapping case. Moreover, because of the

effective AoA adjustment of the pitching motion, the breakdown of vortices becomes less severe, which indicates less energy waste.

## 4. Conclusions

In this study, a three-dimensional high-order unstructured dynamic grid based spectral difference (SD) Navier-Stokes (N-S) flow solver was used to investigate the effects of wing planforms on the aerodynamics performance of the thin finite-span flapping wings. The formation process of the two-jet-like wake patterns behind the finite-span flapping wing is found to be closely related to the interaction between TEVs and TVs. It is found that for the flapping motion in the vertical direction, the rectangular wing can generate larger thrust than the bio-inspired wing because of the dynamic behaviors of LEVs. However, the thrust production for such kind of motions is very small. In order to enhance the thrust production, a combined plunging and pitching motion is adopted and it increases the amount of the thrust production by about thirty times when compared with the flapping motion only in the vertical direction.

## References

[1] W. Shyy, H. Aono, S. K. Chimakurth, P. Trizila, C. K. Kang, C. E. S. Cesnik and H. Liu, Recent progress in flapping wing aerodynamics and aeroelasticity, Prog. Aerosp. Sci. (2010), vol.46, iss.7, pp.284-327.

[2] D. Lentink and M. Gerritsma, Influence of airfoil shape of performance in insect flight, AIAA Paper, 2003-3447.

[3] W. Shyy, M. Berg and D. Ljungqvist, Flapping and flexible wings for biological and micro air vehicles, Prog. Aerosp. Sci. (1999), vol.35, iss.5, pp.455-505.

[4] A. Spentzos, G. N. Barakos, K. J. Badcock, B. E. Richards, F. N. Coton, R. A. McD., Galbraith E. Berton and D. Favier, Computational fluid dynamics study of three dimensional dynamic stall of various planform shapes, Journal of Aircraft (2007), vol. 44, No. 4, pp. 1118-1128.

[5] W. Shyy, Y. Lian, J. Tang, D. Viieru, and H. Liu, Aerodynamics of low Reynolds number flyers, Cambridge University Press, 2008.

[6] M. J. Ringuette, M. Milano, and M. Gharib, Role of the tip vortex in the force generation of low-aspect-ratio normal flat plates, J. Fluid Mech. (2007), vol. 581, pp. 453-468.

[7] J. M. Birch, and M. H. Dickinson, Spanwise flow and the attachment of the leading-edge vortex on insect wings, Nature (London, 2001), vol. 412, pp. 729–733.

[8] H. Dong, R. Mittal, and F. M. Najjar, Waketopology and hydrodynamic performance of low-aspect-ratio flapping foils. J. Fluid Mech., 566, 0 (2006).

[9] C. P. Ellington, C. van den Berg, A. P. Willmott, and A. L. R. Thomas, Leading-edge vortices in insect flight, Nature (London, 1996), vol. 384, pp. 626–630.

[10] H. Hu, L. Clemons, and H. Igarashi, An experimental study of the unsteady vortex structures in the wake of a root-fixed flapping wing, Exp. Fluids, vol.51, No.2, 2011, pp347–359.

[11] W. Shyy, P. Trizila, C. Kang, and H. Aono, Can tip vortices enhance lift of a flapping wing?, AIAA J. (2009), Vol. 47, pp. 289-293.

[12] K. D. von Ellenrieder, K. Parker, and J. Soria, Flow structure behind a heaving and pitching finite-span wing, J. Fluid Mech. (2003), vol. 490, pp. 129-138.

[13] K. Parker, K. D. von Ellenrieder, and J. Soria, Using stereo multigrid DPIV (SMDPIV) measurements to investigate the vortical skeleton behind a finite-span flapping wing, Exp. in Fluids (2005), vol. 39, No. 2, pp. 281-298.

[14] Y. Liu, M. Vinokur, Z. J. Wang. Discontinuous spectral difference method for conservation laws on unstructured grids, J. Comput. Phys. (2006), vol. 216, pp. 780–801.

[15] D. A. Kopriva and J. H. Kolias. A conservative staggered-grid Chebyshev multi-domain method for compressible flows. J.Comput.Phys.,125(1):244–261, 1996.

[16] Z. J. Wang, Y. Liu, G. May, A. Jameson, Spectral difference method for unstructured grids II: extension to the Euler equations. J. Sci. Comput. (2007), vol. 32, pp. 45–71.

[17] G. May, A. Jameson, A spectral difference method for the Euler and Navier–Stokes equations (2006), AIAA Paper No.2006–304.

[18] Z. J. Wang, Y. Sun, C. Liang and Y. Liu, Extension of the SD method to viscous flow on unstructured grids. In Proceedings of the 4th international conference on computational fluid dynamics, Ghent, Belgium, July 2006.

[19] Y. Z. Sun, Z. J. Wang, Y. Liu, High-order multidomain spectral difference method for the Navier-Stokes equations on unstructured hexahedral grids, Commun. Comput. Phys. (2006), vol. 2, No. 2, pp. 310-333.

[20] K. Van den Abeele and C. Lacor. An accuracy and stability study of the 2D spectral volume method, J. Comput. Phys. (2007), vol. 226, pp.1007–1026.

[21] K. Van den Abeele,C. Lacor, and Z. J. Wang. On the stability and accuracy of the spectral difference method, J.Sci.Comput. (2008), vol. 37, pp.162–188.

[22] H. T. Huynh. A flux reconstruction approach to high-order schemes including discontinuous Galerkin methods, AIAA Paper, 2007-4079.

[23] A. Jameson, A proof of the stability of the spectral difference method for all orders of accuracy, J. Sci. Comput. (2010), doi: 10.1007/s10915-009-9339-4.

[24] M. L. Yu, Z. J. Wang and H. Hu, A high-order spectral difference method for unstructured dynamic grids, Computers & Fluids, 2011, Vol.48, No. 1, 2011, pp.84-97.

[25] C. L. Liang, K. Ou, S. Premasuthan, A. Jameson and Z. J. Wang, High-order accurate simulations of unsteady flow past plunging and pitching airfoils, Computer & Fluids (2010), vol.40, pp.236-248.

[26] K. Ou, P. Castonguay and A. Jameson, 3D flapping wing simulation with high order spectral difference method on deformable mesh, AIAA Paper, 2011-1316.

[27] M. S. Liu, A sequel to AUSM, Part 2: AUSM$^+$-up for all speeds, J. Comput. Phys. (2006), vol. 214, pp.137–170.

[28] F. Bassi and S. Rebay, "A high-order accurate discontinuous finite element method for the numerical solution of the compressible Navier–Stokes equations," J. Comput. Phys., vol. 131, pp. 267-279, 1997.

[29] P. O. Persson, J. Peraire and J. Bonet, Discontinuous Galerkin solution of the Navier-Stokes equations on deformable domains, Computer Methods in Applied Mechanics and Engineering (2009), vol. 198, pp. 1585-1595.

[30] J. M. Anderson, K. Streitlien, D. S. Barrett, and M. S. Triantafyllou, Oscillating foils of high propulsive efficiency. J. Fluid Mech., 360, 41 (1998).

[31] G. K. Taylor, R. L. Nudds, and A. L. R. Thomas, Flying and swimming animals cruise at a Strouhal number tuned for high power efficiency, Nature (London, 2003), Vol. 425, pp. 707–711.

[32] H. Hu, L. Clemons and H. Igarashi, "An experimental study of the unsteady vortex structures in the wake of a root-fixed flapping wing," Experiments in Fluids, vol. 51, pp. 347-359, 2011.

[33] C. W. Shu, "Total-Variation-Diminishing time discretizations," SIAM J. Sci. Stat. Comput., vol. 9, pp. 1073-1084, 1988.
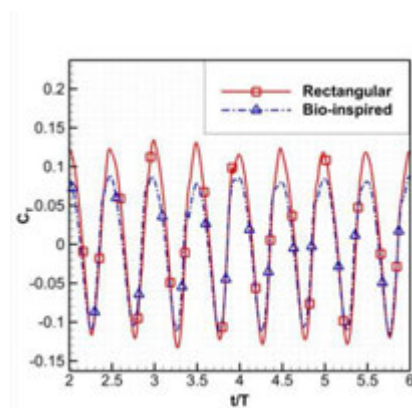
(a)
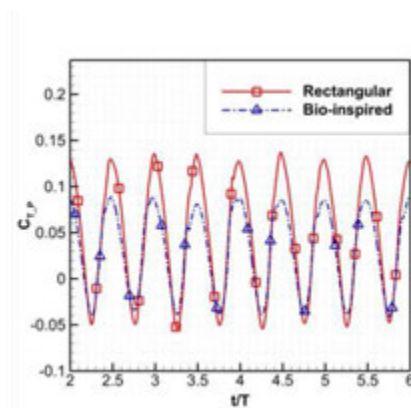


(b)
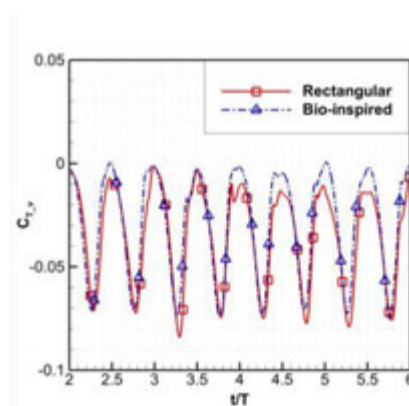


(c)

**Figure 7.** The thrust coefficient histories for different wing planforms with the flapping motion. (a) total thrust; (b) contribution from the pressure force; (c) contribution from the viscous force.

| | $\bar{C}_T$ | $\bar{C}_{T\_P}$ | $\bar{C}_{T-v}$ |
|---|---|---|---|
| Rectangular | $1.36 \times 10^{-2}$ | $4.72 \times 10^{-2}$ | $-3.36 \times 10^{-2}$ |
| Bio-inspired | $0.17 \times 10^{-2}$ | $3.07 \times 10^{-2}$ | $-2.90 \times 10^{-2}$ |
| Rectangular(Com.) | 0.366 | 0.466 | -0.100 |

**Table 1.** Time-averaged thrust coefficient histories for different wing planforms with the flapping motion or the combined motion indicated by 'Com.'. $\bar{C}_T$ stands for the time-averaged total thrust; $\bar{C}_{T\_P}$ stands for the contribution from the pressure force; $\bar{C}_{T\_v}$ stands for the contribution from the viscous force.



(a) $\phi = 0^o$  (b) $\phi = 90^o$  (c) $\phi = 180^o$  (d) $\phi = 270^o$
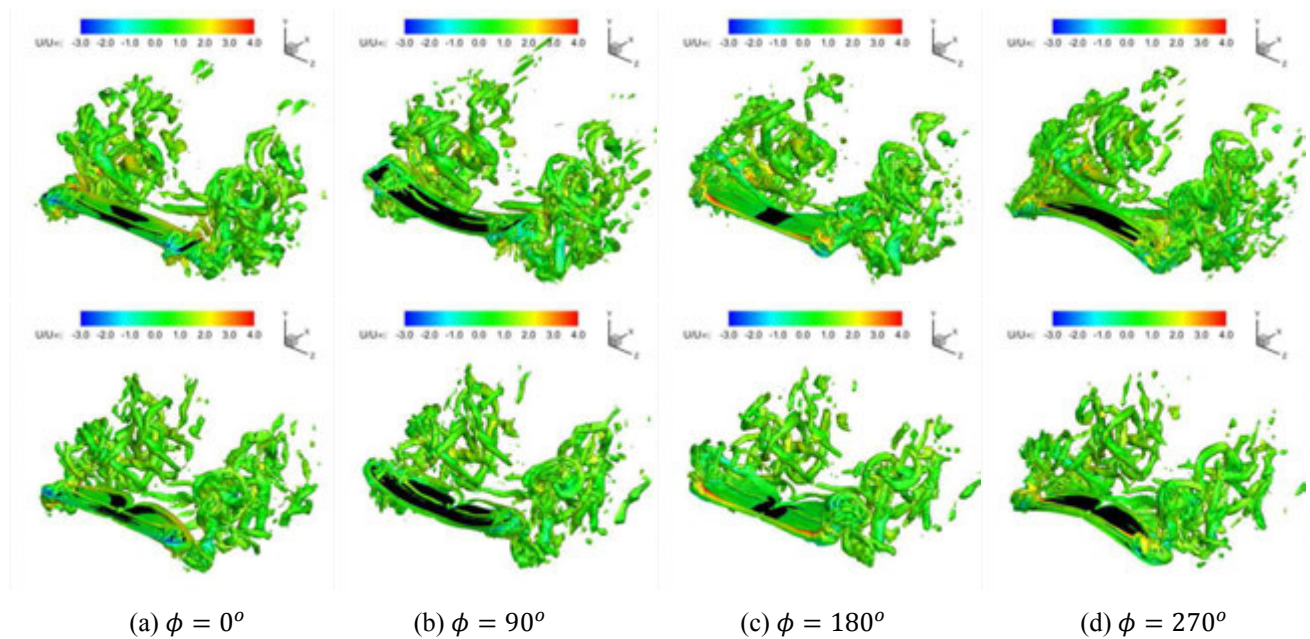
**Figure 8.** Comparison of the vortex topology for the rectangular and bio-inspired wings at four phases ($0^o, 90^o, 180^o$ and $270^o$) with the flapping motion. The upper row is for the rectangular wing while the lower row is for the bio-inspired wing.

(a) 50% wingspan                  (b) 75% wingspan               (c) wingtip
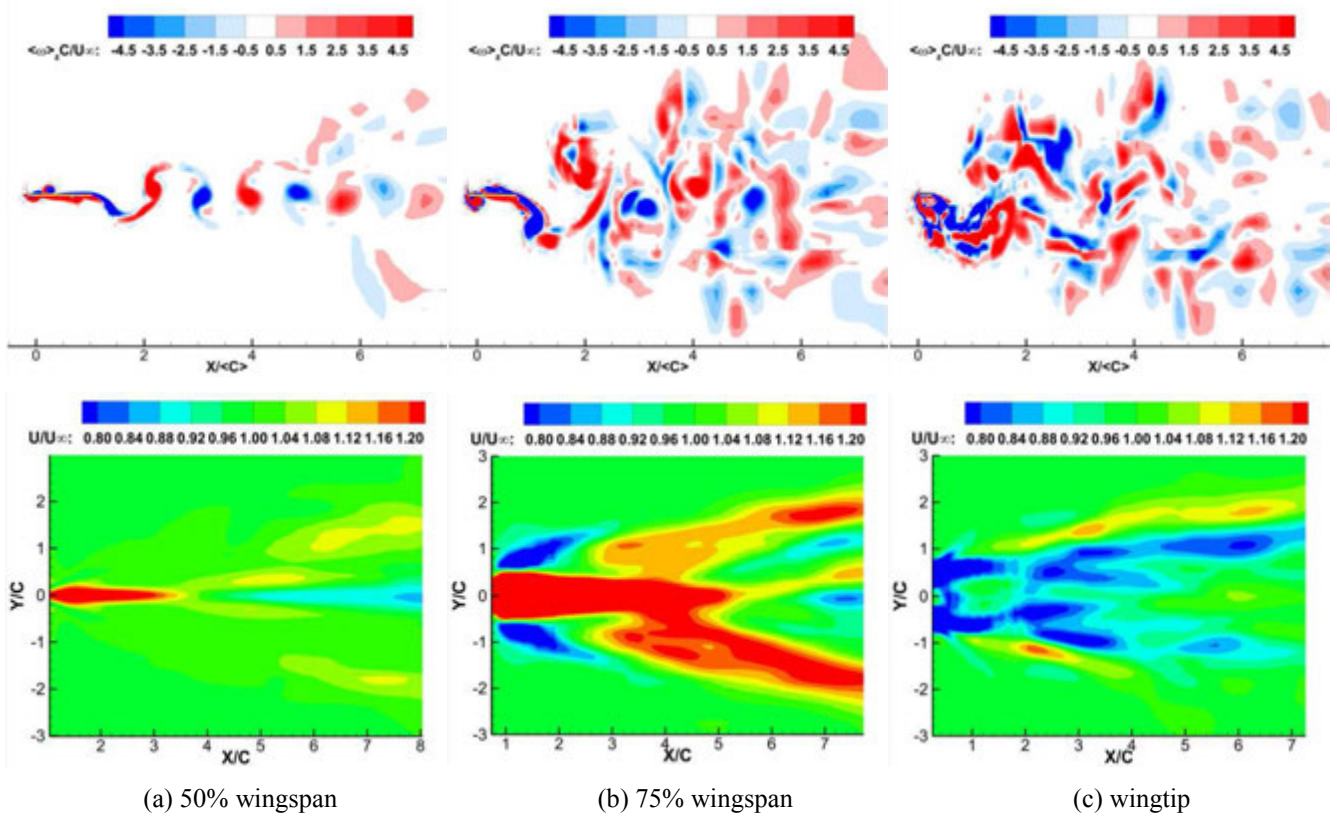
**Figure 9.** Instantaneous vorticity fields and the corresponding time-averaged velocity fields at (a) 50%, (b) 75% wingspan and (c) wingtip for the flapping bio-inspired wing.
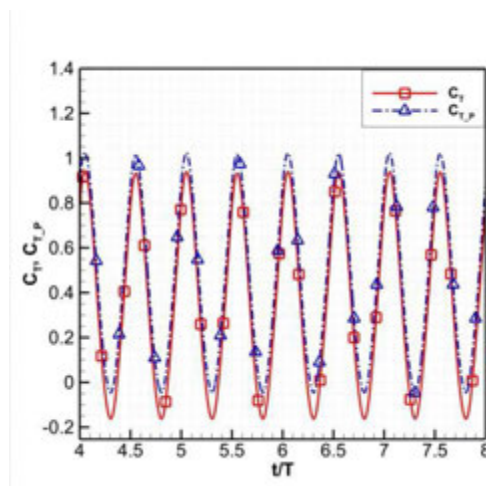


**Figure 10.** The total thrust coefficient history and that from the pressure force for the rectangular wing with the combined motion.

(a) $\phi = 0^o$    (b) $\phi = 90^o$    (c) $\phi = 180^o$    (d) $\phi = 270^o$
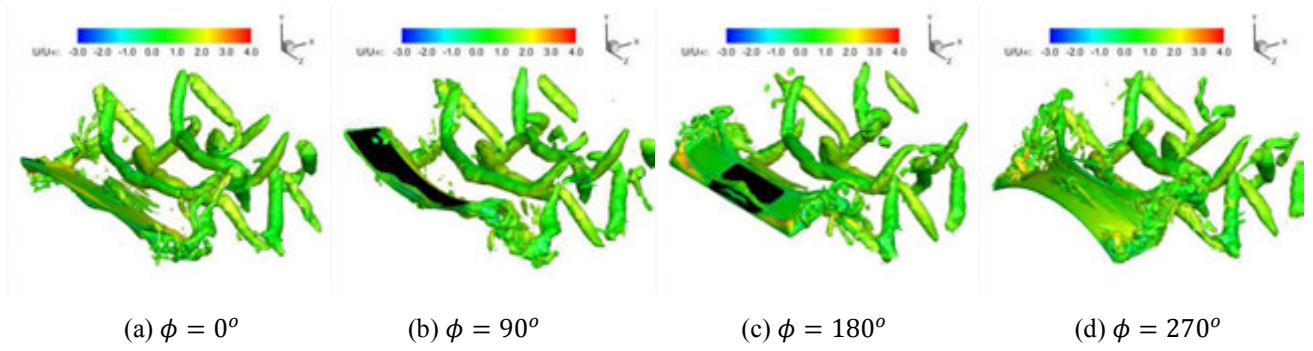
**Figure 11.** Vortex topology for the rectangular at four phases ($0^o, 90^o, 180^o$ and $270^o$) with the combined motion.

# CHAPER 8. General Conclusion

A dynamic unstructured grid based high-order SD compressible Navier-Stokes solver is developed to perform high-fidelity simulations for flapping-wing aerodynamics. A gradient-based cost-effective multi-level optimization algorithm is incorporated into the solver to carry out flapping wing related optimizations. Both the GCL and low Mach number preconditioning procedure work well with the high order accuracy SD method and it is demonstrated that the developed algorithm preserves the high-order accuracy of the SD method on dynamic grids and works efficiently for bio-inspired flow problems.

In the experimental and numerical analyses of the wake structures behind an oscillating NACA0012 airfoil, two types of wake transition processes (i.e. the transition from a drag-indicative wake to a thrust-indicative wake and that from the symmetric wake to the asymmetric wake) are identified. The wake transition point from the drag-indicative type to the thrust-indicative type is found to be $S_t = 0.12$; the transition point from the symmetric type to the asymmetric type is at $S_t = 0.31$. The asymmetric wake is believed to be closely related to the formation of a dipole-like vortex pair shed in one pitching cycle and can be treated as an inviscid phenomenon. The deflective angle of the asymmetric wake is determined by the initial phase angle and the asymmetric wake structures are more sensitive to the Strouhal number than the reduced frequency.

In the numerical assessments of the airfoil thickness effects, it is found that viscous force plays a substantial role in thrust production for thin airfoils. For the airfoils with relatively large thickness, viscous force contributes mainly to drag production, and its effect is almost negligible. The role change of viscous force in the thrust generation of the plunging airfoils is found to be closely related to the dynamics of the unsteady vortex structures around the plunging airfoils.

From the numerical simulations of a series of NACA 4-digit airfoils with different kinematics, it is found that the combined plunging and pitching motion can outperform the pure plunging and pitching motions by sophisticatedly adjusting the airfoil gestures during the oscillation stroke. With the same kinematics, thin airfoils outperform thick airfoils. For all airfoil thicknesses, relatively low reduced frequency is conducive to the thrust production and propulsive efficiency. In the kinematics optimization of the oscillating airfoils, four

kinematics parameters, namely the oscillation frequency, plunging and pitching amplitudes and the phase lag between the plunging and pitching motion, are optimized. The maximum propulsive efficiency of a flapping NACA 4-digit airfoil can achieve more than 50% when the oscillating kinematics is optimized. From the simulations using high-order accuracy scheme, it is found that the maximum propulsive efficiency appeared to occur right before the incipience of leading edge separation.

The formation of a two-jet-like wake pattern after the 3D flapping wing is explained by analyzing the interaction between wake and wingtip vortex structures. It is found that the bent wingtip vortices play a vital role in the two-jet-like wake pattern formation. The vortex structures around flapping wings with different wing planforms and the corresponding aerodynamic performances are analyzed. It is confirmed that the aerodynamic force production during cruise flight is dominated by the pressure force and is closely related to the dynamics of LEVs. From the comparison of the aerodynamic forces generated with different wing kinematics, it is found that the pure plunging motion is not conducive to the propulsive performance. A combined plunging and pitching motion can drastically increase the thrust production.

# ACKNOWLEDGEMENTS

I would like to take this opportunity to thank the many people who made this thesis possible. First and foremost, I would like to thank my advisors Dr. Z. J. Wang and Dr. Hui Hu, for their invaluable guidance and support throughout this research and for giving me the freedom to shape my own research framework, providing me with the opportunity to attend international conferences.

I would like to thank my committee members, Dr. Paul Durbin, Dr. Alric Rothmayer, Dr. Xinwei Wang and Dr. Jue Yan, for their efforts and contributions to this work. I say thanks to my fellow group members, Dr. Haiyang Gao, Dr. Haga Takanori, Dr. Varun Vikas, Dr. Ying Zhou, Mr. Lei Shi, Dr. Zifeng Yang, Mr. Yan Zhang, Mr. Hirofumi Igarashi, Mr. Lucas Clemons, Mr. Travis Grager, Mr. Daniel Dvorak, Mr. Ahmet Ozbay, Mr. Anand Gopa Kumar, Dr. Wei Tian, Dr. Blake Johnson, Dr. Yi Li, Ms. Yanan Li, Ms. Cheng Zhou, Mr. Kai Zhang and Mr. Zhenyu Wang for the pleasant and inspiring working environment. I also would like to thank all other friends for the happy memories during my stay in Ames. Special thanks also go to Mr. John Dickerson and Mr. James Wellman for their help with the cluster maintenance, and Mr. Bill Richard and Mr. James Benson for their help with building the experimental setup during this study, and all staff members in the main office, especially Ms. Delora Pfeiffer, for being so considerate and helping keep track of my degree progress.

Finally, I would like to thank my parents and my maternal grandmother for their selfless love and support during my life. Also, I am in debt to my wife Bin Wang for her unconditional support and devotion in everyday life. Her genuine love and confidence in me make me strong in my way to fulfillment.